Endocavitary applicator of therapeutic ultrasound integrated with RF receiver coil for high resolution MRI-controlled thermal therapy

Mihaela Rata

N° d'ordre 282-2009 Année **2009**

THESE DE L'UNIVERSITE DE LYON

Délivrée par
L'UNIVERSITE CLAUDE BERNARD LYON 1

ECOLE DOCTORALE
EDISS

DIPLOME DE DOCTORAT
(arrêté du 7 août 2006)

soutenue publiquement le 15 décembre 2009

par
Mlle. Mihaela RATA

TITRE :

Endocavitary applicator of therapeutic ultrasound integrated with RF receiver coil for high resolution MRI-controlled thermal therapy

Directeur de thèse : **M. Rares Salomir**

JURY:

M. Hervé Saint-Jalmes,	**Rapporteur**
M. Ian Rivens,	**Rapporteur**
M. François Cotton	
M. Philippe Douek	
M. Mihai Todica	
M. Rares Salomir	

UNIVERSITE CLAUDE BERNARD - LYON 1

Président de l'Université	**M. le Professeur L. Collet**
Vice-président du Conseil Scientifique	M. le Professeur J-F. Mornex
Vice-président du Conseil d'Administration	M. le Professeur G. Annat
Vice-président du Conseil des Etudes et de la Vie Universitaire	M. le Professeur D. Simon
Secrétaire Général	M. G. Gay

COMPOSANTES SANTE

Faculté de Médecine Lyon Est – Claude Bernard	Directeur : M. le Professeur J. Etienne
Faculté de Médecine Lyon Sud – Charles Mérieux	Directeur : M. le Professeur F-N. Gilly
UFR d'Odontologie	Directeur : M. le Professeur D. Bourgeois
Institut des Sciences Pharmaceutiques et Biologiques	Directeur : M. le Professeur F. Locher
Institut des Sciences et Techniques de Réadaptation	Directeur : M. le Professeur Y. Matillon
Département de Formation et Centre de Recherche en Biologie Humaine	Directeur : M. le Professeur P. Farge

COMPOSANTES SCIENCES ET TECHNOLOGIE

Faculté des Sciences et Technologies	Directeur : M. Le Professeur F. Gieres
UFR Sciences et Techniques des Activités Physiques et Sportives	Directeur : M. C. Collignon
Observatoire de Lyon	Directeur : M. B. Guiderdoni
Institut des Sciences et des Techniques de l'Ingénieur de Lyon	Directeur : M. le Professeur J. Lieto
Institut Universitaire de Technologie A	Directeur : M. le Professeur C. Coulet
Institut Universitaire de Technologie B	Directeur : M. le Professeur R. Lamartine
Institut de Science Financière et d'Assurance	Directeur : M. le Professeur J-C. Augros
Institut Universitaire de Formation des Maîtres	Directeur : M R. Bernard

Remerciements

Heureusement, ces lignes me permettent de laisser une trace de ma gratitude à tous ceux qui, scientifiquement ou humainement, ont aidé au bon déroulement de cette thèse.

Premièrement, je tiens à remercier mon directeur de thèse, monsieur Rares Salomir pour son aide à découvrir des choses intéressantes et nouvelles, pour sa disponibilité et ses conseils bienvenus. Son énergie et son enthousiasme nous ont permis de surmonter les obstacles qui se sont présentés.

J'exprime ma gratitude à messieurs Hervé Saint-Jalmes et Ian Rivens d'avoir accepté la fonction de rapporteurs de cette thèse, ainsi qu'à messieurs François Cotton, Philippe Douek et Mihai Todica pour l'intérêt qu'ils ont montré à ce travail en acceptant d'être membres du jury. Je remercie également M. François Cotton du Service de Médecine Nucléaire et Radiologie du CHU Lyon-Sud pour ses conseils et la mise à disposition du temps machine sur l'imageur clinique RMN 1.5 T corps entier.

Je remercie monsieur Jean-Yves Chapelon, directeur de l'unité 556 de l'Inserm, pour m'avoir accueilli au sein du laboratoire. Je remercie plus particulièrement messieurs Dominique Cathignol et Cyril Lafon, ancien et actuel directeurs de l'équipe 1, d'avoir facilité mon intégration au sein de l'équipe.

Je remercie chaleureusement M. Onuc Cozar de l'Université Babes-Bolyai, Cluj-Napoca, Roumanie de m'avoir offert l'opportunité d'effectuer un stage à Lyon dans le cadre du programme "Socrates/Erasmus". Je remercie aussi M. André Briguet de l'Université Claude Bernard Lyon 1 de m'avoir accueilli dans cette Université dans le cadre de la même mobilité "Socrates/Erasmus".

Merci encore à messieurs Michael Bock, Jürgen Jenne et Reiner Umathum de DKFZ, Heidelberg, Allemagne pour la fructueuse collaboration au sujet des antennes RF. Egalement, un grand merci à M. Christian Paquet de l'Ecole Vétérinaire de Lyon pour sa disponibilité et son énergie nocturne pendant les expérimentations *in-vivo*. Je remercie aussi M. Adrien Matias pour tous les montages réalisés ensemble et M. Alain Birer pour son savoir-faire au sujet des transducteurs.

J'adresse mes remerciements sincères à l'ensemble du personnel de l'unité pour leur gentillesse et leur soutien. Je pense en particulièrement à Isabelle Besançon, Christophe Béra, Remy Souchon, Françoise Chavrier, Bernard Lavandier, David Melodelima.

Je suis reconnaissante d'avoir connu des gens extraordinaires pendant ces années de thèse avec lesquels j'ai partagé des moments merveilleux au laboratoire, mais aussi en dehors. Merci pour votre amitié: Adriana, Guillaume, Lorena, Apoutou, Izella, Vincent, Jhonny, Lucie, Jérémy et tous les autres.

Dernièrement, mais les premiers dans mon âme, merci à mes proches, à Cédric, à ma famille, à mon frère et à mes amis depuis toujours, pour leur soutien inconditionnel durant toute cette thèse. J'espère que vous serez content de moi.

Contents

Chapter I. Introduction

I.1 Cancer in general context

I.1.1 Esophageal cancer

Statistics
Characteristics
Classical treatments
New treatments

I.1.2 Rectal cancer

Statistics
Characteristics
Classical treatments
New treatments

I.1.3 Ultrasound for digestive cancer treatment

I.2 Therapeutic ultrasound

I.2.1 Ultrasound basics

Definition
Generation
Acoustic field
Characteristics

I.2.2 Biological effects of ultrasound

Thermal effects
Non-thermal effects

I.2.3 Applications

I.3 MRI introduction

I.3.1 MRI basics

Physical principles
Relaxation phenomena
Signal and image acquisition
Image quality

I.3.2 MR thermometry and tissue heating control

Temperature dependence of water proton resonance frequency
Pulse sequences for PRFS thermometry
Thermotherapy with closed-loop feedback control

I.3.3 RF receive-only coils

I.1 Cancer in general context

Although the possibilities to cure cancer reach more than 50%, with some cancer completely cured (as testicular cancer, for example), and despite the incessant progress made in terms of treatment, detection, and prevention, the disease remains feared by the majority of patients. At global level, cancer data are always collected and compiled sometimes after the events to which they relate, so that the most recent statistics available are always "old". Moreover, because the sources of data are continuously improving in quality and extent, estimates may not be truly comparable along time.

The most recent worldwide cancer statistics available is GLOBOCAN 2002 database [Ferlay *et al*, 2004]. Figure I.1 is derived from this source and presents the incidence and mortality of cancer, for men and women, in 2002. Lung cancer was the first cancer in term of incidence, showing also a high mortality rate. At that time, 10.9 million people worldwide were annually diagnosed with cancer and 6.7 million people died. These deaths represented around 12% of deaths worldwide. The same source (GLOBOCAN 2002) estimated that 24.6 million people worldwide were diagnosed with a cancer in the last five years and around half of these people lived in Europe and North America.

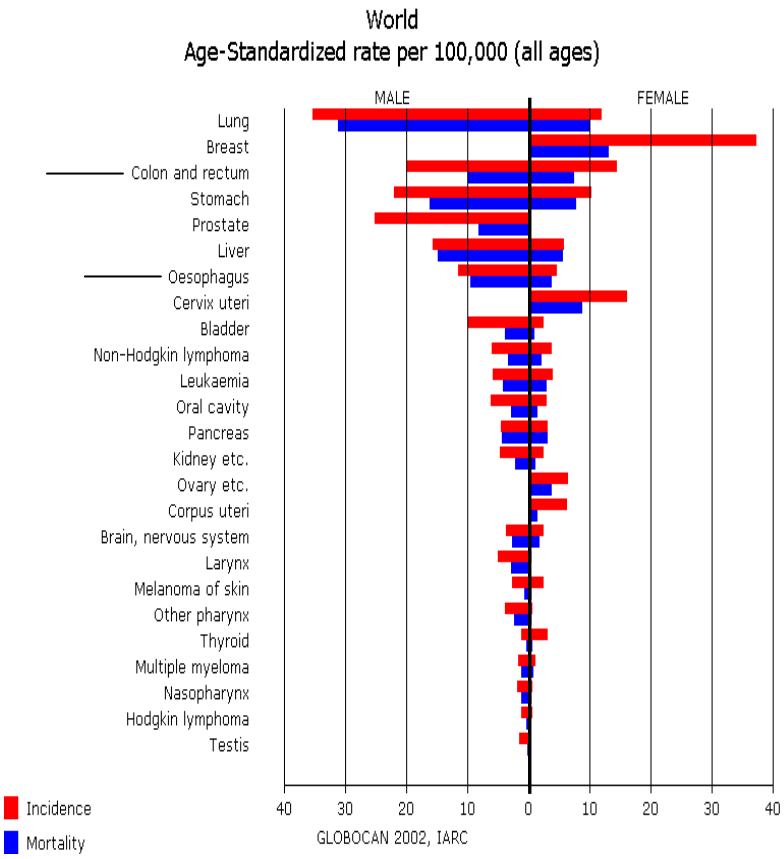

Figure I.1. Age-standardized incidence/mortality rates, all cancers, world, 2002 estimates.

At national level, cancer data are more recent and cancer trend may be observed. In France, cancer becomes, in 2004, the first cause of death [Aouba *et al*, 2007]. Also, cancer remains the most lethal disease for people between 45 and 64 years. One of two men and one of three women are concerned. According to the latest data from French National Institute of Health Monitoring [Belot *et al*, 2008], cancer incidence doubled from 1980 to 2005, but the mortality risk declined with 25%. This divergence may be explained by a diminution of aggressive cancers (such as esophagus or stomach) and an increase of favorable prognosis cancers (breast, prostate). In 2005,

at national level, 320 000 new cases of cancer (180 000 for men and 140 000 for women) were diagnosed and 146 000 deaths were registered (please see Table I.1 for further details). Contrary to the worldwide behavior observed in 2002 (GLOBOCAN 2002), in France, the most common cancer was breast cancer, followed by colon and rectum, lung and prostate. This classification of cancer changed [Belot *et al*, 2008], especially due to the rising incidence of prostate cancer (for men) and of lung cancer (for women). Therefore, the prostate cancer becomes the most frequent cancer, for both sexes. For men, the three most common cancers are prostate, lung and colon/rectum cancers, while women are mostly affected by breast, colon/rectum and lung cancers.

In the work described in this thesis, regions of the digestive tract containing a natural cavity, i.e. esophagus, and colon & rectum, are considered. Table I.1 [Belot *et al*, 2008] summarizes statistics data trends for esophageal and colon/rectum cancer in French population for a period of 25 years. Data for all cancers are also presented for comparative purpose.

Incidence	1980	1985	1990	1995	2000	2005
Esophagus	494	5 591	5 542	5 381	5 091	4 721
Colon-rectum	23 804	26 470	29 187	31 990	34 623	37 413
All cancers	**168 850**	**188 742**	**211 776**	**239 792**	**273 518**	**319 380**

a).

Mortality	1980	1985	1990	1995	2000	2005
Esophagus	5 378	5 147	4 875	4 568	4 222	3 850
Colon-rectum	15 153	15 238	15 446	15 778	16 141	16 865
All cancers	**129 274**	**136 335**	**141 751**	**145 378**	**146 165**	**145 762**

b).

Table I.1. a), b). Incidence (a) and mortality (b) cases for esophageal and colon/rectum cancer, over 1980-2005, in France.

I.1.1 Esophageal cancer

Statistics. Esophagus cancer shows, in 2002, a worldwide incidence of about 462 000 cases annually (the eighth most common cancer, corresponding to 4.2% of the total) and causes 386 000 deaths (the sixth most common cause of death from cancer, i.e. 5.7% of the total) [Parkin *et al*, 2005]. The majority of cases (80-85%) are diagnosed in developing countries where it is the fourth most common cancer in men [Cancer Research UK, 2005]. The area with the highest reported incidence is the so-called Asian "esophageal cancer belt", from Turkey to China, but restrained region from south/south-east Africa, South America or parts of Europe were also reported.

Within European countries, the GLOBOCAN 2002 data shows that French men had the highest incidence rates, followed by men from the UK and Hungary, while UK women had the highest reported incidence of female esophageal cancer. In 2005, esophageal cancer was the 9th

cancer in term of incidence in UK (7 823 new cases with a male/female ratio of 1.8) [Office for National Statistics, 2008]. With 7 405 deaths in 2006, esophageal cancer is responsible for around 5% of all cancer deaths, making it the 5th most lethal cancer. In France, esophageal cancer incidence represents 1.5% of all cancers (see Table I.1.a), year 2005), i.e. the 15th most frequent cancer, men and women together. With a sex-ratio of 5.3, this cancer is one of the highest men-oriented diseases. A mortality rate of 2.6% of all cancers (the 11th rank of cancer in terms of mortality), closely related to that of incidence, reflect the lethal character of this type of cancer, unfortunately worldwide valid.

Characteristics. Esophagus (gullet) extends from the pharynx to the stomach and in adults is approximately 26 cm in length and 2 cm wide [Cancer Research UK, 2005]. The normal wall thickness varies in function of its state (contracted/dilated) and also for the different segments of esophagus (cervical, thoracic, retrocardiac and intra-abdominal). When contracted, the average thickness varies between 4.05-5.68 mm (the intra-abdominal segment has the highest value). In dilated state, the thickness varies from 1.87 to 2.7 mm (with cervical esophagus the thickest part) [Xia *et al*, 2008]. A cross-section of esophageal tissue shows 4 layers, from the lumen to the periphery: a) *mucosa* containing stratified squamous epithelial cells, glands and muscularis mucosa; b) *submucosa* – adipose, fibrous connective tissue and blood vessels; c) *muscularis externa (propria)* – circular and longitudinal muscle layers; and d) *serosa (adventitia)*.

Esophageal cancer has two main histological causes. Sixty percents of esophageal cancers appear in the cells lining the esophageal tube (squamous cell carcinoma-SCC), usually in the upper two-thirds of the esophagus. The remaining 40% is represented by adenocarcinomas (AC-malignant cells developed in the glandular tissue), and generally this type of cancer is localized in the lower esophagus. Before an adenocarcinoma can develop, glandular cells (which normally do not cover the esophagus) must replace an area of squamous cells, as in the case of Barrett's esophagus. Over the past several years, the incidence of adenocarcinomas was found increasing in Western populations, but the underlying reasons for this are unclear. If these trends continue, AC will become the dominant histology; this has already happened for white men in the USA and UK [Wild *et al*, 2003].

The principal risk factors are age, sex, alcohol, tobacco, other type of irritation of the esophagus and medical history. In Europe and Northern America most esophageal cancers are caused by tobacco and alcohol, but in South America the consumption of hot beverages (maté) are thought to be important. Nutritional deficiencies (zinc) may underlie the high rates in Central Asia and China [Cancer Research UK, 2005]. There are well established risk factors for both types of esophageal tumor. American data [Engel *et al*, 2003] suggest that smoking, higher body mass index, low intake of fresh fruit and vegetables, and gastro-esophageal reflux are responsible for an

estimated 79% of AC; while tobacco consumption, excessive alcohol consumption, and low fruit and vegetable intake are estimated to cause 89% of SCC. Tobacco and/or alcohol remain the main risk factors, whose effect is directly related to quantity and duration of consumption. For example, smoking cessation induces an immediate esophageal risk decline, but a value equal to that of a non-smoker will be obtained only 10 or more years after giving up. Risk of esophageal cancer is increased in people who have had radiotherapy to the mediastinum for another primary cancer: breast cancer [Roychoudhuri *et al*, 2004] or Hodgkin's disease [Dores *et al*, 2002].

The most common symptom is difficulty in swallowing (obstructive dysphagia). It can also be associated with weight loss and sometimes pain or discomfort behind the breast bone or in the back. However, these are not regarded as certain signs of cancer. Esophageal cancer is usually diagnosed with an endoscopic examination of the esophagus (esophagoscopy) or barium swallow X-ray. Generally, biopsy is performed during endoscopy in order to establish the histological diagnosis: SCC or AC. More detailed examinations (endoscopic ultrasound, bronchoscopy, thoracoscopy/laparoscopy, CT-computer tomography, PET-positron emission tomography or MRI -magnetic resonance imaging) are essential to delimit the cancer position/size and to detect the lymph nodes state or possible distant metastases. Generally, cancer staging (TNM system) describes important data about primary tumor (T), lymph nodes (N) and metastases (M). Tumor stage is classified from T0 to T4 by the degree of advancement of tumoral cells: **T0** (carcinoma in situ): the cancer is localized only in the epithelium of the esophagus (the first layer of the mucosa); **T1**: the mucosa or submucosa are affected; **T2**: the tumor has invaded the muscularis externa, the third layer of esophageal wall; **T3**: the tumor has advanced through the entire esophageal wall, including adventitia; **T4**: the nearby tissues of esophagus are affected. Note that, when stenosis is observed, the tumor stage is regarded as T3. Concerning the stage of lymph nodes N and metastasis M, a value of 0 indicates no extension, while 1 corresponds to cancer spreading to lymph nodes or distant organs. Finally, all data are combined to assign a complete cancer stage:

- **stage 0** (T0, N0, M0): epithelium, no lymph nodes, no metastases;
- **stage I** (T1, N0, M0): only first or the second layer of esophagus, no lymph nodes, no metastases;
- **stage** II with **IIA (**less aggressive) and **IIB** (more aggressive):

stage IIA (T2 or T3, N0, M0): to the third layer or all esophagus, no lymph nodes, no metastases;
stage IIB (T1 or T2, N1, M0): any of the three inner layers of esophagus (but not adventitia) & nearby lymph nodes, no metastases.

- **stage III** (T3, N1, M0 **or** T4, any N, M0): all esophagus & nearby lymph nodes **or** nearby organs with or without nearby lymph nodes, no distant nodes or organs;
- **stage IV** (any T, any N, M1): metastases.

Classical treatments. A complete and correct staging of the cancer will help the medical staff to decide on an adequate treatment. Unfortunately, esophageal cancer has a high instance of mortality with a prognosis of less than 10% survival rate at five years after diagnosis, all stages included (0% if metastasis, 10% if lymph nods are involved, 25% if there is no adenopathy or metastasis) [Simon *et al*, 2003].

Currently, the single option for curative treatment is surgery (with lymph nodes removal), but only for stage I and II. Metastatic cancer or tumor invasion of surrounding structures (e.g. trachea, bronchi, aorta, pericardium) is not considered for surgery. Also, clavicular or celiac lymphadenopathy is counted for metastasis. However, regardless tumor staging, the patient general condition (age, weight loss, cardiovascular or pulmonary problems, liver) may be a contraindication to surgery. Only about a third of cancer patients are candidates for esophageal surgery. Moreover, after a surgery with curative resection (R0), only 30% of patients shown a 5-year survival rate [Bouvier *et al*, 2006]. After surgery, most patients are able to resume normal activities within 2 months. Side effects of the procedure include pain and tenderness, which usually can be controlled with medication. Complications may be severe (bleeding, cardiac or pulmonary complication, infection at the incision site, nerve injury) and occur in about 40% of patients.

For advanced stages of disease (i.e. tumor invading adjacent structures such as mediastinal extension), surgery must be associated with chemotherapy (ChT) and radiotherapy (RT) [Mariette *et al*, 2007]. The single association of chemotherapy [Hwang, 2007], [Urschel *et al*, 2002] or radiotherapy [Lordick, 2005], [Mariette *et al*, 2007] with surgery does not offer good results. A study investigating the role of chemotherapy and radiation therapy [Graham *et al*, 2007] showed that neoadjuvant (before surgery) radiochemotherapy (RCT) appears to be correlated with the best survival rates and the largest improvement in quality of life, but definitive proof is not currently available. The role of surgery, radiotherapy, and chemotherapy, alone or combined, in the optimal management of esophageal cancer is still under intensive research.

However, for inoperable patients, the combination of radiotherapy (dose limit: 50 Gy) and chemotherapy (reference drugs: 5FU-fluouracil and cisplatin) remains the standard curative treatment. These techniques are also widely used for palliation. Nevertheless, important side effects must be considered: fatigue, reddening of the skin (radiotherapy), and nausea, alopecia, skin rash and itching, mouth and lip sores (chemotherapy). Generally, the outcome is improved when patients are managed by multidisciplinary teams at specialized units.

New treatments. Numerous endoscopic therapy are proposed as an alternative to classical treatment: endoscopic mucosal resection (EMR) [Ell *et al*, 2000], photodynamic therapy (PDT) (Photofrin®, 5-aminolevulinic acid) [Lightdale *et al*, 1995], laser therapy (Nd:YAG – neodymium:

yttrium-aluminum-garnet, KTP – potassium-titanyl-phosphate)[Gossner *et al*, 1999], intraluminal stents [Siersema, 2006], endoscopic radiofrequency (RF) ablation [Sharma *et al*, 2007], argon plasma coagulation (APC) [May *et al*, 1999], or, recently reported, cryospray ablation [Cash *et al*, 2007].

Because of their small penetration depth –APC, PDT and laser therapy– are generally indicated for the treatment of early stage cancers, when only the mucosal layer (typically 2 mm width) is affected. However, even if such endoscopic ablative techniques have high success rates in removing Barrett's epithelium or other superficial cancers, their effect at the genetic level is unclear and the remaining tissue may still contain genetic alterations associated with malignant progression to cancer [Hage *et al*, 2006]. Among the currently available endoscopic treatments of the superficial cancers in esophagus, only endoscopic mucosal resection offers the advantage of histological analysis of the removed sample [Gossner, 2006] and may therefore represent a truly curative treatment. Moreover, EMR is indicated for cancer size of less than 2 cm in diameter.

Endoscopic palliation is the most suitable approach for metastatic patients with poor performance status (not capable to support radiochemotherapy) or with esophago-tracheal fistula. Palliation aims to improve the patient quality of life, and especially, to relief the dysphagia. Two modalities are generally used: stenting the stenose (expandable metal/plastic stent) or reducing the tumor mass using thermoablation (methods cited above). The risks associated with these strategies cannot be neglected (esophageal stricture, hemorrhage, stent migration, wall perforation, temporary light sensitivity). Also, single dose brachytherapy (12 Gy) may be an effective option for palliation.

I.1.2 Rectal cancer

Generally, the colon (especially the sigmoid colon) and rectum cancers are widely grouped together because their similarities (risk factors, histological pathology). We have preserved this classification only for the following paragraph (statistics). Furthermore, we refer exclusively to rectal cancer, since this was the object of interest of a part of the work described in this thesis.

Statistics. Colon and rectum cancers account for about 1 million new cases in 2002 (9.4% of the world total) and 529 000 deaths [Parkin *et al*, 2005]. In terms of incidence, colorectal cancers rank fourth in frequency in men and third in women, showing very little difference between sexes (men/women ratio of 1.2:1). Contrary to the esophageal cancer, colorectal cancer has a relatively good prognosis, with mortality to incidence ratio of about 50%. Therefore, the worldwide prevalence (in 2002) of colorectal cancer is second after breast cancer, with an estimate of 2.8 million people alive with colorectal cancer within 5 years following diagnosis. Geographic variation in occurrence of colorectal cancers appears at the level of world area. A 25-fold variation

is observed between high-risk region (North America, Australia/New Zealand, Western Europe, and, in men especially, Japan) and low-risk region (Africa and Asia, parts of South America). Moreover, in high-risk populations, the ratio of colon to rectal cancer incidence is 2:1 [Parkin *et al*, 2005].

American data from National Cancer Institute/ Surveillance Epidemiology and End Results [Ries *et al*, 2008] estimates 148 810 new cases of colorectal cancer and 49 960 deaths, in 2008. However, American population has the highest survival rate at 5 years after diagnosis: 65%. This rate may be explained by a descending trend in terms of incidence and mortality rates. Unfortunately, this trend is not the case of France. From 1980 to 2005, according to Table I.1, the cases of colorectal cancer (both terms of incidence and mortality) continue to increase in French population. In 2005, 37 413 new cases were diagnosed (11.7% of all cancers) and 16 865 deaths (11.6% of all) were noted. In France, the colorectal cancer is the third most common cancer (incidence) and the second cancer in term of mortality.

Characteristics. The normal rectum is 11 to 15 cm long and has a maximum diameter of 4 cm [Santoro *et al*, 2006]. It is continuous with the sigmoid colon superiorly and the anal canal inferiorly. The mean thickness of normal rectal wall is estimated at 2.57 mm with individual variation thickness from 2.2 to 3.6 mm [Huh *et al*, 2003]. However, a maximal thickness of 4 mm for the entire wall is still considered normal. Moreover, maximal values of 1 mm for mucosa and 2 mm for muscularis propria are considered normal [Van Outryve *et al*, 1993]. Component of digestive system like the esophagus, the rectum wall has also 4 layers (see Fig. I.2): *mucosa, submucosa, muscularis propria,* and *serosa with perirectal fat.*

Rectal cancer is, with an overwhelming majority (90%), an adenocarcinoma-type [Gasowski *et al*, 2003]. Other rarer types include lymphoma and squamous cell carcinoma. Generally, it develops from adenomatous polyps (adenomas); it was observed that an adenoma may develop a cancer over an average period of 9 years. The number of these polyps increases with age, but only large polyps (size >1 cm) are potentially dangerous. However, people with some hereditary condition like familial adenomatous polyposis (FAP) or hereditary nonpolyposis colon cancer (HNPCC or Lynch syndrome) must be periodically screened. Also, people who had inflammatory bowel disease (Crohn's disease, ulcerative colitis) or cancer history (colon, ovary, and uterus) must be under surveillance. Important risk factors –that may be controlled– are diet (read meat), smoking, alcohol, obesity and physical inactivity.

Symptoms for rectal cancer are not specific and generally appear for advanced stage: weight loss, blood in the stools, abdominal/pelvic pain, changes in bowel activity. Diagnosis is based on endoscopy (sigmoidoscopy - for rectum and sigmoid colon visualization; colonoscopy when entire colon is investigated) or the less accurate DRE (digital rectal examination). After

cancer confirmation by endoscopy, staging techniques (endosonography, MRI, CT) are used in order to determine how far the cancer has spread. The TNM system (substitute of an ancient system known as Dukes') is similar to the description of the esophageal system. The T and M stages are the same, while the N stage is subdivided into N0 (no lymph node involvement), N1 (extension to 1 to 3 nodes), and N2 (extension to more than 3 nodes). Metastases are generally observed in liver, lungs, colon or pelvis. The external iliac nodes are also considered as metastasis. Finally, the stage grouping is slightly different. Figure I.2 summarizes this classification: **stage 0** (T0, N0, M0), **stage I** (T1 or T2, N0, M0), **stage II** (T3 or T4, N0, M0), **stage III** (any T, N1-2, M0), and **stage IV** (any T, any N, M1).

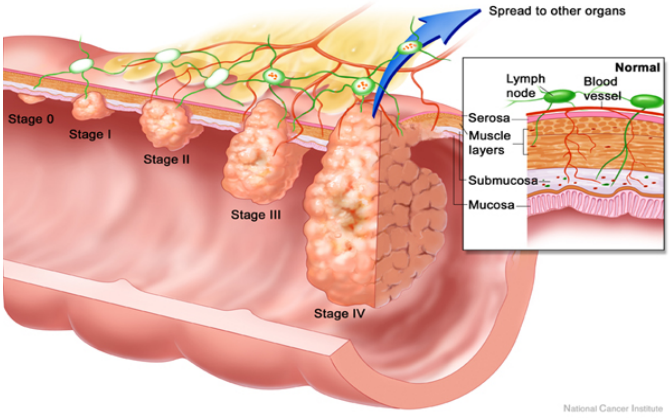

Figure I.2. Cancer staging (0 to IV) and normal wall structure (4 layers) for the rectum.
Source: site of Siteman Cancer Center /Barnes-Jewish Hospital /Washington Univ. School of Medicine-www.siteman.wustl.edu

The most suitable staging technique is endosonography (endorectal ultrasonography ERUS) since it allows exact differentiation of the rectal wall layers [Beynon, 1989], and tumor staging (up to stage 3) with median accuracy of 89% [Maier *et al*, 2003]. But, lymph nodes staging by ERUS is less accurate (80%) [Glaser *et al*, 1990]. When compared to endosonography, MRI has less accuracy (85%) in tumor staging [Maier *et al*, 2003], but it permits the mesorectum and the mesorectal fascia evaluation [Beets-Tan *et al*, 2001]. This is a very important feature concerning the cancer resectability and the risk of recurrence. Furthermore, MRI can be employed in cases of stenosing tumors and also for the detection of metastases located at different sites within the body. However, important improvement in technologies for all imagistic methods (contrast agent or higher field for MRI, combination PET-CT) may lead to more accurate cancer staging and that it is only the benefit of the patient.

Classical treatments. Clinical decision in treatment of rectal carcinoma depends on several factors: tumor location, penetration of bowel wall, lymph node status, and metastasis. Hence, an exact preoperative staging of the cancer will help to decide the best treatment. For example, a standard curative surgery must contain a total excision of the mesorectum*. Therefore the cancer resectability is decided –before the surgery– on the basis of MR image of the mesorectal fascia (the external limit of the mesorectum). A safety lateral margin of minimum 1 mm is demanded for a curative resection (R0). Also, the localization of the tumor (upper, middle or lower rectum) with respect to the anal sphincter is an important criterion for the preservation of the anal function and

* fatty tissue envelop of the rectum, containing blood and lymph vessels, lymph nodes and autonomic nerves.

for choosing the type of exeresis. A distal margin of resection (distance between inferior limit of the tumor and the distal limit of rectum) of at least 1 cm may be an appropriate clearance of cancer, still preserving the anal sphincter [Shirouzu *et al*, 1995].

Like in the case of esophageal cancer, surgery remains the standard curative treatment. This time, the prognosis is considerably better. The survival rate at five years after tumor resection is 100% (stage 0), 85-100% (stage I), 65-75% (stage II), 50% (stage III, with 1-3 nodes involved), 25% (stage III, more than 3 nodes) and 0% (stage IV) [Gasowski *et al*, 2003]. The two main types of rectum surgery are the low anterior resection (LAR) and the abdominal perianal resection (APR). The LAR technique consists in partial/total rectum resection with anastomosis to the rest of rectum (colorectal) or the anus (coloanal), together with total mesorectal excision (TME) and at least 8 lymph nodes removal. The introduction of TME [Heald *et al*, 1982] as a standard procedure represented a large improvement in recurrence decrease and overall survival. Unfortunately, the APR technique is performed for patients without possible preservation of anal sphincter. The morbidity (fistula, abscess) rate for rectum surgery is less than 15%. However, surgery alone is curative only for stage I (tumors T1 or T2, N0).

For stages II or III, surgical resection (with TME) may still be curative, but only associated to (chemo)radiotherapy. The association of radiotherapy prior to surgery reduces the recurrence rate, when compared to surgery alone, but no differences were observed regarding the overall survival (at 2 years after intervention) [Kapiteijn *et al*, 2001]. The radiotherapy (RT) –long therapy (45 Gy in 5 weeks) or more recently, short therapy (25 Gy in 5 days)– can be delivered pre-, intra-, or post-operatively, but preoperative variant is preferred for his efficiency and reduced toxicity. The potential advantage of preoperative radiation is tumor down-staging, hence an enlarged resectability with possible sphincter-spare procedure. Also, the radiation therapy works better in well-oxygenated tissues prior to surgery and that conducts to a decrease in tumor viability, which results in less local recurrence. The recurrence rate may be further reduced by the addition of chemotherapy to RT, and once again the preoperative radiochemotherapy (RCT) option is preferred [Sauer *et al*, 2004]. The chemotherapy (ChT) is based on 5FU (fluouracil) associated with folinic acid (FUFOL) or more recent drugs (oxaliplatin, irinotecan), and may be adjuvant (for tumors with nodes involvement) or neoadjuvant, enhancing the RT effects. Overall, there is still debate (European countries, USA, Japan) regarding the best association of RT or/and ChT to surgery for rectal cancer, especially in terms of survival. The difficultly of a final conclusion on benefits of RCT to surgery may also arise from the leak of standardized surgery (with or without TME) in some trials. However, a worldwide consensus considers the multimodal therapy involving a multidisciplinary team of cancer specialists (gastroenterologists, surgeons, medical and radiation oncologists, radiologists and pathologists) as the best approach to the management of

rectal cancer. Moreover, RT and ChT are the standard methods used to fight cancer when surgical resection is not possible.

New treatments. Alternative endoscopic techniques are suitable for patients who are not candidates to standard methods (surgery or RCT), or may be used as complementary approaches. Also, alternative methods are more widely used for recurrent cancer treatment since, generally, patient condition is poor after a primary rectal cancer treatment. But, their use is mainly limited to palliation. Three main types of treatment can be counted: local excision (transanal endoscopic microsurgery), ablative techniques and stent application. The utilization for curative purpose of the less invasive transanal endoscopic microsurgery versus the radical surgery is still controversial, but its role in T1 and possibly T2 tumor treatment is growing in acceptance [Zieren *et al*, 2007]. The ablative technique includes various tools: Nd-YAG laser ablation [Rao *et al*, 2005], photodynamic therapy (PDT) [Ross *et al*, 2006], Radiofrequency ablation (RF) [Green *et al*, 2008], argon plasma coagulation (APC) [Dees *et al*, 2006] or the almost abandoned techniques of electrocoagulation [Eisenstat *et al*, 1992] and cryotherapy [Meijer *et al*, 1999]. Their applications vary from palliation (laser ablation), recurrent cancer treatment (neoadjuvant PDT to surgery, RF alone) to treatment of a specific complication of pelvic radiation therapy (hemorrhagic radiation proctitis) manifesting by bleeding (APC). More recently, the self-expanding metal stents [Sebastian *et al*, 2004] become widely used to palliate rectal cancer. Overall, although the endoscopic techniques may offers solutions for bleeding, tenesmus (difficulty to defecate) or obstructions, they show limited efficacy in pain management or distant metastasis. Consequently, a multidisciplinary approach including radiotherapy and chemotherapy should be considered in incurable patients with a reasonable life expectancy.

I.1.3 Ultrasound for digestive cancer treatment

This paragraph discusses the potential use of ultrasound for the treatment of digestive cancers (esophagus and rectum) among all the possibilities used to fight cancer.

Currently, an ideal treatment to cure cancer regardless of the type of cancer staging doesn't exist. We have seen that for both types of cancer discussed here and it is widely valid for another cancer. Standard techniques are currently used to cure cancer, but they are limited to a specific stage (surgery alone for early stages and in association with chemo-, and radiotherapy for more advanced stage). Unfortunately, the existence of distant metastasis gives no hope for curative treatment and in these cases the objective is rapidly reduced from "cure" to "palliation". On the other hand, in the case of superficial cancer (carcinoma in situ or early stage I), alternative endoscopic techniques for curative purpose are investigated [Saurin, 2000]. These curative ablative techniques aim to limit the invasiveness of surgery or the toxicity of radiochemotherapy. However,

these methods (and every other except surgery) lack a real, histological evidence of cured cancer. Nevertheless, even a clear curative surgery (respecting all standard procedures) may be unsuccessfully, and especially when fighting highly recurrent cancer, like rectal cancer. The necessity of constant surveillance of the patient after a curative treatment of cancer is then obvious. Only a sufficient period of time like the actual 5-year period may permit to consider that a cancer is cured. Further clinical studies are needed to determine equivalence or superiority between these endoscopic ablatives technologies with respect to success rates and complications.

When considering palliative purpose, endoscopic procedures are proposed for patients with contraindication to surgery or RCT, and also for recurrence cases. Specific drawbacks of these techniques are known: inaccurate monitoring for RF heat delivery [Viallon *et al*, 2010], necessity of multiple treatment sessions for laser ablation [Norberto *et al*, 2005], [Rao *et al*, 2005], side effects like 6 weeks of hypersensitivity to light after a PDT with Photofrin® [Saurin, 2000] and, overall, possible complications such as bleeding or perforation. The small number of randomized trials cannot conclude with an ideal palliation. Therefore these procedures are primarily used only for patients with very advanced disease and short life expectancy, or as an adjuvant therapy. However, the optimal treatment must be decided by a multidisciplinary team for each case.

In this context, a minimal invasive endoscopic method using therapeutic ultrasound has been initially proposed by Lafon *et al* [2000] and further applied to esophagus by Melodelima *et al* [2005]. The extracorporeal focused ultrasound approach is not indicated because of the anatomical position of esophagus and rectum, i.e. the vicinity of important organ such as trachea, spinal column or genito-urinary organs. Therefore, on the basis of the natural cavity of these structures, the high intensity contact ultrasound (HICU) was considered as an adequate method to treat esophageal/rectal cancer. HICU, under MRI guidance, may offer some advantages over other endoscopic methods. These advantages include increased penetration depth (versus laser therapy or PDT), accurate control of heating (versus RF ablation, electrocoagulation, cryotherapy) and absence of side effects (like the case of PDT). The intents of the MRI-guided HICU method are both palliative and curative (depending on tumor staging). The curative purpose is motivated by the increasing number of early diagnosed cancer due to the introduction of nationwide screening of digestive cancer. A limit in palliation –with HICU– is the total obstruction of the lumen, induced by very large tumors. In these cases, there is no physical space to position the transducer inside the lumen, in direct contact with tumor. Hence, possible indications for HICU procedure are palliation of tumor causing only partial stenosis, recurrent cancers, and superficial cancer cure (stage I, II, without lymph node involvement), without complications. The goal of this thesis was to develop an ablative technique (MRI-guided HICU) for esophagus or rectum cancer having the potential for safe, effective and long term outcome.

I.2 Therapeutic ultrasound

This section is meant to be a brief review of the physics underlying the clinical application of therapeutic ultrasound. For further details the reader is kindly referred to "Biomedical ultrasonics" by P.N.T Wells [1977], "Ultrasound Physics and Instrumentation" by Hedrick *et al* [1995] or Duck's "Physical properties of tissue" [1990].

I.2.1 Ultrasound basics

Definition. Ultrasound is a form of vibrational energy propagating as a mechanical wave, with a frequency superior to 20 kHz, the limit of human hearing. The mechanical wave is a periodic motion of particles* within a medium, transmitting its energy successively from one particle to the next. Contrary to light, which, as an electromagnetic wave can propagate in vacuum, the ultrasound needs a medium to support its propagation. When propagating through a medium, the wave entails local vibrations of the particles constituting the medium. If the displacement of the particles and the propagation of the wave have the same direction, then the wave is said longitudinal. The wave is said to be transversal when vibrations are normal to the direction of wave propagation. In medical applications (frequency range 1-20 MHz), ultrasound is a longitudinal wave, unless some particular conditions exist, like soft tissue-bone interface [Fujii *et al*, 1999], when both types of wave are observed. The result of such longitudinal vibrations is the creation of compression and rarefaction regions along the wave propagation axis, i.e. high and low pressure regions. Therefore, a longitudinal acoustic wave propagating as repeating patterns of pressure through a medium is also named a pressure wave.

Generation. Ultrasound may be generated, in a large range of frequency (from 50 kHz to 20 MHz) by various methods: mechanical (whistles, sirens), electric (piezoelectric materials) or magnetic (magnetostrictive materials). Since the achievable frequency is strongly related to the modality of ultrasound generation, piezoelectric material (with a frequency on the order of MHz) became the most indicated for medical transducers. The reverse piezoelectric effect demonstrated in 1881 by the Curie brothers consists in generation of a mechanical deformation of a piezoelectric material when applying an electric field over a direction of polarization.

Some natural piezoelectric crystals like quartz, Rochelle salt or tourmaline were initially used, but synthetic ceramics like lead zirconate titanate (PZT) introduced by Jaffe in 1955 rapidly demonstrated their superiority in converting energy. PZTs are still widely used today due to their good piezoelectric properties and their ease of manufacture into a variety of shapes and sizes. They

* A particle is a volume element which is large enough to contain millions of molecules, so that it is continuous with its surroundings; but it is so small that quantities variable within the medium (like displacement amplitude) are constant within the particle.

also operate at low voltage and are usable up to about 300°C. Currently, the newly developed generation of piezoelectric materials is represented by piezocomposite: large number of piezoceramic rods embedded into a matrix of polymer [Fleury *et al*, 2002]. Using piezocomposite materials, Imasonic S.A. (Besancon, France) has developed two technologies named HI-1 (air backing) and HI-2 (solid backing). The "HI-1" transducers working at frequencies up to 10 MHz have an efficiency of 60-70% and a maximal acoustic intensity of 10 W/cm². The "HI-2" generation, limited at a frequency of 5 MHz, was developed to deliver a higher intensity (up to 30 W/cm²), but with a reduced efficiency (40-60%). The resonance frequency of a piezoelectric transducer depends on the intrinsic characteristics of the piezoelectric material, and also on its form and thickness. Therefore, high frequency transducers must be used with caution since the active element layer is very thin.

Acoustic field. Medical transducers may be flat (plane wave) or focused (convergent wave). The pressure field generated with a typical flat transducer of diameter D excited by a sinusoidal signal of frequency F is shown in Fig. I.3. Note that the acoustic beam originates from the entire surface of the piezoelectric element, and not from a point. Therefore, the pattern of the acoustic beam is affected by constructive and destructive wave interference. Two different regions are distinguished: a near field (or Fresnel zone) with important fluctuation in the pressure field and a far field (or Fraunhofer zone) characterized by a relatively uniform field. The transition from the near to the far field occurs at a distance L from transducer:

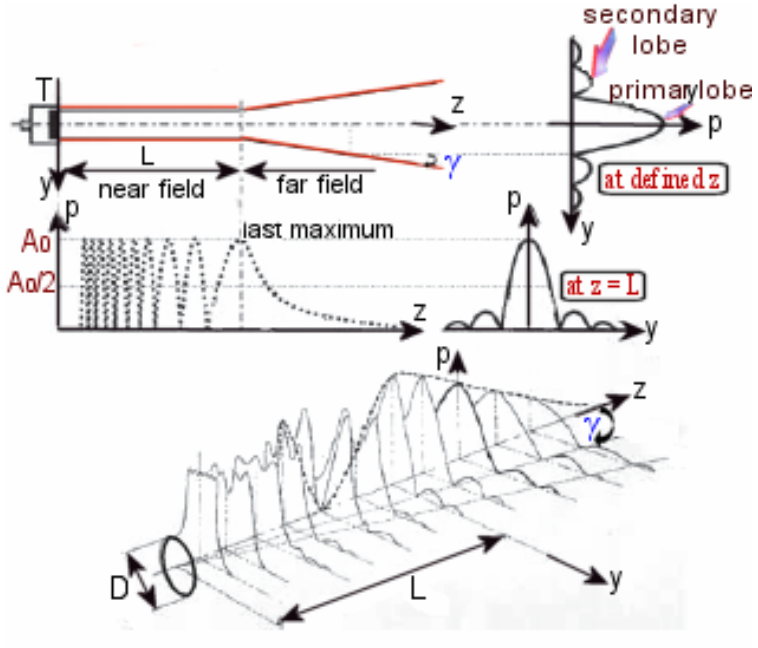

Figure I.3. Pressure acoustic field for a flat transducer.
Adapted image from Acoustique & Techniques [Lefebvre et al, 2004]

$$L = \frac{D^2}{4\lambda} \qquad \text{Eq. I.1,}$$

where λ is the wavelength. The pressure amplitude has, at this limit-point, a maximal strength A_0 and begins to spread out from the acoustic axis (z) of the transducer as it propagates through the medium.

The divergence angle γ of the beam is related to the transducer diameter D and to the wavelength λ by the following equation:

$$\sin\gamma = 1.22\frac{\lambda}{D} \qquad \text{Eq. I.2.}$$

This deviation from the central axis of the transducer (also called beam divergence or acoustic diffraction) causes a smooth decline of the pressure amplitude and the apparition of secondary acoustic lobes (see Fig. I.3). The same phenomena appear when using a focused transducer. However, in this case, the pressure field has more strength than a flat transducer and the distance L (now named focal distance) is nearer to the transducer [Lefebvre *et al*, 2004].

Characteristics. The characteristics of the acoustic wave are determined by the source of disturbance, i.e. the transducer in our case, and the properties of the medium through which the wave travels. The parameters used to characterize ultrasound are: frequency **F** (in Hz, or practical unit MHz), wavelength λ (in m, or commonly mm), period τ (in s), acoustic velocity *c* and particle velocity *v* (in m/s), acoustic impedance **Z** (in kg/(m²·s) = Rayl), amplitude **A**, acoustic pressure *p* (in N/m² = Pa), acoustic intensity **I** (in W/m², usually expressed in W/cm²), acoustic energy **E** (in W). The acoustic velocity *c* depends on the elastic properties of the medium (compressibility χ and mass density ρ), varying from 330 m/s in air to 1480 m/s in water [Wells, 1977] and 1540 m/s (average value) in soft tissue. Different values of *c* in biological media (biological fluids, soft tissue, bone and teeth, and even some pathological tissue) are available thanks to Duck's review work. Note that acoustic velocity has a constant value for a specific tissue, but it may slightly vary with temperature and frequency inside that tissue. However, important[*] variation in acoustic velocity with frequency was found only for lung and bones [Duck, 1990]. The ultrasound wavelength in soft tissue is approximately 1.5 mm, at 1 MHz, and about 0.3 mm at 5 MHz.

Another intrinsic characteristic for a specific tissue is the acoustic impedance Z, which is defined by the following relation (in the particular case of plane wave):

$$Z = \rho \cdot c \qquad \text{Eq. I.3.}$$

Similarly to the definition of the electrical impedance, Z represents the resistance of the tissue to ultrasound propagation and therefore an "Ohm's law applied to acoustics" may be expressed as follows: $p = Z \cdot v$ Eq. I.4,

where *p* is the acoustic pressure (the local pressure deviation from the equilibrium pressure, caused by the traveling ultrasound), and *v* is the particle velocity (the speed at which the particles vibrate with respect to their rest positions). The values of acoustic impedance Z are important when referring to an interface between two media. An ultrasound incident wave is totally transmitted to a second medium if the acoustic impedances of these two media are equal. However, this assumption is idealistic and, in practice, the impedance mismatches at the interface between two media causing both a reflection and a reduced transmission. Hence, the incident wave is partially reflected (reflection angle identical to the incidence angle) and partially transmitted (transmission

[*] Example of velocity variation with frequency for lung (Dunn, 1986): 644 m/s at 1 MHz and 1472 m/s at 7 MHz.

angle governed by the Snell-Descartes's law). Note that this type of reflection appears at smooth interfaces larger than the wavelength (e.g. diaphragm, heart valves or air bubble) and it is usually named specular reflection (*speculum (lat.) = mirror*). On the contrary, when the objects are smaller than λ (like red blood cells for example), the wave is scattered in all directions (Rayleigh scattering). The interference of these scattered waves causes a fluctuation of the (backscattered) signal and, hence, brightness nonuniformities called speckle, in ultrasound imaging of a homogeneous object.

An important parameter in therapeutic ultrasound is its intensity. The acoustic intensity I is defined as the acoustic power P_{ac} per unit area *S*. For a continuous wave, the time-averaged intensity over a period may be expressed as in Eq. I.5:

$$I = \frac{Pac}{S} = \frac{p_{\max}^2}{2\rho \cdot c} \qquad \text{Eq. I.5,}$$

where $p_{\max}$ is the maximal pressure amplitude.

I.2.2 Biological effects of ultrasound

When an ultrasound beam travels through a real medium, its intensity is reduced as a function of distance: $I(z) = I_0 \cdot \exp^{-\alpha \cdot z}$ Eq. I.6,

where I_0 is the acoustic intensity at the origin ($z = 0$), $I(z)$ is the acoustic intensity at a distance z from the transducer and α is the (intensity) attenuation coefficient (in Nepers/m). The coefficient α is often expressed in dB/m and, for that reason, a multiplication by a factor 8.686 must be used. Since the intensity and the amplitude of a mechanical wave are linked by a square function, then:

$$\alpha = 2\,\mu \qquad \text{Eq. I.7,}$$

with μ the (amplitude) attenuation coefficient.

For a specific tissue, the attenuation coefficient is affected by temperature and frequency. For example, at a frequency of 1 MHz, the ultrasonic attenuation in soft tissue is approximately 0.7 dB/cm, whereas at 2 MHz, it is 1.4 dB/cm [O'Brien, 2007]. Numerous studies reported measurements of attenuation coefficients under different conditions (temperature, frequency) and for various tissues. The results of these studies were collected by [Duck, 1990] in a helpful database of attenuation values. Moreover, the attenuation coefficient, as a result of frequency dependency, influences the ultrasound penetration into the tissue. Hence, when the frequency is increased, the attenuation is increased, and the penetration is reduced. Also, although isotropic for most tissues, the attenuation is anisotropic for skeletal muscle, nerve or tendon. The longitudinal attenuation (along the fibers) measured in muscle is greater than the across attenuation by a factor 2 to 3 [Duck, 1990].

This wave attenuation is explained by several factors: deviation from a parallel beam (divergence); mode conversion (two or more wave traveling at different velocities and in different directions); scattering (non-specular reflection) by objects that are of the size of the wavelength or smaller (i.e. blood cells), and absorption (conversion of acoustic energy into heat). The most important contribution to wave attenuation arises from two factors: absorption and scattering. Hence, the attenuation coefficient is often defined as the sum of these two components. The absorption accounts for 60-80% of total attenuation [ter Haar, 1999].

Thermal effects. An ultrasound wave traveling through a tissue is partially absorbed by the tissue, causing the heating of the medium (thermal effect of ultrasound). Initially, the ultrasound absorption was explained only by frictional forces (due to the viscosity of the medium), which oppose the periodic motion induced by the ultrasound wave. According to this classical theory, the absorption coefficient would be proportional to the square of the frequency (see calculations based on viscous forces in [Rayleigh, 1945]). Yet, the quadratic relationship was confirmed only for pure water (at frequency higher than 3 MHz) [Duck, 1990], whereas in tissue, the absorption coefficient α_a shows experimentally a near-linearly relationship with frequency: $\alpha_a = \alpha_0 \cdot F^m$ Eq. I.8.

The α_0 (absorption coefficient at 1 MHz) and *m* parameters are both intrinsic characteristics of the tissue. For soft tissue, *m* varies from 1 to 1.2 [Goss *et al*, 1979]. A linear relationship between absorption and frequency is governed by relaxation mechanisms of the medium. Therefore, the absorption mechanism is currently explained by the relaxation theory, in addition to the viscosity theory. During the acoustic wave propagation through the medium, the structures of the medium endure a cyclic motion of compression and decompression. Ideally, in the case of a perfectly elastic medium, this motion is associated with a reversible energy transfer, i.e. the energy transferred from the acoustic wave to the system during the compression part will be entirely returned during the decompression part. But, since the tissues are not totally elastic, a part of the transferred energy during compression will remain stored into the tissular structure. This is a result of relaxation phenomena of the system, which try to redistribute the surplus of energy brought by the acoustic wave in order to guaranty the stability of the system. This energy redistribution causes the absorption of ultrasound and, hence, the increase in tissue temperature. Implicitly, the acoustic wave is attenuated, loosing at every cycle a constant quantity of energy (as a hysteresis-type mechanism). Concurrently, relaxation mechanisms may explain the observed velocity variation with frequency (dispersion phenomena).

The absorbed acoustic energy determines the heating of the medium in the case of a rate of heat production greater than the rate of heat removal. For a small control volume, the balance of thermal energy can be stated as:

$$Q_{gain} = Q_{storage} + Q_{loss} + W \quad \text{Eq. I.9,}$$

where Q_{gain}: heat rate gained by absorption process and from the surrounding control volumes, $Q_{storage}$: heat rate stored by the tissue, Q_{loss}: heat rate lost through the boundary of the considered volume and *W*: work performed by the tissue and metabolic heating. Without considering the boundary conditions, the two mechanisms of heat flowing inside a tissue are: conduction (diffusion, i.e. the temperature gradient) and convection (the perfusing blood). The heat conduction flux (conducted heat per unit area per unit time) q_{cond} is governed by the Fourier law:

$$q_{cond} = -k\nabla T \quad \text{Eq. I.10,}$$

where *k* is the heat conductivity in *W/(m·K)* and ∇T is the temperature gradient (variation of temperature with distance) in *K/m*. The heat convection term, introduced by Pennes [Pennes, 1948] describes the thermal interaction between tissue and perfused blood. The temperature distribution in the tissue is then expressed by the bio heat transfer equation (BHTE), as a summation of different mechanisms (diffusion, convection, metabolism, and external source of heating):

$$\rho \cdot C \frac{\partial T}{\partial t} = -\nabla \cdot q_{cond} + \omega_b \cdot \rho_b \cdot C_b (T_a - T) + Q_m + Q \quad \text{Eq. I.11,}$$

where ρ: tissue density in *kg/m*^{3}, *C*: tissue specific heat in *J/(kg·K)*; $\frac{\partial T}{\partial t}$ temporal derivative of tissue temperature T in *K/s*;

$\nabla \cdot q_{cond}$ is the divergence operator applied to heat conduction flux vector in *W/m*^{3};

ρ_b: blood density, C_b: blood specific heat, ω_b: blood perfusion rate in m^3 *of blood* /(m^3 *of tissue* ·s) and T_a: arterial blood temperature in *K*;

Q_m: rate of metabolism heat generation per unit volume in *W/m*^{3}*;*

Q: rate of heat generation per unit volume in *W/m*^{3}.

The last factor (*Q*) is the external source of heating for the tissue. Different methods (ultrasound, laser, microwave or radiofrequency) may be used in order to induce controlled hyperthermia of a tissue. In the case of ultrasound, *Q* is defined as the product of (intensity) absorption coefficient, and acoustic intensity *I* calculated from Eq. I.5. Therefore, for an ultrasound heating source, the BHTE becomes:

$$\rho \cdot C \frac{\partial T}{\partial t} = k\nabla^2 T + \omega_b \cdot \rho_b \cdot C_b (T_a - T) + Q_m + \alpha_a \cdot I \quad \text{Eq. I.12,}$$

where $\Delta T = \nabla^2 T = \nabla \cdot (\nabla T)$ is the Laplacian operator applied to tissue temperature *T*. The BHTE remains the most widely used thermal model of living tissues.

The temperature elevation in tissue may lead to cell death, depending on both temperature and duration of applied ultrasound energy (see Fig. I.4). Two possibilities of tumor treatment are available: hyperthermia and thermal ablation (ultrasound surgery). Hyperthermia consists of applying of a relatively low temperature (43-45°C) during a long period (around 60 minutes) [ter

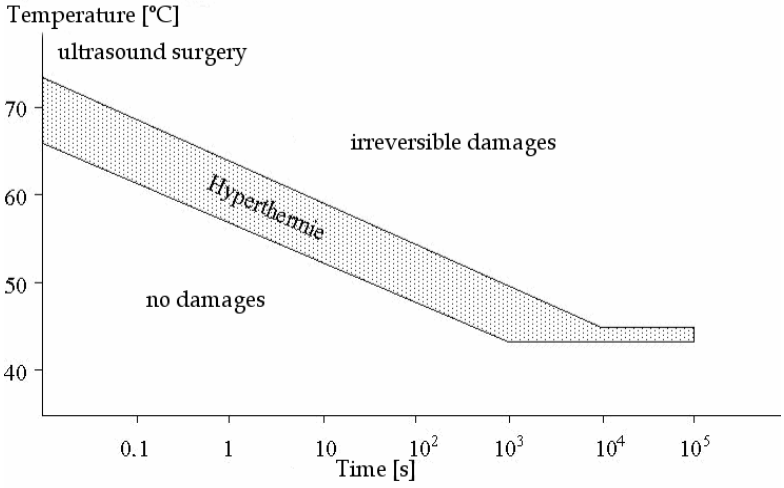

Figure I.4. Thermal damages on biological tissue, function of temperature and duration. *Adapted from [Lele, 1977]*

Haar, 1999]. This modality of energy delivery is based on the sensitivity of malignant cells to temperature rise. More sensitive to temperature than the normal cells [Li and Liu, 1997], the tumoral cells dies while the normal cells suffer only reversible damages [Hahn, 1984]. Since the process is relatively slow, blood perfusion becomes impossible to neglect and therefore inhomogeneous tissue heating may appear. Quite differently, thermal ablation (generally based on focused transducers) relies on a high temperature (above 55°C) being applied for a very short time (several seconds) causing irreversible cell death through tissue coagulative necrosis[*]. For example, Chapelon *et al* [1992] achieved kidney necrosis, by keeping the tissular temperature at 80°C for 5 s (focus intensity on the order of 1000 W/cm²). Contrary to hyperthermia, in the case of high intensity focused ultrasound (HIFU), the perfusion may be neglected, but cavitation effects are susceptible to appear [Kennedy *et al*, 2003].

Quantification of thermal damage induced by ultrasound may be expressed by the thermal dose TD (in minutes) or the thermal index TI. The TI is defined by the AIUM (American Institute of Ultrasound in Medicine) standards as the ratio of the in situ acoustic power to the acoustic power required to raise tissue temperature by 1°C, under specific conditions. Three thermal indices corresponding to soft tissue (TIS) [O'Brien and Ellis, 1999], [Karagoz and Kartal, 2006], bone (TIB), and cranial bone (TIC) have been developed for different examinations.

The thermal dose concept relates any time and temperature data combination to cell death. The relationship between the rate of cell killing, and time & temperature has been found to be strongly non-linear. In order to compare different heating regimes, the time-at-temperature data must be normalized to a common unit. As proposed by Sapareto and Dewey in a classical paper [1984], an empirical formula introduces the isoeffective thermal dose:

$$t_{43} = \sum_{0}^{t} R^{43-T} \Delta t \qquad \text{where} \qquad R = \begin{cases} 0.25, & for\ T \le 43°C \\ 0.5, & for\ T > 43°C \end{cases} \qquad \text{Eq. I.13.}$$

Here t_{43} is the thermal dose in equivalent minutes at 43°C ($EM_{43°C}$), t is the heating exposure time and T is the average temperature during the time interval Δt. Thus, the thermal dose represents the

[*] Swelling of the cells and their organelles leading to disruption of the cell membrane [de Zwart, 2000].

necessary time –at temperature *T*– to accumulate the same thermal damage (isoeffect) as the damage that would occur at a temperature of 43°C. No particular reason can justify the choice of 43°C as reference, except that this value is near the break point for some cell lines [Dewhirst *et al*, 2003]. The constant *R* is derived from experimental studies for different biological systems and endpoints. Theoretical considerations based on reaction kinetics (thermodynamic Arrhenius analyses) led to the prediction that the temperature dependence of the rate of protein denaturation is determined primarily by the activation energy. Hence, *R* is an expression of the relative increase in reaction rate for a 1°C increase in temperature [O'Brien, 2007]. Note that Eq. I.13 assumes an accumulation of thermal dose only during heating, neglecting any contribution from the cool-off period. Moreover, this equation does not imply that all cells exhibit the same sensitivity to heat, but only that a consistent relationship (for many types of cells) between time and temperature may correlate to cellular damage. An equivalent time of 240 minutes at 43°C is often regarded as a threshold for tissue necrosis [Sapareto and Dewey, 1984], [Daum and Hynynen, 1998] and 250-300 $EM_{43°C}$ permit already visible coagulation [Damianou *et al*, 1995], [Diederich *et al*, 1999].

Non-thermal effects. Non-thermal mechanisms such as cavitation, radiation force, acoustic streaming, microjets and strain may occur in ultrasound exposed tissue [O'Brien, 2007]. Cavitation refers to the creation, oscillation and collapse of gas bubbles within a medium under the action of an ultrasound wave. The existence of nucleation sites within the medium is primordial to initiate cavitation. These nuclei can be, for example, particles in suspension, interfaces or microbubbles. The onset of cavitation depends also on several factors, such as acoustic intensity, frequency of the wave, static temperature and pressure, viscosity or superficial tension, making the control of cavitation difficult. Note that, for identical conditions, the cavitation threshold increases with the frequency of the ultrasound. Thus, by operating at a higher frequency, cavitation may be avoided.

In stable cavitation, microbubbles expand and contract during each cycle in response to the applied pressure oscillations. The bubbles grow, as far as dissolved gas leaves the medium during the negative-pressure phase, a process called rectified diffusion. Each bubble oscillates for many cycles without collapsing completely. These oscillations can produce high shearing forces in the nearby surrounding areas and may give birth to microstreaming. These phenomena can fragment biomolecules or cellular membranes.

Transient (inertial) cavitation is a more violent form of microbubbles dynamics in which short-lifetime bubbles undergo large cycle changes over a few acoustic cycles before completely collapsing. Contrary to stable cavitation, inertial cavitation appears at intensities typically above 700 W/cm²/MHz in *in-vivo* tissues [Hynynen, 1991]. Transient cavitation shows a threshold that depends on the peak negative pressure *p*- of the acoustic wave and on frequency *F*, exhibiting a p^2/F dependence. The bubble implosion produces highly localized (within 1 μm^3) shock waves,

very high temperatures (up to 10 000 K) and pressures (100 MPa or higher) [Hedrick *et al*, 1995] generating tissue damage. Also, decomposition of water to free radicals (H• and OH•) may be observed [Verral and Seghal, 1988], [Villeneuve *et al*, 2009]. However, these radicals tend to have very short lifetimes *in-vivo* (~10^{-9} s, equivalent to a mean free path of ~0.5 μm) [Henglein and Kormann, 1985]. Moreover, the bubble collapse generates new microbubbles, which will further act as new nuclei, and maintain the cavitation [Brennen, 1995].

Generally, the use of inertial cavitation in therapeutic treatment (HIFU) is avoided. First, in case of tumor cell, the risk of dissemination by inertial cavitation cannot be neglected [Oosterhof *et al*, 1996]. Second, inertial cavitation leads to uncontrolled geometry of the lesion* induced by ultrasound, which makes the success of the treatment uncertain. For example, incomplete ablation of tissue volumes was observed [Sibille *et al*, 1993], [Malcolm and ter Haar, 1996], mainly because of undesired pre-focal damages induced by inertial cavitation [Malcolm and ter Haar, 1996], [Coussios *et al*, 2007], [Zderic *et al*, 2008]. However, the use of inertial cavitation (and/or boiling) for therapeutic purpose is regarded today as a possible advantage, since these pre-focal lesions are 2-3 times larger than lesions formed without bubbles (purely thermal lesions) [Sokka *et al*, 2003], and, therefore, the total treatment could be faster. Second, these lesions may be observed in real-time as a hyperechoic region in ultrasound images (strong correlation between the onset of the inertial cavitation and the appearance of the hyperechoic region), allowing treatment monitoring and guidance [Rabkin *et al*, 2006], [Coussios *et al*, 2007]. However, further work is needed for characterizing the size, shape, and location of these lesions, to achieve safe and efficient treatments.

I.2.3 Applications

A non-medical application of ultrasound, i.e. the sonar, developed by Langevin in 1917 permitted the first observation of biological effects of ultrasound. Using a quartz crystal working at a frequency of 150 kHz, he noted that: “fish placed in the beam in the neighborhood of the source operation in a small tank were killed immediately, and certain observers experienced a painful sensation on plunging the hand in this region” [Langevin, 1917]. Only some decades later, in 1942, was reported the first utilization of ultrasound as therapeutic agent [Lynn *et al*, 1942]. This study used focused ultrasound as a neurosurgery technique and demonstrated the ability to destroy specific areas of the animal brain, with minimal disruption of the non targeted tissue.

Today, therapeutic ultrasound applications include tissue ablation, targeted drug delivery (by temporary opening of the blood-brain barrier, or enhanced immune response), and

* In this thesis, the term **lesion** refers exclusively to the ultrasonically-induced destruction of a volume of tissue. It has no correlation with the medical practice, when doctors refer to tumoral tissue as a lesion.

extracorporeal shock wave lithotripsy (standard treatment of calculosis). This thesis refers only to the thermally ablative effect of ultrasound. The raised interest gained by this technique is worldwide demonstrated by various applications (benign or malignant disorders): prostate [Chapelon *et al*, 1999], [Ross *et al*, 2004], [Chopra *et al*, 2005], uterine fibroids [Tempany *et al*, 2003], liver [Kennedy *et al*, 2004], kidney [Damianou, 2003], [Illing *et al*, 2005], esophagus [Melodelima *et al*, 2008], breast [Hynynen *et al*, 2001] or brain [Pernot *et al*, 2007]. Depending on the anatomical location, an optimal transmission of the acoustic energy is achieved either by extracorporeal access (abdomen, uterus, brain, bone, kidney or breast), transrectal/transurethral access (prostate), or endoluminal access (biliary duct, esophagus, rectum).

Since the concept of ultrasound surgery demands a clear delimitation between the treated tumor and the adjacent healthy tissue, which must be preserved, imaging guidance is essential. The most obvious* method for guiding ultrasound treatment is ultrasound imaging. Although successful in practice, ultrasound guidance has two limitations. First, ultrasonography has less contrast than CT or MRI in accurately detecting the location of tumor (before and after therapy). Second, ultrasound imaging is (still) not capable to detect real-time temperature changes in *in-vivo* applications. However, recent work [Miller *et al*, 2005] presented this ability in *in-vitro* studies. While ultrasound imaging still needs technical improvements, MRI already demonstrated an excellent sensitivity for 3D-imaging of soft tumor and accurate measurement of temperature elevation inside the body. Moreover, continuous MR-monitoring of the temperature rise and the accumulated thermal dose permits an automated closed-loop strategy to control tissue heating. The feedback loop significantly enhances the safety and efficacy of ultrasound treatment. Therefore, MRI-guided ultrasound therapy has been suggested as a powerful approach for cancer therapies, either with extracorporeal [Jolesz *et al* 2005] or endoluminal [Chopra *et al* 2005] applicators. On the other hand, MRI guiding demands that the ultrasound transducers should be highly MR-compatible [Schenck, 1996].

The therapeutic regime of heating used in this thesis is between hyperthermia and HIFU. Because of the relative fragility of the contact transducers, the acoustic intensity was limited to 20 W/cm². Therefore, in order to obtain tissue necrosis, the sonication time should be longer (60-90 s) than for a typical HIFU sonication (up to 5 s). On the other hand, cavitation is almost improbable at such intensities, so the lesion is purely due to the thermal effect. Contrary to HIFU heating, which is considered perfusion-independent for a sonication time below 3 s [Chen *et al*, 1993], this particular heating regime is susceptible to be influenced by the vascularization of the digestive duct. However, the reduced perfusion of the digestive tract (when compared with liver or kidney) and the temperature rise of ~ 30°C are expected to limit the influence of the blood perfusion.

* use of same technique

I.3 MRI introduction

The purpose of this section is to provide a succinct overview of the basic principles of magnetic resonance imaging. For more detailed information please refer to Keeler [2002], Haacke *et al* [1999], or Kastler *et al* [2006].

I.3.1 MRI basics

Physical principles. Nuclei posses an intrinsic property named spin (spin angular momentum), which value depends on the constituent number of neutrons and protons. The NMR (nuclear magnetic resonance) phenomenon is based on the interaction of a RF wave (at a specific frequency) with atomic nuclei of non-zero spin placed in an external magnetic field $\vec{B}_0$. Within a human body, diverse atomic species have non-zero spin such as: ^1H, ^{23}Na, ^{31}P, ^{17}O or ^{19}F, but very different abundance. Since hydrogen is the most abundant element in human body (88 M = 88 molar = 88 moles/liter), clinical MRI uses it predominantly, while the use of other species remains only experimental. Compared to ^1H, the molarity of other elements is significantly lower, varying from 80 mM (sodium) to 4 μM (fluorine) [Haacke *et al*, 1999].

A nucleus of ^1H (i.e. a proton) has a net spin $\vec{S}$ characterized by the nuclear spin quantum number I (I = ½) and an associated nuclear magnetic momentum $\vec{\mu}$ characterized by a spin magnetic quantum number $m_s = \pm ½$. The two nuclear moments are related by a constant (specific to each nuclear specie) called gyromagnetic ratio γ:

$$\vec{\mu} = \gamma \cdot \vec{S} \qquad \text{Eq. I.14}^*.$$

For the proton, the gyromagnetic factor is 2.675 x 10^8 rad/s/T (or $\not\gamma = \gamma/2\pi = 42.58$ MHz/T), where T is Tesla unit of magnetic field (1 $Tesla = 10^4 Gauss$). When placed in an external magnetic field $\vec{B}_0$, the rotation-axis of the spinning proton precesses around the magnetic field at a specific frequency ω_0, called Larmor frequency. The precession frequency ω_0 (in rad/s) depends on the strength of the magnetic field and the gyromagnetic factor:

$$\omega_0 = \gamma \cdot B_0 \qquad \text{Eq. I.15.}$$

Furthermore, according to the Zeeman effect, the magnetic momentum can align in strictly 2I+1 orientations with respect to the external magnetic field. Hence, only two orientations are possible in the case of the proton, one parallel and one anti-parallel with B_0, see Fig. I.5. These orientations represent discrete levels of energy, separated by a quantified amount of energy ΔE:

$$\Delta E = E_\beta - E_\alpha = \hbar \cdot \omega_0 = \hbar \cdot \gamma \cdot B_0 \qquad \text{Eq. I.16,}$$

* This equation permits us to refer to proton, spin and magnetic moment in equivalent terms.

where h is the Planck's constant, with $\hbar = h/2\pi$. The fundamental state of energy has the lower energy E_α (parallel to B_0) , while the excited state has a higher energy E_β (anti-parallel to B_0).

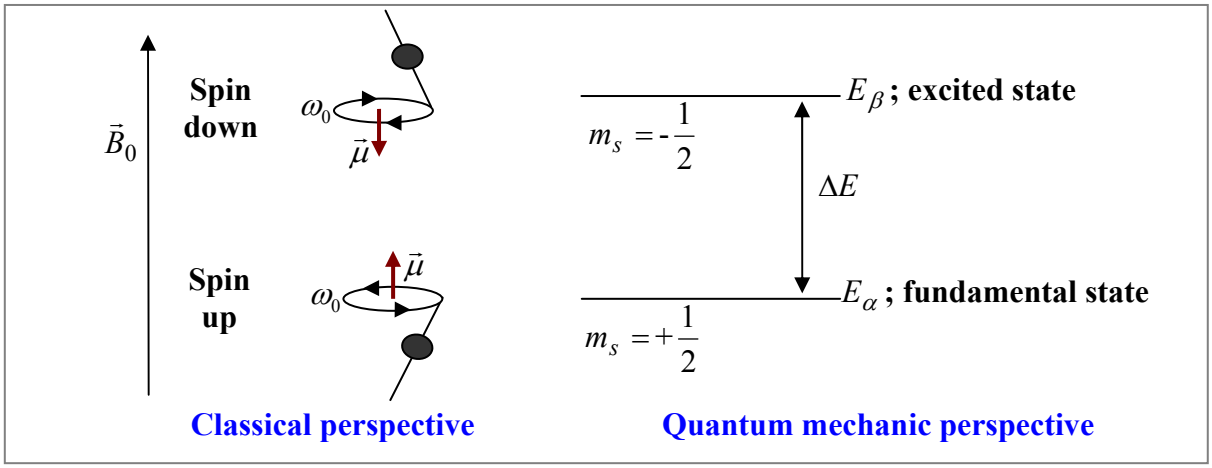

Figure I.5. The two possible orientations and the energy levels for a half-spin system (here ^1H) placed in an external magnetic field B_0.

In an ordinary NMR experiment, not only a single nucleus, but a large number of nuclei (on the order of 10^{20}) are observed. Therefore, the summation of all magnetic moments $\vec{\mu}$ constituting the sample results in a bulk magnetization $\vec{M}$. In the absence of the external magnetic field, the randomized orientations of each $\vec{\mu}$ generate a null magnetization. This behavior changes in the presence of the magnetic field $\vec{B}_0$, when the population of protons has only two possible orientations. The two energy states exhibit very small* difference in populations, governed by the Boltzmann distribution:

$$N_\beta = N_\alpha \cdot \exp^{-\Delta E/kT} \qquad \text{Eq. I.17,}$$

where k is the Boltzmann constant and T is the absolute temperature. Thus, in conditions of thermal equilibrium, the spins in the fundamental energy state (N_α) exceed the number of those in excited state (N_β). This translates in a non-zero bulk magnetization vector, orientated parallel to $\vec{B}_0$ and called (longitudinal) equilibrium magnetization $\vec{M}_0$.

Because the equilibrium magnetization $\vec{M}_0$ is very small with respect to the strength of $\vec{B}_0$, the direct measurement (along the $\vec{B}_0$ direction, i.e. the z-axis) is not possible. Also, the MR-signal is based on the detection of a precession movement and, at equilibrium, the magnetization vector does not precess (no angle with $\vec{B}_0$-direction). Therefore, a second magnetic field $\vec{B}_1$ is applied perpendicular to the static magnetic field $\vec{B}_0$, in order to flip the longitudinal magnetization into the *xy*-plane, making the detection possible. The $\vec{B}_1$-field, produced by a short RF pulse applied to a

* Because the ratio $\Delta E/kT << 1$, since the thermal energy kT is, at human body temperature, millions of times larger than the quantum energy difference ΔE .

transmission coil, oscillates (around the *x*-axis) at a frequency ω_{RF}. The resonance condition ($\omega_{RF} = \omega_0$) causes a modification in the behavior of the magnetization vector: now, the protons precess not only around $\vec{B}_0$ (at ω_0), but also around $\vec{B}_1$ (at $\omega_1 = \gamma \cdot B_1$). Generally, understanding and imaging this complex behavior of double precession becomes difficult, when using the laboratory frame, i.e. the frame of the static field $\vec{B}_0$. Therefore, the rotating frame of reference, which rotates at frequency ω_0, is further used and "eliminates" the precession around $\vec{B}_0$. Consequently, the magnetization precesses, during excitation, around the $\vec{B}_1$ field only. The flip angle of the pulse defines the degrees of rotation of the magnetization vector towards the *xy*-plane and may varies between 0° and 180°, in function of the type of the sequence. For example, flip angles between 0° and 90° are typically used in gradient echo (GE) sequences, 90° and a series of 180° pulses in spin echo (SE) sequences, and an initial 180° pulse followed by a 90° and a 180° pulse in inversion recovery (IR) sequences. An angle of 90° represents a flip from $\vec{M}_0$ to $\vec{M}_{xy}$, while 180° represent a flip to $-\vec{M}_0$. In terms of quantum mechanic, the $\vec{B}_1$-field oscillating at the resonant frequency determines the disturbance of the Boltzmann distribution observed at the equilibrium. Thanks to the absorbed energy from the RF pulse, spin transitions from N_α (low level) to N_β (high level) are possible. In function of the RF pulse (i.e. the flip angle), the transitions continue until the populations are equal (saturation, only transverse magnetization) or completely inversed (anti-parallel longitudinal magnetization).

Relaxation phenomena. The spin system disturbed by the resonance condition tends to return to its equilibrium state – process known as relaxation. The time evolution of the magnetization along each axis is described by the Bloch equations [Haacke *et al*, 1999]:

$$\begin{cases} \dfrac{dM_x}{dt} = \omega_0 M_y - \dfrac{M_x}{T_2} \\ \dfrac{dM_y}{dt} = -\omega_0 M_x - \dfrac{M_y}{T_2} \\ \dfrac{dM_z}{dt} = \dfrac{M_0 - M_z}{T_1} \end{cases} \qquad \text{Eq. I.18.}$$

This set of equations incorporates both relaxation and precession effects.

The T_1 and T_2 constants (measured in ms) characterize the two relaxation processes: longitudinal and transverse relaxations. The T_1 (longitudinal or spin-lattice relaxation) describes the recovery of the M_z-component of the net magnetization vector (thus, after a time T_1, the magnetization M_z recovers 63% of the equilibrium magnetization M_0). A full M_0-recovery (99%)

occurs after a time equal to $5 \cdot T_1$. This relaxation type is related to the energy transfer from the nuclear spin system to its molecular environment (historically called "lattice" since this phenomenon was first observed in crystals). The energy transfer becomes possible when the spin interacts, at Larmor frequency, with a local oscillating field produced by the surrounding molecules. This transfer corresponds to the spin transitions necessary to reestablish the Boltzmann distribution. The second constant, the T_2 (spin-spin relaxation) describes the decay of the M_{xy} component of the net magnetization vector (after a time T_2, 63% of M_{xy} is lost). The spin-spin interaction purely refers to the loss of phase coherence of the spins (change in individual precession frequency) as they interact with each others via their own oscillating field. In practice, an additional dephasing effect appears in tissue due to magnetic field inhomogeneities. This lead to a decay curve characterized by a time constant named T_2^*, which is shorter than T_2. The phase loss induced by the field inhomogeneities may be recovered by using a spin echo sequence (refocusing pulse) and then the "true" value of T_2 is measured. The relaxation constants are intrinsic characteristics of various tissues (see Table I.2), but vary with the strength of the $\vec{B}_0$-field.

Tissue	T_1 [ms]	T_2 [ms]
Gray matter	950	100
White matter	600	80
Cerebrospinal fluid	4500	2200
Muscle	900	50
Fat	250	60
Blood	1200	100 (venous) -200 (arterial)

Table I.2. ***Representatives values of relaxation parameters, for hydrogen components of different human body tissues at B_0=1.5 T and 37°C*** (*source [Haacke et al, 1999]*).

Signal and image acquisition. In the laboratory frame, after a RF pulse, the spatial evolution of the magnetization is seen as a spiraling-downward motion showing the combined regrowth of the longitudinal magnetization and decay of the transverse component. Within these, only the transverse decay is acquired, in the *xy*-plane, by a receiver coil. This oscillating signal, decaying with an envelope described by T_2^* (or T_2 in spin echo sequences) time constant is the free induction decay (FID):

$$M_{xy}(t) = M_{xy}(0) \cdot \exp^{-t/T_2^*} \cdot \cos(\omega_0 t) \qquad \text{Eq. I.19,}$$

where $M_{xy}(t)$ is the transverse magnetization at time t after the RF pulse application and $M_{xy}(0)$ is the maximum transverse magnetization, observed immediately after the RF pulse (at time 0). The MR signal (FID) is a time-dependent voltage (damped sinusoid) measured by the

detection coil as a consequence of Faraday's law of electromagnetic induction. The information carried out by this signal may be further exploited as NMR spectra or as MR image. However, both MR spectroscopy and imaging are based on the Fourier Transform (FT) of the time-domain signal which generates the constituting spectral frequencies.

The beginnings of MRI are related to the pioneer work of Lauterbur and Mansfield (1973). They proposed to introduce a spatially varying magnetic field (called gradient) across the object in order to create spatially varying Larmor frequencies, as defined in Eq. I.20:

$$\omega_0(\vec{r}) = \gamma B_0 + \gamma \cdot G(\vec{r}) \cdot \vec{r} \qquad \text{Eq. I.20,}$$

where $G(\vec{r})$ is the gradient and $\vec{r}$ is the spatial coordinate along one specific direction. In this manner, the different frequencies constituents of the RM signal could be separated to give spatial information about the object.

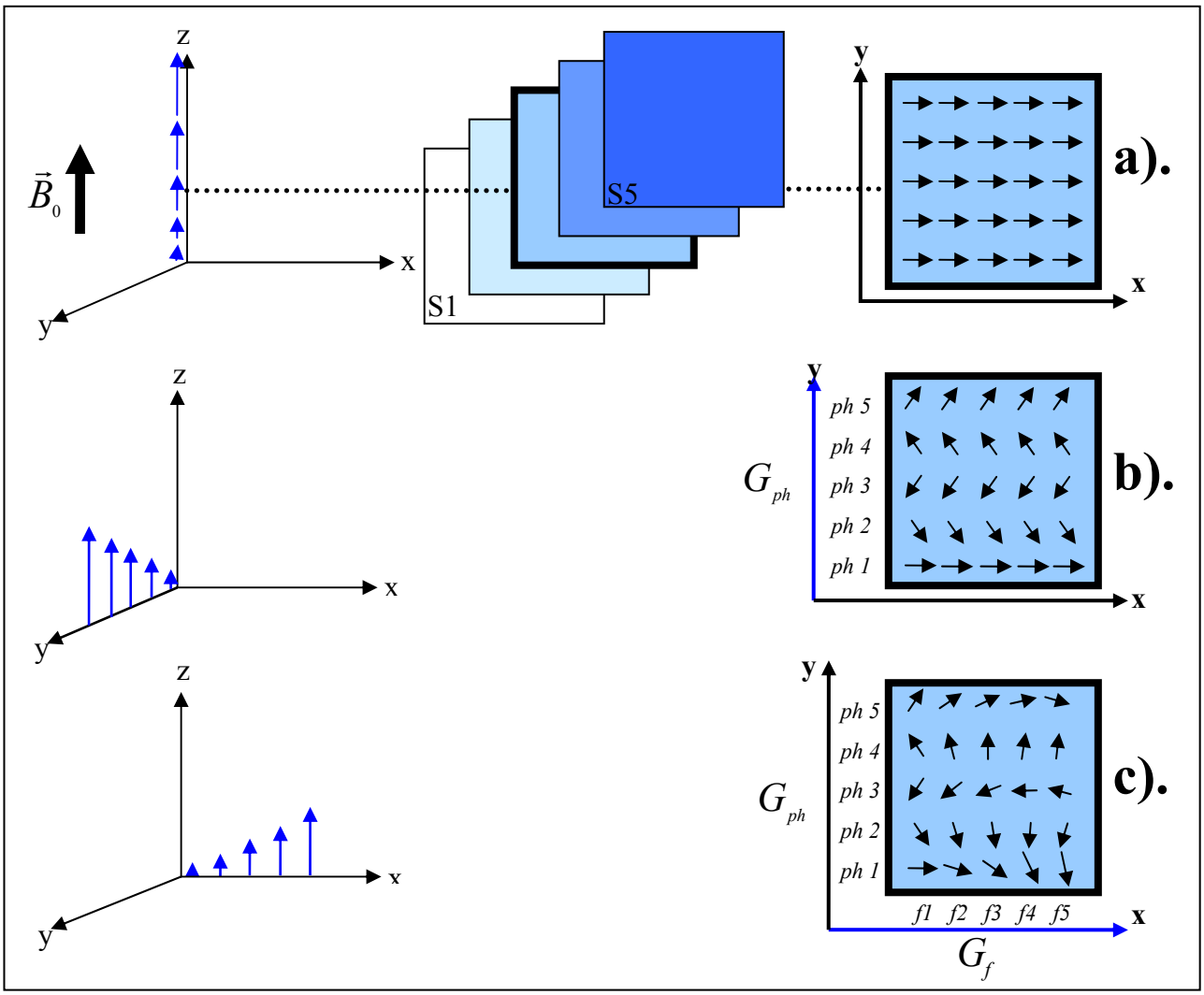

Figure I.6. Representation of the MR-data acquisition, using magnetic gradients.
a). Application of a slice selection gradient ➔ one slice (here 25 spins in the xy-space).
b). Phase encoding gradient ➔ the spins are grouped in 5 rows of different phase.
c). Frequency encoding gradient ➔ each spin is characterized by a unique set of parameters.

Consequently, the application of three linear gradient fields (see Fig. I.6) permits the acquisition of a MR-image. First, a slice of the sample must be defined (3D is reduced to 2D, see Fig. I.6.a). For that purpose, concomitant with the RF pulse, a gradient field G_{ss} (called slice selection gradient) is applied over the sample, along the *z*-axis ($\vec{B}_0$ direction). According to Eq. I.20, only a limited region within the sample is on-resonance, while the rest of sample spins are off-resonance. The slice thickness Δz depends on the gradient intensity G_{ss} and the bandwidth of the RF pulse:

$$\Delta z = \frac{BW}{\gamma \cdot G_{ss}} \qquad \text{Eq. I.21.}$$

Note that the gradient field could be applied in any orientation and therefore slices of various orientations may be acquired. Typically, a rectangular shape of the slice needs the application of a RF pulse which is a sinc-function (*sin(x)/x*) in the frequency domain. The second step in the acquisition of a 2D-image is the successive application of other two gradients (G_{ph}, G_f) along the resting directions [Kumar *et al*, 1975]. The phase gradient G_{ph} applied along the *y*-axis makes the spins to precess at different frequencies (see Eq. I.20) along this axis. Furthermore, this frequency distribution also produces phase variation in the movement of each spin. Contrary to frequency variation, which disappears after the gradient is turned off, the phase dispersion is conserved. This represents the phase encoding along one direction and, at this moment, the *xy*-plane is divided into lines of spins (see Fig. I.6.b). Each line has a characteristic phase in function of its distribution along the *y*-axis and inside each line the spins precess with the same phase. The second gradient, the frequency (or read-out) gradient G_f, is further applied along the *x*-axis in order to realize the frequency encoding. Thus, the former line is now segmented by the frequency distribution along *x*: $\omega(x) = \gamma \cdot x \cdot G_f$. This last gradient is also called read-out gradient because it is applied simultaneously with the signal acquisition, in order to permit the frequency variation acquisition. So, finally, each spin of the slice is characterized by a unique pair of phase and frequency (see Fig. I.6.c). In the special case of 2D-Cartesian acquisition, after slice selection, the application of a phase encoding gradient, followed by a read-out gradient (frequency encoding) allows the acquisition of one line in *k*-space. The entire acquisition of an image demands a line per line acquisition, i.e. a repetition of this sequence (excitation/ phase-encoding/ frequency-encoding and data acquisition). The increment loop is represented by the linear variation of the G_{ph}-gradient. The signal acquired from a slice is then depending on the two encoding gradients and on the spin density distribution within the slice:

$$S(t) = \int_{-\infty}^{\infty} M(x,y) \cdot \exp^{i\gamma(G_f \cdot x + G_{ph} \cdot y)t} \, dx \cdot dy \qquad \text{Eq. I.22.}$$

Even if the MR signal is analog, only a digital representation (sampling along encoding directions) is recorded. The digitized MRI data (or raw data) are temporary stored in a frequency domain, usually known as *k*-space (or Fourier-space). The frequency domain (k_x, k_y) and the spatial location (*x, y*) are related by the following relationship:

$$k_i = \frac{\gamma \cdot G_i \cdot t}{2\pi}, \text{ where } i = \text{axis}\begin{cases} x - \text{frequency} \\ y - \text{phase} \end{cases} \qquad \text{Eq. I.23.}$$

Furthermore, after filling the k-space, a double inverse Fourier Transform of Eq. I.22 permits to determine the spatial spins distribution $M(x, y)$. Their intensity is converted to grayscale values of the MR image. The digitized MR signal represents only an approximation of the continuous signal, and therefore the sampling factors Δk_i become important with regards to the image quality.

Important spatial parameters concerning an MR-image acquisition are: number of slices, field of view (FOV) representing the physical sizes of the image (in mm²), acquired /reconstructed matrix (N_x, N_y - number of points on k_x and k_y axis), and spatial resolution (pixel size and slice thickness). The in-plane resolution (or pixel size $\Delta x \times \Delta y$) is defined as the ratio between the FOV and the reconstruction matrix. From temporal point of view, an image is characterized by the duration of application of each encoding gradient, by the necessary time to acquire one single line of the *k*-space (repetition time TR), and by the acquisition time of one slice: $T_{acq} = N_y \cdot TR$. The total acquisition time for multi-slices MR data depends on the acquisition sequence: interleaved or sequential. For example, for a sequential acquisition*, the total acquisition time will be T_{acq} multiplied by the number of slices. This relation is not correct for an interleaved sequence, when all slices are excited within each TR. Note that for same total acquisition time, the interleaved technique increase the SNR (signal-to-noise ratio) compared to the sequential acquisition [Herzka *et al*, 2000]. In addition to the repetition time TR, another time parameter called echo time (TE) must be introduced, when using sequences with an echo–field (spin echo or gradient echo) in order to ameliorate the signal acquisition. TE represents the moment of signal acquisition after the RF-pulse application, and it is generally shorter than TR.

Image quality. The quality of an MR-image refers to resolution, contrast, signal-to-noise ratio (SNR), or artifacts. The MR-resolution does not depend on the input RF field (wavelength ≈ meters); it depends only on the way of sampling and filtering the signal.

Contrary to other imaging techniques restricted to only one measuring parameter (such as transmission radiation for X-ray or reflected wave for echography), MRI is more versatile,

* This type of acquisition completes the acquisition of data for one slice before preoceeding to the next (only one slice is excited per TR).

showing sensitivity to different variables: proton density, relaxation times, temperature, proton motion, chemical shift in the Larmor frequencies. Classically, the contrast features of an image may be weighted with respect to proton density or relaxation times (T_1, T_2). While the proton density refers to water content within tissues, the relaxation times characterize the water state (bulk or bounded water) and implicitly its interaction with other biological molecules. Contrast behavior may be understood by examining the recorded signal expression. For a RF-spoiled gradient echo sequence (commonly used in MR-thermometry), the signal S is [Wehrli, 1990]:

$$S = ct \cdot M_0 \sin\alpha \frac{1-\exp^{-TR/T_1}}{1-\cos\alpha \cdot \exp^{-TR/T_1}} \exp^{-TE/T_2^*}, \qquad \text{Eq. I.24,}$$

where *ct* is a constant depending on the MR hardware and α is the flip angle (always $\alpha \leq 90°$ for this sequence). Note that the signal is maximal, for a given TR, when the flip angle is a solution of the relation $\cos\alpha = \exp^{-TR/T_1}$. This value of the flip angle is called the Ernst-angle. Varying the duration of TR (relative to T_1) and TE (relative to T_2), images with different contrast may be acquired. Thus, a long TR and short TE conduct to proton density-weighted images. A $TR \approx T_1$ and a short TE generate a T_1-weighted image, while T_2-weighted images are acquired with long TR and $TE \approx T_2$. Note that some paramagnetic ions such as gadolinium (Gd^{3+}) enhance the image contrast by reducing the relaxation time (T_1).

While the contrast permits to differentiate tissues within an image, the SNR characterizes the effectiveness of the image. The SNR represents the degree to which noise can affect the accuracy of the measurement. The noise derives from random fluctuations in the receiver coil electronics and the sample (the patient). Generally, these random thermal fluctuations in the measured signal are referred to as "white" noise because the noise power spectrum is constant (within all frequencies used to sample the MR signal, i.e. the receiver bandwidth). White noise typically follows a Gaussian distribution centered at 0, with a variance σ^2. SNR/voxel is function of the voxel volume $V_{voxel} = \Delta x \times \Delta y \times \Delta z$, of the number of sampling points ($N_x \cdot N_y \cdot N_z$) of the *k*-space, of the number of acquisitions N_{acq}, and of the receiver bandwidth *BW* [Haacke *et al*, 1999]:

$$SNR/voxel \approx V_{voxel} \sqrt{\frac{N_{acq} \cdot N_x \cdot N_y \cdot N_z}{BW}} \qquad \text{Eq. I.25.}$$

If considering a doubling of resolution in one direction (say *x*), then the sampling points along *x*-direction will be also doubled, but the voxel volume will be halved. Therefore, the corresponding *SNR/voxel* (see Eq. I.25) will be divided by $\sqrt{2}$. Hence, an intrinsic* improvement of the

* Intrinsic means without modifying the parameters of the MR sequence; it may be, for example, an improvement of the receiver coil.

SNR/voxel, by a factor of $\sqrt{2}$, would allow a doubling of resolution in one direction. In practice, the SNR of an image is calculated as the ratio between the mean pixel value (signal intensity) and the standard deviation of the noise σ. A typical method to improve the SNR is the multiple acquisition of the same slice. While the signal is linear with the number of acquisition, the noise has only square root dependence. Thus, while the average signal (over N acquisition) remains constant, the average noise is decreasing with a $\sqrt{N}$ factor, and hence ameliorates the SNR. Remember, however, that multiple acquisitions require more acquisition time and that a MR experiment is always a compromise between scanning time and image quality.

Numerous *artifacts* (patient- or system- related) may influence the quality of a MR-image, causing obvious degradations or only subtle effects. Furthermore, the presence of artifacts makes the image difficult to analyze, leading (when not detected) to misinterpretation. Therefore, knowing each artifact category permits to reduce or even to eliminate their effects. The most known artifact –ferromagnetic metal (external or internal to patient)– causes large distortions in the magnetic field. The same effect (susceptibility artifacts) may appear at natural interfaces (air/tissue or bone/muscle) between two regions with different magnetic susceptibilities. Another important patient-related artifact concerns the different motions within the body: peristalsis, breathing, cardiac beats, blood flow. Motion artifacts manifest as blurred images (if random motion), or as replicated images (ghost) of the moving object (if periodic motion). These ghost-images appear mainly in the phase-encoding direction and their repetition rate is strongly related to the TR interval. Different techniques, mostly based on TR synchronization with the motion, permit the artifacts limitation. They may be general (such as swap of the encoding direction or saturation bands) or adapted to each type of motion: respiratory (breath-hold, triggering, compensation, navigator echoes), cardiac gating.

The second category of artifacts (system-related) assembles contributions from all operations covered in a MR-experiment. The most frequent artifacts are: aliasing, chemical shift, truncation (Gibbs), cross talking. Aliasing (or phase wrapping, foldover) appears when the Nyquist sampling criterion –FOV larger than the size of the investigated object– is not respected. The chemical shift refers to variation of the protons precession frequency due to their chemical environment (water or fat). Thus, a difference of 3.5 ppm, i.e. about 208 Hz at 1.5 T, exists between protons originating from water or fat tissues [Kastler *et al*, 2006]. Fat suppression techniques are aimed to eliminate this difference. Like the susceptibility artifact, Gibbs (truncation) artifact appears at interfaces where a high variation of the signal is observed. This steep variation is difficult to translate in a reconstructed image due to the finite number of sinusoids used. Hence, parallel lines appear adjacent to interfaces. A possible solution is to increase the matrix size, which will smooth these lines until they can be masked by the image

noise. The cross-talking artifacts refers to multislices techniques (with contiguous slices) when the selective RF pulse may partially excite the adjacent slices corrupting the signal acquired from a single slice. Overall, the specificity of some artifacts permits an additional not-conventional tissue characterization. For example, susceptibility is used for hematomas detection or perfusion imaging*.

I.3.2 MR thermometry and tissue heating control

Most of the parameters measured in an MR experiment (proton resonance frequency PRF, relaxation, diffusion coefficient, equilibrium magnetization M_0) are sensitive to temperature changes. This characteristic makes MR imaging an attractive modality for monitoring ultrasound or other heating methods, for thermal therapy.

The first study reporting a temperature mapping method [Parker *et al*, 1983] was based on the T_1 *relaxation time*. T_1 varies exponentially with temperature, but, for a small temperature range, it may be considered linear. Thus, a T_1-sensitive temperature coefficient of $1.4 \pm 0.2\%$ per °C was found in *ex-vivo* sample of bovine muscle, for a temperature evolution from 15 to 40°C [Cline *et al*, 1994]. The principal advantage of T_1-dependent temperature imaging is its relative insensitivity to motion. Also, this method permits to calculate thermal maps in fatty tissues (such as breast). However, the usefulness of the method is severely limited by two important restrictions. First, the temperature sensitivity depends on tissue type. Secondly, the T_1-correlation with temperature changes as tissue is heated and coagulated [Jolesz *et al*, 1988] and furthermore the signal is no longer strictly related to T_1. The accuracy of the measured temperature may be enhanced, when two different methods are combined within the same experiment. Thus, the T_1-based thermal mapping was successfully combined with M_0-based method [Germain *et al*, 2001], [Germain *et al*, 2002], or with the PRF method [Cline *et al*, 1996].

The same limitations (tissue dependence and changes within coagulation) appear for the thermometry method based on *diffusion coefficient* measurement. Diffusion characterizes the thermal Brownian motion of an ensemble of molecules. Like T_1, diffusion is exponentially related to temperature. The diffusion coefficient D may be calculated using specific MR sequences such as PGSE (pulsed gradient spin-echo) or PGSTE (pulsed gradient stimulated-echo). The D-measurement is based on the supplementary attenuation of the spin-echo in the presence of the applied magnetic field gradients. The signal expression depends on diffusion and on the mode that the gradients are applied (intensity, duration and separation). The variation of D with temperature

* After the administration of a paramagnetic contrast agent such as ferrite.

is on the order of 2% per °C, for water [Le Bihan *et al*, 1989]. Diffusion-based thermometry method shows therefore a good sensitivity, but additional problems (diffusion anisotropy or limited mobility of the bulk water) reduce its application.

Temperature dependence of water proton resonance frequency. The temperature sensitivity of the proton resonance frequency (PRF) was first observed by Hindman [1966] while studying, over a wide temperature range, the intermolecular forces and hydrogen bond* formation between water molecules. We know that the resonance frequency of a proton is determined by the local magnetic field it experiences, noted here B_{nuc}. But, this local field depends on the chemical environment of the molecule, i.e. the totality of electrons, (characterized by the shielding/screening constant *s*) and, also, on the bulk magnetic susceptibility χ :

$$B_{nuc} = (1 - s - \frac{2}{3}\chi) \cdot B_{mac} \qquad \text{Eq. I.26.}$$

The term B_{mac} describes the macroscopic magnetic field which appears when an object with a volumic susceptibility χ is placed in a uniform magnetic field B_0. If the susceptibility effect is not considered, then B_{mac} is reduced to B_0.

In his model, Hindman assumes that liquid water is a temperature-dependent equilibrium between two phases. These two water phases (with or without hydrogen bonds) have different shielding constants and are influenced by the temperature elevation. Note that hydrogen bonds between neighboring molecules distort the electronic configuration, causing a less efficient shielding. When a temperature rise is applied to the sample, the bonded-fraction of the water stretches, bends, and finally breaks. Consequently, with less hydrogen-bond, the total shielding constant is higher, and according to Eq. I.26, the local field B_{nuc} is lower. Moreover, a lower local field means a lower proton resonance frequency. Thus, the proton resonance frequency shift (PRFS) is induced by the average number of hydrogen bonds within the sample, which varies with temperature. Hindman calibrated, for pure water, the average shielding constant evolution over a large temperature range (from -15 to 100°C), which includes the actual range for thermal ablation. He obtained a linear coefficient of -0.0103 $\pm$ 0.0002 ppm/°C. This coefficient, noted $\beta = \partial\sigma/\partial T$, is currently named PRFS coefficient. It must be reminded, however, that the biological tissues do not have a pure liquid behavior. For that reason, eight different *ex-vivo* tissue samples (freshly excised brain, muscle, liver, and kidney from rabbits/pigs) were investigated under various

* Hydrogen bond is an attractive intermolecular force (type donor-acceptor) between one electronegative atom (nitrogen, oxygen or fluorine) and hydrogen covalently bonded to another electronegative atom. It may occurs in inorganic (H_2O, HF) or organic (DNA) molecules. The hydrogen bond is a strong van der Waals force (dipole-dipole), but weaker than covalent or ionic bonds.

conditions by Peters *et al* [1998]. The results showed a tissue-independent coefficient of -0.0101 ± 0.0004 ppm/°C, very close to that of pure water.

Note that both screening- and susceptibility- constants from Eq. I.26 are temperature-dependent. However, most implementations of the PRFS method assume only the temperature dependence of the screening constant, since its coefficient (in water) $\partial\sigma/\partial T \approx 0.01$ ppm/°C is several times greater than the temperature-dependent susceptibility coefficient $\partial\chi/\partial T \approx 0.0026$ ppm/°C [De Poorter, 1995]. If not considered, the susceptibility effect may induce negligible temperature errors (less than 10%) [De Poorter, 1995]. According to Peters *et al* [1999] the susceptibility-induced temperature errors may be greater for a particular geometry of heat-delivery device and its associated heat pattern. A maximal error (up to 30%) may appear when cylindrical heating device* is oriented perpendicular to the main magnetic field B_0. On the contrary, in parallel position, the error is less problematic, and even less important if the heat pattern is spherical. Therefore, corrections of the relative error induced by susceptibility are indicated particularly for a critical design of the heating-device.

Temperature imaging based on PRFS was first implemented for spectroscopy, and later adapted for MR-temperature imaging [Ishihara *et al*, 1995], [De Poorter *et al*, 1995]. Spectroscopic thermometry [Kuroda, 2005] uses the frequency shift calculated from MR spectra, which permits to detect multiple resonance peaks. The water peak is reported to an internal reference (which remains constant with temperature) such as lipids, and therefore this method allows an absolute temperature measurement, relatively immune to field drifts, interscan motion or susceptibility effects. Unfortunately, the spectroscopic method has limited applicability to real-time temperature monitoring due to its low temporal (1 minute) and spatial (3-4 mm) resolution.

MR-temperature imaging based on PRFS uses the phase acquired in RF-spoiled gradient-echo sequences. The phase of a pixel in the reconstructed image is proportional to the microscopic magnetic field (B_{nuc}) averaged on the corresponding voxel. Furthermore, any change in this magnetic field, due to temperature rise, can be correlated to a relative phase between successive gradient-echo images. The subtraction method (between a current heated image and a former, pre-heated image called reference or baseline image) is necessary in order to eliminate any temperature-independent contributions (due to field inhomogeneities). The temperature evolution (ΔT) is then calculated from the signal phase changes ($\Delta\phi$), as follows:

$$\Delta T = \frac{\Delta\phi}{\beta \cdot \gamma \cdot B_0 \cdot TE} \qquad \text{Eq. I.27.}$$

* The heating device used by Peters *et al* [1999] was a long glass cylinder (170 x 8 mm²). The heating source was a volume of water (heated at 90°C) circulating through the glass cylinder, at a flow of 1.7 liters/min, during 19 minutes.

The phase accuracy (phase standard deviation σ_{phase}), also affected (as the magnitude-signal) by the "white" noise, is closely related to the magnitude SNR [Haacke *et al*, 1999]:

$$\sigma_{phase} = 1/SNR_{mag} \text{ (in radians)} \quad \text{or} \quad \sigma_{phase} = 180/(\pi \cdot SNR_{mag}) \text{ (in degrees)} \qquad \text{Eq. I.28.}$$

The temperature accuracy (standard deviation of temperature SDT), calculated from Eq. I.27 & I.28, may be then expressed as:

$$SDT \cong \frac{1}{SNR_{mag} \cdot \beta \cdot \gamma \cdot B_0 \cdot TE} = \frac{1}{SNR_{mag} \cdot B_0 \cdot TE} \cdot \frac{1}{0.01 \cdot 10^{-6} \cdot 2.675 \cdot 10^{8}} \approx \frac{0.4}{SNR_{mag} \cdot B_0 \cdot TE}$$

Eq. I.29, with B_0 in Tesla and *TE* in seconds. In addition, according to Eq. I.24, SNR_{mag} (for a RF-spoiled gradient echo sequence) depends on both TR and TE. Its maximal intensity is reached for the Ernst-angle and for a TE equal to T_2^*, and leads to the best accuracy of the temperature [Chung *et al*, 1996].

All the MR thermometry experiments presented in this thesis are based on the proton resonance frequency shift (PRFS) method. In contrast to T_1- or D- based thermometry, the PRFS method offers two important advantages: 1) the temperature dependence may be considered, at first approximation, independent to tissue type [Peters *et al*, 1998]; and 2) the thermal coagulation does not corrupt the measurements [Kuroda *et al*, 1998], [Jolesz *et al*, 2005]. Notice that the chemical shift is the only frequency-based parameter and is independent of other MR parameters, whereas all others methods exploit changes in the signal amplitude. In addition, this method has been found to be the most sensitive, with a study [Kuroda *et al*, 1998] reporting a coefficient of PRFS-temperature dependence of -0.00876 $\pm$ 0.00069 ppm/°C for *in-vivo* rabbit skeletal muscle under focused ultrasound heating. The slightly difference between these values and those reported by Peters *et al* [1998] should be seen as an effect of the *in-vivo* physiological responses, and the magnetic susceptibility-related errors [Peters *et al*, 1999]. In this thesis, the PRFS coefficient is set to -0.01 ppm/°C [Peters *et al*, 1998], [McDannold, 2005], without considering the uncertainty of the PRFS coefficient. Therefore, the thermometry uncertainty reported here, i.e. the standard deviation, is only related to the measured phase noise.

The two major weaknesses of the PRFS method are its motion sensitivity (due to the necessity of a reference image) and its lack of temperature sensitivity in lipids (no hydrogen bonds in lipid). Therefore, fat suppression (by frequency-spatial selective RF pulses) is required in fatty tissues in order to assure a non-corrupted signal. Several strategies have been proposed to overcome the motion problem: respiratory gating, triggering and multiple baseline images over various points in the breathing cycle [Vigen *et al*, 2003], referencing the water PRFS to lipids shift (instead of just a baseline image) [Kuroda *et al*, 1997] or using unheated areas surrounding the heated region instead of baseline subtractions [Rieke *et al*, 2004]. Another factor which may

influence the PRFS method is the temporal instability of the magnetic field. In long sequences, dealing with intense gradients, an extra phase shift (the phase drift) may affect the thermometry. If necessary, a linear correction of the baseline is easy to apply [Peters *et al*, 1998], [De Poorter *et al*, 1995].

Pulse sequences for PRFS thermometry. Continuous MR thermometry (with good spatial resolution, such as 2 x 2 x 2 mm^3) during a heating procedure may permit the optimization of the thermal therapy. The image acquisition must be sufficiently fast (when compared to temperature change during treatment) in order to permit the operator intervention in case of problems. This near real-time* has different values, depending on the heating-type: a temporal resolution of a minute is generally sufficient for hyperthermia, while for thermal ablation the update-time must be reduced to 1 second [Rieke *et al*, 2008].

The standard gradient-echo† sequence, called FLASH (see Fig. I.7.a) permits the acquisition of one single *k*-space line per TR, which signifies an insufficient time resolution.

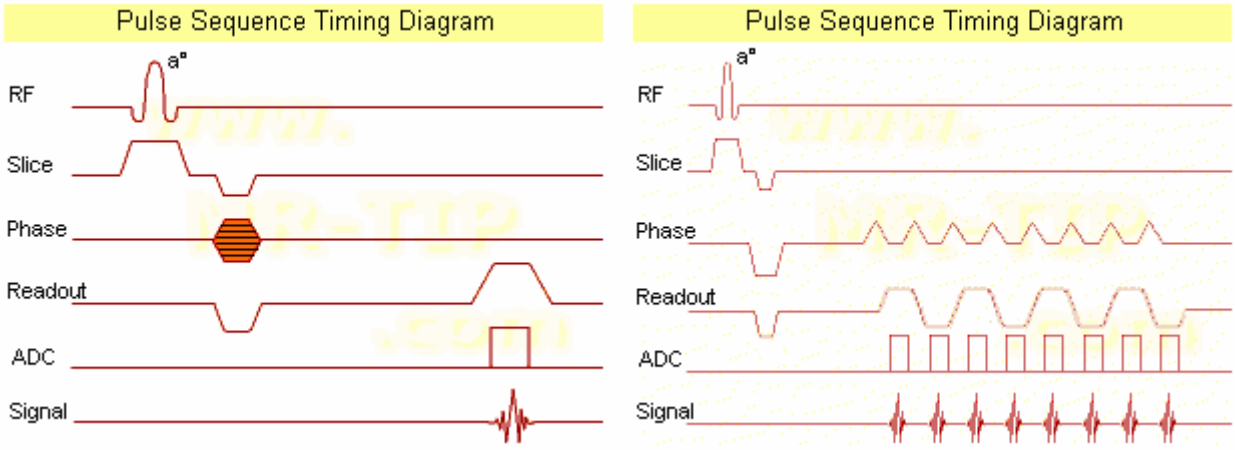

a) ***b)***

Figure I.7. Pulse sequences: a typical signal acquisition during one TR.
a). Standard gradient echo sequence (FLASH) ➔ one single k-space line acquisition.
b). Gradient-echo EPI sequence ➔ multiple k-space lines acquisition (here 8 echo-train pulses).
The k-space may be acquired totally (single shot) or segmented (multiple lines) during one TR.
ADC stands for analog to digital converter. *Images adapted from* http://www.mr-tip.com.

Hence several methods aimed to accelerate this rate have been proposed. All are gradient-echo sequences, characterized by a flip angle lower than 90° and an absence of the 180° RF rephasing pulse (like in the case of the spin echo-sequence). The lower flip angle decreases the amount of magnetization tipped into the transverse plane and permits a faster recovery of longitudinal magnetization. This translates in shorter TR/TE and finally, faster acquisition time. On the other hand, the absence of the refocusing pulse determines the acquisition of T_2^*-weighted images.

* Note that, in MRI guiding thermal therapy, the term (near) real-time refers to temporal resolution of 1 to 2 seconds.
† The name of gradient echo is due to the bipolar readout gradient, which includes a dephasing and a frequency – encoded gradients applied in a such manner that cause the apparition of an echo during data acquisition.

Therefore, the images acquired using gradient-echo sequences are more sensitive to magnetic susceptibility artifacts than those acquired in spin-echo sequences. However, inversion (for T_1-weighting) or spin echo (for T_2-weighting) pulses may be applied during preparatory pattern of the gradient-echo sequences in order to preserve a desired contrast. When fast gradient-echo sequences (i.e. short TR) are aimed for thermometry, residual transverse magnetization may not have completely disappeared after the echo acquisition and hence, it may corrupt the next repetition step. Therefore, for an accurate thermometry, spoiler (crusher) gradients are added to the sequence in order to destroy any remaining magnetization after each echo.

Figure I.7 compares a standard gradient echo sequence to a significantly faster (~100 ms/slice) sequence: the gradient-echo echo planar imaging (GE-EPI). The echo planar (EPI) method is based on the collection of all the data necessary to reconstruct an image using one set, or train, of echoes after a single RF excitation pulse. For that reason, a short phase encoding gradient (a blip) is repetitively applied (see Fig. I.7.b) in correlation with the continuous readout gradient. Each blip corresponds to an echo, and furthermore, to a *k*-space line acquisition. The number of the acquired echoes during one TR is called the EPI factor. Thus, in the example showed in Fig. I.7, the EPI factor was 8 and the acquisition time of FLASH sequence is then reduced by a factor of 8 when the EPI sequence is used. Note that the k-space may be filled by different strategies (zigzag, rectilinear or spiral acquisition) determined by the form of phase-encoding and readout gradients. EPI sequences demand intense, high-performance gradients (frequent gradient-switching, fast signal readout) and long echo-train. The sequence is hence sensitive to magnetic susceptibility and tissue motion that may appear during acquisition. Because the PRFS method is based on gradient echoes with long TE (ideally equal to T_2* of the tissue), conventional gradient echo sequences may result in a relatively long TR. Therefore, when the resulting temporal resolution is inadequate to monitor the thermal treatment, the echo shifting principle (i.e. TR<TE) can be applied [de Zwart *et al*, 1999].

Thermotherapy with closed-loop feedback control. MR thermometry can predict the threshold for thermal tissue damage [McDannold *et al*, 2000] and the spatial extent of the ablated volume during ultrasound thermal therapies [Hazle *et al*, 2002]. With these special features, MR thermometry can be successfully used over a large range of temperature from sub-threshold exposures (necessary to localize the beam distribution before ablation occurs) to over-coagulation temperature changes. Using fast sequences adapted to PRFS thermometry, slices with 2 mm spatial resolution, 1 second temporal resolution and less than 1°C temperature accuracy are available for immobile tissue [Quesson *et al*, 2000]. These real-time temperature (and thermal dose) maps can be used as a feedback to adjust the thermal therapy, in order to ensure safety and efficacy.

The temperature distribution depends on the tissue composition (which influences the energy absorption) and on the physiological parameters of the tissue (perfusion and diffusion). Temperature map intrinsically considers the heat removal by tissue vascularization and may be affected by the blood flow only if a big blood vessel (higher than half-pixel) is present. These tissue parameters are not exactly known for a given target volume and, moreover, they can change during the heating procedure. In addition, variations from patient to patient or even from location to location may occur and therefore the feedback-loop of heating control is essential [Jolesz *et al*, 2005]. Several strategies on temperature closed-loop feedback control have been proposed and implemented in animal experiments. Such a feedback control-method based on proportional, integral and derivative controllers [Salomir *et al*, 2000], [Quesson *et al*, 2002] forces the temperature elevation at a given position (experimental measurement) to follow a predetermined target profile, over a defined time. This experimental profile of temperature acquires the maximum value of temperature within a region of interest, defined prior to sonication. The initial* acoustic parameters are continuously modified during sonication, as demanded by the feedback control based on temperature maps. Further explanations on this feedback strategy will be given in Chapter III. Another feedback approach [Ross *et al*, 2004], [Chopra *et al*, 2009] using multiple adjacent sonications (stepwise rotation of the transducer) controls the temperature threshold, at specific points (representing the tumor margins), which are updated at each new rotation of the transducer.

The clinical thermotherapy intervention (for ablative purposes) currently implements, in one procedure, three important steps. First, prior to ultrasound exposure, a thermal dosimetry planning must be defined with respect to the target location. After that, the heating sequence is applied. Finally, contrast-enhanced images, acquired immediately after treatment, permit to assess the ablated volume and, hence, the efficacy of the treatment. The main step of the treatment –the heating sequence– can be performed with or without the feedback-control of temperature, in function of its application. For benign tumors, the treatment is considered successful when an important volume of the tumor is ablated, as no completely destruction of the tumor is needed. Therefore, the feedback control is only indicated, but not imperative when dealing with benign tumors. However, for safety purposes, the temperature and thermal dose distribution is inspected at some intervals, when the ultrasound beams are not activated. On the contrary, in the case of malignant tumors, the temperature and thermal dose are continuously monitored as the intraoperative feedback control becomes critical for the success of the treatment. To date, MR-guided ultrasound has already been clinically tested for benign tumors such as breast fibroadenoma [Hynynen *et al*, 2001] and uterine fibroid [Tempany 2003], [Pilatou *et al*, 2009], but also as cancer

* determined from previous studies and simulation adapted to the target volume

treatment in breast [Gianfelice *et al*, 2003]. Its application for other malignancies in the brain, liver, and prostate is under development [McDannold *et al*, 2003], [Jolesz *et al*, 2004], [Smith *et al*, 2001]. Moreover, the successfully MR-guided FUS method (the ExAblate 2000 system) was approved, in 2004, by the American Food and Drug Administration for the treatment of symptomatic leiomyomas (uterine fibroids).

I.3.3 RF receive-only coils

The success of the MR-guided ultrasound therapy depends on the quality of the MR-images, i.e. adequate spatial and temporal resolution and also, accuracy in temperature measurement. The applications investigated in this thesis were the esophagus and the rectum. In this case, a well controlled energy deposition in the region of interest is requested, especially to avoid external wall fistula of the digestive duct. For that purpose, local RF receive-only coils were conceived in order to enhance the MR signal.

Coils –shim, gradient or RF– represent a vital component of the MR hardware and are aimed to create a magnetic field, or to detect a change in the magnetic field. The shim coils ensure the homogeneity of the main magnetic field B_0, by producing auxiliary magnetic field in order to compensate the possible inhomogeneities of B_0. The gradient coils are used to produce controlled variations in the main field B_0 (for the spatial localization of the signals) and to apply reversal pulses in some imaging techniques. The RF-coil can be transmitters, receivers, or both, and are directly related to the signal acquisition. In transmission, the goal is to deliver uniform excitation throughout the scanned volume. On reception, the coils must be sensitive and have the best possible SNR. Generally, a MR scanner contains a "whole body" coil (transmitter & receiver), located in the cylinder of the machine, homogeneously covering the entire scan volume. Since the body coil has a large homogeneity field, but a low SNR, it is generally used as a transmit coil, while the signal is often acquired by a smaller coil as the receiver. In term of patient safety, attention must be paid to the RF energy that may be deposited in the body as heat, usually called specific absorption rate (SAR) and measured in W/kg [Chen *et al,* 1998], [Collins *et al*, 2004], [Gorny *et al*, 2008]. SAR is proportional to the square of the strength of the static magnetic field, and the square of the flip angle [Armenean *et al,* 2007]. The safety standards [The International Commission on Non-Ionizing Radiation Protection, 2004] accept a whole body average SAR (average over 6 minutes, at environmental temperatures below 24°C) of maximum 4 W/kg and a temperature increase of maximum 1°C for patients under MR scanning.

The RF receive-only coil is essentially a resonant loop of conducting material such as copper, placed directly on or over the investigated region and therefore called surface coil [Scheck *et al,* 1986], [Knee land and Hyde, 1989]. This receiver coil has a good SNR for tissue adjacent to

the coil, but the signal will decrease with the distance. The homogeneity and sensitive volume can be improved by combining multiple smaller coils into a phased-array system as in the parallel imaging technique [Golay *et al,* 2004], [Ohliger and Sodickson, 2006]. Successful use of the local adapted MR receiver coils is demonstrated by the wide range of applicability in diagnostic purpose: vessel imaging [Hillenbrand *et al*, 2004], pelvic region exploration [Quick *et al*, 2001], [Hricak *et al*, 1994] or endoluminal investigation [Kandarpa *et al*, 1993], [Gilderdale *et al*, 2003], [Beuf *et al*, 2004].

Similar to this concept, but this time for therapeutic purpose, one of the objectives of the work described in this thesis was the integration of local MR coils with the ultrasound transducer. A good spatial resolution, together with an improvement in MR thermometry precision (further information will be given in the next chapters) was aimed for. In order to demonstrate the sensitivity improvement brought by the integrated coils, comparative studies between the miniature coils and an external coil were conducted. Note that for the locations investigated in this thesis, i.e. rectum and esophagus, the most adequate clinical external coil seemed to be the Sense Body coil (4 elements phased-array, see Fig. I.8.a). Nevertheless, another clinical coil (the endo coil, see Fig. I.8.b) suggested the idea of integrating a coil inside the therapeutic device. Therefore, the integrated coils were designed to match the static RF parameters of this dedicated coil. Furthermore, the dynamic tuning and matching, during MR acquisitions, were realized by a commercial available unit (the white box in Fig. I.8.b).

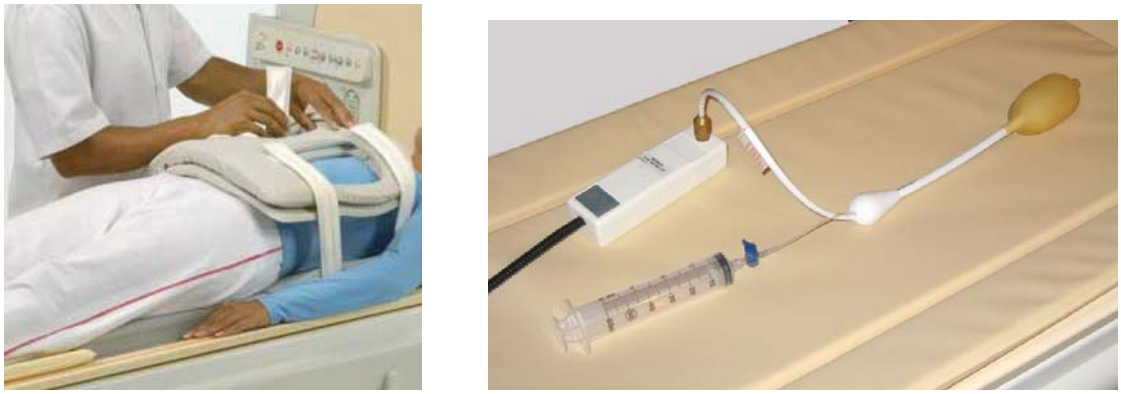

a **b**

Figure.I.8. ***Philips clinical coils.***
a). 4-element SENSE Body coil (body imaging: abdominal, pelvic and thoracic);
b). endo coil (dedicated coil for prostate and rectum). The white box realizes the coil tuning and matching during acquisitions.
http://www.medical.philips.com/us_en/products/mri/options_upgrades/coils/achieva/coils_body.wpd

Chapter II. Experimental *ex-vivo* validation of a RF coil integrated with a planar ultrasound transducer for esophageal applications

II.1 Introduction

II.2 Material and methods

II.2.1 Ultrasound device and experimental setup
II.2.2 Coil design and RF parameters
II.2.3 MR data acquisition
II.2.4 Active temperature control

II.3 Experimental results

II.3.1 Image acquisition
II.3.2 Comparative study: miniature versus standard coil
II.3.3 *Ex-vivo* esophagus study
II.3.4 Temperature monitoring and therapy control

II.4 Discussion

II.5 Conclusion

II.1 Introduction

The objective of this chapter was to investigate the feasibility of an endoscopic device integrating a RF coil with a therapeutical ultrasound transducer, for esophageal applications. The esophageal ultrasound transducer was built in our laboratory [Melodelima, 2004], formerly to this thesis. The RF coils were designed and built as a part of the work of this thesis. The miniature RF receive-only coil aimed to offer high resolution MRI guidance of the thermotherapy, in order to assure the treatment safety and efficiency. The local miniature coils are widely used in applications for diagnosis purpose, but their use in therapy [Piel *et al*, 2005], [Wharton *et al*, 2007] is very limited. A single-loop geometry of the coil [Kandarpa *et al*, 1993], [Gilderdale *et al*, 2003], [Beuf *et al*, 2004] was adapted to the transducer shape in order to offer a maximum sensitivity field in the axial plane, in front of the acoustic region. The new device was studied *ex-vivo,* with respect to the benefit for MR image quality and the benefit for accurate control of thermotherapy, taking into account the possibility of electromagnetic interactions between the ultrasound transducer and the integrated MR coil. Coupling of a near real-time closed-loop temperature controller with the high-resolution MR thermometry, as provided by the miniature coil, was also investigated in *ex-vivo* porcine esophagus samples. When compared to the sensitivity of an external coil, the integrated coils are expected to achieve inframilimeter in-plane resolution, together with temperature measurement accuracy better than 1°C.

II.2 Material and methods

II.2.1 Ultrasound device and experimental setup

The endoscopic HICU (high intensity contact ultrasound) device was based on a cylindrical applicator of ultrasound (see Fig. II.1.a). The plastic tip (11.5 mm diameter, 40 mm-long) had a rounded end and incorporated a commercially available, single-element flat transducer (active zone: 8 x 15 mm², P7-62 ceramics, Quartz & Silice, Nemours, France) operating at 9.45 MHz. The transducer generated an unfocussed, planar beam. A tip cooling balloon of degassed water set at room temperature was used to protect the transducer against overheating, and to achieve acoustic coupling with the neighboring tissue. Water was circulated by a peristaltic pump (Masterflex, Cole-Parmer Instruments Co., Chicago, Illinois, USA) inside a latex balloon via two 7 m-long thin pipes of 3.2 mm internal diameter that ended outside the RF cabin in a 1-liter water tank. The flow rate ranged between 15 and 20 mL/min.

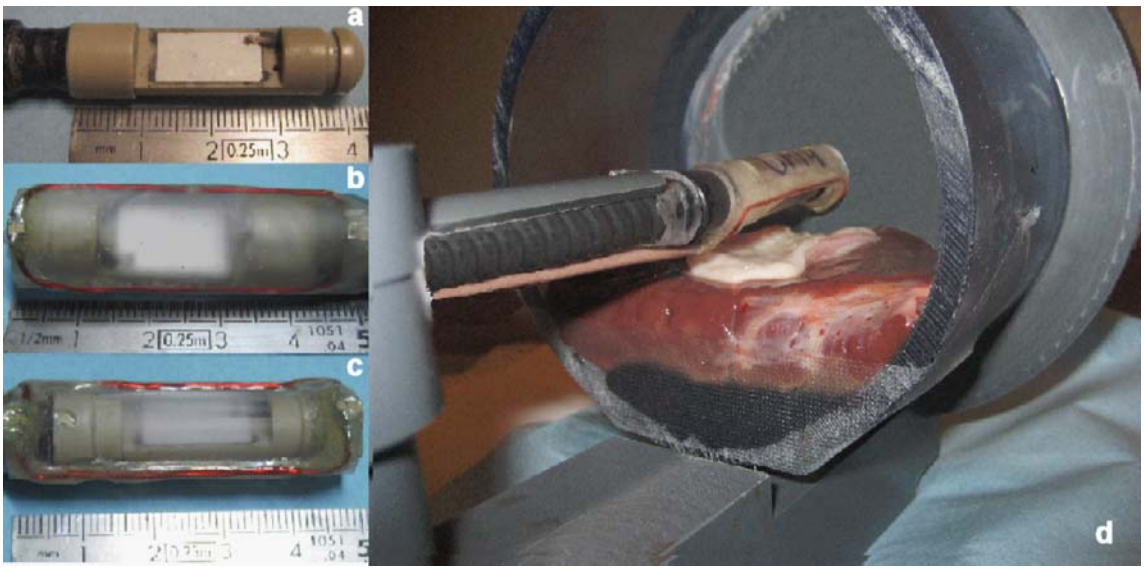

Figure II.1. a). Head of the esophageal ultrasound applicator alone (single element, flat transducer). Diameter: 11.5 mm; active surface: 8 x 15 mm²; frequency: 9.45 MHz.
b) and c). The integrated endoscopic device (with RF coil inside, and respectively, outside the cooling balloon). d). Experimental setup for active temperature control within the ex-vivo esophageal wall.

Figure II.1.d illustrates the experimental setup for *ex-vivo* studies on a porcine esophagus sample, which was used due to its similar anatomy to the human esophagus (wall thickness 3 to 4 mm). The esophagus sample (white region in Fig. II.1.d) was fitted on a 2.5 cm-thick layer of freshly excised pig liver. This reproduced morphological conditions similar to those of a large tumor, with respect to ultrasound propagation and thermal therapy control. A standard echographic coupling gel was used to achieve acoustic coupling between tip balloon, esophagus and liver. The device was aligned with the B_0 axis, as it would be inside the patient's esophagus, within a horizontal, close-bore magnet.

An MR-compatible impedance matching unit was inserted at 80 cm from the transducer to optimize the energy transfer. The final efficiency of the transducer as measured by force radiation method (with 9 m-long cable) was 56.8%. Further details on this method are presented in the next chapter (section III.2.1). The electric driving system (PC interfaced wave generator Hewlett Packard 33120 A; power amplifier, Adece, France, 40 dB gain, maximum power 50 W, integrated power meter) was operated outside the scanner room (see Fig. II.2). The band rejection filter (-80 dB) inserted on the power line was tuned at the MR frequency (i.e. 63.9 MHz) and eliminated the RF interferences from the transducer driving electronics. Grounded coaxial cable (6 m length inside the MRI room and 3 m outside) connected the transducer to its driving power electronics, through the Faraday cage.

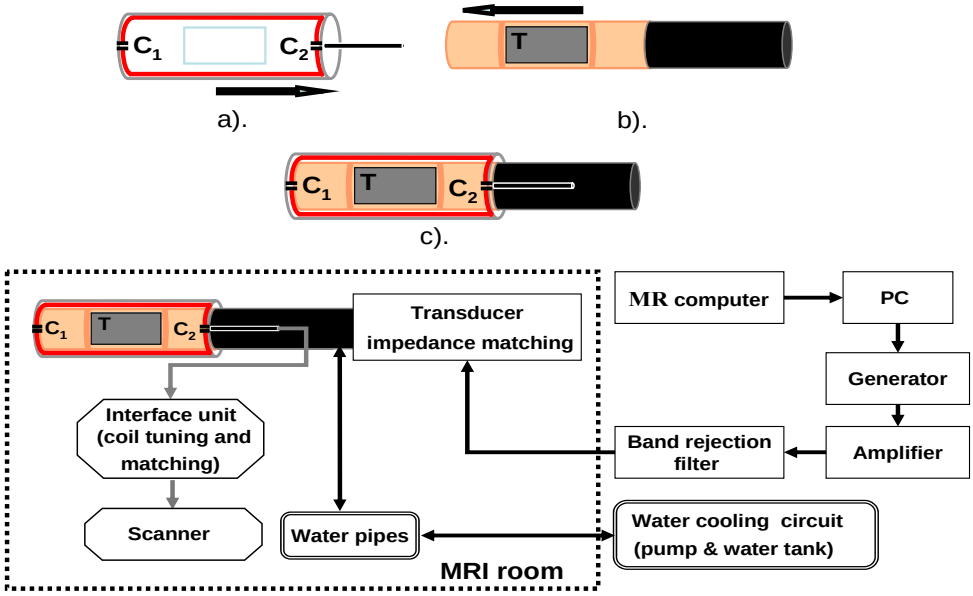

Figure II.2*. Up: *Outline of the integrated device: a). RF coil with acoustic window; b). HICU transducer mounted on its plastic support and c). Operational integrated device. Device assembling is indicated with arrows. Down: Diagram of the electronic setup.

II.2.2 Coil design and RF parameters

Two prototypes of a water-proof endocavitary RF receive-only coil were manufactured: one with the coil inside the cooling balloon and one outside the balloon (see Fig. II.b,c). The diameter of the device was restricted because of obvious anatomical constraints. However, the coil had one freedom degree, which was the longitudinal size. This parameter has been adjusted within a moderate range, in order to: 1). minimize electromagnetic (EM) interactions between coil and transducer, and 2). extend the coil sensitivity range along the ultrasound beam as far as possible. The EM interaction was observed by studying the coil with and without the transducer. This EM interaction was considered acceptable if the quality factor of the integrated coil was at least 30, and if the depth of the coil sensitivity field decreased by less than 30% in presence of the transducer.

A single-turn rectangular loop of copper wire (of 14 mm inner width x 43 mm long, 0.7 mm wire diameter) was mounted and sealed (Epoxy adhesive, RS components, Corby, UK) on a cylindrical plastic support (OD: 14 mm, thickness: 1 mm, length: 48 mm), see Fig. II.1.b. The second model of coil (positioned outside the balloon, see Fig. II.1.c) was similar to the first one, but 2 mm wider. An elongated saddle was chosen as the geometry of the integrated coil in order to maximize the depth of the useful sensitivity field along the acoustic beam. An acoustic window was cut into the coil support in front of the piezoelectric active zone to allow propagation of the acoustic beam. The coil on its plastic support was placed over the head of the ultrasound applicator from the distal end. Two non-magnetic capacitors per coil, disposed as seen in Fig.

II.2.a, were used for initial static RF tuning and matching (frequency range from 63.0 to 63.5 MHz). The used values (C_1/C_2) were 116.7 pF /224 pF for the first coil and, respectively, 92.3 pF /224 pF for the second one.

Measurements of coil resonance/impedance (see Fig. II.3) curves were performed with a network analyzer (Rhode & Schwartz ZVB 4, two port configuration, München, Germany). An inductive coupling method with a broad band antenna (also home-made, see Fig. II.3.a) was used to trace the resonance curve of the integrated coils. The quality factor, Q, of the integrated coil was calculated as the ratio of its resonant frequency divided by the -3 dB bandwidth.

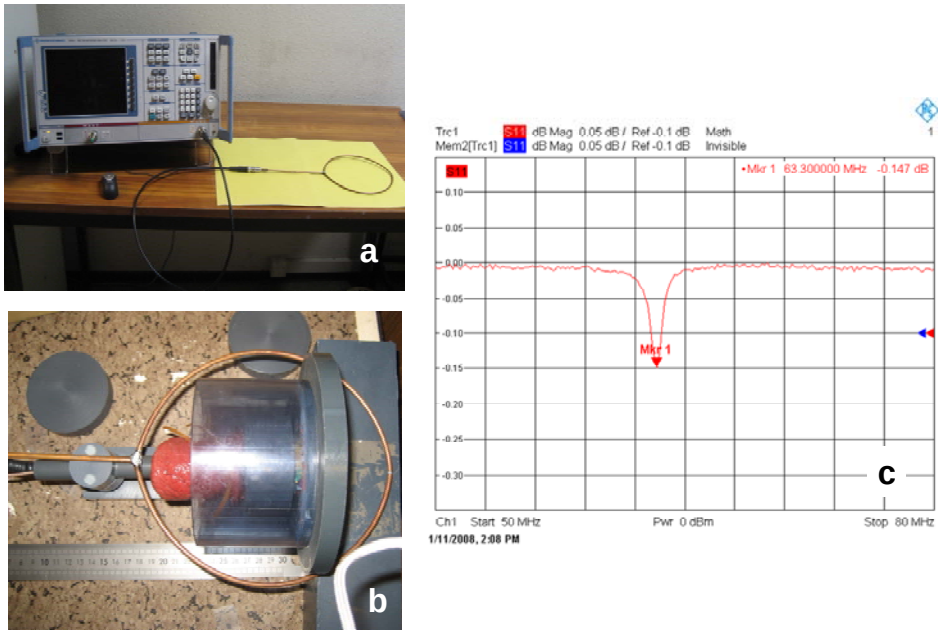

Figure II.3. Experimental setup in order to measure the RF (static) parameters of the integrated coil. a). 2-channel network analyzer and a home-made broad band coil; b). The endoscopic device (not visible) loaded within fresh muscle; c). Typical resonance curve acquired using the setup from b).

The results of these measurements (frequency F, quality factor Q, and impedance Z) with or without transducer, under unloaded (i.e., in air) or loaded (i.e., water or *ex-vivo* tissue) conditions are given in Table II.1. The coil parameters, measured for both types of coil integration with respect to the cooling balloon, were very similar (variation of less than 9%). Therefore, the Table II.1 presents only the parameters of a single coil (the outside balloon integration), making it easy to follow the variation of F and Q under different conditions. The integrated coil should have a good Q (at least 30 units), for a frequency from 63.0 to 63.5 MHz, in tissue. Only this tissue-loading environment is important for further MR experiments. The other loading environments demonstrated the parameters variation and helped me to design the coil, before insulating it. Note that the Q decreases from 109 units (coil alone, in air) down to 74 units (coil integrated within the transducer, in tissue). In addition, the frequency decreases when the coil is more loaded (air/water), but increases when the transducer is present. As a general rule, the transducer

decreases the Q-factor and increases the resonance frequency of the coil, for all loading environments.

Coil Parameter	Unloaded (air)		Loaded (water)		
	Coil alone	Coil +T	Coil alone	Coil +T	Coil + T + tissue
F [MHz]	63.2	63.8	62.9	63.35	63.3
Quality factor, Q	109.0	99.7	101.5	88.0	73.6
Real Z [Ω]	47	83	32	66	81
Imag Z [Ω]	-243 j	-325 j	-202j	-275j	-279j

***Table II.1.** Electrical static parameters of the integrated coil (the outside balloon coil), with/without the transducer (T), for unloaded (air) and loaded (water or tissue) media.*

However, note that these coil parameters were measured for a static tuning of the coil, prior to the MR examination. The real parameters, as they appear during the MR experiment, were difficult to measure. For this final operating setup, a Philips standard electronic unit automatically performed the detuning during the excitation pulse, and the final tuning and matching (at the Larmor frequency, here 63.9 MHz) during the echo train acquisition. The length of coaxial cable connecting the coil to this interface unit must be close to λ/4 at 63.9 MHz (i.e. a 68 cm-length for the coaxial cable used here) with a tolerance of ±2%. The same λ/4 cable was used to electrically connect the loop coil to the network analyzer when measuring the real and imaginary impedance.

II.2.3 MR data acquisition

All MRI acquisitions were performed on a clinical Achieva 1.5 T scanner (Philips, Best, the Netherlands) equipped with Copley 274 Master gradient, maximum strength 30 mT/m, and maximum slew rate 150 T/m/s. MR shimming was performed for all acquisitions. Table II.2 summarizes the MR parameters used for all acquisitions within this chapter, with single slice geometry each. The MR imaging slice was positioned either sagittally or axially[*], centered on the transducer longitudinal or transverse mid-plane, respectively. Additionally, two saturation slices were placed parallel to the imaging slice to reduce the flow artifacts originating from the tip cooling balloon.

For comparison, spin echo (TSE - turbo spin echo) and RF-spoiled gradient echo (FLASH/ TFE - turbo field echo, and segmented EPI/FFE - echo planar imaging/fast field echo) images were acquired in both sagittal and axial planes, using either a standard 4-element phased array extracorporeal coil (4-channel SENSE Body coil) or the integrated miniature coil, on fresh samples of porcine muscle. Phantoms with salty water were not considered appropriate here,

[*] In this thesis, axial or sagittal planes refer generally to the MR slice. When discussing the ultrasound planes, this is explicitely specified.

because liquid convection in large volumes would compromise the GE-phase map stability. The acquisition parameters were set as a compromise between integrated and standard coils performance.

An IR-T_1-w (inversion recovery T_1-weighted) spin echo sequence was used with the integrated coil only, for visualization of the *ex-vivo* esophagus morphology.

Sequence	Purpose	FOV [mm²]	Voxel [mm³]	TR/TE [ms]	Flip angle [°]	Lines /TR	Acq./ Reconstr. matrix	Acq. Time [s]
T_1-w-TFE-comp Gradient echo	Morphology *Coils comparison*	64 x 64	0.25 x 0.25 x 6	200/14	35	1	256 x 240 256 x 256	48
IR-T_1-w-TSE-IC Spin echo	Morphology *Dedicated for IC*	64 x 64	0.25 x 0.25 x 3	3000/12 TIR = 500	90	16	256 x 256 256 x 256	48
FFE-EPI-comp Gradient echo	MR thermometry *Coils comparison*	80 x 80	0.63 x 0.63 x 5	180/20	45	11	128 x 121 128 x 128	1.98
FFE-EPI-IC Gradient echo	MR thermometry *Dedicated for IC -HICU*	64 x 64	0.5 x 0.5 x 5	200/17.1	45	11	128 x 121 128 x 128	2.2

IC – integrated coil

***Table II.2.** Summary of acquisition sequences and parameters used for this study.*

For fast MR thermometry, the proton resonance frequency shift (PRFS) method was chosen because of its linearity and tissue-type independence. The dynamic acquisition of baseline image* (30 dynamics, i.e. 60-second acquisition time) was performed without sonication, to map the intrinsic standard deviation of experimental temperature data (SDT). No sonication was performed, then no temperature rise was induced, and therefore the SDT-maps measured directly the accuracy of the temperature measurement. To correct for possible B_0-drift over the 30-dynamic acquisition period, the experimental values of the complex phase as recorded in each pixel of interest were plotted versus time and a first order polynomial fit was performed. That first order polynomial fit was subtracted from the original data set before computing the standard deviation of the pixel. No spatial averaging of MR data was performed in any experiment. The mask for SDT-maps was a large circular ROI (region of interest) covering almost the entire image, within an upper limit of 3°C-SDT was defined (see Fig. II.5, b and f). SDT was punctually compared for the standard extracorporeal coil *versus* the integrated coil, at 10 mm and 20 mm distance from the surface of the cooling balloon.

MR thermometry for active control of the procedure (see the last row of Table II.2) was performed in the axial plane, on freshly excised porcine esophagus using the integrated coil only. The thermal imaging slice was set orthogonal to the transducer long axis, centered on transducer

* The same MR-thermometry slice was repetitively measured 30 times (no sonication, hence no temperature rise).

mid-plane. The median position of the slice guaranteed the most extended acoustic beam profile. Slice thickness was equal to 33% of the transducer length. Under these conditions intravoxel temperature averaging in slice select direction had no significant apodisation effect at the spatial scale of the acoustic beam pattern. RF contamination of MR signal during sonication was checked based on phase maps standard deviation (with and without power application), within the same dynamic acquisition, outside the beam pattern.

II.2.4 Active temperature control

For active temperature control, reconstructed MR data (magnitude, phase) were transferred via an Ethernet connection to a local PC using a real-time data export interface (DRIN Package - direct reconstructor interface, Philips, Best, The Netherlands). Total latency including reconstruction, data transfer, calculation of the thermal map, and display was estimated to be less than 200 ms per acquired data volume. In each measurement, the first 5-time frames of the 50 to 70 dynamic scans were averaged to form the reference phase map. The remaining dynamic scans covered the heating sequence, including an initial active stage when the automatic feedback was applied during sonication, and a later passive stage, to monitor the temperature return to equilibrium. Total duration of dynamic acquisition ranged from 110 to 154 s.

Given the acoustic beam pattern, out of plane (*i.e.* longitudinal) heat diffusion was not significant for the current slice geometry, thus this component of diffusion was neglected. Two-dimensional thermal imaging accounted for both energy deposition and heat conduction. The method for feedback temperature control was based on the Fourier transformation solution of the Bio Heat Equation [Quesson *et al*, 2002], adapted to the contact ultrasound therapy. For this reason, the cooling effect of the tip balloon was considered when programming (Visual C++ and Matlab) [Salomir *et al*, 2006]. The proportional, integral and derivative (PID) compensation algorithm takes into account the physical characteristics of tissue (diffusion, absorption) and allowed the power level to be updated [Salomir *et al*, 2000] every time a new MR data set was available, i.e. every 2.2 s. The typical target curve of temperature consisted of a continuously rising portion (30 s) followed by a steady-state region for 30 s. The target temperature level during the steady state was arbitrarily chosen to correspond to 32 times the lethal thermal dose [Sapareto and Dewey, 1984]. The thermal dose calculation was performed assuming an initial temperature at 37°C. Assessment of temperature controller performance was based on the correlation between the predefined target curve and the experimental temperature evolution. The experimental temperature curve was defined as the maximum temperature value within a predefined region of interest, collected for each dynamic scan. In different experiments, the temperature (and consequently, the thermal dose) was actively controlled at three different locations in *ex-vivo*

esophageal tissue, selected on the symmetry axis of the ultrasound beam, at 1). the inner superficial layer *i.e.* close to the device (~ 1 mm); 2). the half of total depth of the wall (~ 2.5 mm); and 3). the distal wall of esophagus *i.e.* at the interface to surrounding liver (~ 4 mm). In the final experiment the temperature was controlled deeper, at 10 mm in the liver, reproducing the geometrical conditions for a larger tumor.

An effective absorption coefficient was defined as the ratio of the temporal derivative of temperature to the electrical power applied on the transducer. This parameter is proportional to the ultrasound absorption in tissue, but takes also into account the electroacoustic efficiency of the transducer, the section area of the beam, the mass density, the specific heat and the beam attenuation between the transducer and the control location. In our calculation, an effective absorption coefficient of 0.08°C/(W·s) was used for the control location at 2.5 mm depth. This value of absorption, in the current setup, corresponded to an attenuation of 0.06 MHz·(Np/cm) in the rectum wall, the most closely type of tissue available as reference [Duck 1990, p105]. The diffusion coefficient (also called diffusivity, denoted here as D) was defined as the ratio of the heat conductivity to the product (mass density) x (specific heat). A reduced value of the diffusion of 0.03 mm²/s was assumed, which was four times lower than the corresponding typical value in skeletal muscle [Duck 1990, p16]. Overall, the underestimated D value represented a condition to improve the controller robustness against measurement noise [Salomir *et al*, 2000]. As the temperature gradients were weak with planar applicator of ultrasound, a moderate error in the D-parameter had no significant impact on the temperature convergence.

II.3 Experimental results

The purpose of each experiment was given in Table II.2. A comparative study between the integrated coil and an external coil was performed. The improvement brought by the integrated coil was demonstrated on both anatomical (T_1-w-TFE) and thermometry images (FFE-EPI). Furthermore, a high-resolution image of ex-*vivo* esophagus was acquired with the integrated coil (IR-T_1-w-TSE). Finally, the ultrasound-induced temperature rise was automatically controlled, at different depths, by a feedback-controller. The integrated device enhanced the control accuracy.

II.3.1 Image acquisition

No RF-related artifacts were found to corrupt the MR data obtained with the integrated coil during the HICU sonication. Phase map acquired to assess for the local field homogeneity, as illustrated in Fig. II.4, showed a radial phase variation in the sample. With the current echo time, 2π phase wrapping corresponded to 0.92 ppm field variation, at the spatial scale of several centimeters (see Fig. II.4). That local field gradient was on the order of 0.1 mT/m which can be neglected as

compared to the encoding gradient strength (up to 30 mT/m). No magnitude signal loss due to the local field gradients in the vicinity of the device, i.e. no T_2* reduction, was noticed. Flow artifacts, caused by the water movement inside the cooling balloon, were seen as localized ghost pattern in phase-encoding direction on either magnitude (Fig. II.5.e) or phase images (Fig. II.4, see the black arrow-heads). The use of parallel saturation slices attenuated, but did not completely eliminated these flow artifacts, as water flow is laminar, but not purely orthogonal to the acquisition slice. Furthermore, if necessary, rotation of the phase encoding direction by 90° [Kastler *et al,* 2006] lead to an artifact-free region in front of the transducer, in the direction of the ultrasound beam (see white arrows in Fig. II.4).

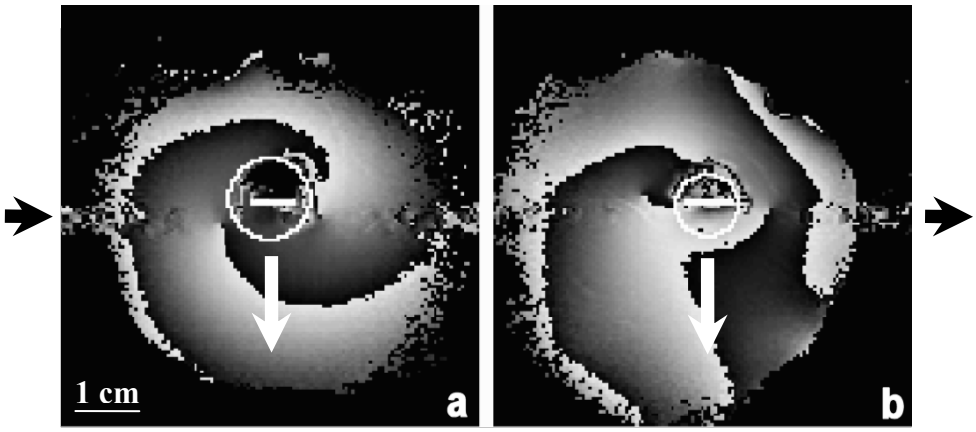

Figure II.4. Phase images acquired with the endoscopic device, axial plane, ex-vivo muscle (see parameters in Table II.2, 4th row): a) coil inside the balloon; b) coil outside the balloon. The white horizontal bar is the transducer active surface, while the circle indicates the cooling balloon (this information is overlaid as extracted from magnitude data). The water is situated mainly in the lower part of the cooling balloon. The black arrow-heads indicate the direction of the flow artifacts which coincides with the phase-encoding direction. The white arrows show the direction of sonication. The scale bar is 1 cm. FOV: 64 mm, 1 voxel: 0.5 x 0.5 x 5 mm3.

II.3.2 Comparative study: miniature versus standard coil

Both miniature coils showed a similar gain in sensitivity. Therefore, only one coil (positioned outside the balloon) was directly compared with the extracorporeal coil. The external coil had a relatively homogenous sensitivity field, while the integrated coil showed variability in the sensitivity field. Thus, the sensitivity of the integrated coil was better close to the transducer and decreased with the distance. The miniature coil showed a gain in sensitivity* by a factor of 7 at 10 mm depth in tissue (fresh meat sample) over the extracorporeal phased-array coil. Note that this gain factor may represent an average, being higher if calculated closer to the transducer, and, respectively, lower, if calculated at deeper locations. Figure II.5 summarizes the results in the axial plane for the extracorporeal coil (a-d) and endoluminal coil (e-h). A significant improvement of the SNR was seen in the high-resolution T_1-w-TFE anatomical images (voxel of 0.25 x 0.25 x 6 mm^3) obtained with the integrated coil (Fig. II.5.e), as compared to the extracorporeal coil (Fig. II.5.a). Furthermore, baseline SDT-maps and corresponding horizontal and vertical SDT profiles, obtained with the FFE-EPI sequence dedicated to MR thermometry, are shown for the extracorporeal coil (Fig. II.5.b, c and d) and endocavitary coil (Fig. II.5.f, g and h). The sensitivity field of the integrated coil was symmetric (up down) with respect to the loop plane. Since the therapeutic region was located in front of the transducer (i.e. in the lower half of the image), the horizontal (Fig. II.5. c and g) and vertical (Fig. II.5. d and h) profiles were extracted from that region. With a voxel size of 0.63 x 0.63 x 5 mm^3, the SDT was 1.9°C for the extracorporeal coil. The SDT was improved by using the integrated coil down to 0.3°C at 10 mm from the tip of the balloon, and down to 0.75°C at 20 mm distance.

The same data set (i.e. baseline acquisition with integrated coil, no sonication) was used to evaluate possible temperature change in tissue, in the near vicinity of the miniature RF coil, due to E field coupling, particularly close to the copper wire. Within the current noise standard deviation at that location (0.2°C, see Fig. II.5.h), no temperature increase could be detected. If local heating occurred because of the E-field coupling, this was inferior to 0.2°C.

* Because of the variability of the coils sensitivity field, a direct comparison (other than visual) between the corresponding SDT-maps was difficult. Therefore, the sensitivity gain factor was calculated punctually, at defined depths. Here, for example, the gain factor was the ratio between the SDT-values corresponding to each coil, values measured at 10 mm-depth from the surface of the balloon.

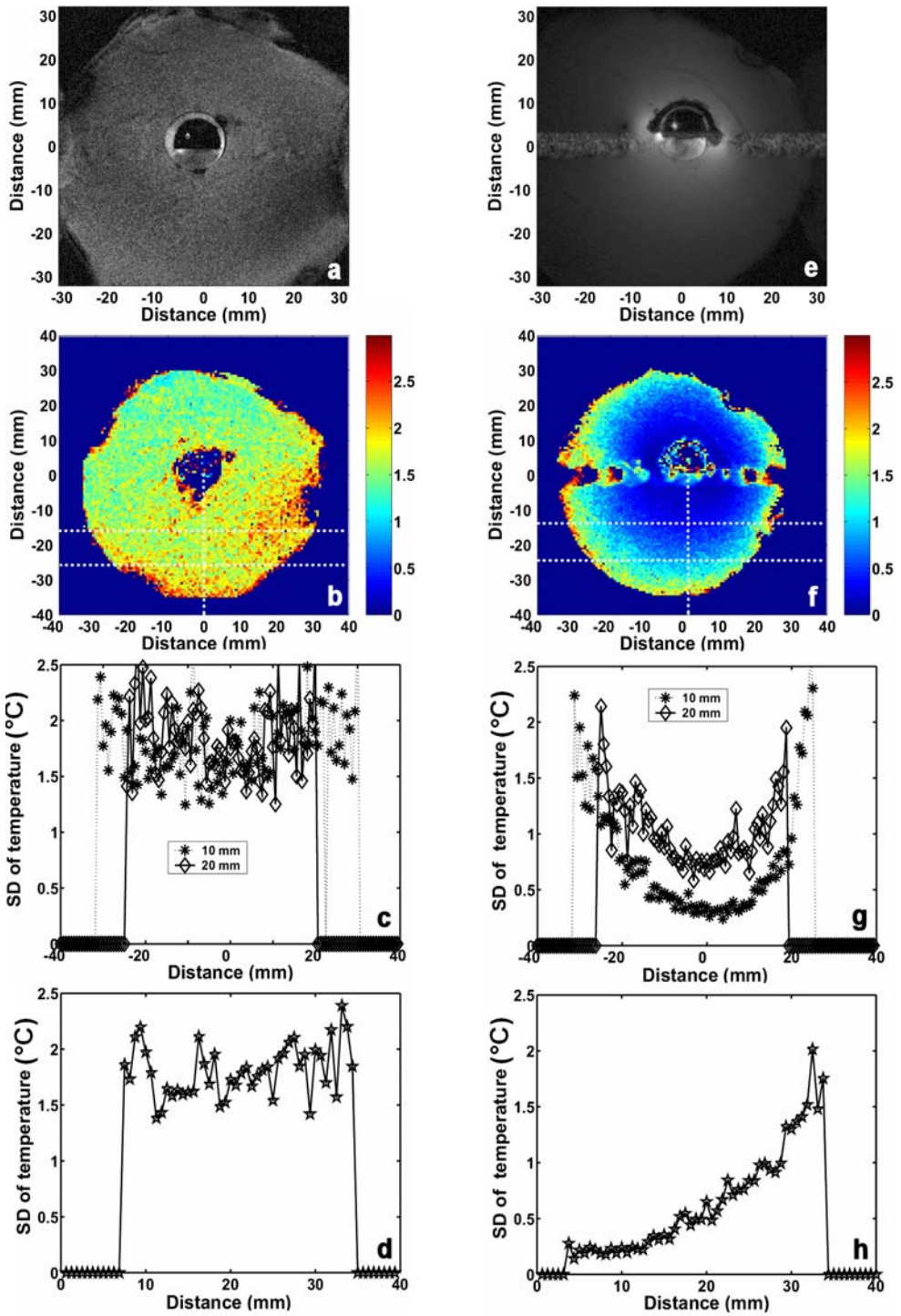

Figure II.5. ***Comparative study of coils (left: extracorporeal coil, right: integrated coil), axial plane, ex-vivo muscle.***

a) and e): ***anatomical image (see parameters in Table II.2, first row). Visible are the US applicator (black hemisphere) and its water filled guide pipe (white spot in image), the cooling balloon (white circle) and freshly excised porcine muscle surrounding the device tip. The upper black semicircle (seen in e) is the plastic support of the miniature coil. FOV: 64 mm, 1 voxel: 0.25 x 0.25 x 6 mm^3.***

b) and f): ***baseline SDT-maps in °C units (no sonication, SDT limited to 3°C), centered on the transducer (see parameters in Table II.2, third row). FOV: 80 mm, 1 voxel: 0.63 x 0.63 x 5 mm^3, 2 s/dyn. The dotted lines indicate the SDT profiles, horizontal (plotted in c and g) at 10 mm (* symbols) and respectively 20 mm (◊ symbols), and vertical (plotted in d and h). Note that useful sensitivity of endocavitary coil (SDT < 1°C) extends up to 26 mm depth (see h), which is twice the loop width.***

II.3.3 *Ex-vivo* esophagus study

The optimal spatial resolution for appropriate visualization of the freshly excised porcine esophagus was found to be 0.25 x 0.25 x 3 mm^3 (T_1-w-TFE or IR-T_1-w-TSE). This optimal value was chosen after testing resolutions ranging from 0.2 x 0.2 mm^2 to 0.5 x 0.5 mm^2 (for in-plane resolution), and slice thickness from 3 to 5 mm. Figure II.6 presents an IR-T_1-w-TSE image of the device setup according to Fig. II.1.d, showing the transducer, the cooling balloon, the esophagus and the liver tissue. The acoustic coupling gel (1 mm average width) between the tip of the balloon and esophageal sample was better visualized in the transverse plane. The region of interest in front of the transducer is free of flow artifacts, as the phase-encoding direction was set to the foot-head direction for the sagittal plane (a) and right-left for the transverse plane (b).

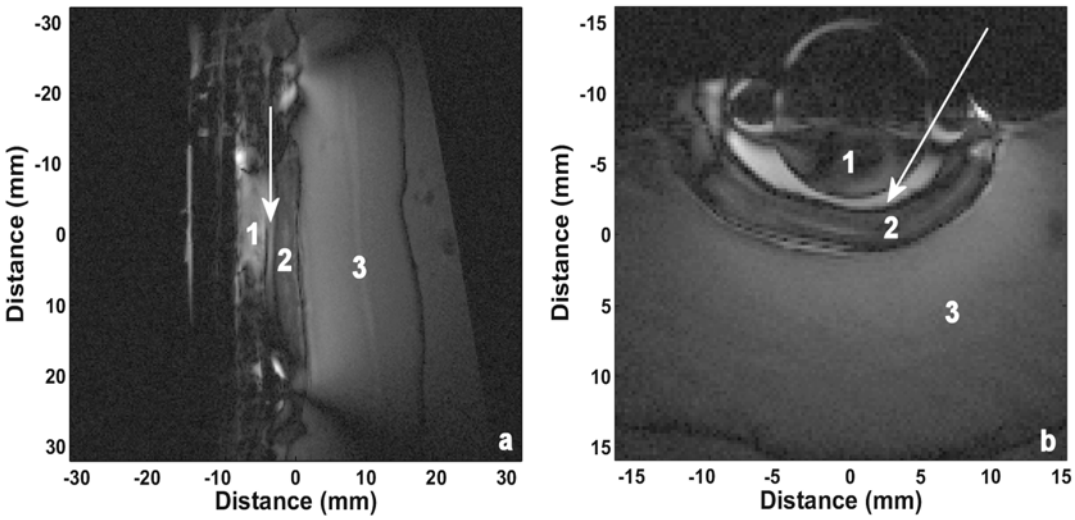

Figure II.6. ***IR-T_1-w-TSE images acquired with the endocavitary coil in ex-vivo porcine esophagus (see parameters in Table II.2, second row) in sagittal plane (a, full FOV shown) and axial plane (b, 32 mm square ROI shown). The water inside the tip balloon (1), the esophagus wall (2), and the liver tissue (3) are clearly visible on these high-resolution slices. The arrow indicates the echographic gel for acoustic coupling. FOV: 64 mm, 1 voxel: 0.25 x 0.25 x 3 mm^3.***

The esophagus wall could also be clearly visualized on segmented EPI gradient echo magnitude images (thermometry sequence), but with less contrast as compared to IR-T_1-w-TSE images. After multiple tests, the optimal resolution for thermal images was found 0.5 x 0.5 x 5 mm^3 with a temporal resolution of 2s /image and an SDT inferior to 0.3°C within the esophagus (see Fig. II.7). For this experiment, the SDT-map (a) and its vertical profile (b) are shown only within the esophagus (sagittal plane). The limit of 1°C set for acceptable SDT was reached at a distance of 20 mm from the tip balloon surface, deep in the liver tissue. Note that these were true voxel-based SDT values without any ROI averaging.

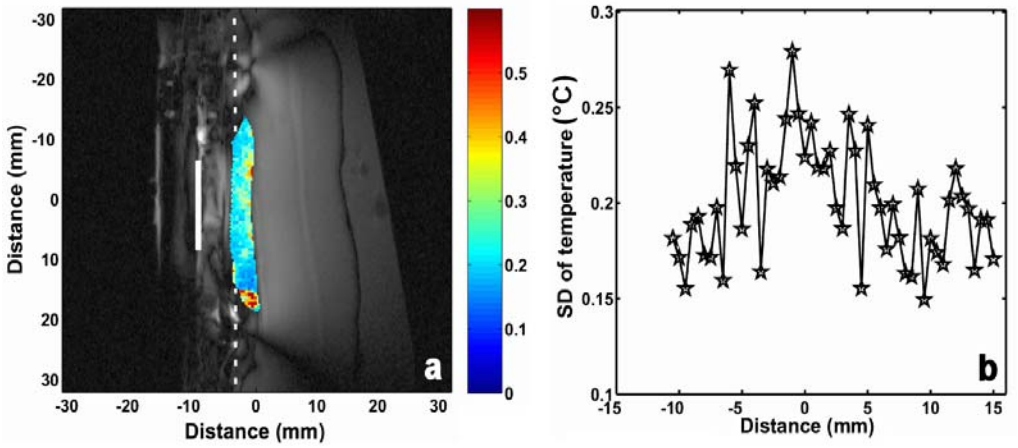

Figure II.7. SDT map (a) and vertical profile (b) for sagittal plane acquired with the endocavitary coil in ex-vivo porcine esophagus. The SDT map obtained with the FFE-EPI sequence was overlaid to an anatomic image obtained in identical position with the IR-T_1-w-TSE sequence. The white bar indicates the active surface of the transducer, and the dotted line indicates the SDT vertical profile, which is plotted in b). This profile was chosen at 1 mm depth in the esophagus. The colorbar corresponding to the SDT-map is in °C.

II.3.4 Temperature monitoring and therapy control

The applied power level, as automatically set by the controller, ranged between 0 and 16 W. The feedback controller accurately matched the experimental temperature profile to the target temperature curve. The average accuracy of the mean experimental temperature at steady-state regime was 1.1% (relative error), with relative SDT of 1.7%. These results were obtained under well-defined conditions: reaching the predefined target (20°C temperature elevation) in 30 s. Figure II.8 illustrates a typical example of temperature rise and thermal dose maps (a), relative temperature time course at the control point (b), and thermal dose control within the esophageal distal wall (c). For this example, the mean temperature over the steady-state regime was 20.13°C (1.1% offset with respect to the targeted value of 19.9°C), with standard deviation of 0.34°C. This residual mismatch was very close to the noise SDT at the control location (0.25°C, see Fig. II.7.b). Note that the experimental noise SDT is the intrinsic accuracy limit of the controller. The experimental thermal dose delivered at the external wall of the esophagus was 31.4 LDU (Lethal Dose Unit defined as the necrosis threshold according to Sapareto and Dewey [1984]). This value is in excellent agreement with the predefined value (arbitrarily set to 32 LDU, and corresponding to the temperature controller target curve, i.e. a temperature elevation of 19.9°C over 30 s). Note that the main contribution to the integrated thermal dose was accumulated during the steady-state phase, whereas the initial rise and the final decrease of temperature did not significantly contribute to the thermal dose.

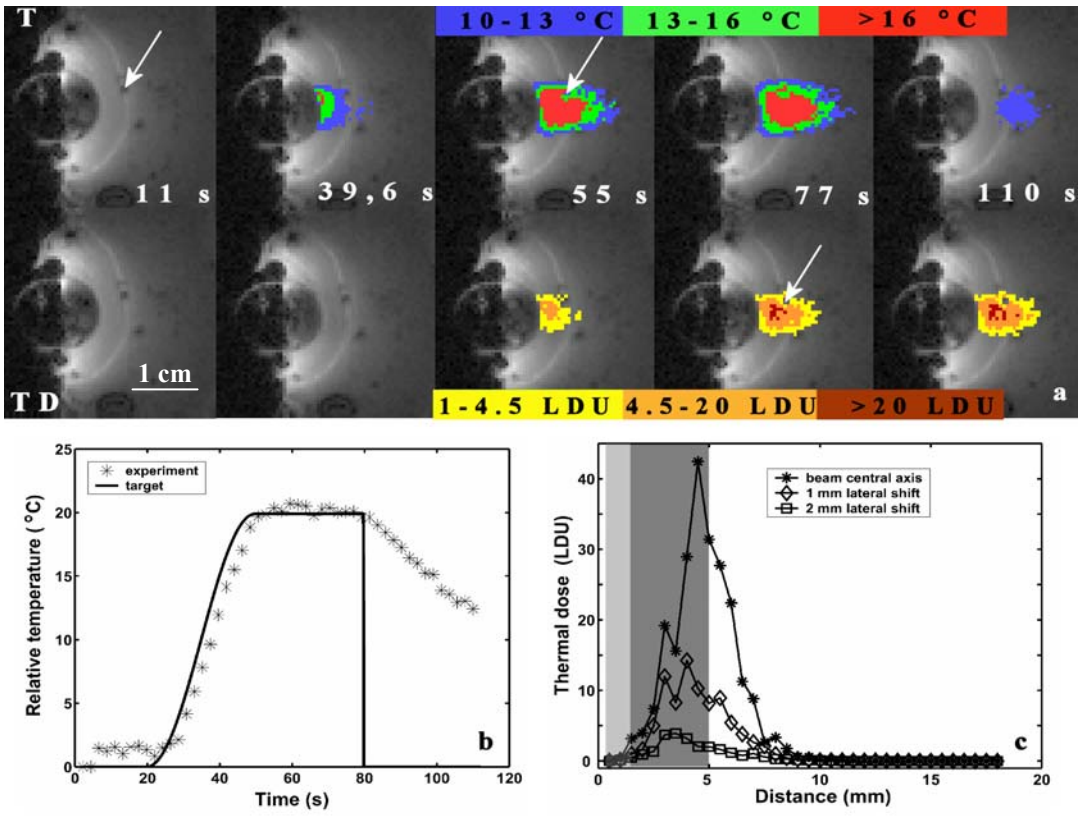

Figure II.8. ***First row: a) Example of relative temperature (up) and thermal dose (down) maps, axial plane (see parameters in Table II.2, fourth row; half FOV shown) for a heating experiment where temperature was actively controlled at half depth of the esophagus wall. Time originates at the MR acquisition start point. Data are shown before sonication (11 s), during actively controlled sonication (11-77 s), and during the period of return to equilibrium (110 s). White arrows indicate a trapped air bubble at the esophagus/liver interface. FOV: 64 mm, 1 voxel: 0.25 x 0.25 x 6 mm^3.***

Second row: b) Time course of the relative temperature at the control voxel (half depth of esophagus wall) for the same experiment; c) Thermal dose control at external esophagus wall interface (the light-gray-shaded domain indicates the acoustic gel, and the dark-gray-shaded domain indicates the esophagus). Horizontal axis originates at the balloon surface.

Table II.3 overviews the results of the heating-control experiments at different locations in the esophagus, for a target temperature elevation of 15°C, 19.9°C or 40°C. Row 5 corresponds to the experiment presented in Fig. II.8. The heating experiment (see Fig. II.8.b) counts two phases: active heating (with two regimes: temperature rise and steady-state), and cooling (when the sonication is cut off). The temperature control refers mainly to the steady-state (or flattop) stage, when the feedback-loop maintains the experimental temperature at the same level as the target temperature, defined prior to the experiment. Therefore, the accuracy of temperature control (i.e. average and standard deviation) was calculated only for this specific stage of the heating experiment (steady-state regime), for each experiment. The control was better for lower target temperature (rows 3 versus 6), and also when the control points were closer to the device (rows 1 versus 2 versus 3).

Experiment ID	Absorption coeff. [°C/(W·s)]	Diffusivity [mm²/s]	Control region	Rise/flattop duration [s]	Target temp. [°C]	Average temp. on flattop [°C], rel. error (%)	Temperature SD on flattop [°C], error (%)
1	0.08	0.03	C1	30/30	15	15.01 (0.06%)	0.35 (2.3%)
2	0.08	0.03	C2	30/30	15	15.02 (0.13%)	0.47 (3.1%)
3	0.07	0.03	C3	30/30	15	15.26 (1.7%)	0.39 (2.6%)
4	0.08	0.03	C1	30/30	19.9	19.78 (0.6%)	0.89 (4.5%)
5	0.08	0.03	C2	30/30	19.9	20.13 (1.1%)	0.34 (1.7%)
6	0.1	0.03	C3	30/30	19.9	20.42 (2.6%)	0.4 (2%)
7	0.08	0.1	C2	90/60	40	41.15 (2.9%)	0.36 (0.9%)

C1 – inner layer of esophageal wall (approximately 1 mm from the cooling balloon)
C2 – half of esophageal wall (approximately 2.5 mm from the cooling balloon)
C3 – external layer of esophageal wall (approximately 4 mm from the cooling balloon)

Table II.3. ***Summary of heating and temperature control sequences used in this study.***

II.4 Discussion

In this work, an ultrasound transducer for HICU therapy was combined with an optimized RF coil to improve the quality of MR temperature measurements acquired for therapy monitoring and guidance. The endoscopic device demonstrated excellent passive and active MR compatibility, as no susceptibility-induced or sonication-related RF artifacts were noticed. Flow artifacts due to tip cooling water could be shifted out of the region of therapeutic interest. These flow artifacts were clearly visible with the integrated coil, as the signal sensitivity was maximal inside the balloon, while for the body coil the artifacts reached the noise threshold and were barely detectable. Flow artifacts were proportional to the fluid flow rate. The flow rate of cooling water (at room temperature, i.e. 20°C) was similar to that reported for *in-vivo* experiments by Melodelima *et al* [2003]. Decreasing the temperature, for example to 2°C, would allow a decreased flow rate, and further a reduced artifact.

A fundamental advantage of this local coil consisted in the capability to acquire images with high resolution (small FOV), without possible phase wrapping from other regions of the chest. This phase wrapping problem appears usually when using external coils and the strategies to eliminate it are generating of extra acquisition-time. Therefore, the small FOV-images were not only of high SNR, but also offered a rapid acquisition.

The goal of the current study was to demonstrate a signal sensitivity gain for MR thermometry sequences using the integrated internal coil versus the external coil. The quantity of

interest was considered to be the SDT (standard deviation of temperature) and not the SNR (signal to noise ratio). However, SDT and SNR are reciprocal quantities, see [Conturo *et al*, 1990], [Salomir *et al*, 2005]. Unlike the isotropic sensitivity of extracorporeal coil over the region of interest, the endocavitary coil has a significant sensitivity gradient, which is higher close to the coil and smoothes with increased depth. Thus, the maximum sensitivity of the coil was located within the balloon, which is not the therapeutic region of interest. For all the experiments described here, the total diameter of the tip cooling balloon was not larger than 16 mm. To illustrate this signal decay with depth, the horizontal profile for SDT was calculated at two different distances from the cooling balloon surface: 10 mm and 20 mm. This range covers the size of most esophageal tumors and a good SDT (inferior to 1°C) still could be achieved in this region. Consequently, this technology is optimal for tumors not exceeding 2.5 cm depth.

For the current application, the most important therapeutic safety issue was to avoid severe complications, such as fistulae. Therefore, a major issue was the thermal dose control at the external esophageal wall. In thermotherapy, temperature and thermal dose are related by a non-linear relationship [Sapareto and Dewey, 1984]. The noise on temperature measurements originates from the phase noise and has therefore a normal distribution [Conturo *et al*, 1990], but the relationship temperature-thermal dose yields to a non-Gaussian noise in TD. The temperature versus thermal dose relationship [Sapareto and Dewey, 1984] is different below and above the 43°C threshold. We are considering here only the case above 43°C since the thermal coagulation regime, when lethal thermal dose is accumulated in tens of seconds, corresponds to an absolute temperature above 50°C. The typical noise of acceptable thermal maps (σ) is on the order of 1°C, hence a Gaussian density of probability for a measured value T around the mathematical expectation T_0 will fall to zero on its left side before the 43°C threshold. We can therefore use a continuous Gaussian distribution to calculate the thermal dose, written as:

$$TD_{\exp}(T_0) = \int_{-\infty}^{\infty} \rho(T) \cdot 2^{T-43}\, dT = \int_{-\infty}^{\infty} \frac{1}{\sqrt{2\pi}\cdot\sigma} \cdot \exp\left[-\frac{(T-T_0)^2}{2\sigma^2}\right] \cdot 2^{T-43}\, dT \qquad \text{Eq. II.1}$$

Furthermore, solving the integral (see Appendix A, at the end of the manuscript, for details) we obtain:

$$TD_{\exp}(T_0) = 2^{T_0-43} \cdot \exp\left[\frac{(\ln 2)^2}{2}\cdot\sigma^2\right] \approx TD_{theor}(T_0) \cdot \exp\left(0.24\cdot\sigma^2\right) \qquad \text{Eq. II.2}$$

This final result translates the SDT into an exponential overestimation of the thermal dose, which depends only on the standard deviation σ of temperature measurements. For instance, 1.9°C STD provided by the extracorporeal coil would have lead to large errors for thermal dose computation, i.e. 130% overestimation, while 0.3°C has only 2% impact on the thermal dose calculation.

PRFS method of thermometry may be affected by temperature-induced changes in the bulk magnetic susceptibility of water as was demonstrated by a study of Peters *et al* [1999]. The variations in the apparent PRFS thermal coefficient were strongly related on the heating device orientation and geometry, and appear only for an orthogonal position to the main magnetic field (B_0). In our study, the planar transducer was positioned parallel to B_0, but the emitted ultrasound beam had an orthogonal orientation to the transducer. Consequently, the heating pattern was indeed orthogonal to B_0, and according to Peters *et al* [1999] the temperature measurements may be affected by errors. A numerical simulation of the measurement errors affecting the un-corrected PRFS T-map (data not shown) indicated in our case no more than ± 0.5°C for the heated region. This corresponded to a 6% impact on the thermal dose calculation. Note the different heating patterns for the two studies. The device described in Peters *et al* [1999] was a very long cylinder (8 mm wide /170 mm long), while our device (active surface of the transducer 8 x 15 mm², at 9.45 MHz) generated a roughly spherical heating pattern (see Fig. II.8).

Positioning of the water-proof miniature coil inside or outside the cooling balloon did not show significant differences in the MR sensitivity. The model with the receiver loop inside the balloon was regarded to be more suitable for *in-vivo* applications for two reasons. First, possible RF pulse-induced local heating in tissues was minimized because of continuous water flow inside the tip cooling balloon. RF heating due to E-field coupling is considered a key safety issue whenever local RF coils are used in interventional MR [Armenean *et al,* 2007], [Schaefer, 1998], [Oulmane *et al*, 2007]. In our case, no temperature increase due to such effect (with the RF spoiled, segmented EPI gradient echo sequence used for MR thermometry) could be detected within the 0.2°C noise standard deviation. Note that the manipulation of the device tip, including the insertion under real-time imaging guidance, was always performed with activated cooling circuit, to maintain a pressurized and appropriately shaped balloon. Second, embedding the coil inside the balloon ensured biocompatibility of the device tip that was obtained with the cooling balloon itself.

A detailed study [Weidensteiner *et al*, 2004] including sequence optimization for abdominal MR thermometry (segmented EPI, RF spoiled gradient echo) on a 1.5 T Philips clinical scanner, using the same type of 4-element standard extracorporeal coil, with or without SENSE parallel acquisition, reported experimental limitation to 0.5°C SDT *in-vitro* (static beef liver sample) for a voxel size of 3 x 3 x 5 mm^3 and an acquisition time of 0.9 s per slice. In our study, the use of the integrated coil permitted the acquisition of thermometry images with voxel size of 0.5 x 0.5 x 5 mm^3, temporal resolution of 2.2 s per slice and a minimal SDT of 0.3°C. Thus, the sensitivity gain brought by an integrated coil may be exploited, within the same sequence, to

improve the spatial, temporal, or temperature resolution as per need, still providing satisfactory value to each parameter.

High resolution, fast and accurate MR thermometry coupled with automatic feedback of the applied power, allowed spatial control of the thermal dose. In addition, small gas bubbles trapped at the interface between the esophagus and liver tissue samples could be detected with the current resolution as a slight inhomogeneity of thermal maps (see the arrows on Fig. II.8.a).

The use of endoluminal coils in therapy is insufficiently investigated to date. We found only two reports [Piel *et al*, 2005], [Wharton *et al*, 2007] describing a HIFU transducer combined with an MR receiver coil. In the study of Wharton *et al* [2007], the SNR improvement with the integrated coil, as compared to a phased-array body coil, depended on the type of ultrasonic transducer used. A factor of 3 was obtained when using a 4-sector piezocomposite transducer. The relative gain of coil sensitivity was significantly smaller in presence of a single sector piezoceramic transducer (improvement by a factor of 1.7), and that transducer needed to be further quartered to reduce the induced eddy currents. One insufficiency of the study [Wharton *et al*, 2007] was the use of two transducers positioned confocally: the first was used as active source of heating while the second, equipped with the RF coil, had only receiving purpose. In our study, one single transducer equipped with RF coil was used for the full therapeutic sequence (US sonication and acquisition of the MR signal) with higher signal gain in the region of therapeutic interest, i.e. a factor of 7. However, a direct comparison of the two studies is not possible, since two different approaches were considered (treatment by focused ultrasound/HIFU versus contact ultrasound/HICU).

The influence on the coil performance from the transducer electrodes, wiring and high electric permittivity ceramics, was not explicitly calibrated in this study. However, the transducer influence on electrical parameters of the coil is demonstrated in Table II.1 (column 2 versus 1 or column 4 versus 3). Quantitatively, the presence of the transducer inside the coil increases the resonance frequency by ~0.5 MHz and decreases the quality factor by ~10 units. Experimental data demonstrated that available "electromagnetic window" between the transducer and the RF coil loop was sufficient for significant improvement of the MR signal sensitivity *versus* extracorporeal coil.

The study reported here demonstrated the feasibility of integrating an RF coil within a therapeutic ultrasound transducer. The number of heating control experiments (7 experiments) was sufficient for a feasibility study, but additional experiments are needed to decide a strategy of therapy.

One major challenge for clinical application of MR-guided HICU to esophageal cancer is the tissue motion in this specific region (respiratory, cardiac and peristaltic motion). Motion robust

PRFS-based MR thermometry must therefore be implemented when aiming *in-vivo* feasibility studies. Note that the therapeutic device will undergo synchronous motion with tissues, therefore beam targeting errors are not expected under such conditions. When using standard, single reference PRFS method, potential variations in the measured phase, due to local motion and distant susceptibility effects from lungs, would far overweight the small SDT reported here with the integrated coil. Respiratory gating of the acquisition should be sufficient to avoid susceptibility-induced errors due to lungs changing their air volume with breathing, although with significant lost in temporal resolution. Multi-reference PRFS thermometry is another option to overcome such temperature artifacts. The most important issue, in our opinion, is to avoid intra-scan motion artifacts, i.e. ghosting, that is to be able to perform rapid enough acquisition whilst providing sufficient SNR. The small FOV and the sensitivity improvement provided by the integrated coil are expected to provide significant benefit for ultra-fast acquisition.

II.5 Conclusion

Two novel technological issues were successfully investigated in this *ex-vivo* study. First, an endoscopic HICU device for digestive applications was combined with a miniature receive-only RF coil. Second, this combined device was coupled to an automatic temperature controller. The miniature RF coil was designed to meet both anatomical and technical constraints. The two investigated coil configurations showed a similar sensitivity, while the coil mounted inside the cooling balloon provides significant advantages with respect to possible RF heating and biocompatibility issues. Available resolution of both anatomical and thermal images permitted the esophageal wall visualization, as a result of significant sensitivity improvement as compared with a standard extracorporeal 4-element phased array coil. Half-millimeter resolution became feasible for fast MR thermometry while providing an excellent SDT. The implemented temperature feedback controller demonstrated high accuracy within 1.1% error in mean value and less than 2% SDT.

Chapter III. *In-vivo* evaluation of high resolution MR-guided thermotherapy for rectal applications: RF coil integrated with phased-array transducer

III.1 Introduction

III.2 Material, methods and preliminary tests

III.2.1 Rectal ultrasound transducer & electronics

Phased-array ultrasound transducer and its cooling circuit
Principle of the beam generation: focused or plane wave
Matching of the electrical impedance
Calibration of the electrical driving circuit
Characterization of the transducer by the radiation force technique

III.2.2 Opposed-solenoid RF coil

Coil design: wiring and insulation
Coil prototype: 1 turn versus 5 turns
Influence of the transducer on the coil

III.2.3 Automatic temperature feedback control

Physical model for temperature estimation
Implementation of the PID controller

III.2.4 MR data acquisition and processing

MR system and experimental setup
Ex-vivo experiments
In-vivo experiments

III.3 Experimental results

III.3.1 Phased-array structure of the transducer

Beam type
Multiple beams

III.3.2 PID controller stability

III.3.3 Comparative studies of the coils

1 versus 5 turns
Transducer influence
Internal versus external coil

III.3.4 *In-vivo* results

Internal/external coil
Thermotherapy with automatic temperature control
Evaluation of tissue destruction

III.4 Discussion

III.5 Conclusion

III.1 Introduction

In Chapter II, it was shown that integrating a local RF coil with an ultrasound transducer leads to a great improvement in thermometry accuracy, and in spatial and temporal resolution. The image quality and the accurate control of thermotherapy were studied, in the present chapter, with another type of ultrasound transducer. A 64-element phased-array ultrasound transducer, for rectal application, was built by Imasonic S.A [Melodelima, 2004]. In the context of the present work, the rectal transducer was adapted in impedance, characterized by the radiation force method, and tested *ex-vivo* and *in-vivo*. In addition, a new RF receive-only coil was defined to be adapted to the geometry of the transducer. Opposed-solenoid geometry of coil [Martin *et al,* 1992], [Hillenbrand *et al*, 2004] was chosen in order to offer homogenous sensitivity in the axial plane. The new integrated device was studied *in-vivo* on healthy pigs, under automated temperature control. In this chapter, the coil design was more restrictive, because of the transducer geometry involving a 360°-acoustic opening. However, the same resolution as the one obtained in Chapter II was expected.

III.2 Material, methods and preliminary tests

III.2.1 Rectal ultrasound transducer & electronics

Phased-array ultrasound transducer and its cooling circuit. The endorectal cylindrical ultrasound transducer (Imasonic, Besançon, France) was similar to those described in former studies by Lafon *et al* [2000] and Melodelima *et al* [2002]. The 1D phased-array MR-compatible applicator included 64 piezocomposite parallel elements disposed around the entire lateral surface of a cylinder (see the head of the applicator in Fig. III.1), and each element operated at 3.57 MHz. The cylindrical acoustic active zone was 20 mm-long and 14 mm in diameter. The width of each element was 0.6 mm, with an inter-element gap of 0.085 mm. The transducer head had a rounded distal end in order to facilitate the endocavitary insertion. The body of the transducer consisted of a rigid tube (25 cm-long and 18 mm OD) for an easier handling, and of a 2.75 m-long flexible tube (11 mm OD) ending with the multi-channel connector. The phased-array geometry of the transducer allowed an electronic rotation of the ultrasound beam with an angular step of 5.6° (i.e. 360°/64).

Figure III.1. Head of the 64-element rectal ultrasound applicator (diameter: 14 mm; working frequency: 3.57 MHz). The surface of a single element (20 x 0.6 mm²) is highlighted with the green line. The arrows indicate the opening of the two thin pipes, which ensure the water flow, along the active zone of the transducer and on its rigid backing part.

During sonication, the active surface of the transducer and the backside of the reflector were cooled down by a closed-loop circuit of degassed water. The internal cooling system consisted of 2 thin pipes (input and output) of 1.1 mm internal diameter (ID), positioned inside the head and the rigid part of the transducer. Each pipe continued outside the transducer by the same cooling system described in Chapter II: a 7 m-long pipe (Tygon R3603) of 3.2 mm ID, which ended, outside the MRI room, in a 1L-water tank. Positioned outside the MR room, a peristaltic pump (Masterflex LS 7518-60, Cole-Parmer Instruments Co., Chicago, Illinois, USA) continuously drove the degassed water through the circuit. The flow rate ranged between 20 and 30 mL/min. This low water flow was compensated during the *in-vivo* experiments by an ice-bath heat exchanger, inserted on the closed circuit in order to diminish the water temperature. The water temperature was initially set at room temperature (20°C). The most important part of the cooling circuit was the cooling balloon, which covered the active head of the transducer. The balloon ensured the water to circulate from the input to the output pipe, around the active part of the transducer. In addition to the protection of the transducer, the balloon ensured the acoustic coupling to the tissue to be treated, and also the biocompatibility of the system.

Principle of the beam generation: focused or plane wave. The specific geometry of the phased-array transducer permitted, with an appropriate phase law* application, to obtain either a plane beam or a focused beam [Poguet *et al*, 2002]. A previous study [Melodelima *et al*, 2002] showed that the optimal configuration to generate an ultrasound beam uses 8 adjacent elements of the transducer. Each element was activated independently, and could be controlled in terms of phase and amplitude. Moreover, one of the most important advantages of this type of geometry was the electronic rotation of the transducer. Compared to a classic planar transducer which must be mechanically rotated in order to change the treatment direction, the phased-array system needed only to activate another set of eight elements.

The phase law is based on the phase difference between the waves generated from adjacent elements, and depends on the geometry of the device. Considering the mid-plane of the transducer (light blue circle in Fig. III.2.a,b,c), the position of each element on the circle periphery is characterized by an angle θ it makes with the acoustic axis. This angle θ varied with a step of 5.6°. Figure III.2.b shows the diagram used to calculate the phase difference, for a single element (black square), in the case of a focused beam. For a given focus *f*, radius *R*, and angle θ, the wave derived from this single element has a phase difference φ (Pitagora's theorem):

$$\varphi = \frac{2\pi}{\lambda} \cdot \delta = \frac{2\pi}{\lambda} \cdot [-f + \sqrt{2R(R+f)(1-\cos\theta) + f^2}] \qquad \text{Eq. III.1.}$$

* Phase law refers to the use of electronic time delays, applied during emission, to each element independently. These delays enable focusing the beam at different depths, by acting as a focusing lens.

Note that R was 7 mm for the rectal transducer, while λ was 0.43 mm (F = 3.57 MHz, c = 1540 m/s). In the case of a plane wave (Fig. III.2.c), the phase difference φ depends only on R and θ:

$$\varphi = \frac{2\pi}{\lambda} \cdot \delta = \frac{2\pi}{\lambda} \cdot [R \cdot (1 - \cos\theta)] \qquad \text{Eq. III.2.}$$

Furthermore, for each element, the phase difference φ depends on the corresponding θ-angle. The phase law, applied to a set of 8 elements compensates then their phase difference, and generates in this manner coherent waves. The in-plane symmetry of the transducer (θ-angle can be positive or negative) is generally used and, thus, only 4 phases are calculated. An example of the resulting ultrasound beam is shown in Fig. III.2.d, and e.

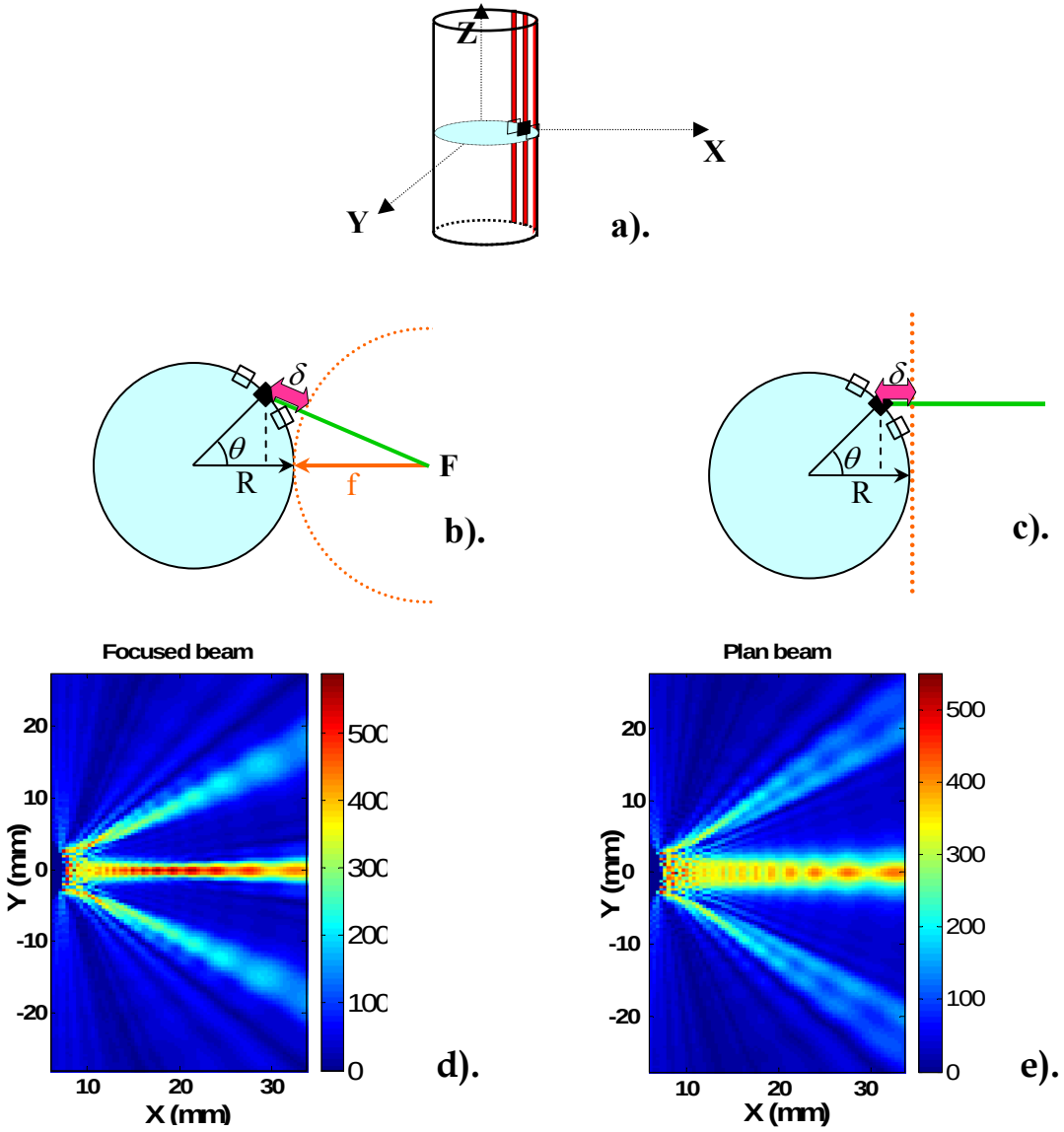

Figure III.2. *a). Transducer's symmetry axis. Three vertical elements (red lines) and the mid-plane (light-blue circle) are shown.* ***b) and c).*** *Principle of calculation of the phase difference (pink double-arrow), for one element (black square), in the mid-plane, for focused (b) or plane (c) beam. The green line is the distance covered by the wave originating from this single element.* ***d) and e).*** *Corresponding simulated ultrasound beams, in axial plane, as resulting from the phase law application to 8 elements of the rectal transducer. Acoustic pressure of beams is calculated for a circle of 50 mm-radius, with a spatial resolution of 0.4 mm; shown images are enlarged views of computing space. The focus (see d) is set to 15 mm. Colorbar scale is in kPa.*

Matching of the electrical impedance. During MR experiments, the phased-array ultrasound transducer was always positioned at the center of the MR scanner. The generator and the amplifiers were installed outside the MR room and 64 grounded cables (RG 174) connected them to the transducer, through the RF cage. The total length of the transmission cable (3 m outside and 6 m inside the MR room) was important, and, therefore, the electrical impedance matching of the transducer was essential. The electrical impedance Z of each element of the phased-array transducer was matched, as close as possible, to 50+0j Ω at 3.57 MHz, in order to optimize the power transfer. The reactance was cancelled out (see second line of Table III.1) by home-made air coils connected in series. The average value of the inductance of the matching coil was 5.18 μH and corresponded to 42 winding-loops (copper wire diameter: 0.7 mm; support Plexiglas tube diameter: 10 mm). The MR-compatible impedance matching unit containing the 64 air coils was positioned at 3 m-distance from the active part of the transducer, inside the MR room, see Fig. III.3. Table III.1 summarizes the impedance values, before and after the impedance matching of the rectal transducer.

Electrical impedance	BEFORE			AFTER		
	Min	Average ± SD	Max	Min	Average ± SD	Max
Real Z [Ω]	41.14	**55.63** ± 4.06	62.01	40.87	**55.06** ± 3.8	61.63
Imag Z [Ω]	-111.16	**-118.34** ± 10.27	-181.7	-4.04	**0.6** ± 2.26	4.21

***Table III.1.* Electrical impedance of the rectal transducer.**

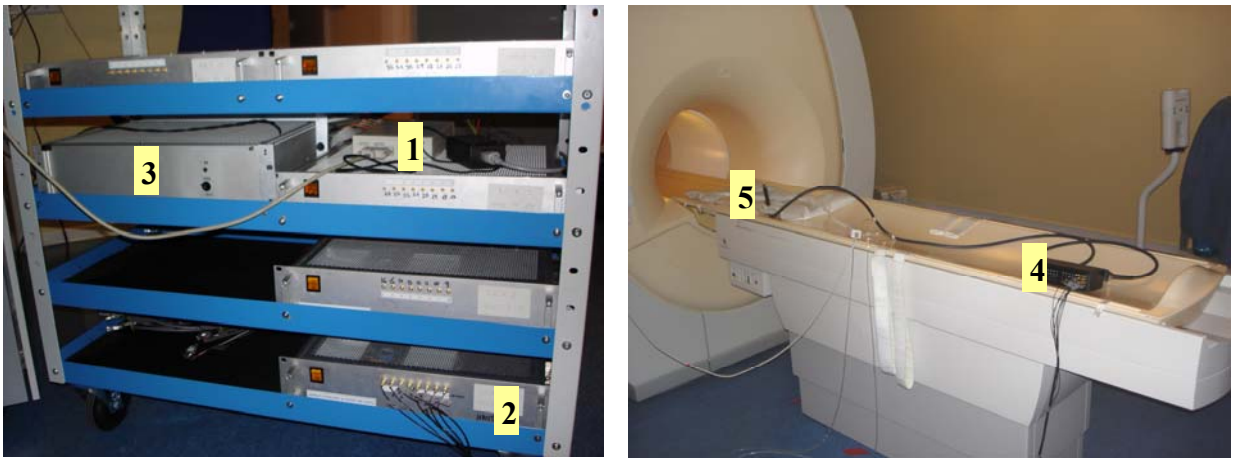

***Figure III.3* Electronic setup for MR experiments using the rectal transducer:**
***left* - outside the MR room, and *right* - inside the MR room.**
1: 50-channel generator; 2: 64 power amplifiers (here a rack assembling 8 power amplifiers);
3: micro-controller; 4: impedance matching box; and 5: rectal transducer.

Calibration of the electrical driving circuit. The driving electronics (see Fig. III.3, left panel), including a central PC, a multi-channel generator, 64 power amplifiers and a micro-controller, provided an independent control of the signal amplitude and phase for each element, up

to a maximal effective power of 6 W per element. The fast update (40 ms latency time) of the output electronic signals permitted the realization of an automatic feedback-loop of temperature control. Independent TTL (transistor-transistor logic) signals were generated by a 50-channel pattern generator (PG 2050, Acute, HsinChuang City, Taiwan) at the operating frequency and with the desired phase law. This type of generator permitted to adjust the phase law with an accuracy of 10 ns. The generator was driven *via* the standard parallel port of the central PC using commercially available libraries provided by Acute. The second element of the driving electronics was the power amplifier (AHF 855, Adece, Artannes, France), which converted the TTL signal into sine wave and amplified it. There were 64 class-D amplifiers grouped in racks of 8 units. Each of them was able to deliver up to 8 W, for a frequency bandwidth varying from 3 to 6 MHz. Moreover, each amplifier could measure the delivered analogue voltages, named here P_+ and P_-, which corresponded to the forward and the reflected powers. The main part of the electronics was the micro-controller (Smart Star, Rabbit, Davis, California, USA) which, interfaced with the master PC via the standard serial RS 232 port, controlled the delivered electrical power. The micro-controller contained 64 DAC (digital to analogue converter) cards, aimed to deliver the command voltage U_C to the amplifiers, and 128 ADC (analogue to digital converter) cards aimed to read-out the analogue voltages, P_+ and P_-, provided by the same amplifiers. Finally, the last element of the setup was a home-made rejection filter, aimed to avoid the possible electromagnetic interferences between the transducer activation and the acquired MR signal.

Prior to MR experiments, each channel of the electronic circuit was calibrated in order to measure the effective electrical power* delivered to each element of the phase-array ultrasound transducer. For this purpose, a wattmeter (NAP equipped with NAP-Z7 power head, Rohde & Schwarz, Germany) was connected to the output of the amplifier, at the end of the cable, and before the impedance matching box. The setup was similar to that used in the MR-guided experiments (9 m-long cable; cooling circuit). The command voltage (U_C) was varied, with a step of 0.1 V, from 1 to 9.4 V, and the corresponding values for forward and reflected power were recorded. Figure III.4 shows a typical calibration curve (effective power as a function of the command voltage), fitted by a quadratic function. Note that for some channels,

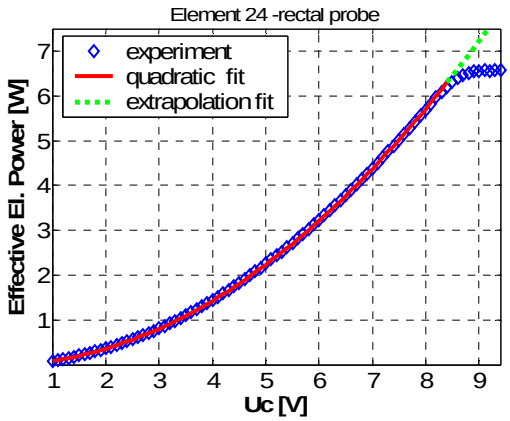

***Figure III.4.** Example of an electronic calibration curve of one element of the rectal transducer.*

* The effective electrical power is the forward power minus the reflected power.

as it was the case of the example in Fig. III.4, the amplifier saturates (see the blue ◊-symbol), typically at voltages higher than 8 V. However, this limitation of the power amplification appeared at levels outside of the working range, and therefore it had no impact on the MR experiments. The effective power was calculated taking into account the energy loss due to the important length of the cable (15% at 3.57 MHz). The fitting coefficient was calculated for each of the 64 elements, showing a mean value of 0.1 W/V². These coefficients were further implemented in the feedback-loop of temperature control. The P_+ and P_- values were used to define a safety level for unexpected overheating of the transducer during experiments. If the reflected power was higher than 10% of the forward power, then the system was automatically turned off, in order to avoid the destruction of the transducer by overheating.

Characterization of the transducer by the radiation force technique. The radiation force balance technique [Davidson, 1991], [Zeqiri, 2007] assumes that the ultrasound radiation force* can be measured by the weight variation of an absorbing target, positioned close to the transducer. The target (RTV60 001-KIT, GE Silicones, Waterford, NY, USA), a silicon rubber with an acoustic impedance of 1.40 MRayl, must be sufficiently large, in order to be considered infinite, when compared to the size of the transducer's active region. Consecutively, the acoustic power can be determined by the following relation:

$$P_{ac} = m/70 \qquad \text{Eq. III.3,}$$

where m is the mass variation (in mg) measured by the balance, and the constant value (70 mg/W) was experimentally defined in water [Davidson, 1991]. A more usual parameter, the acoustic intensity (in W/cm²) at source is defined as the acoustic power divided by the active surface of the transducer. Finally, the electroacoustic efficiency of the transducer represents the amount of electrical power transformed in acoustic power.

Based on the radiation force balance method, three types of measurement were performed, aimed to determine: 1) the electroacoustic efficiency of the transducer; 2) the acoustic calibration for 8 elements; and 3) the attenuation of the acoustic intensity through the cooling balloon. The same setup, see Fig. III.5, i.e. generator (Tektronix AFG 3102, max 100 MHz), amplifier (max 50W, Adece, France), oscilloscope (LeCroy waveSurfer 422, max 200 MHz), wattmeter (NAP-Z7), and balance (CP64, Sartorius, max 64 mg)] was used for all measurements. The attenuation of the cooling balloon was measured by comparing the delivered intensities, for the same element, without and then, with the balloon.

* the time-averaged force exerted by an acoustic field on an any object intercepting the field, either partially or completely

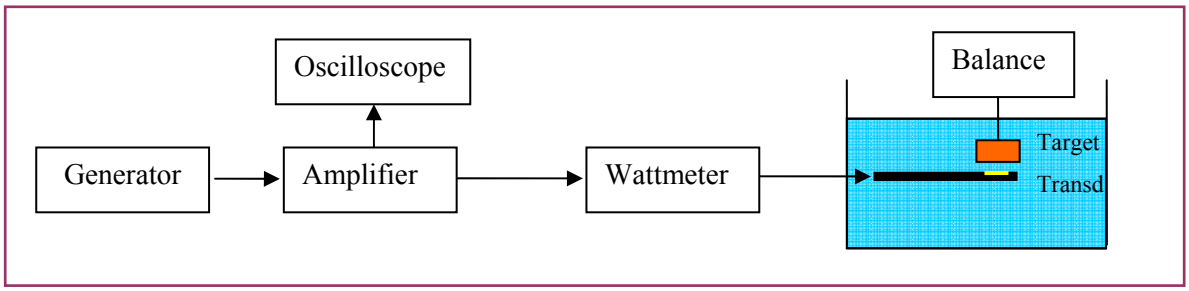

Figure III.5. ***Setup used for the characterization of the rectal transducer by the radiation force balance method.***

The electroacoustic efficiency of the transducer was measured for 8 random elements, in the same configuration as for the MR experiments (i.e. 9 m-long cable). However, note that the results of these measurements (see Table III.2) are only informative, since various combinations of elements of the rectal transducer generated the ultrasound beams, making it difficult to exactly quantify the efficiency for each beam. In order to protect the transducer, the delivered electrical power was not set to its maximum, but a simple extrapolation of the curve presented in Fig. III.6 permitted to determine the acoustic intensity at higher powers. The fitting coefficient of the curve varied between 3.5 cm^{-2} and 4 cm^{-2}, showing a mean of 3.76 cm^{-2}. The higher fitting coefficient signified the most efficient element. Note that the least efficient element was the element the most exposed to overheating. Considering the limit of 20 W/cm² (under water cooling) defined by the transducer manufacturer and the highest coefficient value, then the maximal electric power that could be applied to one element was 5 W. Note that these values were measured without the cooling circuit, and that the cooling balloon attenuated the final acoustic intensity. Hence, the threshold of the maximal applied power per element was higher than 5 W. The cooling balloon (Synsation™ PF-Vinyl, Ansell Health-care, Brussels, Belgium) attenuated the acoustic intensity by 18.68 ± 2.14 % (applied power: 2.76 W).

Element	Eff. el. power [W]	Ac. intensity [W/cm²]	Electroac. efficiency %
1	2.78	9.94	42.81
2	2.72	9.85	43.39
3	2.8	10.73	45.97
4	2.79	9.66	41.51
5	2.78	11.13	48.02
6	2.79	10.73	46.05
7	2.81	10.55	44.96
8	2.76	10.33	44.81
Av. ±SD	**2.77 ± 0.02**	**10.36 ± 0.5**	**44.69 ± 2.07**
Precision of measurement	± 0.17	± 1.17	± 2.8

Table III.2. ***Electroacoustic efficiency for 8 elements of the rectal transducer, measured using the 9 m-long cables and without the cooling circuit.***

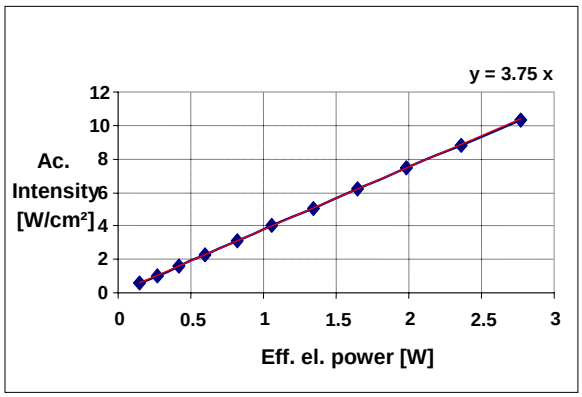

Figure III.6. ***Typical acoustic calibration for one element of the rectal transducer.***

III.2.2 Opposed-solenoid RF receive-only coil

Coil design: wiring and insulation. In order to define the final prototype coil, various materials (wire or strip, different wires and insulating cables) and configurations (one or more turns) were tested, see Fig. III.7. The aim of these tests was to design a coil with minimal dimensions (outer diameter and length), but still offering a reasonable quality factor (at least 30 units), particularly in conditions of full loading, i.e. in tissue. Also, as it was explained in Chapter II, the static resonance frequency should be between 63.0 and 63.5 MHz. In addition to these requirements, all materials constituting the coil (support, wiring, capacitors, insulation, and connecting cable) should be, obviously, highly MR-compatible. Therefore, the coil performance was sometimes limited by the non-compatibility of a specific element. For example, an insulating tape and a coil connecting cable offered higher Q-factor, but were MR-incompatible.

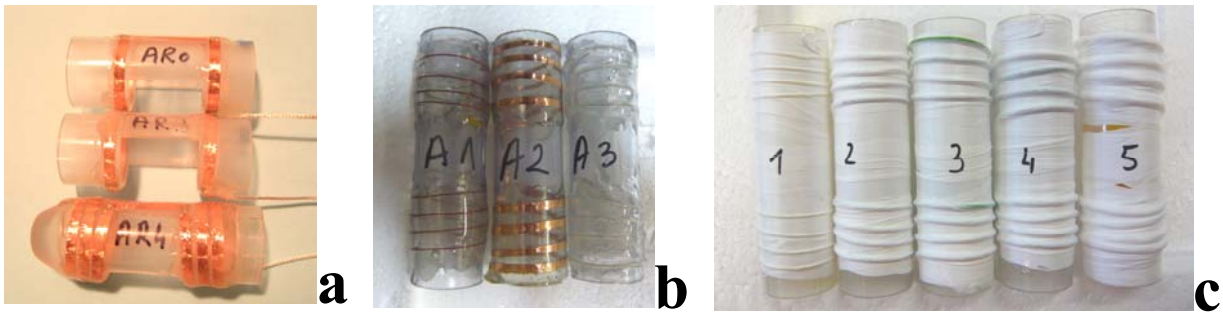

***Figure III.7.** Diverse material tested in order to define the prototype rectal coil. a). copper strips; b). copper: non-insulated wire, insulated wire, and strip; c). 5 types of insulation material.*

The final prototype coil (see Fig. III.8) was an opposed-solenoid made of polytetrafluoroetylene-coated copper wire (total diameter of the insulated wire: 1.67 mm) with the active elements lying in the coil gap. The cylindrical plastic support of the coil was 70 mm-long, 1.5 mm-thick, and had an outer diameter of 20 mm. The coil wiring and capacitors were sealed on the plastic support using a resin (Epoxy adhesive, RS components, Corby, UK). The coil on its support was placed over the head of the ultrasound applicator from the distal end. Like in the case of the monoelement transducer (Chap. II), a window was cut into the plastic support, in front of the acoustic active zone. The length of this opening was identical to that of the active acoustic zone

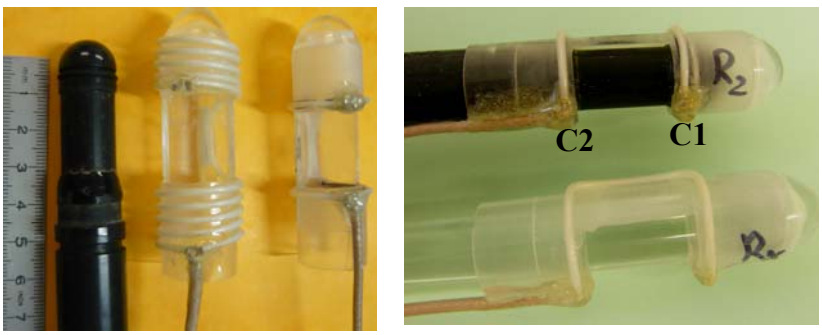

***Figure III.8.** Rectal RF coils. Left (study of the number of turns): single-turn and 5-turn coils. Right (study of the transducer influence): two single-turn coils. Letters C1 and C2 indicate the two capacitors.*

(i.e. 20 mm), but the aperture could not match the entire acoustic aperture, which was 360°. The opened window had an aperture of 270°, which enabled activation of only 48 elements. This limitation can be overcome with a new design of the transducer, adapted to the coil presence (see Chapter IV). Two non-magnetic capacitors per coil (C1, C2) were used for initial static RF tuning and matching (within a frequency range from 63.0 to 63.5 MHz). Three coils were built (see Fig. III.8) in order to study the influence of the number of turns (1 turn versus 5 turns) and of the transducer (1-turn coil functioning with or without it). The capacitors values and the static RF parameters, for each coil, are listed in Table III.3. The same setup as previously described in Chapter II was used to measure the static RF parameters, in air, water, and tissue. A 68 cm-long coaxial cable (diameter: 2.45 mm) connected the coil to the electronic standard unit which realized the final active tuning (at 63.9 MHz) and matching of the coil, during the MR experiments.

Coil	C1/ C2 (pF)	Loading environment	Frequency [MHz]	Quality factor, Q	Real Z [Ω]	Imag Z [Ω]
5-turn coil (with transducer)	2/ 4.7	Water	63.1	53.9	66	-180 j
		Tissue	62.2	20.5	62	-104 j
1-turn coil (with transducer) *In-vivo*	62.6/ 156	Air	63.3	57.5	74	-300 j
		Water	63.1	58.5	64	-278 j
		Tissue	63.0	**53.2**	67	-272 j
1-turn coil (without transducer)	58.2/ 156	Air	63.4	72	65	-290 j
		Water	63.1	72.5	55	-275 j

***Table III.3.** Electrical static parameters of the rectal coils.*

Coil prototype: 1 turn versus 5 turns. The optimal coil configuration with respect to the number of turns (see left side of Fig. III.8) was investigated for different loading environments (air, water, and tissue), see Fig. III.9. Note that, during MR experiments, the coil was activated under fully loading conditions (i.e. in tissue). For unloaded medium (air), the quality factor of the 5-turn coil was slightly higher than the one of the single-turn coil. Then, in water, the situation changed and the Q-factor of the 5-turn coil became lower than the Q-factor of the single-turn coil. Finally, when placed in direct contact with the tissue, the Q-factor of the 5-turn coil was drastically reduced to 38% of its value in water, and, consequently became much lower than the corresponding Q-factor of the 1-turn coil. Further investigations (MR thermometry) were carried out, but the reduced Q (in tissue) already indicated the deficiency of the multi-turn coil and the possible preference for the single-turn coil, in this particular case.

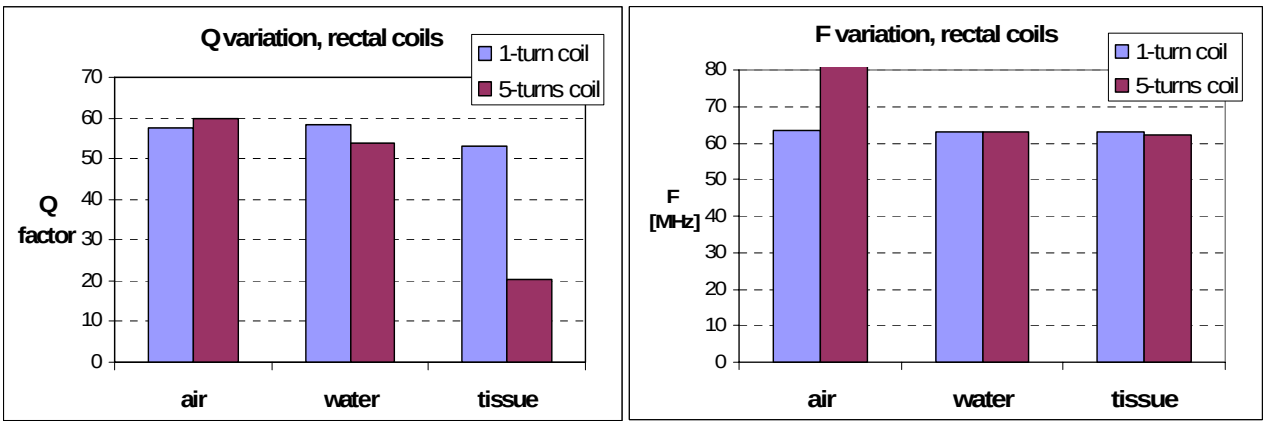

***Figure III.9.** Influence of the number of turns on the Q-factor and on the resonance frequency of the coils, for air, water and tissue loading media.*

Influence of the transducer on the coil. A second comparative study was conducted to determine the transducer influence on the coil performance. The endoscopic device was detachable, showing a clear separation between the transducer and the coil. Hence, the influence of the transducer could be easily observed by two successive measurements: a) coil only; and b) the same coil integrated within the applicator. For the 1-turn coil, the transducer slightly decreased the Q-factor and increased the resonance frequency.

However, this initial observation of the influence of the transducer was not rigorous because the resonance frequency of the coil was shifted. Therefore, this influence was measured by comparing two separate coils (see right side of Fig. III.8). One coil was the 1-turn coil designed to be operated with the integrated transducer. The second coil had also 1-turn geometry, but their capacitors were slightly modified in order to tune the coil to the same frequency as the original integrated 1-turn coil. This second coil was designed to be operated without the transducer. Therefore, a plastic cylinder of the same diameter as the transducer was placed within this coil, in order to ensure as much as possible the configuration of the integrated coil. In this way, the influence of the transducer was studied with respect to its internal structure and electrical wiring. The preliminary results showed that the transducer induced a loss of the Q-factor of 14 units (~ 20%), but only the MR experiments will indicate the real effect of the transducer on the coil sensitivity field.

III.2.3 Automatic temperature feedback control

An ordinary MR-thermometry experiment repetitively acquires images of the same tissue slice (called a dynamic) during a defined time interval, and evaluated continuously the temperature evolution in time, within a specific region of the slice. A typical MR experiment contained about 100 dynamics, differentiated into three parts: baseline acquisition (~ 5% of time); heating by ultrasound exposure (~ 70% of time) and cooling period (~ 25% of time). The imaging slice was

positioned either sagittal or axial, but always centered on the transducer longitudinal plane or respectively, on the transverse mid-plane. Given the acoustic beam pattern, the axial imaging* was preferred (see Fig. III.10). The longitudinal heat diffusion was neglected. The temperature feedback control method, performed only during sonication, coupled two subprograms: a physical model of heat transfer and a proportional, integral and derivative (PID) compensation algorithm.

Physical model for temperature estimation. The physical model estimated the temperature evolution within the tissue exposed to ultrasound. The temperature elevation (in space and time), was modeled in the transverse plane, by solving the Bio Heat Transfer Equation. A simplified BHTE considered only the conductive term (isotropic diffusion D) and the ultrasound heating (absorption α), neglecting the tissue perfusion. However, both perfusion and diffusion induce heat losses (i.e. same effect on the local delivered energy). Therefore, the perfusion could be indirectly considered as a component of the local diffusion [Quesson *et al*, 2002]. In this case, the diffusion constant should be set at a higher value than when the perfusion was neglected. The Fourier transform solution of the BHTE was adapted to the contact ultrasound method, by integrating borderline condition represented by the cooling balloon. The temperature evolution, for one ultrasound beam, was expressed as follows:

$$T(x,y,t+\Delta t) = FT^{-1}\left\{ e^{-k^2 \cdot D \cdot \Delta t} \cdot FT\left[M(x,y)\cdot T(x,y,t)\right] + \alpha \frac{1-e^{k^2 \cdot D \cdot \Delta t}}{D \cdot k^2} \cdot FT\left[I(x,y)\right] \cdot P(t) \right\} \qquad \text{Eq. III.4}$$

where $T(x,y,t)$ was the temperature evolution in the xy-plane, at time t; $I(x,y)$ - the spatial distribution of the heat deposition (i.e. the acoustic field intensity); $P(t)$ - the total applied electrical power (considered constant in the time interval Δt), uniformly distributed among the 8 activated elements of the beam. Note that the parameter $I(x,y)$ had a different expression in function of the desired type of ultrasound beam (planar or focused). The time interval Δt was the temporal incremental step of the temperature calculation. Its value was correlated to the temporal resolution of the MR thermometry acquisition, i.e. to the acquisition time for one dynamic (here 2 s).

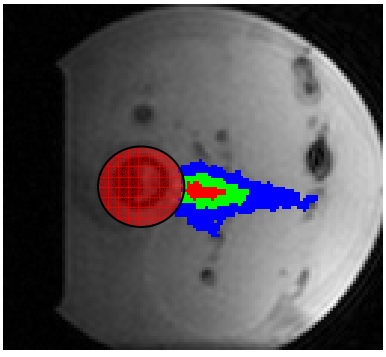

***Figure III.10.** The mask (red circle) and temperature function intervening in Eq. III.4.*

The user-defined mask representing the cooling balloon $M(x,y) = \begin{cases} 0, & \textit{inside the balloon} \\ 1, & \textit{outside the balloon} \end{cases}$ was applied at each incremental temperature calculation (see Fig. III.10), in order to describe the continuous cooling effect due to the water circuit. The 2D-domain of temperature modelization was equal to the field of view (FOV) of the MR thermometry; thus, the digital resolution of the k-space was $2\pi/FOV$.

* Transverse plane, orthogonal to the longitudinal axis of the ultrasound transducer and parallel to the acoustic beam.

This physical model of temperature estimation had two important applications. First, parameters of the model (T, α and D) represented input data for the PID controller. Note that the modelization was on-line compatible with the PID implementation; the computing time was 8 to 10 times shorter than the sonication sequence itself. Second, the physical model provided also pre-operative optimal planning therapy (see the next chapter).

Implementation of the PID controller. The entire procedure incorporating the automatic temperature control was governed by a home-written software interface, running on a standard PC. The software, developed by other colleagues, was extensively described in Salomir *et al* [2009]. The Matlab/Visual C++ program included five parallel threads (see Fig. III.11): 1) on-line connection with the MR scanner; 2) electronics monitoring (read-out of the direct and reflected powers, power update); 3) the temperature feedback-loop (on-line and modeled thermometry data calculation); 4) graphic interface display; and 5) the treatment planning (preparation stage prior to sonication). During the preparation stage, the cooling balloon and the region of interest* were manually defined on a pre-sonicated MR image, loaded within the graphic interface.

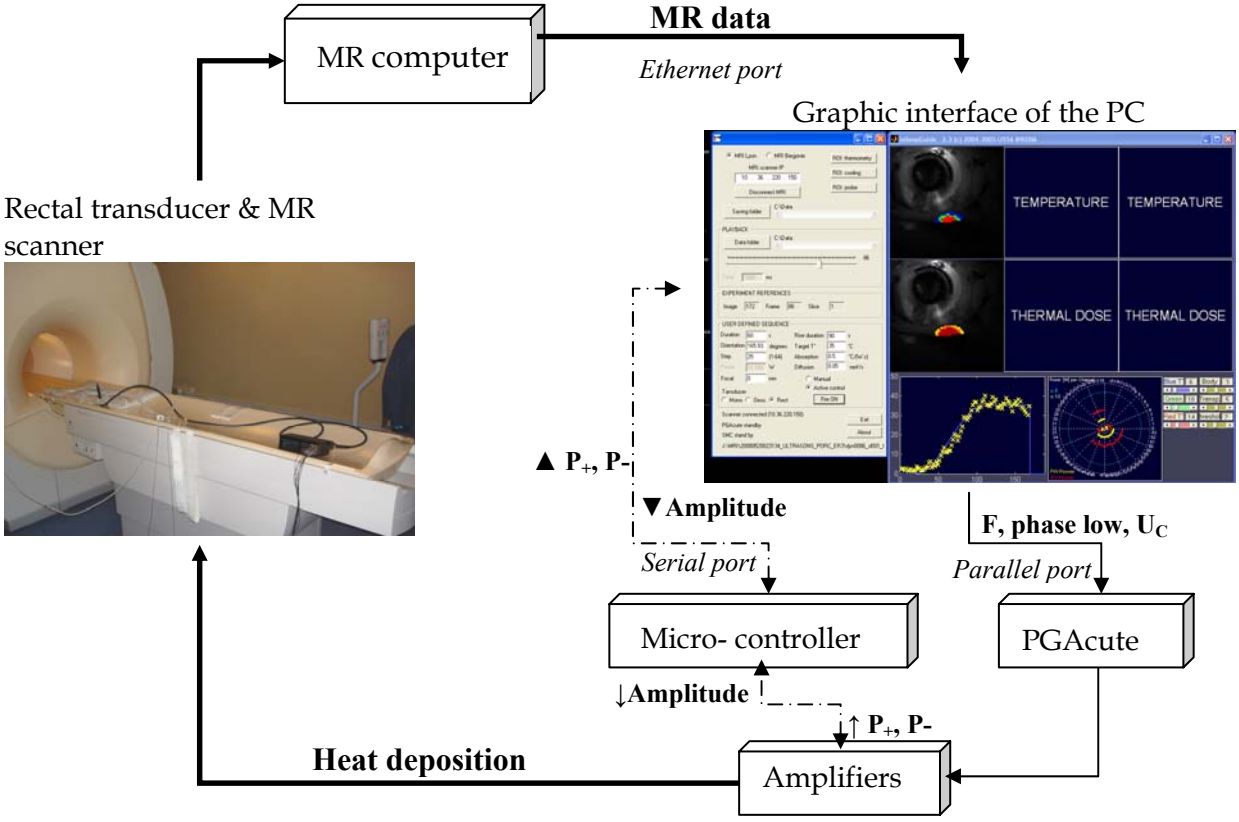

***Figure III.11.** Principle of the feedback-loop, as implemented on the MR-guided ultrasound therapy system (rectal application).*

* The control point of the temperature feedback-loop was defined inside this region.

The temperature control feedback-loop was realized using a PID compensation algorithm. Its goal was to automatically control the temperature evolution (and implicitly the thermal dose) during the ultrasound exposure. For this purpose, the compensation algorithm continuously compared the measured temperature and the desired (target) temperature and rapidly adjusted the output electrical power, at each dynamic, in order to keep a minimal error between the two temperatures. The PID-corrective action involves three separate actions: proportional, integral and derivative. The *proportional* value determines the reaction to the current error, the *integral* value determines the reaction based on the sum of recent errors, and the *derivative* value determines the reaction based on the slope of the target curve (see right side of Fig. III.12). The controller response characterized the rapidity and stability (no oscillation or overshooting) of the system.

In our case, the desired temperature evolution was a target curve (typically a rising part and a flattop region) defined over a time interval, see red line on Fig. III.12. The measured temperature (2D-map updated every 2 s) was acquired by the PRFS method during the MR thermometry. In

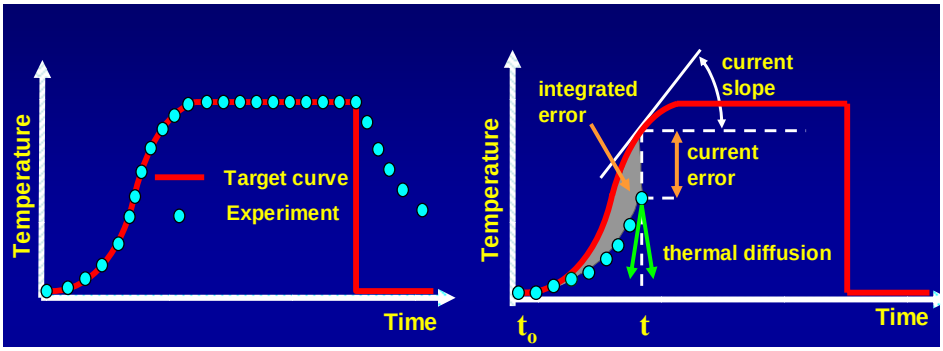

Figure III.12. ***Experimental and target temperature evolution. Left: ideally matching (no PID needed). Right: PID controller intervention during a real experiment.***
Reproduced with permission from Salomir [2001].

practice, the feedback loop forced the measured temperature (at a defined control point (x_0, y_0)) to follow the predetermined target curve. In the case of an ideal experiment (left side of Fig. III.12), the error between these two temperatures should be null, i.e. the first term of Eq. III.4 should be equal to the target temperature. But, in a real experiment, this error, noted here $E(t) = T_{target} - T_{experimental}$ exists and must be corrected. Hence, the PID compensation algorithm automatically calculated and adjusted the output of the electrical power to be delivered to the ultrasound transducer [Salomir *et al*, 2000]. The first step of this calculation was to approximate the temperature measured at the dynamic n, $T(x,y,t+\Delta t)$, to the sum of the anterior temperature $T(x,y,t)$, and the first derivative of the target temperature θ, at the incremental step Δt:

$$T(x,y,t+\Delta t) \approx T(x,y,t) + \frac{d\theta(\Delta t)}{dt} \qquad \text{Eq. III.5.}$$

But, according to Eq.III.4, the current temperature (at dynamic *n)* can be estimated as:

$$T(x,y,t+\Delta t) = FT^{-1}\left\{e^{-k^2 \cdot D \cdot \Delta t} \cdot FT[M(x,y) \cdot T(x,y,t)]\right\} + \alpha \cdot FT^{-1}\left\{\frac{1-e^{k^2 \cdot D \cdot \Delta t}}{D \cdot k^2} \cdot FT[I(x,y)] \cdot P(t)\right\} =$$
$$= T^{diff}(x,y,t) + \alpha \cdot P(t) \cdot FT^{-1}\left\{\frac{1-e^{k^2 \cdot D \cdot \Delta t}}{D \cdot k^2} \cdot FT[I(x,y)]\right\} \quad \text{Eq. III.6,}$$

where the term T^{diff} is the anterior estimated temperature (affected by diffusion and the presence of the cooling balloon). Furthermore, equaling the last two equations and adding the proportional and integrative terms, the outputted power that should be applied to the dynamic *n* can be defined as follows:

$$P(t) = \frac{1}{\alpha \cdot FT^{-1}\left\{\frac{1-e^{k^2 \cdot D \cdot \Delta t}}{D \cdot k^2} \cdot FT[I(x,y)]\right\}} \cdot \left\{\frac{d\theta(t)}{dt} + \frac{T(x,y,t) - T^{diff}(x,y,t)}{\Delta t} + q \cdot E(t) + \frac{q^2}{4}\int_0^t E(t')d(t')\right\}$$

Eq. III.7,

with *T(x,y,t)* - the measured temperature at moment *t*. Eq. III.7 is the main equation governing the feedback-loop for each new on-line MR temperature map. The *q*-parameter, defined as *2/response time of the loop,* was set to $0.5/\Delta t$; hence the feedback system should react to eventual errors within $4 \cdot \Delta t$, i.e. 8 s, trying to converge to the target curve, under stable regime conditions.

Note that this iterative calculation needs an initial value of temperature (generally set to 37°C) and good initial estimates for α and D parameters. The stability and precision of the system depend on these initial values. Also, the quality of the thermometry (i.e. the measurement noise of temperature) influenced the controller. Nevertheless, the feedback method was robust, enabling to control either focused or plane wave. Moreover, the control point of the temperature evolution could be defined manually (at a specific depth of the tissue) or automatically*. Thus, the feedback-loop controlled either the heat delivered at a critical point of the region of interest (such as the distal or proximal layer of the rectum) or the maximal heat delivered over a region of interest. Note that the region of interest must be sufficiently large, in order to cover the entire beam width. The value of α, the absorption coefficient, was adjusted according to the position of the control point, i.e. absorption was maximal in the vicinity of the ultrasound transducer.

III.2.4 MR data acquisition and processing

MR system and experimental setup. All MR experiments were performed on a clinical Achieva 1.5 T scanner (Philips, Best, Netherlands), equipped with Copley 274 Master gradient, maximum strength 30 mT/m, and maximum slew rate 150 T/m/s. MR shimming was performed for all acquisitions. The DRIN (direct reconstructor interface) interface of the scanner permitted

* The automatically-defined control point followed the maximum temperature acquired within the region of interest, at each dynamic. Hence, this type of control point could vary spatially during the heating, from one dynamic to another.

real-time export of the MR data (magnitude and phase images). The total latency including reconstruction, data transfer, calculation of the thermal map, and display was estimated to be less than 200 ms per acquired data volume. Standard surface coils (Synergy Flexible Small-SFS and Synergy Flexible Body-SFB) were used. The SFS coil had two phased-array elements (of 11 cm in diameter each), which were positioned at the extremities of the sample in order to ensure an optimal signal in the center. The same setup was used for the SFB coil (4 phased-array elements). The SFS coil was operated for the *ex-vivo* experiments investigating the feasibility of the phased-array structure of the transducer, and the stability of the PID controller. For further experiments (particularly *in-vivo)*, the integrated internal coil was used. Additionally, the SFB coil acquired only the survey image and some thermometry images (no sonication) in order to compare the internal and the external coils. The internal and external coils were alternatively plugged in, in order to avoid any possible interaction between them during acquisitions.

The normal operating position of the ultrasound device was parallel to the B_0 field (see Fig. III.13), as it would be in the case of clinical application. Morphological images (T_1-w, T_2-w, IR-T_1-w) were centered either sagittally or axially on the transducer, while the imaging slice for thermometry images (PRFS method, EPI sequence) was generally axial. The thickness of the thermometry slice was set to 5 or 8 mm. The thickness was sufficiently small (25% to 40%) when compared to the active length of the rectal transducer, and therefore the longitudinal heat diffusion could be neglected. Additionally, two saturation slices were placed parallel to the imaging slice to reduce the flow artifacts originating from the tip cooling balloon.

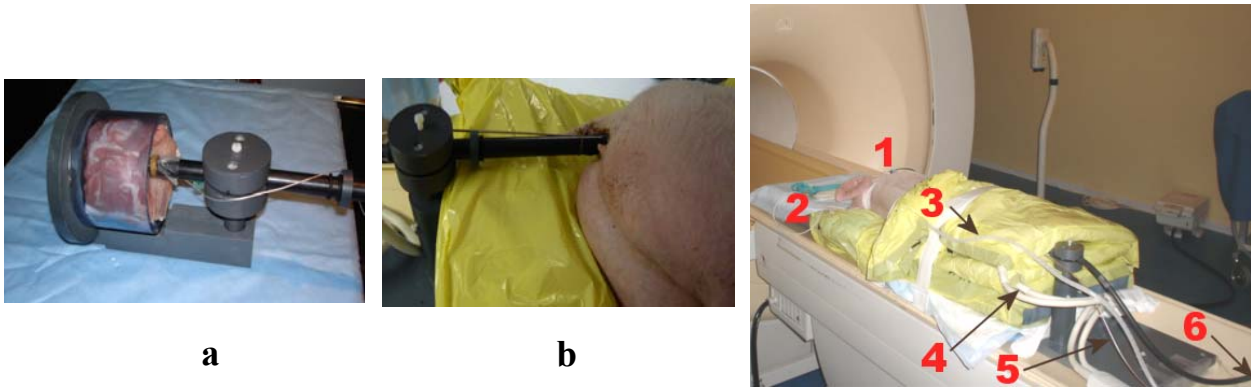

a **b** **c**

Figure III.13. ***Ex-vivo (a) and in-vivo (b, c) experimental setup for rectal application. 1: intubation canula (oxygen enrichment); 2: anesthetic perfusion; 3: respiratory gating; 4: external coil; 5: internal coil; and 6: towards the transducer's electronic and cooling circuits.***

***Ex-vivo* experiments.** Three important issues were investigated *ex-vivo,* in order to prepare for the animal experiments: the feasibility of the phased-array structure of the transducer, the stability of the PID controller, and an initial study on the integrated coil performance.

A MR-compatible sample holder (see Fig. III.13.a) was built for the *ex-vivo* tests, permitting the ultrasound device to be centered within the sample. Two configurations (diameter

80 mm, and respectively 96 mm) of the 100 mm-long plastic cylinder were used. The e*x-vivo* tests were conducted on fresh pig muscle, immersed in degassed water. Morphological images (all three planes) were initially acquired in order to establish the optimal position of the thermometry slice (i.e. centered on the acoustic beam, guarantying the most extended pattern). Each thermometry experiment had 60 to 120 dynamics in function of the desired temperature level to be reached. The mean temporal resolution for thermometry images was 2 s/dyn. An average over the first 10 dynamics, prior to sonication, represented the reference phase-map demanded by the PRFS method.

The feasibility of the phase-array structure of the transducer was investigated with respect to the possibility to activate two interleaved beams (duty cycle of 50% per beam), or to choose the type of beam (planar or focused). The sonication parameters (applied electric power and time) were correlated to the measured temperature and thermal dose, and finally to the size of the necrosed tissue.

The performance and the precision of the temperature controller were studied for a temperature elevation ranging from 10°C to 30°C, for both focused and plane waves. Concurrently, the stability of the PID controller (i.e. tolerance to errors in the initial estimates of parameters α and D) was investigated. Note that the PID controller should be robust against the parameters variation that may appear *in-vivo,* due to the variability of each individual organism. Moreover, parameters may also vary during the thermal procedure. Therefore, erroneous values of diffusion and absorption coefficients were deliberately tested in order to evaluate the efficiency of the PID controller in these cases. The "correct" value of the diffusion coefficient D (0.1 mm²/s) was empirically determined, in similar samples of porcine muscle, from the negative slope of the temperature versus time curve, immediately after the applied power was turned off. This value corresponded to the typical value reported for skeletal muscle [Duck, 1990, p.16]. The absorption coefficient α (see definition in Chapter II) could be estimated with a test sonication performed at constant power, as the ratio of the initial positive slope of the temperature rise to the applied electrical power. Physical values ranged between $0.04\,°C/(W \cdot s)$ and $0.10\,°C/(W \cdot s)$, depending on both the beam conformation and the depth of control location in tissue. The stability and convergence of the feedback loop were investigated, in plane wave mode, for 15 configurations associating 5 values for α (respectively 25%, 64%, 100%, 160% and 400%) and 3 values for D (0.1%, 100% and 300%). In this setup (plane wave, control point at 10 mm from the balloon), the correct values (100%) were D = 0.01 mm²/s, and $\alpha = 0.05\,°C/(W \cdot s)$. The typical temperature target curve was defined as follows: 60s (rising part)/ 90s (constant stage-15°C target)/ 70s (cooling period). A pause of 30 minutes between each experiment (each set of α and D) was respected in order to permit the tissue cooling.

The last addressed issue in the *ex-vivo* experiments investigated the performance of the integrated coil. First, preliminary tests (1-turn coil versus 5-turn coil) were performed in order to define the final prototype coil. Second, the influence of the transducer on the performance of this prototype coil was investigated. Third, the integrated coil was compared to a standard extracorporeal coil (the SFB coil) with respect to the available standard deviation in temperature measurements (SDT). A series of 30 dynamics of the same thermometry slice, without heating, was acquired in order to calculate the SDT (as explained in Chapter II). Note that the parameters of the MR sequences acquired for the coil comparative study (either morphological or thermal images) were chosen as a compromise* between the integrated and external coil performance. The optimal acquisition parameters of the integrated coil were used in further *in-vivo* studies.

	Application/ purpose	Sequence/ technique	FOV [mm²]	Voxel [mm³]	TE/TR [ms]	Flip Angle [°]	Lines /TR	Acq./recon. matrix	Acq. Time [s]
Ex - vivo	**Phased-array**	**PRFS**/ GE-EPI (45, 75, 100, 120 dyn)							
	▪ foc. beam		100x100	0.78x0.78 x5	16/600	45	15	96x90 128x128	3.6 (3 slices)
	▪ plane beam		100x100	0.78x0.78 x8	16/200	45	9	96x90 128x128	2
	▪ 2 beams		80x80	0.63x0.63 x8	14.5/250	50	11	96x88 128x128	2
	PID stability -1beam -		100x100	0.78x0.78 x8	16/200	45	9	96x90 128x128	2
	Coils	**T_1-w**-TFE/ GE	80x80	0.31x0.31 x5	10.6/200	40	24	252x240 256x256	56
	▪ 1/ 5 turns	**PRFS**/GE-EPI (30dyn)	80x80	0.63x0.63 x8	17.5/180	45	11	128x121 128x128	2
	▪ Int./ext. ▪ Intern coil (with/without transducer)	**T_2-w**-TSE/ SE	102x102	0.4x0.4 x4.9	65/2000	90	16	252x248 256x256	126
		PRFS/GE-EPI (30dyn)	80x80	0.63x0.63 x5	18/145	45	9	128x117 128x128	1.88
In - vivo	**Coils comparison**	**T_2-w** -TSE/ SE	96x96	0.37x0.37 x4.9	75/1250	90	16	252x248 256x256	80
			160x160	0.63x0.63 x4.9	50/1250	90	16	212x208 256x256	67.5
	▪ Int./ext.	**PRFS**/GE-EPI (30dyn)	96x96	0.75x0.75 x5	17.5/180	45	11	128x121 128x128	2
			226x226	0.88x0.88 x8	17.5/180	45	11	252x242 256x256	3.96
	PID and 2 beams	**PRFS**/GE-EPI (100, 120dyn)	96x96	0.75x0.75 x8	17.5/180	45	11	128x121 128x128	2
	Lesion observation	**IR-T_1-w**-TSE/ SE	128x128	0.5x0.5 x8	54.7/ 2500 TIR=500	90	16	256x256 256x256	123

***Table III.4.** MR acquisition parameters for all experiments using the rectal transducer.*

Table III.4 summarizes the MR acquisition parameters and sequences, and their purpose, for all experiments presented in this chapter.

* The MR parameters for coil comparison sequences were not optimal, neither for the extracorporeal coil, nor for the integrated coil. Hence, average parameters were used without favoring any coil.

***In-vivo* experiments.** Morphological and thermometry images were acquired *in-vivo* on three healthy pigs (female, two of 35 kg body weight and one of 20 kg). The animals were positioned in lateral decubitus (see Fig. III.13.b,c), while the endorectal device was horizontally positioned, parallel to B_0. Acoustic coupling gel was used to facilitate the device insertion. Since no tumor model was available, the peri-rectal muscles were chosen as target region for the ultrasound exposure. The experimental protocol, approved by an ethics committee, required continuous monitoring (visual, respiratory and cardiac) of the anesthetized animal. The respiratory function of the animal was continuously assisted by a MR-compatible mechanical ventilator connected to an oxygen supply. The general anesthesia of the animal was induced, before intubation, by an intramuscular injection of Zoletil® (6 mg/kg). A continuous perfusion of Propofol® (0.15 mg/kg/min) further maintained the anesthesia during the entire duration of experiments. At the end of the experiment, the animal was euthanized, and muscle sampling was performed for histology examination.

The prior-defined experimental goals (accuracy of the PID controller, sensitivity field of the miniature coil compared to the external coil, interleaved activation of two beams) were now investigated in *in-vivo* conditions. The optimal MR acquisition parameters offered by the internal coil were used in anatomical and thermometry sequences. The experiments studying the performance of the coils (thermometry without sonication) had only 30 dynamics, while the active control experiments (heating) varied from 100 to 120 dynamics. In addition, an IR- T_1-w spin echo sequence (with gadolinium enhancement) was used in order to highlight the morphologic visualization of the lesion associated to the administered thermal dose. See Table III.4 for complete sequence parameters, classified in function of the specific addressed issues.

III.3 Experimental results

III.3.1 Phased-array structure of the transducer

Beam type. No RF or susceptibility artifacts were detected to corrupt the MR data. The application of a different phase law permitted activation of either plane or 1D focused ultrasound beams. Figure III.14 shows the typical thermal pattern for each beam configuration (for MR acquisition parameters, see first and second rows of Table III.4). The applied electrical power was 40 W for 90 s for the plane beam and respectively, 24 W for 90 s for the focused beam. The focus was set to 20 mm from the transducer. Three imagining slices were acquired in the case of the focused beam for an easy detection of the focal point. The temperature scale shows the tissue temperature rise, relatively to an initial temperature assumed to be 37°C. The temporal evolution of the temperature is shown at 50%, 75% and 100% of the sonication time (90 s). The thermal

dose map is calculated at the end of the experiment, after the cooling period, knowing that the post-sonication persisting temperature might contribute to the final thermal dose. The logarithmic scale of the thermal dose begins at the lethal threshold of 240 minutes at 43°C defined by Sapareto and Dewey [1984]. The maximum electrical power supported by the rectal transducer was 44 W per beam, or approximatively 16.5* W/cm² per element. This power applied during 90 s for a plane beam induced a maximum temperature elevation of 36°C and generated a lesion of 30 x 4 mm². The focused mode permitted a higher temperature elevation (42°C), with even less power (36 W per beam), applied during the same 90 s sonication time.

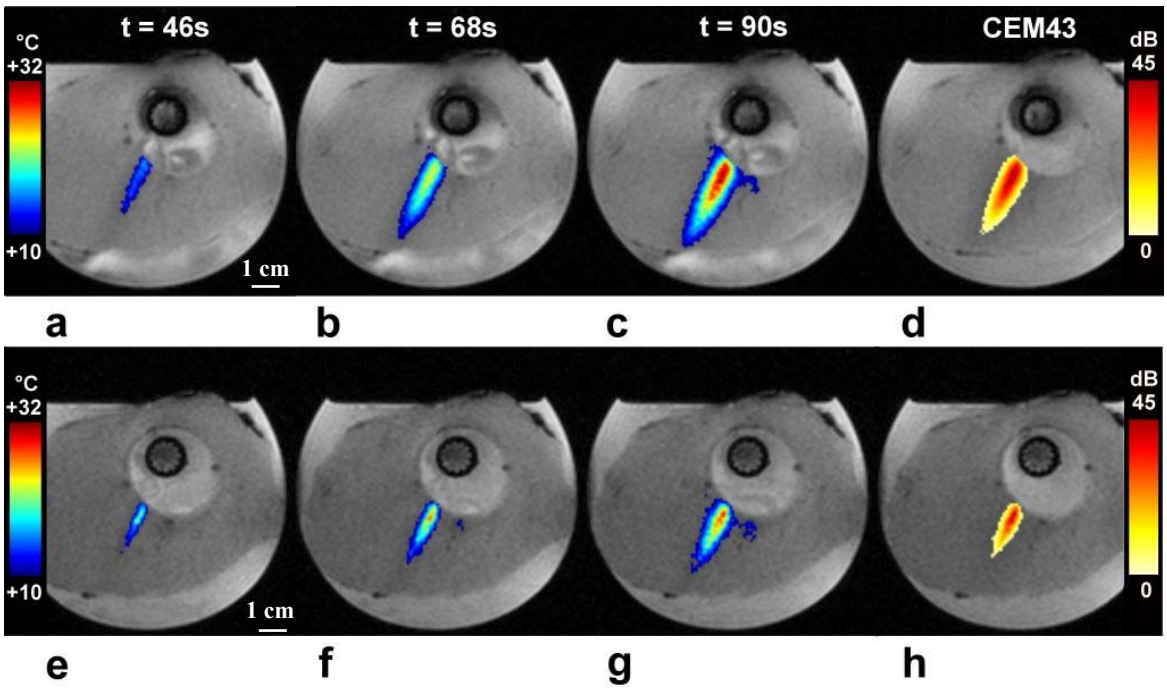

***Figure III.14.** Plane and focused individual beams obtained with the phased-array rectal transducer, axial plane, ex-vivo muscle (see first and second rows, Table III.4). FOV: 100 mm, in-plane resolution: 0.78 x 0.78 mm². Scale bar is 1 cm. See the transducer (black circle) and the cooling balloon (light-gray color around the transducer).*
***First line:** plane beam (40 W during 90 s). **Second line:** focused beam (24 W during 90 s); the focus was set to 20 mm from the active surface of the transducer.*
Maps of relative temperature (a, b, c – plane mode; e, f, g – focused mode) and of thermal dose (d; h). The temperature maps are shown at 50%, 75% and 100% of the sonication time, while the thermal dose map is calculated at the end of the experiment.

Multiple beams. The main advantage of the phased-array structure of the rectal transducer was the capability to rapidly change the sonication direction, without mechanical intervention. This electronic rotation was demonstrated by activating two interleaved radial beams during the same heating procedure. The two beams were fast switched, with a duty cycle of 50% per beam (see principle in Fig. III.15.a). For each beam, a "dead"-time of 40 ms should be considered for a sonication of 1 s. The two interleaved beams could be spatially separated by different angles

* The calculated acoustic intensity, including the attenuation due to the cooling balloon (~20%)

varying from 5.6° to 354.4°, but only apertures of less than 45° are of practical interest. An example of two interleaved beams, separated by 22.5°, 45° and 78.5° is shown in Fig. III.15 (for MR parameters, see the third row in Table III.4). The heating procedure using an aperture of 45° is detailed in panels b, c and d, showing the temperature evolution at three temporal intervals of the experiment (half, total, and 30 s after the sonication). The corresponding thermal dose, calculated at the end of the experiment, is shown in Fig. III.15.f. In addition, the thermal doses corresponding to the other two experiments, i.e. at 22.5° and 78.5°, are shown in the panels e and g, respectively. Within the three experiments described in this figure, the small diameter of the sample holder (80 mm) caused a reflection of the acoustic beam at its borders (see Fig. III.15). Different levels of electrical power were applied to each interleaved beam, during a defined time. For example, during the heating experiment presented in panels b-c-d-f, powers of 22 W/first beam, and 18 W/second beam were applied during 60 s. Even when equal powers were applied to each beam (data not shown here), the heating patterns were different due to the variability of the electro-acoustic efficiency of the beams.

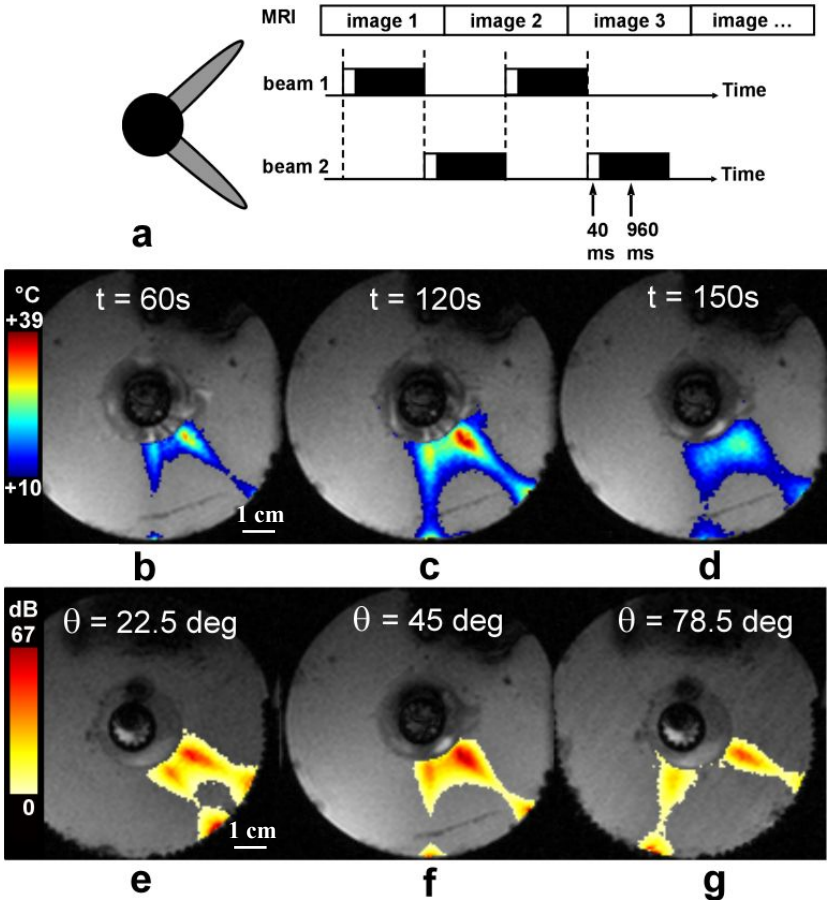

Figure III.15. ***Principle (a), relative temperature (b, c, d) and thermal dose (e, f, g) for two interleaved beams (duty cycle of 50% per beam) of the rectal transducer, axial plane, ex-vivo muscle. Three different heating experiments (see MR parameters in Table III.4, third row) corresponding to a beam angle of 22.5°, 45° and 78.5° are shown. The relative temperature map is shown, at three time-intervals (half, total, and 30 s after sonication) only for the 45°-angle two beams sonication, while the thermal dose maps are presented for all experiments. Beam reflection at borders was observed. FOV: 80 mm, 1 voxel: 0.63 x 0.63 x 8 mm^3, 2 s/dyn. Scale bar is 1 cm.***

III.3.2 PID controller stability

Correct estimates of α and D coefficients, for both types of beam, demonstrated excellent stability and accuracy of the PID controller, within the MR thermometry noise (average SDT: 0.5°C). In all *ex-vivo* PID experiments (see fourth row in Table III.4) the spatial resolution was 0.78 x 0.78 x 8 mm^3 and the temporal resolution was 2 s/dyn. The experimental temperature successfully tracked the predefined target curve, for a temperature elevation range from 15°C to 30°C, planar or focused beam. The active control of temperature temporal evolution (plane wave, target of 15°C) performed at 10 mm depth, had an accuracy of 0.73% error for the mean temperature (i.e. 15.11°C), and 1.8% SDT (i.e. 0.27°C). The same performance was obtained in the case of a focused beam (focus at 20 mm), for a sonication sequence of 90 s (rise)/ 90 s (steady-state)/100 s (cooling) defined for a temperature target of 30°C. The correct estimate of the α coefficient varied in function of the beam type (focused/plane), and depended also on the depth at which the focus was defined. More generally, the correct value of α varied also with the control point depth. For example, the heat deposition rate was 0.05 $°C/(W \cdot s)$ for a plane wave, 0.06 $°C/(W \cdot s)$ for a beam focused at 20 mm, and 0.08 $°C/(W \cdot s)$ for a beam focused at 15 mm. In all three cases the depth of the control point was 10 mm.

Figure III.16 presents the stability and convergence of the feedback-loop, investigated over 15 configurations (vertical axis: α, and horizontal axis: D) for plane wave mode. The central plot (with 100%, 100%) represents the best convergence of the temperature controller, obtained with the correct coefficients values. When the absorption value was correct (third row of plots), the diffusion parameter had little influence on the controller performance. Strong overestimation of the absorption (400%-first row) manifested as undershoots (on the rising part) and overshoots (on the constant part) of the measured temperature, showing however an accuracy of 10% for both relative error and SD. Otherwise, the underestimation of the absorption (25%-last row) conducted to an unpredictable and unstable behavior of the controller, which appeared generally during the second stage of the sonication sequence (the constant temperature part). In this case, the divergence of the controller was irreversible and the active temperature control was jeopardized.

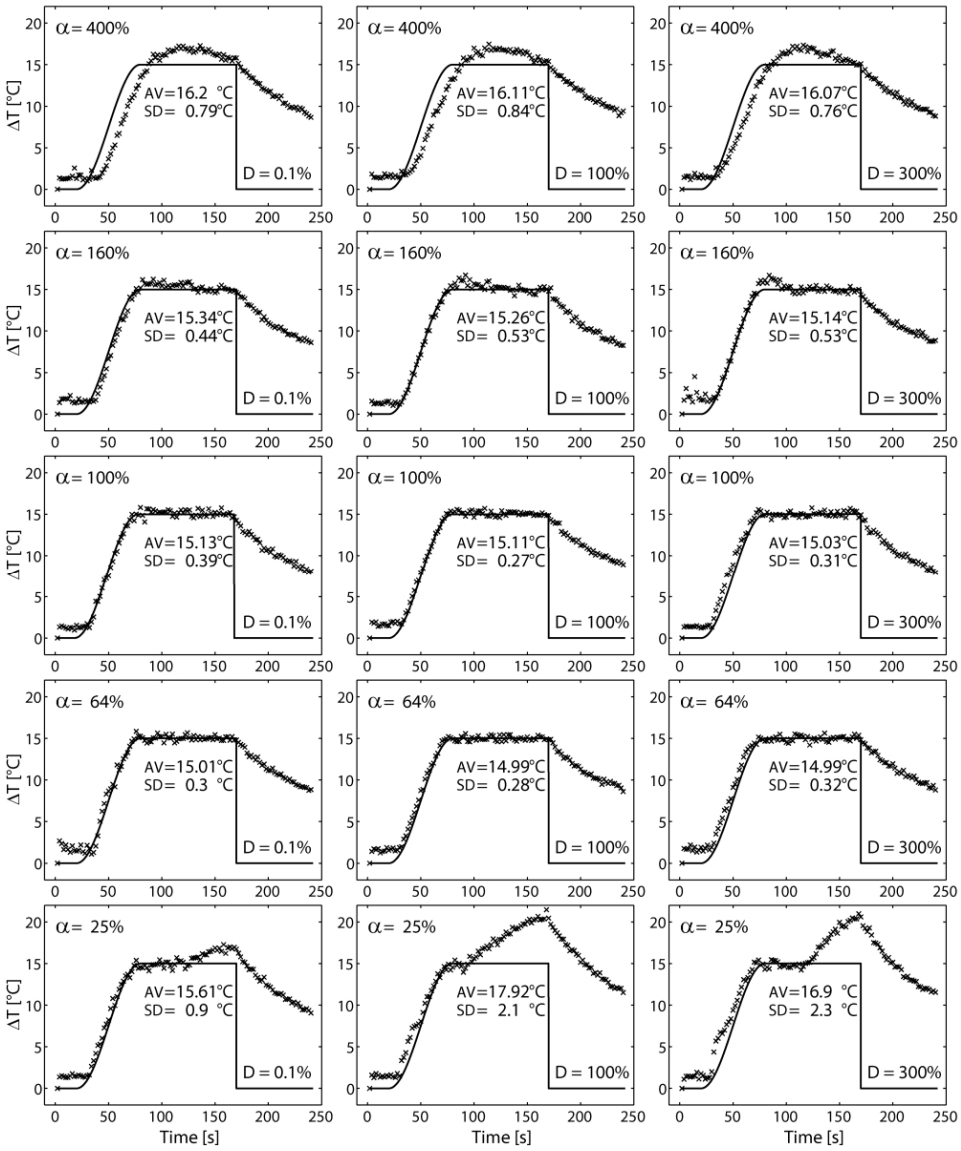

Figure III.16. ***Investigation of the stability and convergence of the PID controller with respect to erroneous values of α (25% to 400%) and D (0.1% to 300%). The target temperature was 15°C. Experimental mean and standard deviation of temperature are expressed within each plot.***

III.3.3 Comparative studies of the coils

1 versus 5 turns. Excellent passive and active MR-compatibility of the integrated device has been demonstrated in morphological and thermometry images. Figure III.17 shows the results of the comparative study concerning the number of turns of the prototype coil (1 versus 5 turns; see rows 5 and 6 of Table III.4 for sequence parameters). The homogeneity of the sensitivity field of the integrated coils was affected by their geometry and wiring. Localized closely to the coil wiring, hypersignal spots (white spots in images in Fig. III.17) could be observed for any type of MR image. The white spots matched, in sagittal plane, each turn of the coil, while in axial plane the hypersignal was associated to the two wires connecting the two groups of turns. The hypersignal was associated to a "shadow cone", i.e. a region of zero signal (black lines in sagittal plane or black spot in axial plane). Overall, this artifact caused a distortion -in axial plane- of the circular

symmetry of the sensitivity field (see Fig. III.17.c,d). However, the multi-turn geometry of the coil offered a smaller "shadow" region than the 1-turn coil (see the SDT maps). Moreover, in sagittal plane, the "shadow region" was localized on the middle turn, not on the first turn of the coil (see the white arrows in Fig. III.17.a, b). Thus, the sensitivity field (see the sagittal images) extended further along its longitudinal axis, when compared to the 1-turn coil field. Nevertheless, despite these advantages, the *ex-vivo* muscle thermometry data (see sixth row in Table III.4) obtained with the single-turn coil showed better sensitivity, i.e. the circular limit of 1°C SDT was reached at 17.5 mm distance* from the tip balloon, instead of 12 mm with the 5-turn coil. Therefore, the 1-turn coil was chosen to be used in all subsequent *in-vivo* experiments.

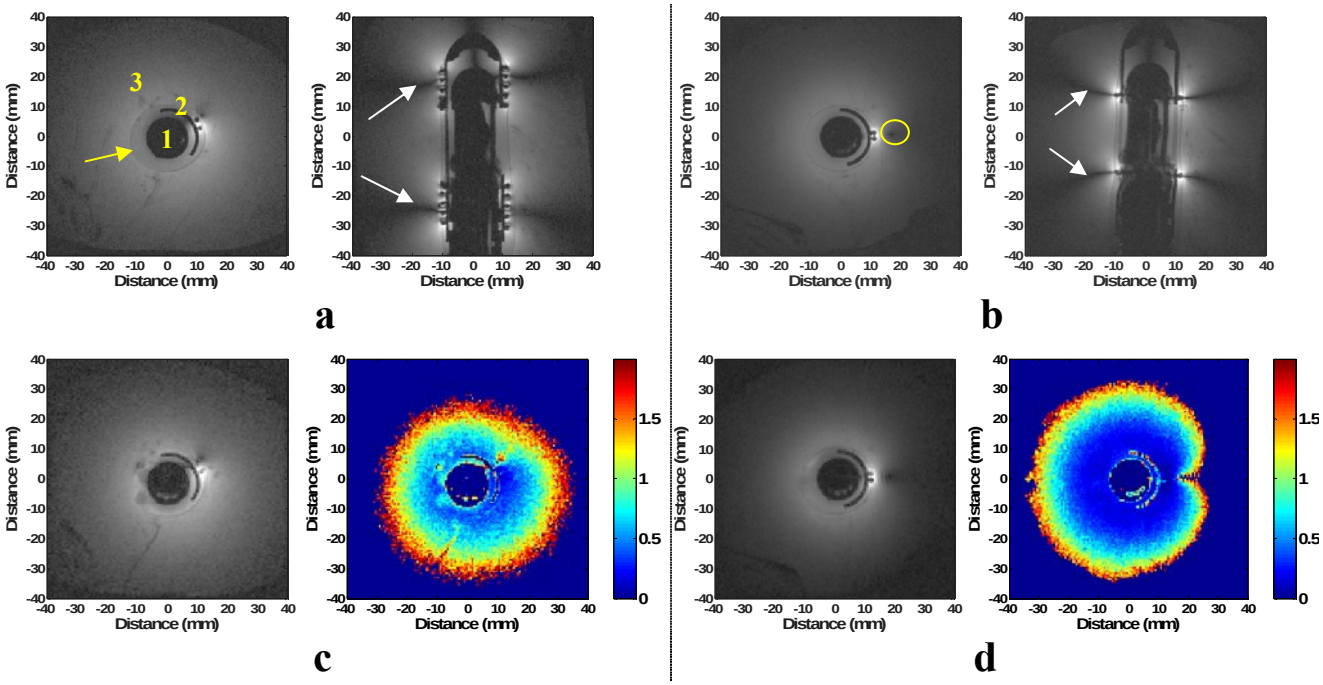

Figure III.17. ***Comparative study of rectal coils: 5-turn coil (left) versus 1-turn coil (right), ex-vivo muscle; see MR parameters in Table III.4, 5th and 6th rows. FOV: 80 mm.***
a), b). ***Anatomical images (T_1-w-TFE, 1 voxel: 0.31 x 0.31 x 5 mm^3), axial and sagittal plane. Visible are the transducer (1), the coil support (2), the tissue (3) and the faint surface of the cooling balloon (the yellow arrow). The white arrows indicate the "shadow regions" in sagittal plane, whereas the circle shows the non-signal region in axial plane.***
c), d). ***Thermometry images (FEEPI, 1 voxel: 0.63 x 0.63 x 8 mm^3, 2 s/dyn) and the corresponding SDT-maps, axial plane. SDT was cut at 2°C. The colorbar is in °C. The non-signal region caused a distortion in the symmetry of the coil sensitivity field.***

Transducer influence. The second comparative study (rows 7 and 8 in Table III.4) studied the influence of the transducer wiring, and the quality improvement of the MR acquisition brought by the internal coil. Both goals were investigated with respect to the 1-turn geometry. The results are summarized in Fig. III.18. The transducer, the coil support, the cooling balloon and the muscle are clearly visible. Distortion of the symmetry of the coil sensitivity field (see the SDT-maps) was induced by the non-signal region. When positioned inside the coil, the transducer had a minimal

* All depths measured for a defined limit of the coil sensitivity were calculated with a precision equal to 1 pixel value.

influence on the coil performance (see columns 1 versus 2, Fig. III.18), for a voxel of 0.63 x 0.63 x 5 mm^3. Quantitatively, the sensitivity limit of 1°C was reached at a depth of 13.1 mm with the coil integrating the rectal transducer, versus 15.6 mm reached with the coil without the transducer.

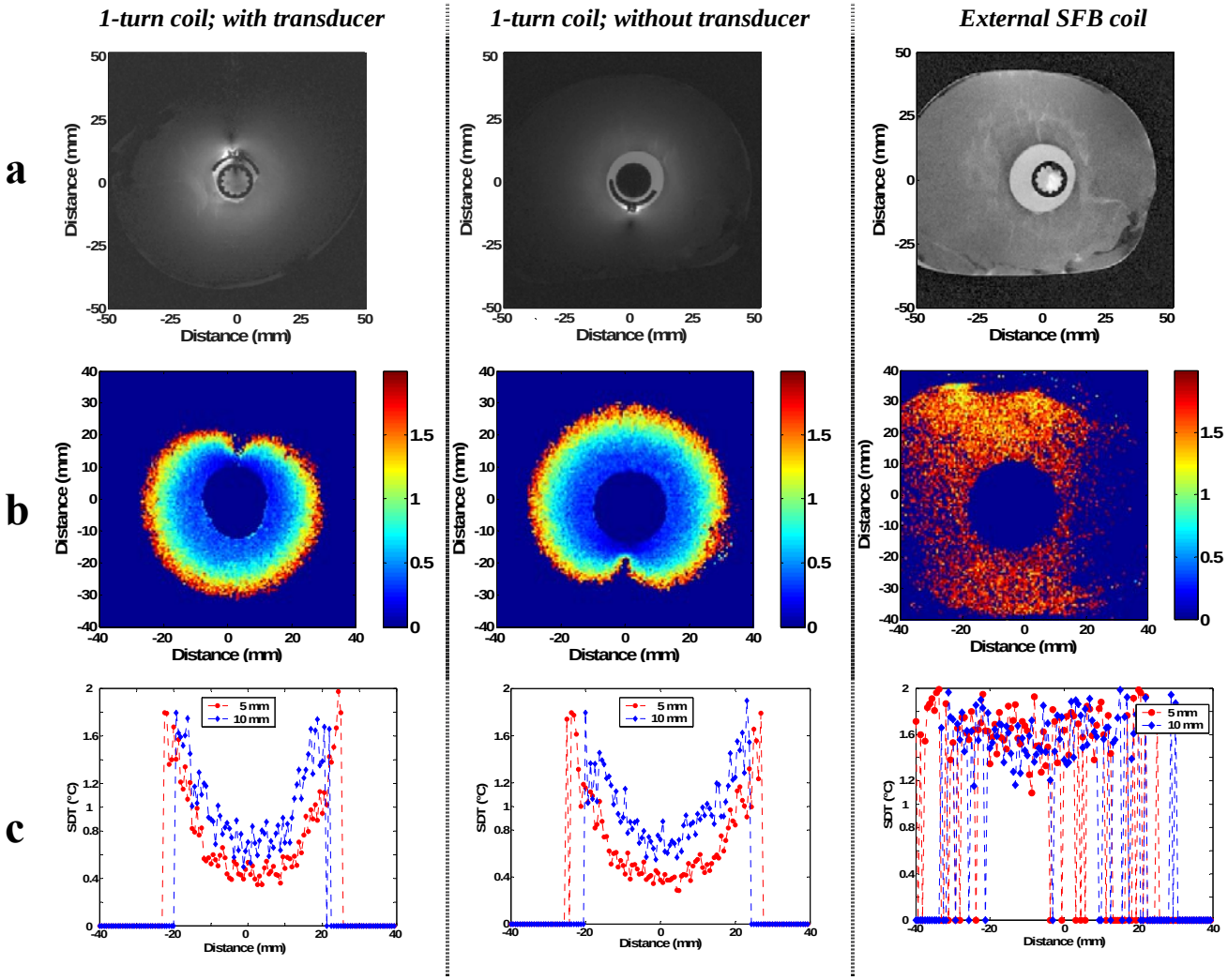

Figure III.18. ***Comparative study of rectal coils: transducer influence (columns 1 vs. 2) and internal/ external coil (columns 1 vs. 3) in ex-vivo muscle, axial plane; see MR parameters in Table III.4, 7th and 8th rows. a) Anatomical images (T_2-w-TSE, 1 voxel: 0.4 x 0.4 x 4.9 mm^3, FOV: 102 mm). b) and c). SDT-maps and corresponding horizontal profiles (at 5 and 10 mm) for thermometry images (FEEPI, 1 voxel: 0.63 x 0.63 x 5 mm^3, 1.88 s/dyn, FOV: 80 mm). SDT was cut at 2°C. The colorbar is in °C.***

Internal versus external coil. The comparison between the internal 1-turn coil and the external SFB (4-element phased array) coil showed significant differences. As expected, the sensitivity field of the external coil had a good homogeneity, while the internal coil demonstrated a steep gradient (see Fig. III.18, columns 2 & 3). Over a relatively short radius (20 mm), the noise of the temperature measurement varied from 0.4°C to 1.8°C. Two profiles of the SDT-maps measured a noise of 0.4°C at 5 mm from the balloon, and respectively 0.7°C at 10 mm. The external coil measured, in the same conditions, an SDT of 1.6°C. Hence, the sensitivity of the internal coil was increased by a factor 4 at 5 mm, whereas no gain in sensitivity was obtained beyond 25 mm.

III.3.4 *In-vivo* results

Internal/external coil. Anatomical (T_2-w-TSE) images, acquired with the optimal resolution specific to each type of coil (see 9th and 10th rows in the former Table), permitted visualization of the structure of the porcine pelvis. Each constitutive element of the therapeutic endoscopic device (i.e. rectal transducer, coil, cooling balloon) were clearly delineated on these high-resolution images (see Fig. III.19). The sonication target, represented by the peri-rectal muscles (see arrows), was only 10 mm-thick, being limited by the sacral bones (see the ellipses). Important volumes of air were observed in the rectum, near the cooling balloon, in front of the transducer (see the black half-moon localized between the two arrows). The possible directions of ultrasonic exposures were hence limited by this air-mass and also by the Plexiglas support of the coil. Flow artifacts caused by the water movement inside the cooling balloon were seen as localized ghost pattern in phase-encoding direction on the images acquired with the home built coil. However, in function of the sonication direction, the phase-encoding direction could be changed by 90° ensuring an artifact-free target region. These artifacts were enhanced on the thermometry images and depended on the flow of the cooling water.

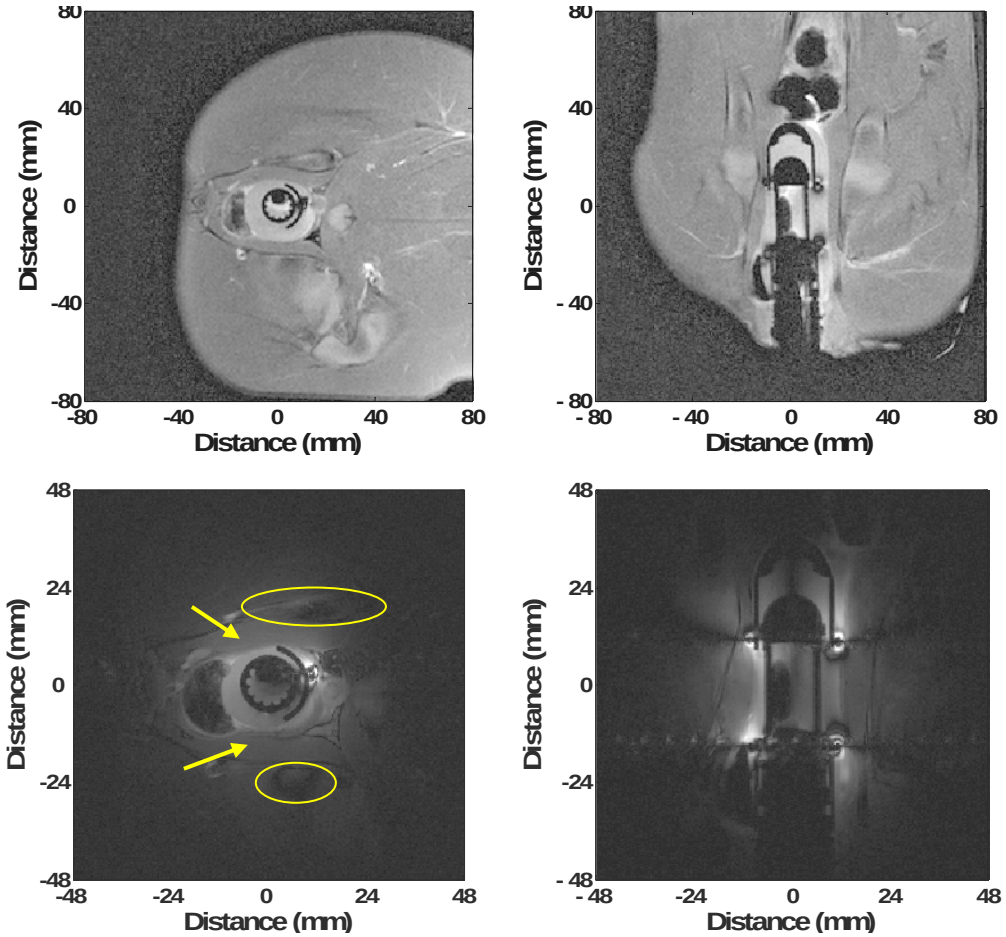

Figure III.19. ***Anatomical images (T_2-w-TSE), in axial and sagittal plane; see MR parameters in Table III.4, 9th and 10th rows. Up: SFB coil (1 voxel: 0.63 x 0.63 x 4.9 mm^3, FOV: 160 mm). Down: internal coil (1 voxel: 0.37 x 0.37 x 4.9 mm^3, FOV: 96 mm). The two arrows indicate the peri-rectal muscles used as sonication target, while the two ellipses indicate the sacral bones.***

The *in-vivo* comparison of internal and external coils was performed on thermometry images at two different resolutions (0.75 x 0.75 x 5 mm^3, 2 s/dyn, and 0.88 x 0.88 x 8 mm^3, 3.96 s/dyn). The images acquired with higher resolution (see left column of Fig. III.20) showed, with the integrated coil, a noise of temperature measurement less than 1°C all over the region of interest (a circular radius of 10 mm from the balloon limit). The minimal SDT was 0.4°C. In the same conditions, the images acquired with the SFB coil were completely useless, having an SDT higher* than 3°C. The second MR sequence (lower spatial and temporal resolution) was more appropriate to the external coil. However, even in these conditions, the SDT measured with the external coil was higher than 1.5°C, while the rectal coil managed to measure temperature with a maximal sensitivity of 0.3°C and doubled the 1°C-sensitivity depth obtained at the higher resolution.

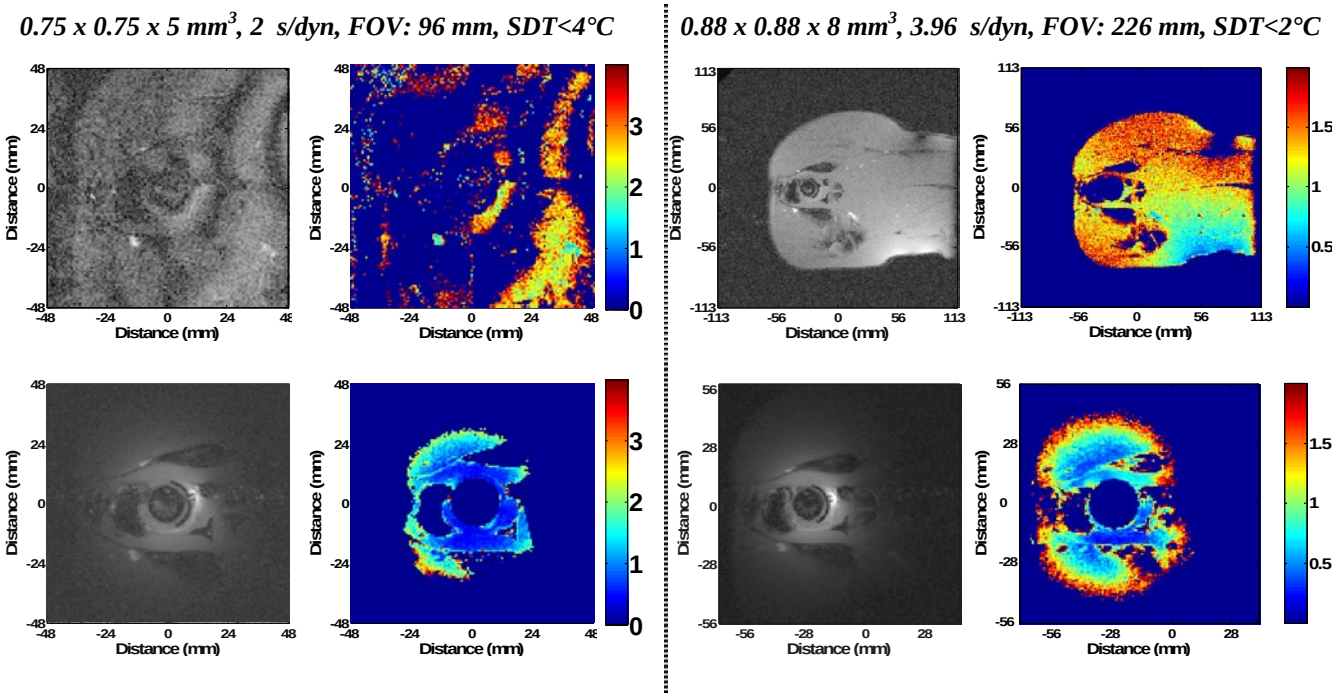

Figure III.20. ***External (first row) versus internal (second row) coil, in-vivo thermometry images (FEEPI) of the rectal region, and the corresponding SDT-maps, axial plane, at two different resolutions (see lines 11 and 12 in Table III.4 for MR parameters). SDT was cut at 4°C, and 2°C, respectively. The colorbar is in °C. For the internal rectal coil, only a quarter of the acquisition FOV (case of 226 mm) is shown.***

Thermotherapy with automatic temperature control. As a result of the previous comparative study, the MR automatic controlled heating experiments were acquired with a voxel of 0.75 x 0.75 x 8 mm^3 and a temporal resolution of 2 s/dyn (see the 13th row in Table III.4). Automatic control of temperature was performed on both plane and focused beam, showing better accuracy in the case of a plane beam. The thermal dose, calculated according to Sapareto and Dewey [1984], was mainly obtained during the flattop region of the target curve. Figure III.21

* Note that the SDT-map calculations cut the SDT to 4°C and respectively 2°C. All SDT measured above that limit were automatically set to zero. This explains the non-existing values from some regions, especially in the case of the external coil.

presents two cases of temperature feedback control, with individual plane beam, for a target temperature rise of 20°C, and respectively 35°C. The accuracy of the controller was 0.3% (relative error of the mean temperature) and 4.3% (SDT) for the 20°C target, and respectively, 1.8% (relative error of the mean temperature) and 6.5% (SDT) for the 35°C target. The average applied power was 20.1 W (max. 32.4 W) and respectively 9.6 W (max. 15 W). The absorption coefficient was set to $0.08\,°C/(W \cdot s)$ and $0.5\,°C/(W \cdot s)$, while the diffusion was 0.05 mm²/s in both cases. The local anatomy (sacral bone) strongly influenced the heating pattern of the second case presented here (second row in Fig. III.21). Hence, the PID controller used a higher estimate of the absorption coefficient. In addition, due to the important reflexion from the bone, the needed power was quantitatively lower (9.6 W for a target temperature rise of 35°C).

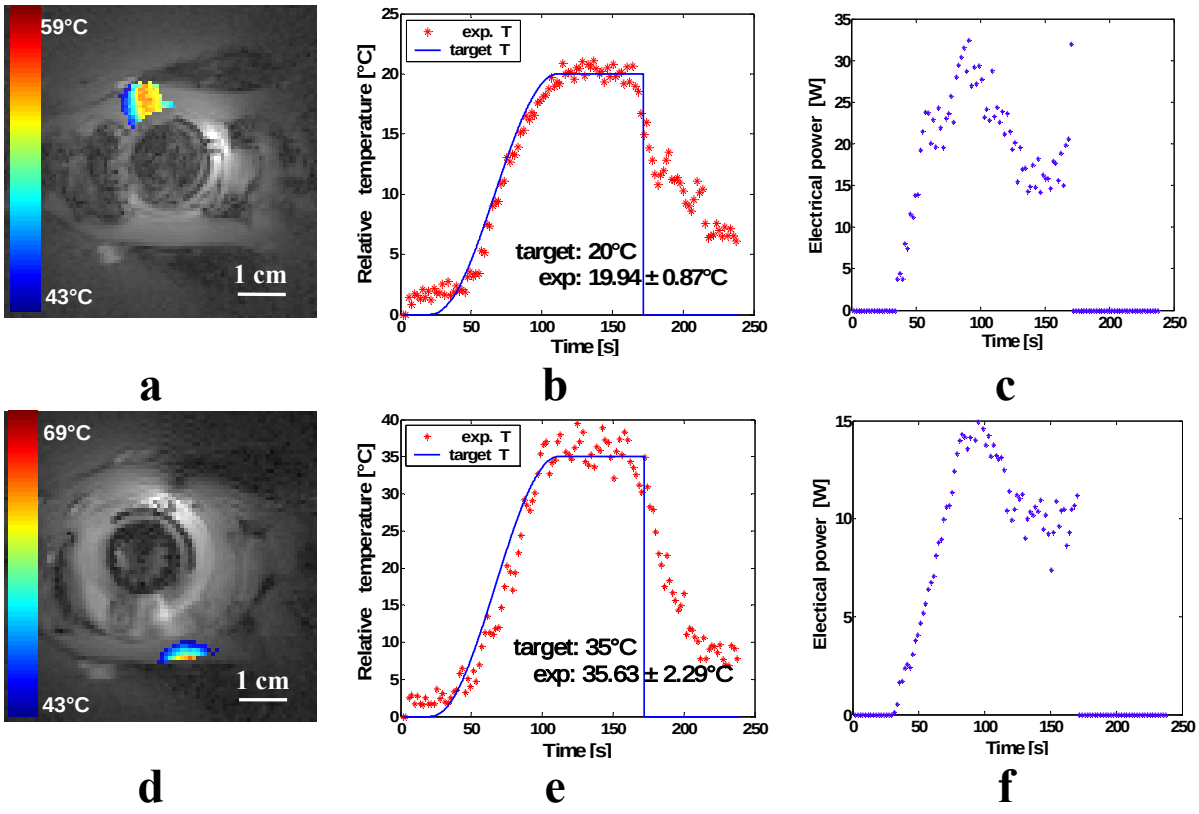

***Figure III.21.** Two cases of in-vivo heating experiment with active temperature control: **first line** (target of 20°C), and **second line** (target of 35°C); axial plane, integrated rectal coil, see MR parameters in Table III.4, 13th row. Thermal maps (absolute temperature) acquired at the end of the heating period (a, d); temporal evolution of the controlled temperature rise (b, e); and applied power (c, f). FOV: 96 mm (here only a central zone is shown), 1 voxel: 0.75 x 0.75 x 8 mm³, 2 s/dyn. The scale bar is 1 cm.*

Figure III.22 summarizes the absolute temperature maps evolution during a MR-controlled heating experiment, for single beam activation (same experiment as previously) and two beams. The bone influenced the heating: the ultrasound beam located in front of the bone showed a higher temperature rise than its adjacent beam. The beam without bone as back reflector could not reach the thermal threshold of necrosis, even if the applied power was doubled (40 W/ 20 W).

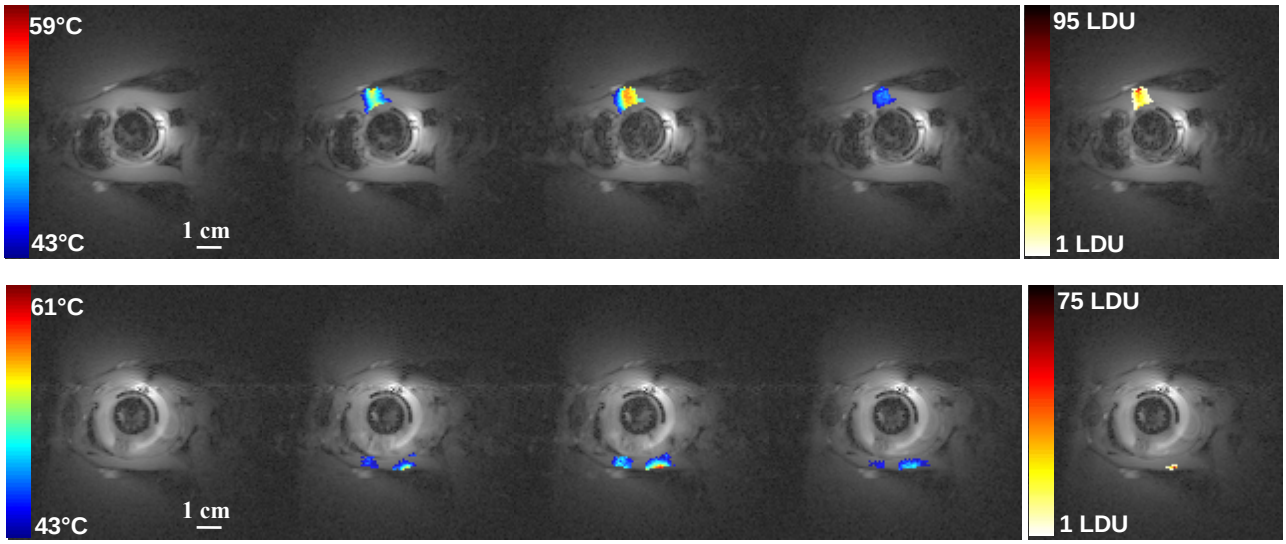

Figure III.22. ***Two cases of in-vivo heating experiment with 1 and 2 beams sonication, axial plane, integrated rectal coil (see MR parameters in Table III.4, 13th row). Up: one beam, with PID controller (20°C target, 150 s sonication). Down: two interleaved beams, no PID, angle 45°. Thermal maps (absolute temperature) are shown at the beginning/half/end of the heating period, and 30 s after, during the cooling period. Corresponding thermal dose maps, acquired at the end of the experiment, are expressed in units of lethal dose (1 LDU = 240 $EM_{43°C}$). FOV: 96 mm, 1 voxel: 0.75 x 0.75 x 8 mm^3, 2 s/dyn. The scale bar is 1 cm.***

Evaluation of tissue destruction. The immediate assessment of the necrosed tissue was investigated with the integrated coil through T_1-weighted inversion recovery TSE acquisition, after gadolinium injection (see last row of Table III.4). The three necrosed regions were seen as non-signal (black) regions, in Fig. III.23 (b and c). Furthermore, at the end of experiments, the animal was euthanized, and samples of rectum and muscle were prepared for histology.

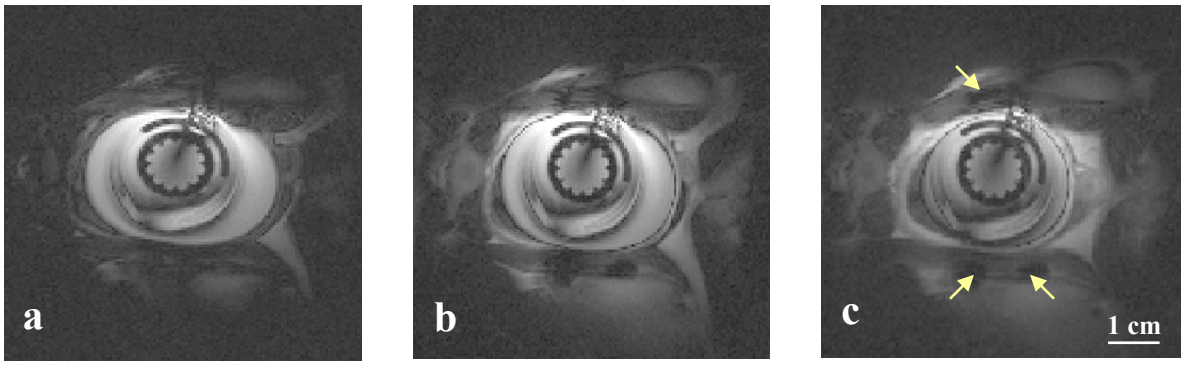

Figure III.23. ***Anatomical images (IR-T_1-w-TSE) acquired in axial plane with the integrated rectal coil (see the last row in Table III.4, for MR parameters). FOV: 128 mm, 1 voxel: 0.5 x 0.5 x 8 mm^3. a) before Gd; b) after Gd (arterial time); and c) after Gd (venous time). Arrows indicate the three unperfused regions heated by HICU, seated each in front of the sacral bones. Here only the center of the FOV is shown. The scale bar is 1 cm.***

Samples of rectum and peri-rectal muscles were histologically inspected with hematoxylin and eosin staining technique*. No lesions were detected on the rectum sample, but cell necrosis was

* Hematoxylin stains nuclei blue and eosin stains cytoplasm pink.

confirmed by the histology of the muscle: moderate neutrophilic myositis (inflammation), associated with degeneration and necrosis of muscular cells. A HICU-induced lesion within the peri-rectal muscle (region 1) and a healthy muscle (region 2) are shown in Fig. III.24. While the healthy muscular tissue is homogenous, three destructive effects could be observed within the lesion: congestion of sanguine vessels; fragmentation of muscular cells and hyperacidity of their cytoplasm (see the yellow arrow-heads); and mini hemorrhages (see the black arrows). Moreover, the anti-inflammatory response of the organism was observed through the agglomeration of polynuclear neutrophiles cells*, which infiltrated the muscular fiber or even the muscular cell (see ellipses containing blue points).

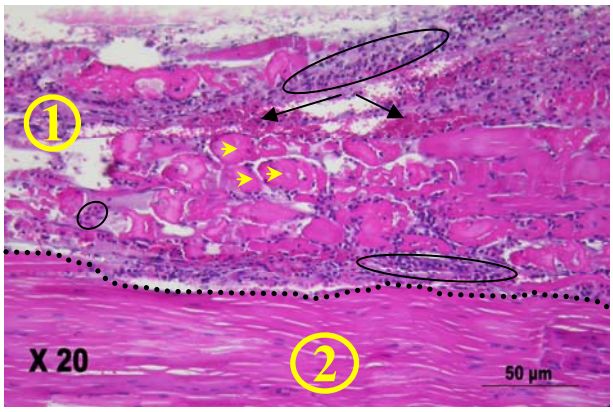

Figure III.24. ***Microscopic view of the peri-rectal muscle sample. The dotted line delineates the necrosed tissue (1) from the healthy tissue (2).***

III.4 Discussion

The potential of the 64 elements phased-array configuration of the rectal transducer was demonstrated within three different applications. *First*, the electronic rotation of the transducer permitted choice of a radial heating direction without any mechanical movement. Normally, the acoustic aperture of the ultrasound applicator was 360°, but the coil presence (especially its plastic support) limited it to 270°. This limitation could not be solved with the actual design of the rectal transducer, but it was overcome in Chapter IV with another transducer. *Second*, the capability to configure plane or slightly focused beam offered the possibility of controlling the heating pattern accurately. The beam could be focused at different depths (from 10 to 20 mm) permitting, therefore, modulation of the location of the lesion. This important aspect may be then exploited for tumors with an asymmetric geometry (multilobes). The thermal lesion (see Fig. III.14) obtained with a focused beam was reduced by 40% in thickness, and by 10% in length, compared to the lesion obtained with a plane beam. Moreover, less electrical power was needed (reduction from 40 W to 24 W). The advantage of the focused beam configuration was a higher delimitation between the different levels of delivered thermal dose, hence a better characterization of target margins. And *third*, the last advantage of the phased-array geometry of the transducer implied the activation of multiple radial beams. The angle separating the two beams could vary from 5.6° to 354.4°, but only lower angles (up to 45°) are of interest for thermal purposes. In these cases, the cross thermal

* a type of leukocytes

diffusion between the two neighboring beams may be exploited, resulting in a possible fusion of the two individual lesions. One important problem of the rectal phased-array transducer was the thermal fragility of its elements. At the end of the experiments presented in this chapter, 14 elements out of 64 were not functional and their randomized location disturbed the use of the neighboring elements.

The integration of the RF receive-only coil with the therapeutic device led to an important improvement in spatial and temperature measurement resolution, without any sonication-related RF artifacts. The opposed-solenoid RF coil, adapted to the phased-array geometry of the transducer, showed a nearly-isotropic sensitivity field around the integrated device, in the axial plane. A fundamental advantage of this local coil was the capability to acquire images with high-resolution (small FOV), without possible phase wrapping from other regions. As previously observed in Chapter II, the cooling balloon enveloping the integrated device offered important advantages, such as biocompatibility and prevention of possible RF heating. The flow artifacts, proportional to the water flow rate, could be shifted out of the region of therapeutic interest by changing the phase-encoding direction. However, because the integrated coil highlighted the flow artifacts, attention should be paid when choosing the phase-encoding direction.

The lower sensitivity of the 5-turn coil compared to the 1-turn coil was explained by the high dielectric losses (larger wiring surface) in conditions of full loading (i.e. tissue). The influence of the transducer on the coil performance was minimal, regardless of voxel size. On the contrary, the gain in sensitivity of the endocavitary coil (1-turn coil) over the standard extracorporeal coil depended on the voxel size. The sensitivity gain was then maximal, i.e. a 7.5 factor, at higher resolution (0.75 x 0.75 x 5 mm^3 voxel) and diminished to a factor 5 at lower resolution (voxel 0.88 x 0.88 x 8 mm^3). This gain in sensitivity was reported in *in-vivo* conditions, near the transducer. However, note that because the coil signal could be distributed between spatial and temperature resolution, the intrinsic SDT becomes better when lowering the resolution. It was observed that the *in-vivo* conditions significantly affected the extracorporeal coil sensitivity (temperature noise higher than 1.5°C), while the performance of the rectal coil was less influenced. On the other hand, the sensitivity field of the endocavitary coil varied rapidly within a circular radius of 30 mm from 0.3°C to 2°C. Therefore, the endocavitary coil may be efficiently used (i.e. with an SDT better than 1°C and for infra-millimeter in-plane resolution) for a tumoral depth up to 20 mm. In the case of larger tumors (30 mm), sufficient SDT could be obtained if the spatial resolution is lowered (e.g. 1 mm^2 in-plane resolution). Note that all thermometry sequences presented in this thesis used no spatial averaging since the SDT values were calculated from true voxels. According to appendix A, an SDT of 1°C will induce an overestimation of the thermal dose of only 27%, while a 2°C causes an error of 161%.

The PID temperature controller demonstrated robustness, good accuracy and also easy implementation. The control point could be defined either spatially or automatically (as the maximum temperature rise obtained over a defined surface), for both planar or focused beam mode. Due to the attenuating profile of the acoustic beam, the spatial definition of the control point guaranteed a higher heat delivery along the beam path, in front of the control point. However, an exception exists: the inner tissue layer, in direct contact with the cooling balloon. The low water temperature of the cooling balloon (20°C for *ex-vivo* tissue and 10°C for *in-vivo* experiments) limited the heat delivery in its close vicinity. This was observed during animal experiment, when no lesion was observed on the rectal wall (~3 mm) although the neighboring muscle was destroyed. This heat-sink phenomenon can be an important disadvantage since an inner, very thick layer of the tumor can remains untreated.

The stability of the controller was demonstrated within the *ex-vivo* study over a large domain of errors of the input parameters (absorption and diffusion), with a good accuracy (less than 10% errors). Variations of the absorption coefficient strongly influenced the convergence of the feedback loop, while diffusion errors have less influence. Overestimation of absorption caused temperature overshoots, but still presenting a stable behavior. More critical was the underestimation of absorption (by a factor 4 or more), which induced, at an unpredictable moment, an unstable behavior. It is therefore preferable to overestimate the absorption rather than underestimate it. Note, however, that anatomical conditions, such as bone, causing beam reflections can be simply integrated into the PID controller by increasing the value of the absorption coefficient. This was the case for the *in-vivo* experiments presented in this chapter. The PID controller demonstrated high *in-vivo* accuracy of temperature, especially in the case of plane wave configuration. In this chapter, the automatic temperature control was performed only for one single point, defined for one beam. Nevertheless, generalization of the automatic control to more beams, rapidly interchanged, was demonstrated in Chapter IV.

The *in-vivo* experiments were performed on three healthy pigs. Unfortunately, only the last animal experience data were relevant[*]. Normally, compared to the esophageal region (respiratory, cardiac motion), the MR imaging of the rectal region should not be affected by motions artifacts. But, in our case, the assumption that the endoscopic device, inserted inside the rectum, will be sufficiently stable to acquire thermometry images was false. No satisfactory thermometry images could be acquired and therefore an MR-compatible mechanical system (see Fig. III.13.b, c) was built in order to ensure the stability of the device for further experiments. Also, the extensibility of the rectum permitted the cooling balloon to extend to a diameter of more than 50 mm (data not shown), which surpassed the useful sensitivity of the rectal internal coil. Hence, the last *in-vivo*

[*] First animal: motion problem; second animal: presence of feces in the rectum.

experience was performed on an animal of 20 kg, which limited the balloon at a maximal diameter of 30 mm. The balloon was more ellipsoidal than circular (30 mm x 23 mm or 25 mm x 28 mm) and its dimension was appropriate for a clinical study (the maximal diameter of human rectum is 40 mm [Santoro *et al*, 2006]). Moreover, the pelvic anatomy of the pig (sacral bones) restricted the lesion formation since the peri-rectal muscle had a reduced thickness (about 10 mm). Therefore the lesion did not have its usual longitudinal form, but was rather circular. Note that the ultrasound device (working at 3.57 MHz) was designed for relatively high tumoral depth (20 to 30 mm in diameter). When working with reduced tumoral depth, the frequency must be increased in order to prevent bone reflections. In addition, another important characteristic of the rectal transducer was observed during the *in-vivo* experimentations. The sonication inside the porcine pelvis could have different orientations. One direction was limited by the sacral bones, but another direction had no limitation. At 3.57 MHz, the ultrasound beam propagated within a relatively homogenous medium and stopped at the interface with the skin. A lesion of the skin produced by the transducer inserted inside the rectum was observed (see Fig. III.25). In order to limit such undesired effects, the working frequency of the transducer should be increased.

Figure III.25 Undesired lesion of the porcine skin obtained with the rectal transducer.

In this chapter, the advantages of the phased-array technology and the improvement of the quality of MR data brought by the internal coil (compared to the external coil) were demonstrated *ex-vivo* and *in-vivo.* As a next step, further statistical animal studies are needed to evaluate the treatment repeatability. However, prevention of undesired heating at interface and improvement in thermal fragility of elements should be addressed prior to additional animal experiments.

III.5 Conclusion

This study successfully investigated three technological issues. The automatic temperature control, adapted to the phased-array configuration of the rectal transducer, showed an accurate *in-vivo* performance (4.35% SD, 0.3% error of mean value) and a good stability over possible errors of the input parameters or temperature measurement noise. Second, the benefits of the phased-array geometry of the transducer (electronic rotation, choice of planar or focused beam mode, multiple beams activation) were experimentally demonstrated. Third, the integration of a RF receive-only coil permitted the *in-vivo* acquisition of high-resolution morphological images (voxel 0.4 x 0.4 x 5 mm^3) and accurate thermometry data (voxel 0.75 x 0.75 x 8 mm^3, 2 s/image). Fast thermometry sequence with lower temperature noise (up to 1°C) for up to 20 mm-depth can be acquired. Important sensitivity gain of the integrated coil (up to a factor 7.5) was demonstrated with respect to an extracorporeal 4-element phased-array standard coil.

Chapter IV. Optimization of high resolution MR-guided contact thermotherapy for digestive applications: treatment planning and embedded integration of the RF coil

IV.1 Introduction

IV.2 Material and methods

IV.2.1 Esophageal ultrasound transducer & electronics

Phased-array ultrasound transducer
Matching of the electrical impedance
Electrical calibration of the transducer
Acoustic calibration of the transducer
Cooling balloon attenuation measurement

IV.2.2 Opposed-solenoid RF coil

Coil prototype: 1 turn versus 3 turns
RF coil integrated within the phased-array transducer

IV.2.3 Planning of the thermotherapy treatment

Algorithm description
Simulation results

IV.2.4 MR data acquisition and processing

MR system and experimental setup
Ex-vivo experiments

IV.3 Experimental results

MR compatibility of the integrated device

IV.3.1 Comparative study of the coils

Comparative study of the coils
Integrated coil performance

IV.3.2 Thermotherapy with automatic temperature control

IV.3.3 Feasibility of the treatment planning

IV.4 Discussion

IV.5 Conclusion

IV.1 Introduction

One major objective of this chapter was to define an optimal strategy for the treatment planning, based on the fast-switched multiple beams approach available thanks to the phased-array geometry of the ultrasound transducer. Concurrently, the temperature controller was developed in order to comply with this approach, permitting, for example, the implementation of additional feedback control points, at the rate of one control point per beam. Another aim of this work was to refine the coil integration with the therapeutic transducer, as a next step of the methodology presented in Chapter III. The integrated rectal device previously presented was a reversible assembling of the two separate constituents: the rectal transducer and the coil. On the contrary, in this chapter, the esophageal phased-array transducer was designed specially to host the coil wiring, creating an indivisible device. For this purpose, a former version of esophageal phased-array transducer was modified by Imasonic S.A in the context of the present work, under specific requirements regarding the coil body. After impedance matching and characterization by the radiation force method, the new device was investigated *ex-vivo* with respect to the defined goals. The new integration of the coil was expected to have a completely circular sensitivity, without the limitation observed in the rectal case.

IV.2 Material and methods

IV.2.1 Esophageal ultrasound transducer & electronics

Phased-array ultrasound transducer. The esophageal cylindrical ultrasound transducer (Imasonic, Besançon, France) was similar to the rectal one, in terms of geometry and handler. However, its intended clinical application requires smaller dimensions and flexibility. Hence, no rigid structure of the handler was allowed, contrary to the rectal application. The cylindrical active surface (14 mm-long and 11 mm in diameter) contained the 64 parallel elements, operating at 5.15 MHz. The angular step of the electronic rotation of the ultrasound beam was 5.6° (i.e.360°/64). The width of each element was 0.48 mm, with an inter-element gap of 0.07 mm. The transducer head (6 cm-long) continued with a 94 cm-long flexible tube (of 7.5 mm in diameter) and ended with a multi-channel connector. As for the rectal ultrasound transducer, a rounded distal end of the transducer head facilitated the endocavitary insertion. The phased-array geometry of the transducer permitted the production of either a plane beam or a slightly focused beam.

Figure IV.1 illustrates the evolution of the actual integrated device (see b and c), built to be adapted to the coil housing, from a former version of ultrasound transducer (see a), conceived to be operated without the RF coil. The initial phased-array transducer was elongated* in order to

* These elongation regions have only support purpose and have no influence on the acoustic region of the transducer.

host the coil wiring. For this purpose, two regions of 12 mm-long each (see the pink arrow) were added in the immediate vicinity of the active acoustic zone. The second modification of the ultrasound transducer regarded the two connecting cables of the coil. Hence, two additional tunnels (of 1.2 mm ID), similar to those existing for the internal cooling circuit, were built inside the transducer. The first tunnel (26 mm-long, see the white cable on Fig. IV.1.b) was aimed to connect, through a copper wiring, the two groups of turns of the coil, placed laterally, at the two sides of the active zone of the transducer. The second tunnel connected, through a coaxial cable, the coil head to its standard control unit, which performed the dynamic tuning and matching of the coil. This second tunnel began at the ending part of the transducer head (see the red cross in Fig. IV.1.b) and covered 45 cm inside the flexible tube of the transducer. The coaxial connecting cable of the coil was 63 cm-long, 45 cm inside plus 18 cm outside the transducer, see Fig. IV.1.c.

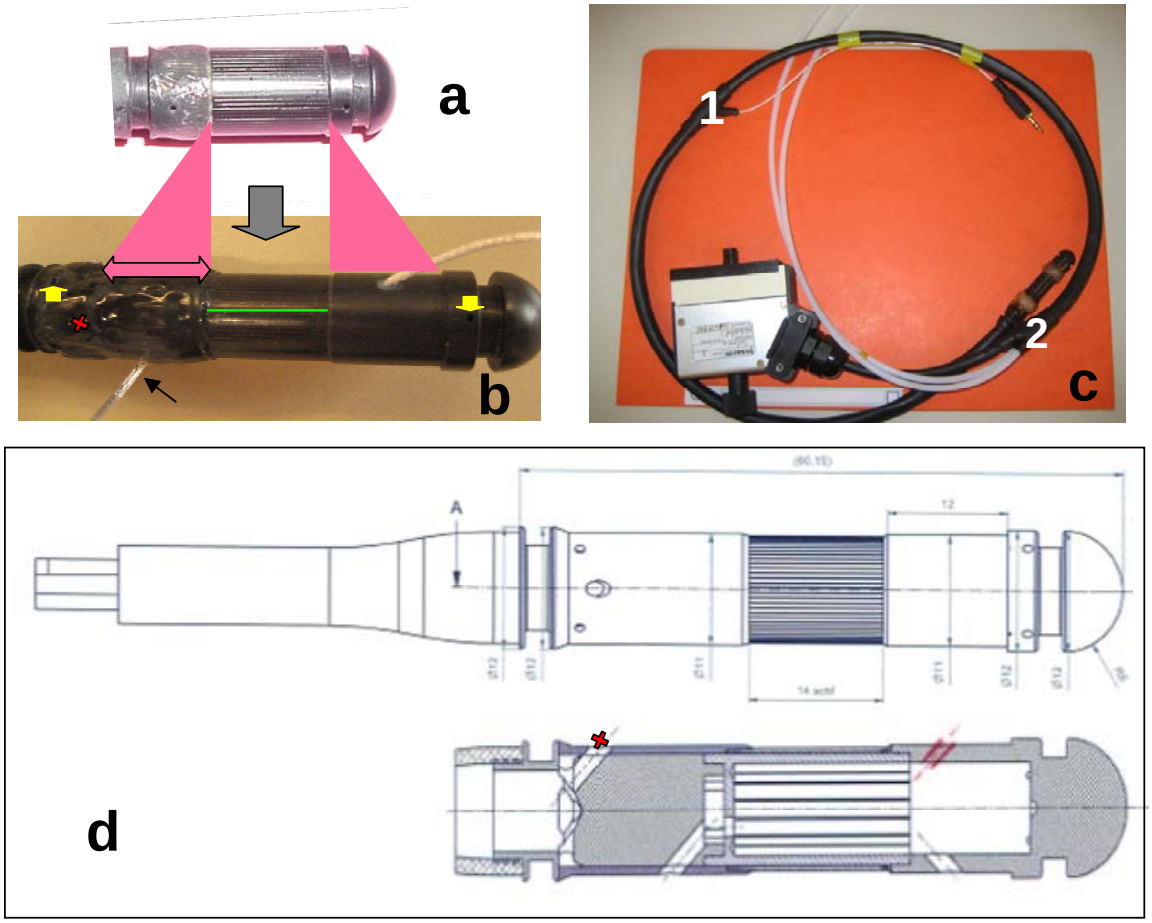

***Figure IV.1**. Head of the 64-element ultrasound applicator (a, b, d) and its general view (c).*
a). Former version of an esophageal ultrasound transducer (without RF coil);
b) and c). Coil integrated version of the esophageal transducer (diameter: 11 mm; working frequency: 5.15 MHz). The surface of a single element (14 x 0.48 mm²) is highlighted with the green line. The yellow arrows indicate the opening (input and output) of the two water cooling pipes, while the red cross marks the opening of the coil cable. The white cable (black arrow) suggests the coil wiring aimed to internally connect the two groups of coil turns. 1: coil cable output (after 45 cm); 2: internal cooling circuit output (after 90 cm).
d). Schematic longitudinal plane of the transducer.

The closed-loop circuit of degassed water aimed to protect the transducer against possible overheating due to intrinsic heating, unexpected reflection, or air bubble formation during sonication. The water cooling circuit could be separated into two parts: one internal and another external. The internal cooling circuit consisted of two 1.2 m-long pipes (1.3 mm ID inside the transducer head, and 1.9 mm ID inside the flexible tube of the transducer). The two thin pipes covered 90 cm inside the transducer and 30 cm outside, where they were connected to the external water circuit. The external circuit was the same as the one used for the rectal transducer (Chapter III): two 7 m-long pipes (Tygon R3603) of 3.2 mm ID ending outside the MR room, in a 1L-water tank, and the peristaltic Masterflex pump (LS 7518-60, Cole-Parmer Instruments Co., Chicago, Illinois, USA) also located outside the MR room. The flow, ranging between 50 and 60 mL/min, was two times higher than the flow of the rectal transducer. However, when the power applied to the transducer was maximal, an ice-bath heat exchanger was inserted on the water cooling circuit in order to diminish the water temperature, initially set at room temperature (20°C). An important constituent of the cooling circuit was the cooling balloon (0.1 mm thick), which covered the active head of the transducer. The balloon ensured the water circulation along the acoustic active surface of the transducer, between the two openings of the internal circuit. The interior surface of the acoustic active region (i.e. its internal solid backing) was cooled by the internal circuit. In addition to cooling, the balloon also ensured the acoustic coupling to the tissue to be treated, and the biocompatibility of the integrated device.

Matching of the electrical impedance. During experimentation, the phased-array ultrasound transducer* was always positioned at the center of the MR scanner, hence, inside the MR shielded room. The drive electronics (the generator and its amplifier) was installed outside the MR room and 64 grounded cables (RG 174) connected it to the transducer, through the RF cage. The total length of the transmission cable (3 m outside and 6 m inside the MR room) was important, and therefore, the electrical impedance matching of the transducer was essential. Only 32 out of the 64 elements of the esophageal transducer were matched, as close as possible, to $(50+0j)\Omega$ at the working frequency of 5.15 MHz, in order to maximize the power transfer. The transducer was assimilated to an electric circuit constituted of a capacitor in series with a resistance. The electrical impedance matching circuit of the esophageal transducer consisted of an inductance connected in series, and a capacitor connected in parallel. The values of the components of the impedance matching circuit were calculated individually, for each element, as follows:

$$C = \frac{1}{2\pi \cdot F} \cdot \frac{\sqrt{Z_R(50 - Z_R)}}{50 \cdot Z_R} \quad \text{and} \quad L = \frac{1}{2\pi \cdot F}[|Z_I| + \sqrt{Z_R(50 - Z_R)}] \qquad \text{Eq. IV.1,}$$

* MR-compatible

where C is the matching capacitor (in μF), L is the matching inductance (in μH), F is the working frequency (in MHz) and $Z = Z_R + Z_I \cdot j$ is the electric impedance of the transducer element before matching. Handmade air coils (copper wire diameter: 0.4 mm; Plexiglas cylindrical support diameter: 10 mm) were used to compensate the reactance. The average values were 203 pF for the capacitor and 4.72 μH for the inductance. This average value of inductance corresponded to 28 winding-loops on the handmade air coil. The MR-compatible impedance matching box, containing the 32 circuits, was positioned 1 m-away from the active part of the integrated device, inside the MR room, as illustrated in Fig. IV.2. Table IV.1 summarizes the impedance values, before and after the matching, for the esophageal transducer (with the 9 m-long cables).

Electrical impedance	BEFORE			AFTER		
	Min	Average ± SD	Max	Min	Average ± SD	Max
Real Z [Ω]	35.2	**45.13** ± 3.8	54.3	57.6	**64.28** ± 4.4	76.6
Imag Z [Ω]	-147	**-138.59** ± 4.87	-131	-8.7	**0.13** ± 4.7	6.6

Table IV.1. Electrical impedance matching of the esophageal transducer.

Electrical calibration of the transducer. The driving electronics (see Fig. IV.2) included a central PC, a 256-channel generator with integrated microcontroller, and its booster. The multi-channel generator (Image Guided Therapy, Pessac, France) provided an independent control of the signal amplitude and phase for each element, and a frequency control per group of 64 elements (bandwidth from 500 kHz to 10 MHz). Since the power gain of the generator only was insufficient at high frequencies, the associated booster permitted to increase the gain by a factor 4. In fact, this booster grouped 4 input channels from the generator and outputted one single channel. Hence, the effective power provided by the generator and its booster reached a maximal value of 8.8 W/element at the working frequency of 5.15 MHz. At this frequency, the new generator could adjust the phase delay with an accuracy of 0.75 ns. The generator was connected to the central PC *via* an Ethernet port. The drivers provided by the manufacturer permitted configuration of the generator settings (frequency, amplitude and phase) and read-out of the delivered electric power (forward and reflected). Due to its capability to update the electronic output signals at 20 commutations per s, with 10 ms latency time, the automatic feedback-loop of temperature control was easily realizable. The latency time for reading the applied power was higher (2 s); however, based on these measurements, the integrated microcontroller automatically turned off any element showing abnormal reflected power. Moreover, the generator could be synchronized with an external input signal (like respiratory gating) which could switch off the generator for an arbitrary period of time. Finally, the homemade rejection filter avoided possible electromagnetic interferences from the transducer activation on the acquired MR signal.

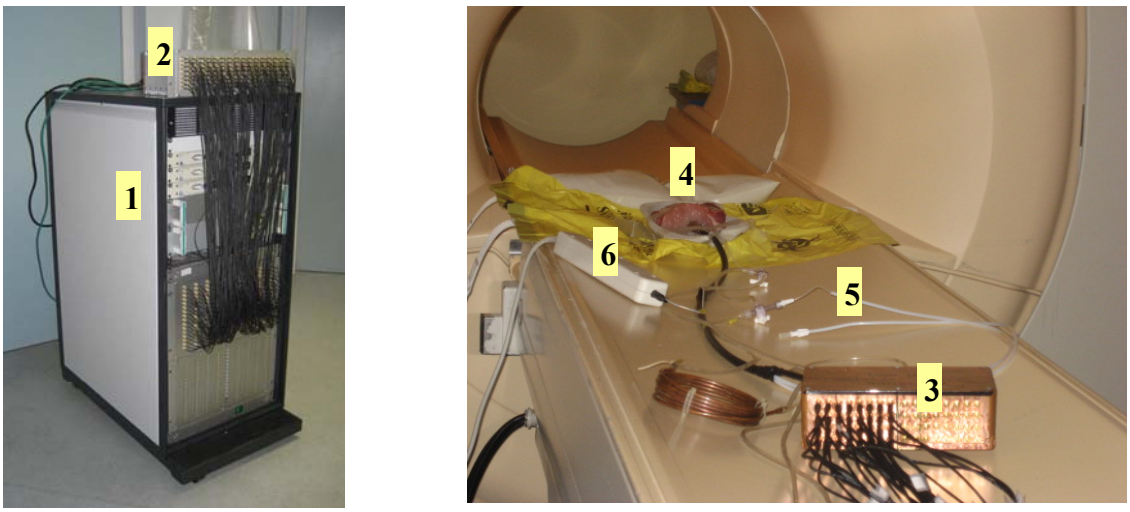

***Figure IV.2.** Electronic setup: **left** - outside the MR room and **right** - inside the MR room. 1: 256-channel generator (here only 128 connected elements); 2: power booster (128 inputs ➔ 32 outputs); 3: impedance matching box (32 elements); 4: esophageal transducer within a muscle sample; 5: water (external) cooling circuit; and 6: coil control standard unit.*

Each element of the esophageal transducer was electronically calibrated in order to associate the delivered electrical power with the internal voltage amplitude (256 levels) defined by the generator microcontroller. The electrical calibration setup was identical to the experimentations performed under MR guidance, i.e. the water cooling circuit and the 9 m-long alimentation cables were used. For calibration, a wattmeter (NAP equipped with NAP-Z7 power head, Rohde & Schwarz, Germany) was inserted on the circuit, at the distal end of the electronic chain, before the matching impedance box of the esophageal phased-array transducer. Four calibration points were considered, representing 25%, 50%, 60% and 70% of the maximal command voltage (U_C) that could be delivered at 5.15 MHz by the generator and its amplifier. The maximal command voltage (100%) was not applied in order to protect the transducer against overheating. A typical calibration curve (effective power as a function of the square of the command voltage) is shown in Fig. IV.3. The effective power intrinsically considered the power attenuation due to the length of the cables. The fitting coefficient, calculated for each of the 32 elements, varied between 6.41 and 8.86 W/V², with an average value of 7.22 W/V². The extrapolation of these results conducted to a maximal effective power of 8.86 W/element. The list of the electric calibration coefficients was further loaded in the program governing the temperature control.

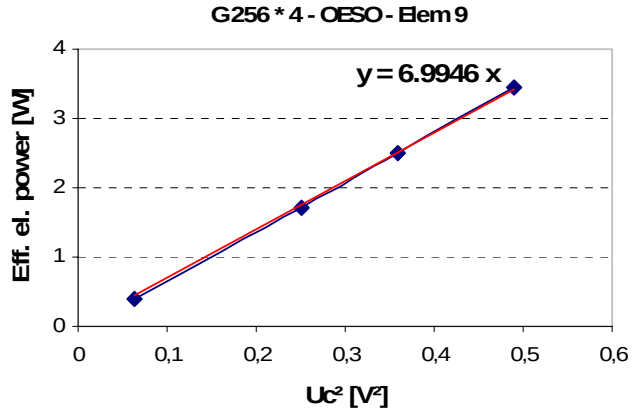

***Figure IV.3.** Example of an electronic calibration curve of one element of the esophageal transducer.*

Acoustic calibration of the transducer. Based on the radiation force balance method (same setup as for the rectal transducer), the electroacoustic efficiency of the transducer and its acoustic calibration were measured. As in the case of the rectal transducer, only 9 random elements were measured. Because an ultrasound beam could be generated by a multitude of elements combinations, it was not possible to measure the exact electroacoustic efficiency for every beam. Therefore, an averaging of 9 random elements was considered sufficient to indicate the general acoustic properties of the transducer. As usually, for preventive reasons, the applied electrical power per element was not set at its maximal value. Note that all measurements were performed considering the electrical power attenuation within the 9 m-long cables.

Table IV.2 summarizes the measured electroefficiency for each of the 9 elements, while Fig. IV.4 presents a typical calibration curve for one of these elements. The fitting coefficient of the curve varied between 4.2 cm^{-2} and 6.5 cm^{-2}, showing a mean of 5.58 cm^{-2}. The higher fitting coefficient corresponded to the most efficient element. Considering the limit of 20 W/cm², under water cooling, defined by the transducer manufacturer and the highest coefficient value, then the maximal electric power that could be applied to one element was 3 W. Since the intensity measurements were performed without the cooling circuit, i.e. without considering the balloon attenuation, it could be concluded that the threshold of the maximal applied power per element was higher than 3 W. The maximal power threshold for the esophageal transducer was lower than for the rectal transducer. This can be easily explained by the smaller size of the elements of the esophageal transducer. One element of the esophageal transducer was 0.06 cm², while the corresponding rectal element was double (0.12 cm²). The electroacoustic efficiency of the esophageal transducer (37.3% at 2.2 W) was slightly inferior to the rectal one (44.7% at 2.7 W).

Element	Eff. el. power [W]	Ac. intensity [W/cm²]	Electroac. efficiency %
1	2.22	10.69	32.33
2	2.26	9.52	28.25
3	2.26	13.15	39.04
4	2.25	12.52	37.38
5	2.26	12.79	38.05
6	2.18	12.75	39.17
7	2.22	12.81	38.75
8	2.24	13.15	39.31
9	2.30	14.92	43.60
Av. ±SD	**2.24 ± 0.03**	**12.47 ± 1.54**	**37.32 ± 4.46**
Precision of measurement	± 0.13	± 1.81	± 2.4

***Table IV.2.** Electroacoustic efficiency for 9 elements of the esophageal transducer, measured using the 9 m-long cables and without the cooling circuit.*

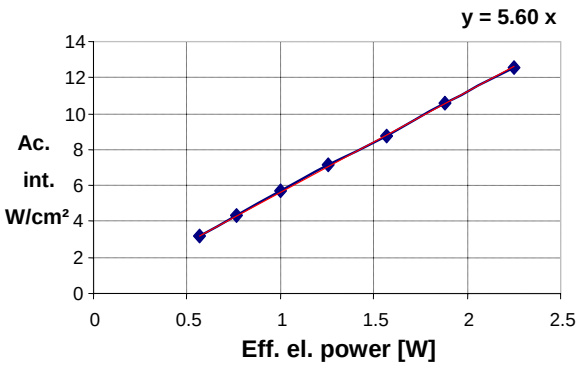

***Figure IV.4.** Typical acoustic calibration for one element of the esophageal transducer.*

Cooling balloon attenuation measurement. The same balance technique was used to measure the attenuation of the acoustic intensity through the cooling balloon (see Fig. IV.5), by comparing the delivered intensities, for the same element, without/ with the balloon. The balloon was inflated at similar dimensions as during MR experiments. Two types of cooling balloon (0.1 mm-thick) were tested: type 1 (Synsation^{TM} PF-Vinyl, Ansell Health-care, Brussels, Belgium), and type 2 (Laboratories Euromedis, Neuilly-sous-Clermont, France). The "type 2"-balloon was more extensible and therefore was used for the esophageal transducer, while the first type covered the rectal transducer head. The acoustic intensity was attenuated by 16.26 ± 2.35 % (first type of balloon), and by 13.9 ± 2.01 % (the second type). The corresponding curve fitting coefficients were: 5.74 (without balloon), 4.68 (type 1) and 4.88 (type 2). These results were obtained at the working frequency of the esophageal transducer (i.e. 5.15 MHz), with an applied effective power of 2.27 W/ element.

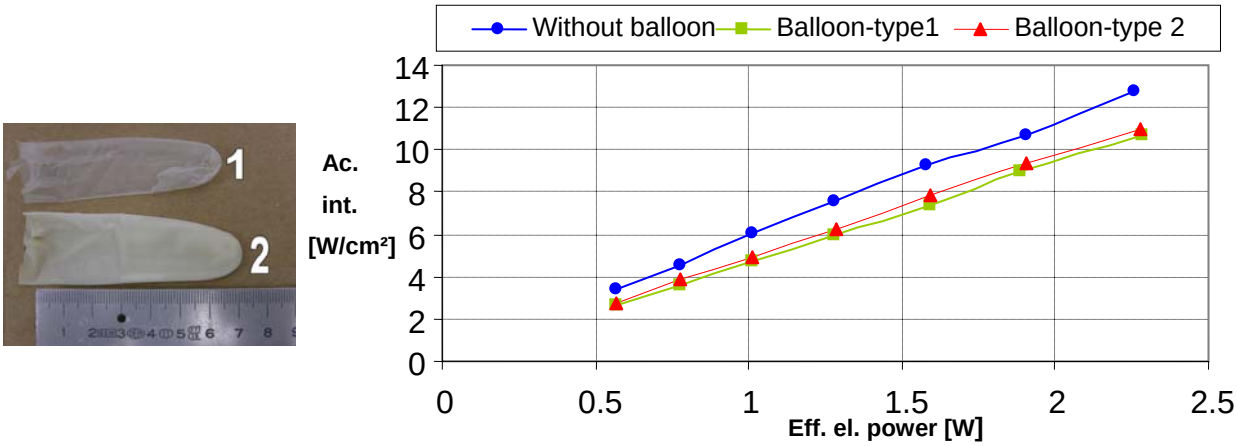

Figure IV.5. Acoustic intensity attenuation through the balloon for the esophageal transducer.

IV.2.2 Opposed-solenoid RF coil

Coil prototype: 1 turn versus 3 turns. The RF coil integrated with the esophageal transducer was built using the same coil geometry as for the rectal transducer, but adapted to the reduced dimensions of the esophageal transducer. Therefore, tests were again conducted in order to define the type of wire and insulation which offered the best compromise between reduced sizes and good quality-factor of the coil (see Fig. IV.6). Moreover, high MR-compatibility was required for all components of the coil. This requirement limited the choice of material and affected the coil performance. The most evident example of limitation was the cable connecting the coil to its standard unit, which performed the active tuning and matching of the coil during experiments.

Figure IV.6. Diverse wiring tested in order to define the prototype esophageal coil.

The cable used for the rectal coil (2.45 mm in diameter) was too large for the tunnel hosting this connecting cable (diameter of 1.2 mm). Therefore, a smaller cable of 1.1 mm in diameter was used for the esophageal transducer, but its drawback was that it halved the Q-factor of the coil compared to the higher diameter cable. Note, however, that the connecting cable was set at $\lambda/4$ at 63.9 MHz, i.e. a 63 cm length for the smaller diameter cable. For the same reason (physical size) the coil wiring was made of copper only, without PTFE-coating as for the rectal coil.

Before defining the esophageal coil final prototype which used the transducer as wiring support, a comparative study was conducted to determine the number of turns needed for the best performance of the coil. For that purpose, two coils with 1 turn and 3 turns were built (see Fig. IV.7). The turns number was chosen keeping in mind the results obtained with the rectal coil. In that case, 5 turns of 20 mm-diameter induced large dielectric losses in such manner that the 1-turn coil was preferred to the 5-turn coil. For the present design, 3 turns of 11 mm-diameter are expected to induce less dielectric losses and may be better than the 1-turn coil. The support of the

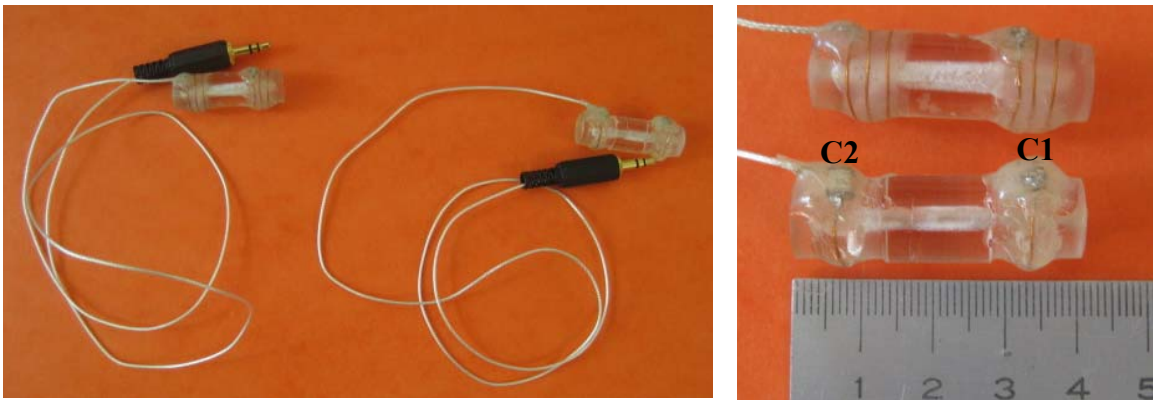

***Figure IV.7.** Esophageal RF coils: single-turn versus 3-turn coil. **Left**: general view (coil, connecting cable, and its connector); **Right:** coil head (turns and capacitors).*

esophageal coils was a Plexiglas solid cylinder which exactly copied the transducer dimensions regarding the coil holder: 4 cm-long and 11 mm in diameter. A tunnel was built inside the solid cylinder, at the same position and with same diameter (1.2 mm) as the tunnel existing within the transducer head. This tunnel permitted internal connection of the two groups of turns (see Fig. IV. 7). Therefore, no acoustic window (see Chapters II and III) was necessary, since this configuration permitted a truly 360° field aperture. The copper wire (diameter 0.4 mm) and the capacitors were sealed with resin (Epoxy Adhesive, RS components, Corby, UK). The two non-magnetic capacitors (see letters C1 and C2 in Fig. IV.7) realized an initial static RF tuning and matching of the coils, for a frequency range from 63.0 to 63.5 MHz. The 63 cm-long coaxial cable of 1.1 mm-diameter connected the coil to its electronic standard unit. As explained before, the coil control standard unit dynamically tuned (at 63.9 MHz) and matched the coil, during the MR examinations.

Coil	C1/ C2 (pF)	Loading environment	Frequency [MHz]	Quality factor, Q	Real Z [Ω]	Imag Z [Ω]
1-turn coil *(without transducer)*	138.6/ 220	Air	63.25	33.1	75	-205
		Water	63.25	31.6	73	-201
		Tissue	63.15	27.2	73	-198
3-turn coil *(without transducer)*	27.5/ 56	Air	64.55	51.6	484	-377
		Water	63.45	48.4	91	-246
		Tissue	63.15	30.2	120	-217
3-turn integrated coil	22.7/ 56	Air	64.2	37.7	177	-233
		Water	63.75	30.6	50	-123
		Tissue	63.2	**26.3**	81	-150

Table IV.3. Electrical static parameters of the esophageal coils.

The same setup as previously described in Chapter II was used to measure the static RF parameters, in air, water, and tissue. The capacitors values and the static RF parameters for the esophageal coils built in this chapter are listed in Table IV.3. Each coil should have, in tissue, a Q-factor of at least 30 units and a frequency between 63.0 and 63.5 MHz. Only this tissue-loading environment is important for further MR experiments. The other loading environments demonstrated the parameters variation (see Fig. IV.8) and helped me to design the coil, before insulating it. Both frequency and Q-factor decreased with the loading environment, from air to tissue, having their minimal values in tissue. The Q-factor values reported here were the smallest for all coils built in this thesis, due to the bad quality of the connecting cable of 1.1 mm-diameter. Contrary to the observations made in Chapter III, the multi-turn coil showed here a better Q-factor than the single-turn coil, even when full-loaded (i.e. in tissue). However, this initial finding needed to be confirmed by the MR experiments.

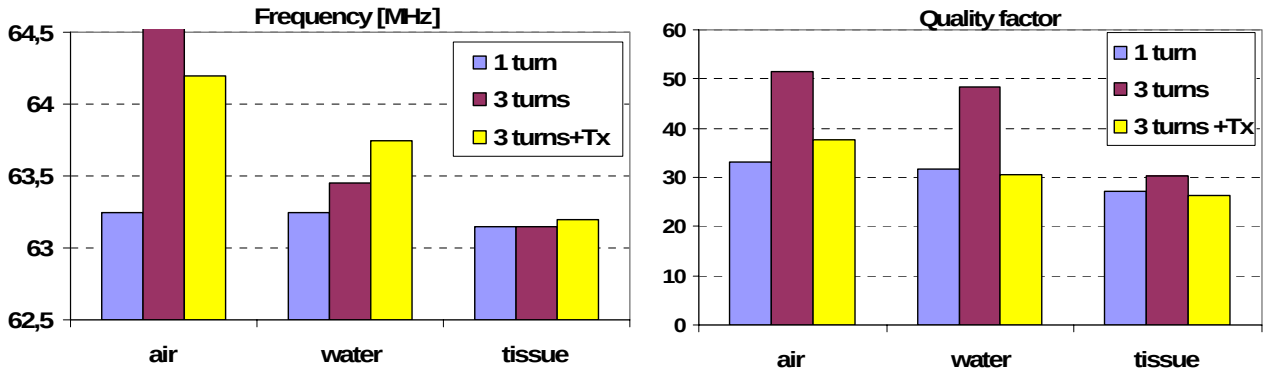

Figure IV.8. Influence of the number of turns and of the transducer on frequency & Q-factor of the esophageal coils, for air, water and tissue loading media.

RF coil integrated within the phased-array transducer. Based on the former results, the 3-turn configuration was chosen to be the final prototype integrated with the transducer (see Fig. IV.9). An isolator scotch band was interposed between the turn-holder part of the transducer and the coil turns. The goal was to avoid the direct sealing of the coil on the transducer, and furthermore, to permit an eventual dismantling of the coil. The internal tunnel permitted a complete geometrical splitting* between the coil and the acoustic active surface, which enabled the activation of all elements of the transducer. Thus, the limitation observed for the former rectal coils was overcome. Table IV.3 and Fig. IV.8 summarize the RF parameters of the integrated coil, and compare them with the non-integrated coils. In tissue, the Q-factor of the integrated coil (with the transducer) was almost equal to that of the 1-turn coil (without transducer). Moreover, the influence of the transducer on the coil performance was easily detectable by comparing the integrated coil with the 3-turn coil (without transducer). The drawback brought by the transducer presence was a reduction of the Q-factor (in tissue) by 4 units (~13%), but only the MR experiments will show the real effect of the transducer on the coil performance.

***Figure IV.9.* Opposed-solenoid RF coil integrated within the phased-array esophageal transducer (without and with the cooling balloon).**

IV.2.3 Thermometry treatment planning

Algorithm description. A pre-operative planning of the thermal dosimetry is mandatory for a successful ultrasound therapy. Therefore, a model estimating the temperature and thermal dose delivery was developed with respect to the rectal ultrasound transducer. The two activation modes of the transducer (planar or focused) were studied. The simulation was performed for the axial plane, generally used in the MR thermometry. In-house written software (Matlab 6.5 and Visual C++ 6.0) was implemented on a standard PC (Dell Precision PWS 670, CPU 3.2 GHz, 1GB RAM) running under Windows XP 2002.

The physical model investigated the best approach for treating tumors of various forms. The objective was to determine the heating sequence which permitted the best matching between the delivered thermal dose and a user-defined tumor. The model was based on the interleaved

* The acoustic active zone lay between the two groups of turns, without any superposition (on the external face of the transducer) with the coil wiring.

multi-beams, activated with constant power, but for different duration. The sonication time for each beam corresponded to the tumoral thickness measured in that specific direction.

Initially, a magnitude MR image (see Fig. IV.10.a) was loaded. The ultrasound transducer (P), the cooling balloon (B) and the tumor (T) were individually selected on this experimental image. The tumor was randomly defined within the muscle sample. The phased-array transducer, positioned in the center of the image, had a 360° ultrasound aperture. The emitted ultrasound beams traversed two different media: one non-absorbing (the balloon) and one absorbing (the user-defined tumor).

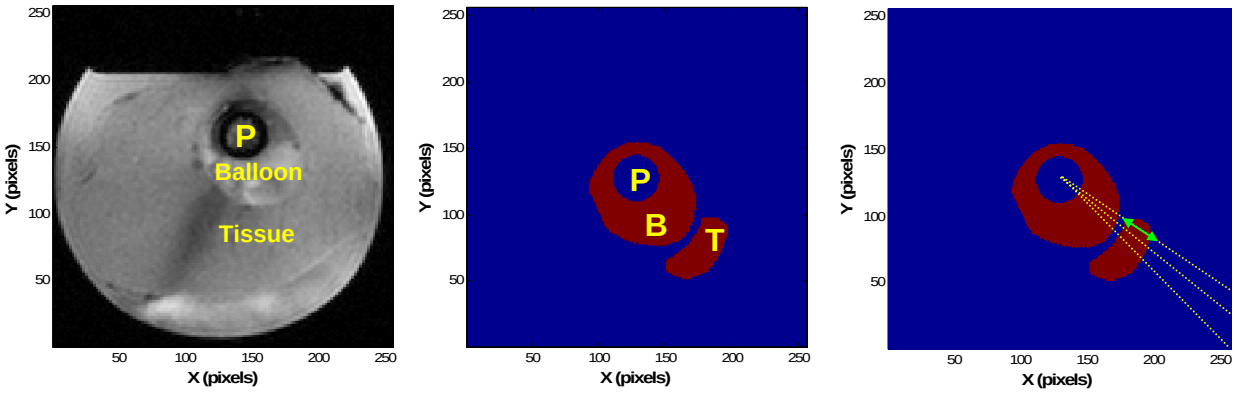

Figure IV.10. ***The magnitude image acquired with the thermometry sequence, axial plane (a), (PRFS-EPI, FOV: 96 mm, 2 s/dyn, voxel: 0.75 x 0.75 x 8 mm^3) used as background for the selection of the ROIs. (b): the transducer P, the balloon B, and the user-defined tumor T. The angular grid (c) characterized the tumor geometry. The green arrow indicates the tumor thickness along one direction of sonication. The spatial resolution of numerical simulation was 0.375 mm.***

In order to characterize the defined tumor, its geometry was divided into an angular regular grid (5.625° step) corresponding to the directions of sonication available with the 64 elements phased-array geometry of the transducer. This segmentation of the tumor geometry permitted the definition of three sonication parameters (see Table IV.4): the number of beams needed to cover the width of the tumor; the orientation of beams (which elements of the transducer were activated); and the tumor thickness along each direction (see the green arrow in Fig.IV.10.c). The precision of the thickness measurements was ±0.375 mm, i.e. the in-plane spatial resolution. Furthermore, this tumor thickness was associated with the duration of sonication for each beam "i":

$$duration\ (i) = \exp(\alpha \cdot f \cdot thickness\ (i)) \qquad \text{Eq. IV.1}$$

where the frequency f was 3.57 MHz, and the attenuation coefficient α was set to

Total beams	Beam orientation (elements)	Tumor thickness (mm)	Calculated duration (s)	Approx. duration (s)
9	50 (46-53)	13.12	1.19	1.0
	51 (47-54)	13.75	1.20	1.0
	52 (48-55)	16.87	1.29	1.5
	53 (49-56)	16.87	1.29	1.5
	54 (50-57)	16.12	1.27	1.5
	55 (51-58)	14.62	1.23	1.0
	56 (52-59)	13.50	1.20	1.0
	57 (53-60)	12.75	1.18	1.0
	58 (54-61)	8.12	1.11	1.0

Table IV.4. ***Example of sonication parameters calculated in function of the tumor geometry.***

an average value correlated with the *ex-vivo* experiments (α =0.06 MHz·(Np/cm)). The isotropic diffusion coefficient was 0.14 mm²/s. The incremental step for temperature and thermal dose calculation was set at 0.5 s. Therefore, the calculated sonication time per beam needed to be approximated by an entire multiple of 0.5 s. The same level of effective electrical power (40 W /beam) was delivered to each beam. This initial part of the numerical simulation determined the primary sonication-sequence to be implemented: number of beams, orientations, electric power and time sonication for each beam. The Table IV.4 shows the sonication sequence (9 beams) corresponding to the tumor defined in Fig. IV.10.b. The orientation of beams, here varying from 50 to 58, as seen by Matlab, was based on a trigonometric numerotation, with the direction no.1 placed in the first quadrant. The numbers in parenthesis represent the constituting elements of the transducer to be activated in order to form each specific direction of sonication, i.e. each beam.

The next part of the simulation (acoustic field-, temperature-, and thermal dose calculation) decided how many repetitions of the primary sonication-sequence were necessary to treat the defined tumor. After each application of the sonication sequence, the superposition between the target region and the thermal dose was compared. The treatment was considered finished when a good correlation between these two parameters was observed. At the end of the treatment, the total sonication time and the accuracy of the correlation were determined.

The pressure acoustic field for one element of the rectal transducer was calculated using the Rayleigh integral, for a radius of 48 mm [Salomir *et al*, 2009]. This acoustic field radius, half of the FOV of a typical MR image, was considered sufficient. The spatial resolution was set to 0.375 mm. The acoustic field computation was performed using polar coordinates. The reason of this choice was the rapidity and easiness of the mathematical operations (a rotation in Cartesian coordinates is a matrix shift in polar coordinates). However, the final form of the acoustic field was in Cartesian coordinates as needed for the thermometry calculation. For that, an extra FOV was considered to permit a correct transformation from polar to Cartesian, generating a total computing FOV of 105 mm. Figure IV.11 summarizes all stages of the acoustic field computing.

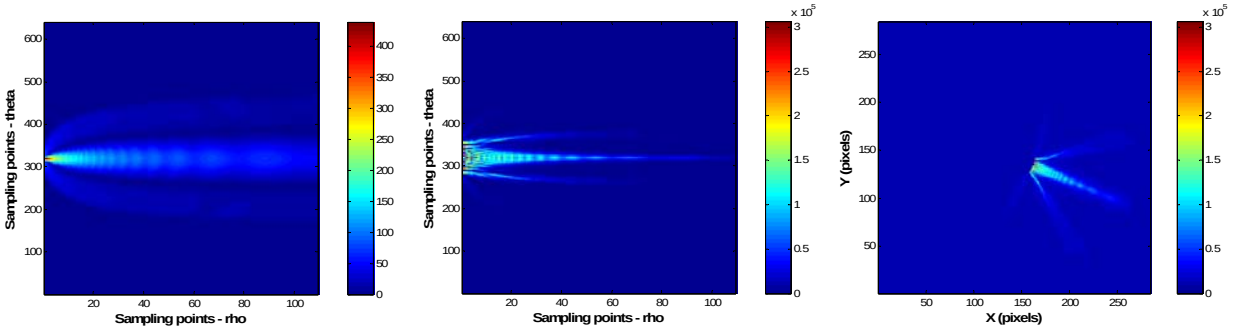

Figure IV.11. Acoustic field, FOV: 105 mm. a). Pressure field of one element (polar coordinates, colorbar in kPa). Intensity field of 8 elements (one beam, plane wave, colorbar in W/m²) in polar coordinates (b), and in Cartesian coordinates (c).

As explained in Chapter III (section 2.3), the temperature was calculated using the Fourier transform solution of the BHTE. Border condition (cooling balloon) was taken into account with a balloon mask which "cooled" the temperature inside the balloon, for each new increment step. Furthermore, the cumulated thermal dose was expressed in equivalent minutes at 43°C, as defined by Sapareto and Dewey [1984]:

$$TD = \int_0^t 2^{T(t)-43} dt \qquad \text{Eq. IV.2,}$$

where $T(t)$ was the temperature at time t. Note that the thermal dose was calculated only for temperature > 43°C. The necrosis threshold was considered reached at 240 minutes at 43°C. The simulated temperature and thermal dose maps corresponding to the defined tumor (Fig. IV.10.b) are presented in Fig. IV.12.

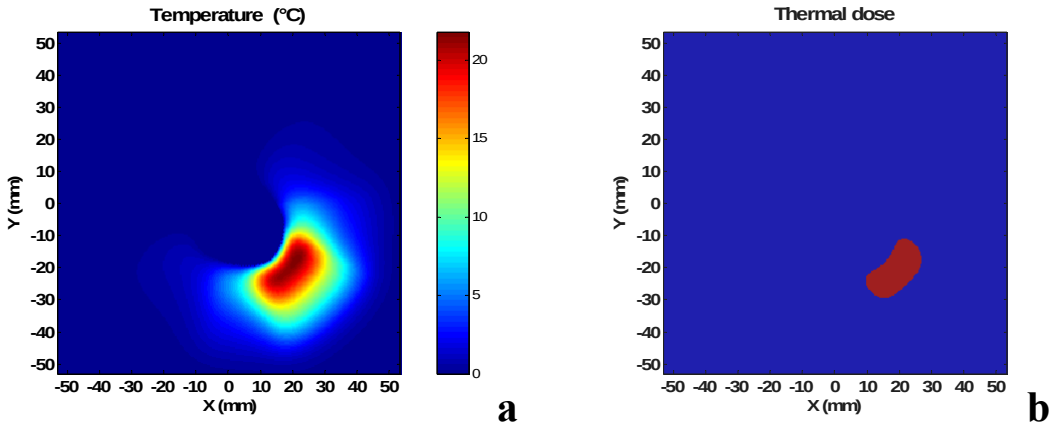

Figure IV.12. ***Temperature (a) and thermal dose (b) calculated at the end of the experiment. FOV was 105 mm. Temperature legend was expressed in °C. Thermal dose was segmented at a value of three times the necrosis threshold.***

Simulation results. The necessary computing time for the tumor defined in Fig. IV.10.b (surface of 2.5 cm²) was about 3 minutes. This short computing time is compatible with an in-situ planning of the dosimetry. The treatment planning was defined as follows: 1) 9 sonication beams (plane wave, max. electrical power); 2) 27 repetitions of the sonication sequence until the end point was reached; and 3) a total sonication time of 216 s. A good correlation was observed between the tumor and the thermal dose (see Fig. IV.13). The error (both under- and over-treatment) represented less than 10% of the tumor size. The proximity of the cooling balloon, with a water temperature of 0°C, induced an undertreated region in the particular case of a tumor seated close to the digestive wall (see the blue color in Fig. IV.13).

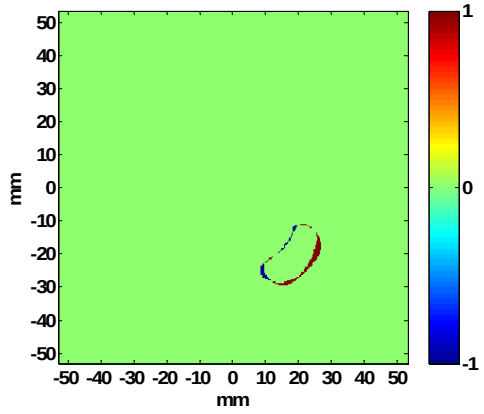

Figure IV.13. ***Difference between the defined tumor and the thermal dose. Blue color - undertreatment; red color - overtreatment.***

The next study investigated the best choice of sonication sequence for another defined tumor (1.8 cm²). The planar and convergent beams were compared, together with the best modality of activating the beams. Two modalities of beam activation were investigated. The first idea considered a successive activation of the beams. For example, if considering a 6-beam sequence then the repetition of the primary sequence should be 123456/ 123456/ etc. The second idea was an alternative activation of beams (left/right, beginning from the tumor center), i.e. 642135/ 642135/ etc. The focal distance was different for each beam, depending on the tumor thickness. Each beam was focused closely to the distal tumor border, at a distance equal to tumor thickness minus 2 mm. The simulated data presented in Fig. IV.14 suggested the successive plane wave approach (d) as the best choice (see also Table IV.5).

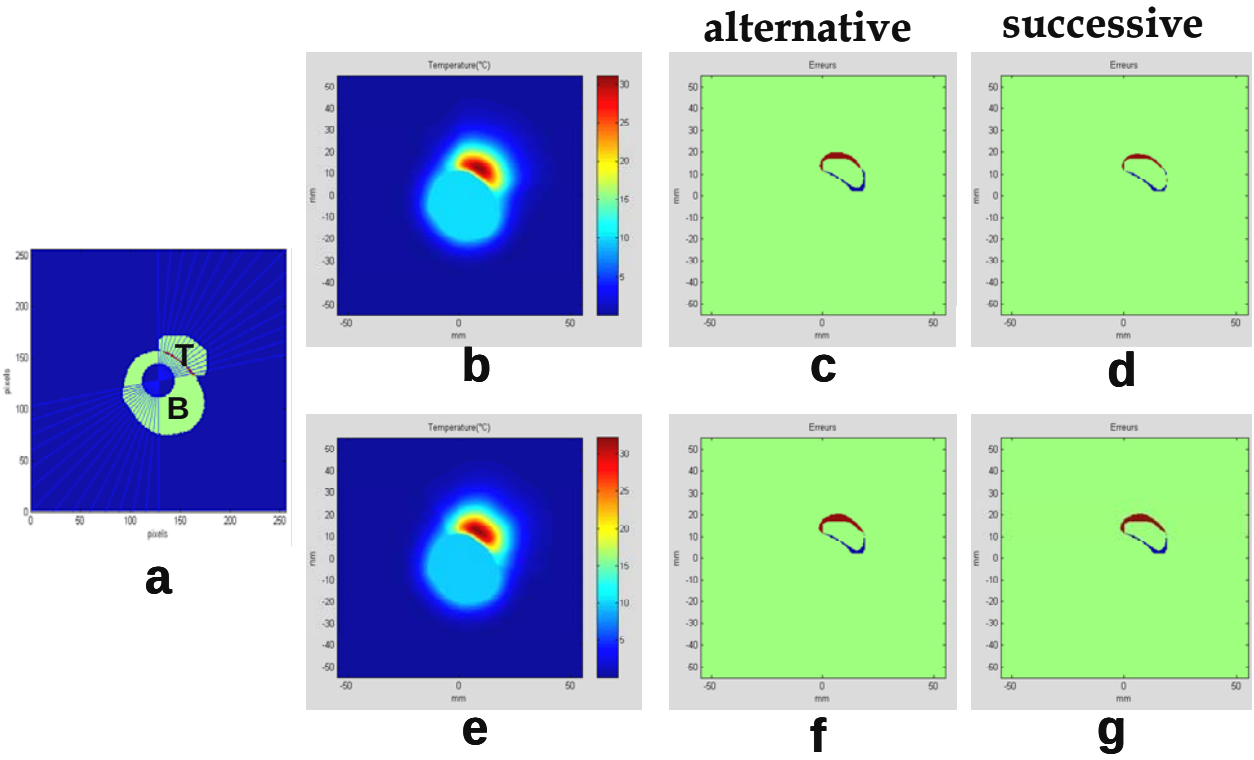

***Figure IV.14.** Choice of the best sonication sequence for the tumor defined in a): plane wave (b, c, d) versus focused wave (e, f, g). Simulated temperature (b and e) and treatment error (c, d, f, g), with undertretment (blue color) and overtreatment (red color). The temperature of the cooling balloon was set to 10°C.*

	N_beams	N_repetitions sonication sequence	Sonication time [s]	Error (under.) [mm²]	Error (over.) [mm²]	Computing time [s]
Planar, alternative	15	7	144	27	43.4	191
Planar, successive				**18.4**	**31.4**	191.5
Focused, alternative		8	154	24.5	54.3	195
Focused, successive				17.5	42.3	197

***Table IV.5.** Sonication parameters and treatment accuracy for the same tumor using 4 different sonication strategies.*

In both cases of user-defined tumor presented here, a layer of undertreated tumor was observed close to the cooling balloon. This may be a serious problem, especially when the purpose of the treatment is purely curative. Ideally, the temperature of the water inside the cooling balloon should be minimal, e.g. 0°C, in order to protect the active part of the transducer from overheating. But, this low water temperature generates the undertreated region, and the volume of untreated tumor depends on the cooling water temperature. Since the correct functioning of the transducer without the cooling circuit is not possible, this undesired effect may be only limited. For that purpose, the temperature of the cooling water should be increased. A water temperature of 10°C (see Fig. IV.14) still induced a thin layer of undertreated tumor. Remember, however, that this region is only undertreated, not untreated, since the thermal dose covering the treated region was 3 times higher than the necrosis threshold defined by Sapareto and Dewey [1984]. Moreover, in clinical conditions, safety margins of the tumor are defined to ensure the complete destruction of the tumoral mass. Such safety margins were not considered in these simulations. On the other hand, such endocavitary tumors may be treated by impeding the blood supply of tumoral cells. This assumes that complete necrosis of distal borders of the tumor isolates the tumor from its blood supply and may indirectly induce its death [Cranston *et al*, 2006]. In this case, the inner undertreated layer could be considered inoffensive. This assumption needs however to be validated experimentally.

IV.2.4 MR data acquisition and processing

MR system and experimental setup. All MR experiments were performed using the same clinical scanner (Achieva 1.5 T, Philips, Best, the Netherlands) previously presented (see Chapters II and III). MR shimming was performed for all acquisitions. The DRIN interface of the scanner permitted the export, in real time, of the MR data (magnitude and phase images). Total latency including reconstruction, data transfer, calculation of the thermal map, and display was estimated to be less than 200 ms per acquired data volume. The majority of experiments were acquired using the integrated coil. The SFB coil (4 elements phased-array standard coil) acquired only the initial survey image and some thermometry images (without sonication) for comparison between the integrated and the extracorporeal coils. The coils were alternatively plugged in, in order to avoid any possible interaction between them during acquisitions.

The normal operating position of the ultrasound device was parallel to the Bo field (see Fig. IV.2), as it would be in the case of clinical application. Morphological images (T_1-w) were centered either sagittally or axially on the transducer, while the imaging slice for thermometry images (PRFS method, EPI sequence) was generally axial*. The morphological images (all three

* Transverse plane, orthogonal to the longitudinal axis of the ultrasound transducer and parallel to the acoustic beam.

planes) helped to optimally position the thermometry slice (i.e. centered on the acoustic beam, guarantying the most extended pattern). The thickness of slice was 5 mm, which represents 35% of the active length of the transducer and therefore the longitudinal heat diffusion could be neglected.

***Ex-vivo* experiments.** Three important experimental goals were investigated *ex-vivo,* on fresh porcine muscle, immersed in degassed water: the performance of the integrated coil; the stability and the precision of the PID controller; and the multi-beam sonication strategy.

The coil study was interested in the absolute performance of the integrated coil, but also in its relative performance to others coils. Therefore, the comparative study of the esophageal coils focused on three directions: 1 turn *versus* 3 turns; integrated *versus* extracorporeal; and 3-turn coil (without transducer) *versus* transducer integrated coil.

The multi-beam approach (interleaved activated beams) represented the standard procedure for the treatment planning of tumors. Hence, an important objective was to experimentally validate this treatment strategy. Moreover, the safety of the procedure was verified with control points of the temperature, positioned at the distal borders of a user-defined tumor. A generalization of the PID controller was then realized in order to exploit this treatment approach. Multiple controllers (as many as the number of beams) calculated, in parallel, the needed power/beam, for the specific control points defined for each beam.

A typical thermometry experiment had about 100 dynamics, differentiated into three parts: preheating (~5% of time), heating (~70% of time) and cooling period (~25% of time). An average over the first dynamics of the preheating period formed the reference phase-map demanded by the PRFS technique. However, the number of dynamics could vary up to 210, for example, if a large surface needed to be treated or if a high temperature-rise (say more than 30°C-rise) was required. Otherwise, as explained in Chapter II, section II.2.3, only 30 dynamics were acquired during no-sonication experiments, in order to calculate the accuracy of the temperature measurement (the SDT), for the coils comparison. No spatial averaging of MR data was performed in any experiment. The mean temporal resolution for thermometry images was 2 s/dyn. The multi-beam activation sequences were acquired with a lower temporal resolution (3.96 s/dyn). Note that the "dead time" between two interleaved beams was of the order of 10 ms. The thermometry slice thickness (5 mm) was almost equal to the width of the active surface of one beam (here 4.4 mm). The PID temperature controller was activated by the same procedure explained previously (Chapter III, section 2.3), and included now the multi-point generalization. The precision of the temperature controller was studied for a temperature elevation of 10°C or 15°C, for the plane wave configuration. The PID performance was investigated for single, two and three beams at control points located at 7.5 mm, 5.5 mm, and 3 mm from the transducer. The absorption was set to $0.08\,°C/(W \cdot s)$, while the diffusion was 0.05 mm²/s.

Table IV.6 summarizes the MR acquisition parameters and sequences, and their purpose, for all experiments presented in this chapter.

	Application	Sequence/ technique	FOV [mm²]	Voxel [mm³]	TE/TR [ms]	Flip Angle [°]	Lines /TR	Acq./recon. matrix	Acq. Time [s]
Ex - vivo	**MR-compatibility of the transducer**	**T_2-w**-TSE/ SE	96x96	0.43x0.43 x2.5	100/ 1000	90	21	192x189 224x224	38
	Coils comparison ▪ 1/ 3 turns ▪ Int./ext. ▪ Intern coil (with/without transducer)	**T_1-w**-TFE/ GE	128x128	0.5x0.5 x5	6.9-7.2 /200	40	24	256x240 256x256	56
		PRFS/GE-EPI (30 dyn)	96x96	0.75x0.75 x5	21/180	45	11	128x121 128x128	2
	Integrated coil (best performance)	**T_1-w**-TFE/ GE	80x80	0.31x0.31 x5	10.6/200	40	24	252x240 256x256	56
		PRFS/GE-EPI (30 dyn)	80x80	0.63x0.63 x5	17.5/180	45	11	128x121 128x128	2
	PID, Multi-beams	**PRFS**/GE-EPI : 100, 150, 210 dyn – MR parameters identical to the previous row							
	Thermal therapy	**PRFS**/GE-EPI (100, 120 dyn)	80x80	0.63x0.63 x5	17.5/360	45	11	128x121 128x128	3.96

***Table IV.6.** MR acquisition parameters for all experiments (esophageal transducer).*

IV.3 Experimental results

MR compatibility of the integrated device. Spin-echo morphological images (see 1st row of Table IV.6), acquired with the external coil, tested the MR compatibility of the esophageal transducer, before building the integrated coil. RF artifacts induced by the metallic structure of the transducer were seen at its basal part and close to its acoustic active zone (see arrows on Fig. IV.15). However, their effect was not important since it appeared only within the cooling balloon, and out of the target regions. The integrated coil brought no RF artifact, but added a susceptibility artifact. The coil constitutive elements were highly MR-compatible. The coil susceptibility artifact (see Fig. IV.17.d.3) was due to an isolator tape, scotched on the two parts of the transducer aiming to host the coil turns. This coil artifact was also outside the ultrasonic target region.

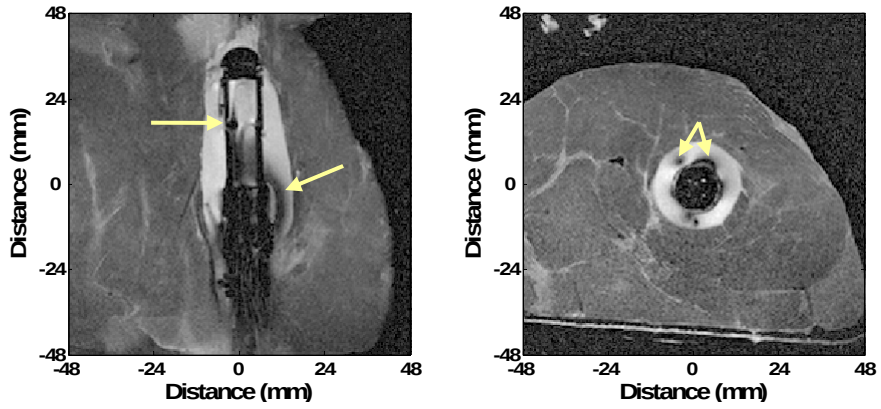

***Figure IV.15.** RF artifacts (see arrows) induced by the esophageal transducer, before the coil integration. T_2-w-TSE images (sagittal and axial planes), acquired with the external coil, in ex-vivo muscle. FOV: 96 mm, 1 voxel: 0.43 x 0.43 x 2.5 mm³.*

IV.3.1 Comparative study of the coils

Comparative study of the coils. The complete integration of the coil within the esophageal transducer showed some advantages. The coil sensitivity field became completely circular (see Fig. IV.16 and 17, axial plane), without showing the typical distortion observed with the rectal coils. The "shadow regions" of zero signal were observed in the sagittal plane only, and

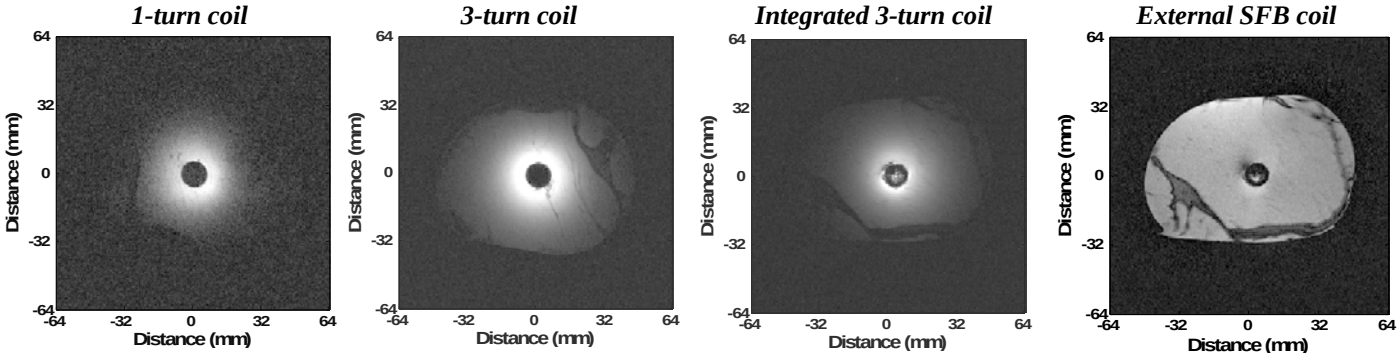

***Figure IV.16.** Comparative study of esophageal coils: anatomical images (T_1-w-TFE, see the 2nd row of Table IV.6), axial plane, ex-vivo muscle, 1 voxel: 0.5 x 0.5 x 5 mm^3, FOV: 128 mm.*

were associated to the coil wiring. Figure IV.17 shows the results of the thermometry comparative study of the esophageal coils (see the third row of Table IV.6 for MR data). The images acquired in both axial and sagittal planes showed same performance of the coils. This equivalence demonstrated the stability and reproducibility of the images acquisition. Also, the SDT maps acquired in the two planes illustrated the 3D sensitivity field of the coils. The sensitivity field of the integrated coil is composed of three sensitivity regions disposed along the longitudinal plane of the transducer (see sagittal planes). The central spherical sensitivity field corresponded to the active acoustic zone. The susceptibility artifacts of the endoscopic device were visible in the sagittal plane (see Fig. IV.17.d, 3rd and 4th columns).

The best coil was the 3-turn coil mounted on the solid plastic support. The 1-turn coil and the SFB external coil showed similar performances. For the esophageal transducer-case, more turns means more signal. Compared to the 1-turn coil, the 3-turn coil improved the accuracy of the temperature measurement (the SDT) by a factor of 3.3, measured at 5 mm-depth from the balloon.

The influence of the transducer was observed by comparing the 3-turn coil with the integrated coil (see 2nd and 3rd columns). The sensitivity of the integrated coil was reduced by a factor 1.3 (at 5 mm) and by a factor 1.2 (at 10 mm). In practice, this means a difference of ~ 0.5 mm for the limit of 1°C of the sensitivity field (15.75 mm versus 15.37 mm). This difference became more important when considering the 0.5°C-limit (11.25 mm versus 8.62 mm). Note that these sensitivity depths were calculated along one direction, away from the balloon surface. Therefore, they represented the radius of the circular sensitivity field of the coil and not its diameter.

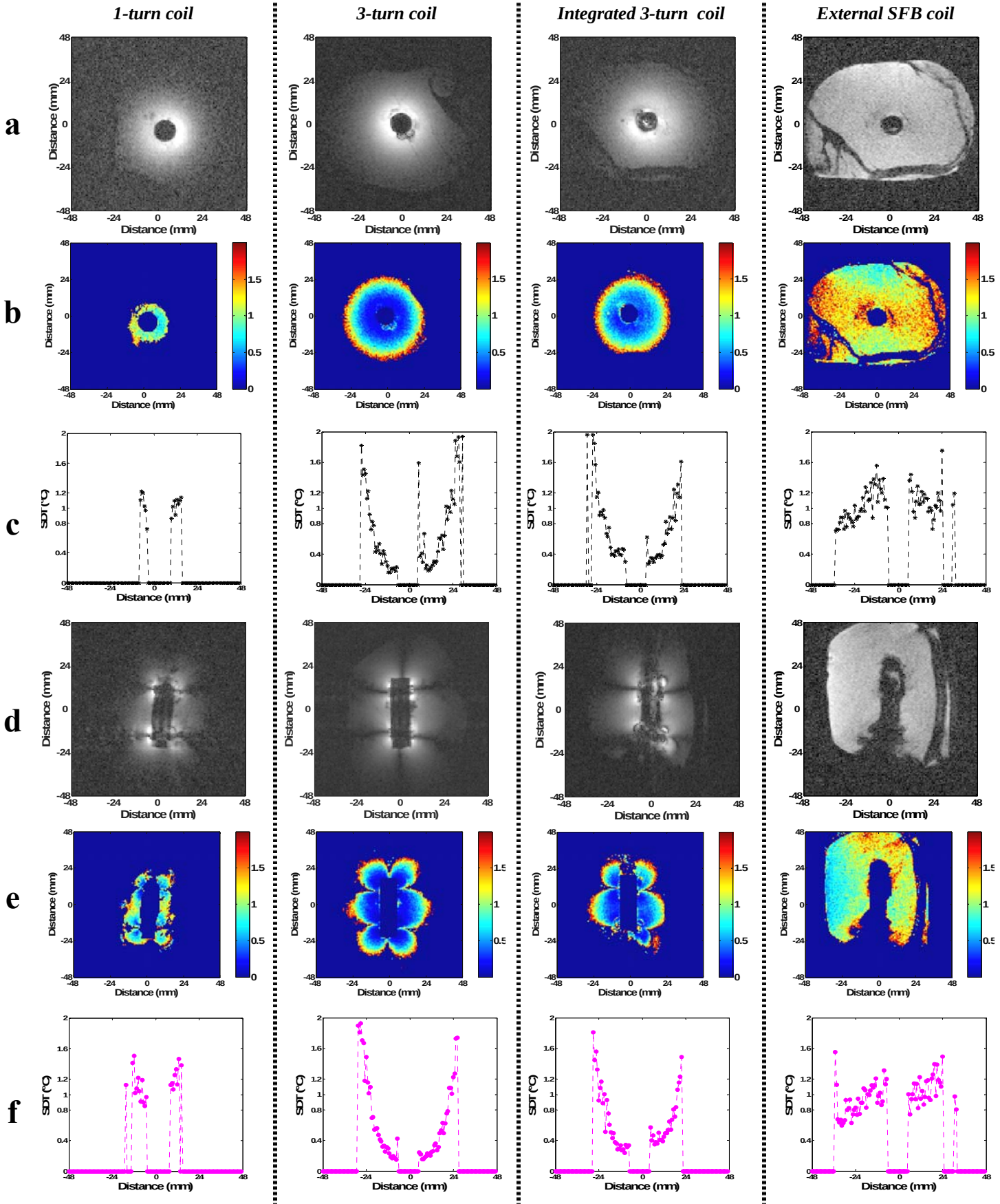

Figure IV.17. ***Comparative study of esophageal coils: turns number (columns 1 vs. 2), transducer influence (columns 2 vs. 3), and internal/external coil (columns 3 vs. 4) in ex-vivo muscle. Magnitude data acquired with the thermometry sequence (FEEPI, 1 voxel: 0.75 x 0.75 x 5 mm^3, 2 s/dyn, FOV: 96 mm), axial plane (a) and sagittal plane (d). Corresponding SDT-maps (b and e), with a linear median profile (c and f), vertical for axial plane and horizontal for sagittal plane. SDT was cut at 2°C. The colorbar is in °C.***

Even affected by the presence of the transducer, the integrated coil was better than the external coil. Its sensitivity gain was a factor 3 (at 5 mm), which diminished to a factor 1.7 at 10 mm. The sensitivity field of the integrated coil varied rapidly from 0.3°C to 2°C, over a short radius (about 20 mm). In the same conditions, the external coil measured an SDT higher than 1°C.

Integrated coil performance. The comparative study of coils investigated the accuracy of the temperature measurement for images with a spatial resolution of 0.75 x 0.75 x 5 mm^3. This voxel size was set to an average value between the integrated and the external coils. Therefore, images with better resolution were acquired exclusively with the integrated coil (see the 4th and 5th rows of Table IV.6). Figure IV.18 presents anatomical images with 0.31 x 0.31 mm^2 in-plane resolution, and thermometry images with a pixel of 0.63 x 0.63 mm^2. The cooling circuit was activated only for the thermometry image acquisition. As a result, minor flow artifacts were seen as localized ghost pattern in the direction of the phase encoding. Therefore, attention should be paid when choosing the phase-encoding direction in order to guarantee an artifact-free target region.

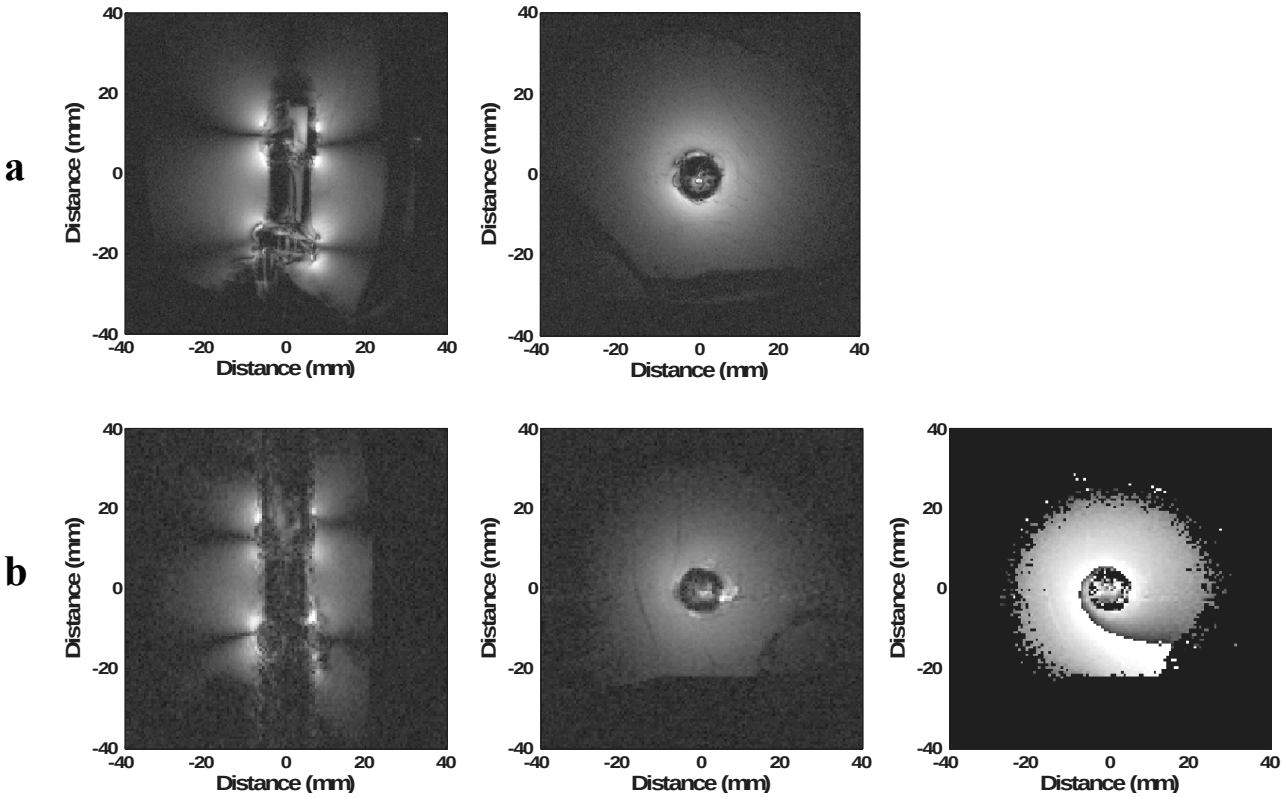

***Figure IV.18.** Images acquired with the integrated esophageal coil, axial and sagittal plane, ex-vivo muscle (for MR parameters see rows 4 and 5 of Table IV.6). FOV: 80 mm. a). Anatomical images (T_1-w-TFE, 1 voxel: 0.31 x 0.31 x 5 mm^3). b).Thermometry images (FEEPI, 1 voxel: 0.63 x 0.63 x 5 mm^3, 2 s/dyn). The last image is the phase image corresponding to the axial magnitude image.*

IV.3.2 Thermotherapy with automatic temperature control

The automatic temperature control experiments were conducted on thermometry images acquired with the integrated coil, at its best resolution. The spatial resolution was 0.63 x 0.63 x 5 mm^3 and the temporal resolution was 2 s/dyn. The generator limited the sonication time at 1.2 s for each dynamic (2 s). The accuracy of the temperature measurement was 0.5°C at 5 mm and 0.9°C at 10 mm. According to appendix A, these SDT values translate in overestimations of the thermal dose of 6% and 21%, respectively. The 1°C-sensitivity depth was reached at 11 mm from the cooling balloon. Note that the balloon was slightly inflated (14 mm in diameter) and that the sensitivity depth decreased for a highly inflated balloon. The external coil measured, in the same conditions, a significantly higher SDT (1.8°C), i.e. a thermal dose overestimation of 117%.

Figure IV.19 presents three cases of temperature feedback control, for single, two, and three beams, performed in *ex-vivo* porcine muscle. The temperature scale shows the temperature elevation within the tissue, relatively to an initial temperature assumed to be 37°C.

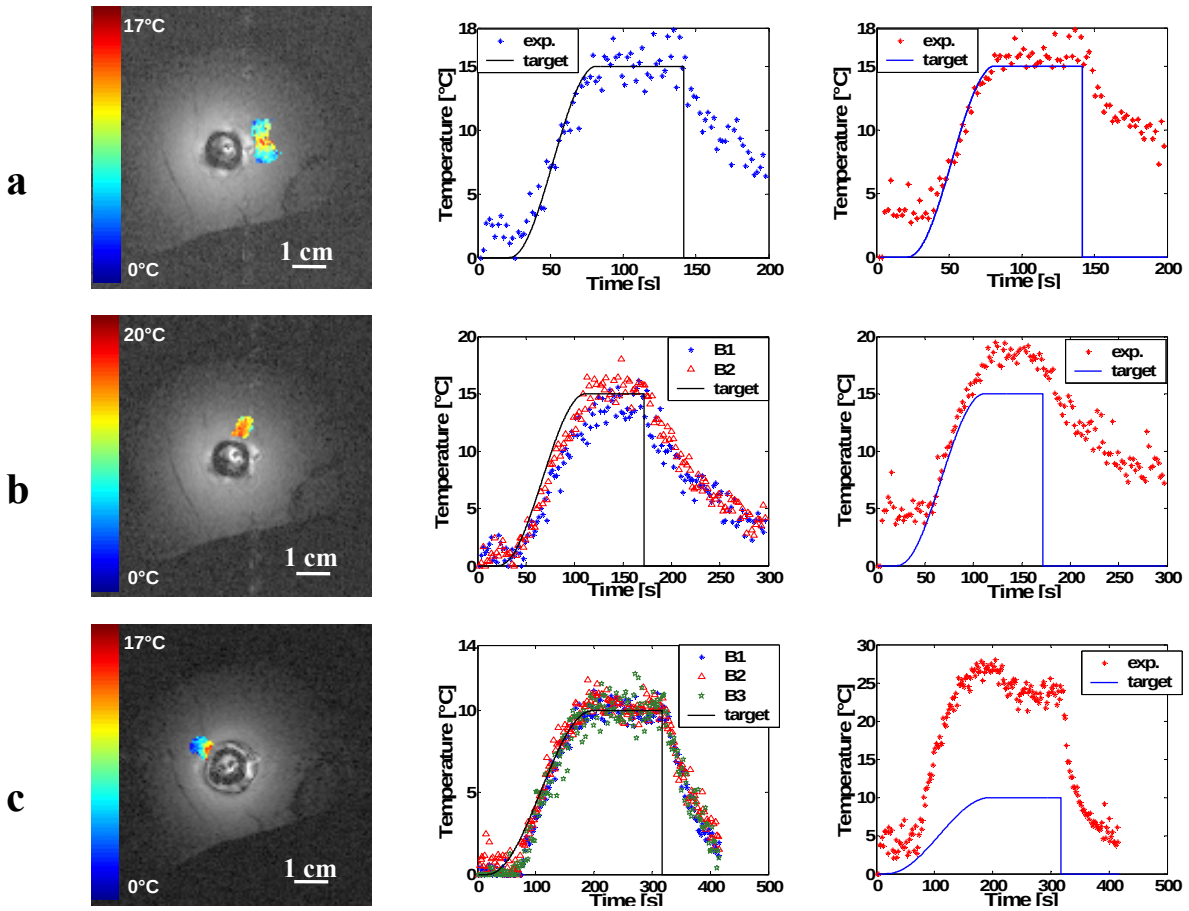

Figure IV.19. *Three cases of heating experiment with active temperature control (see MR param. in Table IV.6, row 5), integrated esophageal coil, axial plane, ex-vivo muscle. FOV: 80 mm, voxel: 0.63 x 0.63 x 5 mm^3, 2 s/dyn. Maps of relative temperature acquired at the end of the heating period and the corresponding temporal evolutions of the temperature rise, for the defined control point(s) and for the maximum heated point within the region of interest. a). single beam: target of 15°C, 1 control point at 7.5 mm-depth; b). two beams: target of 15°C, 2 control points at 5.5 mm-depth; c). three beams: target of 10°C, 3 control points at 3 mm-depth. Scale bar is 1 cm.*

The generalization of the PID controller for the multi-beam approach permitted to control the temperature for each individual beam. The experimental temperature successfully tracked the predefined target curve for the defined control points. The curve of the maximum temperature (see the last column of Fig. IV.19) was not explicitly controlled in these experiments, and therefore it was normally to exceed the target curve. This offset was more important as more beams were activated. Table IV.7 summarizes the target temperature and the accuracy of the PID controller for the three cases. The SDT (see last column of the Table) depended on the control point localization. The control points were localized, along the ultrasound beam, at a penetration depth of 7.5 mm, 5.5 mm and 3 mm from the transducer. Note that for this experimental setup (porcine muscle, attenuation coefficient 0.09 Np/cm, working frequency 5.15 MHz) the ultrasound beam was attenuated at half of its initial intensity after 7.5 mm. The choice of the control points nearer to the coil (i.e. the case of the three beams) determined the best precision for the temperature controller.

PID controller	Target [°C]	Rising stage [s]	Ct. stage [s]	Controller accuracy	
				Mean error [°C]	SDT [°C]
Single beam	15	60	60	15.21 (1.4%)	1.33 (8.86%)
Two beams	15	90	60	13.76 (8.26%)	1.18 (7.86%)
				15.48 (3.2%)	0.92 (6.13%)
Three beams	10	180	120	10.06 (0.6%)	0.52 (5.2%)
				10.3 (3%)	0.54 (5.4%)
				10.17 (1.7%)	0.79 (7.9%)

Table IV.7. Target temperature definition and the corresponding accuracy of the controller for three different heating experiments.

IV.3.3 Feasibility of the treatment planning

Heating experiments using interleaved multi-beams (see the last row of Table IV.6) were performed in order to demonstrate the possibility to implement this treatment strategy. The multi-beams were rapidly switched during a single dynamic. The duration of such an iterative sequence (multi-beams) was correlated with the acquisition time of a single dynamic. During experimentation, the investigator defined, on-line, the tumor location and size (see Fig. IV.20). The defined tumor region determined the number of beams to be activated and their orientation.

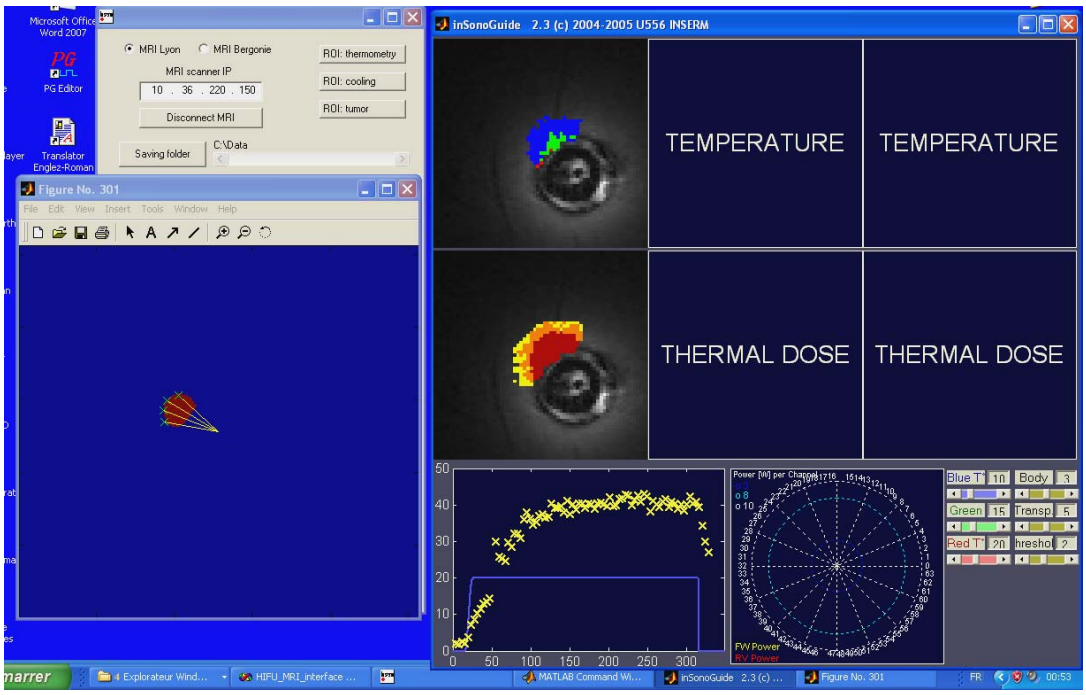

Figure IV.20. ***Example of a heating experiment (print screen of the main PC) aimed to investigate the feasibility of the interleaved multi-beam treatment. Left: the user-defined tumor indicating 4 needed beams. Right: on-line MR-control of the sonication: temperature and thermal dose maps, plot of the maximum temperature evolution in time, and applied power (here, end of sonication).***

Two cases of heating experiments applied to two user-defined tumors are presented in Fig. IV.21. Four (first row) and, respectively, five interleaved beams (second row) were activated in order to treat these tumors. An electrical power of 30 W/beam was applied during 300 s of sonication. Each beam was constituted of 8 individual elements of the esophageal transducer. Two consecutive beams were separated by an angular increment defined as two active elements, which corresponded to an angle of 11.25°. These sonication parameters permitted a maximum temperature elevation of 21°C, and respectively 23°C. The corresponding thermal dose reached a maximum value of 167 LDU and respectively 210 LDU, but only for few pixels (less than 10 pixels). As previously defined, 1 LDU (lethal dose unit) was the necrosis threshold according to Sapareto and Dewey [1984]. This minimal necrosis level covered uniformly the region of interest. The 5-beams case demonstrated correlation between the defined tumor and the 1 LD-thermal dose (see Fig. IV.22 a and b). However, note that the experiments tested here only the implementation of the multi-beam treatment strategy. The optimal sonication sequence permitting the best correlation tumor/thermal dose was not explicitly addressed.

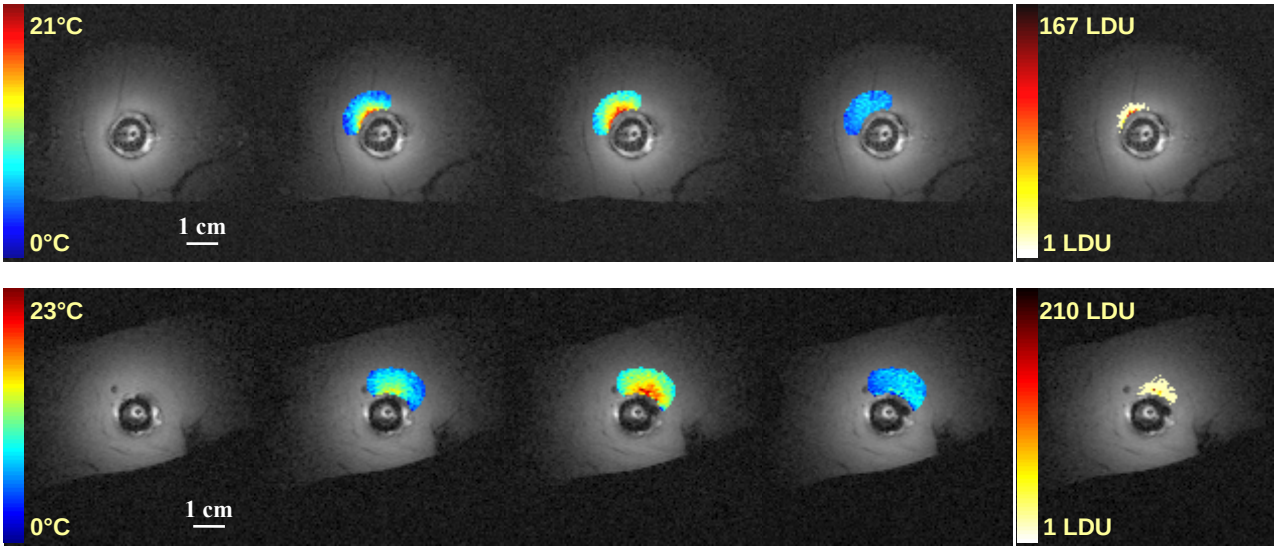

Figure IV.21. ***Two cases of heating experiment with interleaved multi-beams (see MR parameters in Table IV.6, row 7), integrated esophageal coil, axial plane, ex-vivo muscle. Up: 4 beams (B12-B15); Down: 5 beams (B3-B7). Maps of temperature elevation, acquired at 0%, 50%, 100% and 140% of the sonication time, and the corresponding thermal dose maps, acquired at the end of the experiment (1 LDU = 240 $EM_{43°C}$). FOV: 80 mm, voxel: 0.63 x 0.63 x 5 mm^3, 3.96 s/dyn. The scale bar is 1 cm.***

The length of the lesion (see the right side of Fig. IV.22) corresponded to the longitudinal size of the active region of the ultrasound transducer.

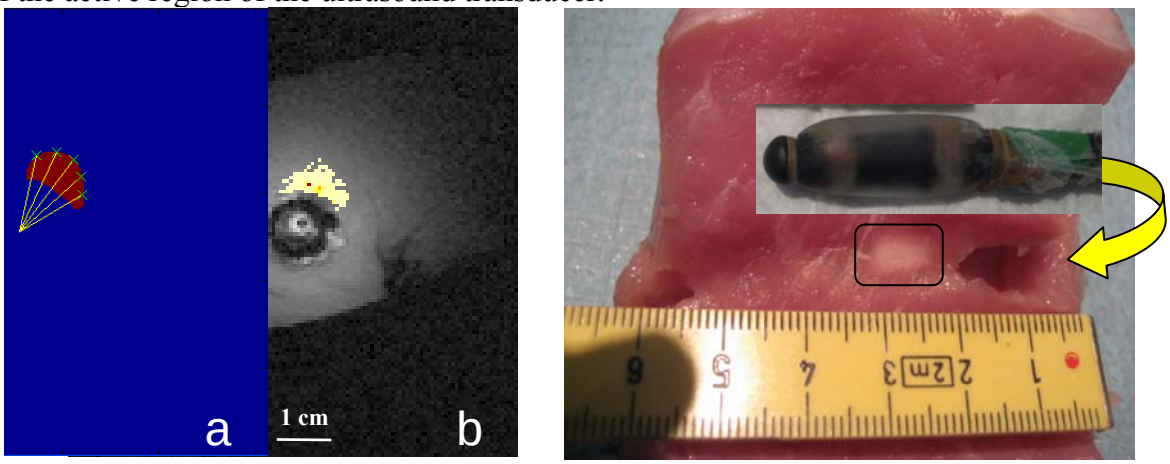

Figure IV.22. ***Feasibility of the multi-beam treatment strategy, case of 5 interleaved beams. Left: tumor (a) and thermal dose (b) correlation, axial plane; Right: macroscopic view of the lesion (black rectangle), longitudinal plane. The yellow arrow shows the insertion of the endoscopic device in the center of the porcine muscle bulk sample.***

IV.4 Discussion

The integration of an RF receive-only coil with the ultrasound transducer, in an indivisible device, was finalized in this chapter. For this purpose, the phased-array esophageal transducer was specially designed to host the coil wiring. This integration of the transducer and the RF coil into a single device was permanent, and not only a temporary assembling as in the case of the rectal coil (Chapter III). The coil holder and its tunnel permitted the avoidance of any superposition between

the coil wiring and the acoustic active zone of the transducer. This translated to an acoustic aperture of 360° for the esophageal transducer, hence no limitation regarding the direction of sonication. The internal connection of the two wirings of the coil, inside the transducer, had two main results, representing a real improvement when compared to the rectal coil case. First, it enabled a full use of the transducer. Second, the integrated coil exhibited a completely circular sensitivity field, in the axial plane, without any distortion from the external wiring of the coil (as it was observed in the rectal coil case).

RF artifacts, induced by the transducer structure, were seen outside the region of therapeutic interest. Minor susceptibility artifacts, caused by the insulating scotch tape covering the coil holder, were detected. The transducer artifacts were visible in both axial and sagittal planes, while the tape susceptibility artifact appeared in the sagittal plane only. However, those two artifacts were observed outside the acoustic zone, and had therefore no influence on the sonicated regions. On the contrary, flow artifacts were seen as ghosts along the phase-encoding direction, and affected the thermometry images. But, like in Chapters II and III, changing the phase direction produced a clear region of interest. Note, however, that this solution reached its limit when dealing with large tumors. In the case of sectorial tumors larger than half a circle, changing the phase direction would be useless. In such conditions, the only possibility to reduce the flow artifacts is to reduce the flow.

Overall, the integrated coil demonstrated its advantages over the 4-element standard external coil, for both anatomical and thermometry images. The results of the comparative study of coils (Fig. IV.17) were obtained for thermometry images, acquired with a spatial resolution of 0.75 x 0.75 x 5 mm^3. Images with lower (1 x 1 x 5 mm^3) and higher resolutions (0.5 x 0.5 x 5 mm^3) were also acquired (data not shown). For all the resolutions tested here, the sensitivity of the integrated coil was three times higher than the sensitivity of the external coil. This value was determined close to the device (5 mm). Note that the intrinsic SDT varied with the voxel size and showed the best SDT (0.2°C) at a lower spatial resolution. Overall, the integrated coil measured an SDT better than 1°C for all the resolutions tested. The sensitivity of the integrated coil became equal to the one of the external coil only for large voxel (1 x 1 x 5 mm^3) and beyond 20 mm from the balloon. Additionally, a higher voxel also increased the sensitivity depth of the coil. The transducer inside the coil seemed to have a minimal influence on the coil performance, as in the case of the rectal coil. The 1°C-sensitivity depth of the integrated coil was reduced by 0.5 mm. At a higher level of sensitivity (0.5°C), this reduction was less than 3 mm. The available SDT obtained with the integrated esophageal coil induced an overestimation of the thermal dose, varying from 1% (for an SDT of 0. 2°C) to 27% (SDT of 1°C). A maximal SDT of 2°C induced an overestimation of the thermal dose of 161%. This explains the interest to measure the temperature

with a minimal SDT. Also, from the same reason, the sensitivity-depth measurements of the integrated coil were performed at 0.5°C or 1°C.

The 3-turn coil improved the accuracy of the temperature measurement by a factor of 3.3 when compared to the 1-turn coil. At the lower resolution, the improvement was even higher (a factor 7). More generally, the performances of the 1-turn coil and the external coil were similar for all the resolutions tested. This result was contrary to the one obtained for the rectal coils. This could be explained by the smaller wiring surface of the coil, considering that there are only 3 turns versus 5 turns in the rectal case. Moreover, the smaller diameter of the turns (20 mm versus 11 mm) influenced the result. Therefore a general conclusion regarding the best number of turns for a coil should always consider the total wiring surface for a specific coil design.

A fundamental advantage of this local coil consisted in the capability to acquire images with small FOV, without possible phase wrapping from other regions. This phase wrapping problem appears usually when using external coils and the strategies to eliminate it require extra acquisition-time. Therefore, the small-FOV images were not only of high SNR, but also offered rapid acquisition.

Another objective of this chapter was the implementation of the fast-switched multiple beams approach for the therapy. The resolution of the thermometry images was set to 0.63 x 0.63 x 5 mm^3, for a time acquisition of 2 s/dyn. The accuracy of the temperature measurement varied up to 1°C, around the device, for a radial depth of 11 mm. Therefore the integrated coil seemed appropriate for a tumoral depth inferior to 15 mm. The PID algorithm was adapted to this treatment strategy and simultaneously controlled the temperature at multiple control points, with one control point per beam. The accuracy of the controller depended on the localization of the control point, showing best precision close to the device, because of better SDT. The increased number of control points is expected to enhance the quality of temperature controlling al over the region of interest.

The esophageal transducer was delivered by the manufacturer with some problems concerning the internal cooling circuit. The output of the internal cooling circuit was not functional. Therefore, an output pipe was inserted directly inside the cooling balloon in order to bypass the internal output circuit (see Fig. IV.22, right side). This pipe connected the balloon directly to the external cooling circuit. However, this partial solution was suboptimal. In normal conditions, the internal circuit has four outputs, ensuring a uniform cooling flow around the active part of the transducer. These 4 outputs were replaced with a single output, affecting the uniformity of the cooling flow. This asymmetry may also explain the singular higher signal (white spot) observed within the balloon in the thermometry images. However, the general strategy of the therapy planning was validated experimentally. Four or five beams were then sequentially

activated, in interleaved mode, in accordance with the user-defined virtual tumor, showing good correlation between the virtual tumor and the thermal dose.

The simulation algorithm, based on the multi-beam activation, demonstrated high accuracy (less than 10% error) for a pre-operative therapy planning. The algorithm permitted the definition of an optimal strategy for the treatment planning of different tumor shapes and locations. Moreover, the short computing time (~ 3 minutes) suggested that in-situ planning of the dosimetry would be realizable. In addition, the algorithm can be adapted to another ultrasound transducer by merely loading the corresponding acoustic field in the main program.

The simulations provided two important results. A first observation, already seen during heating experiments, was that the thermal dose continues growing after the sonication was cut off. Therefore, this effect should be considered when proposing a treatment. The second observation was related to the cooling balloon and tumor located near the ultrasound device. In this context, due to the heat-sink phenomenon, a thin proximal layer of the tumor region remains undertreated. This may be a serious problem, especially when the purpose of the treatment is purely curative. Ideally, the temperature of the water inside the cooling balloon should be minimal, e.g. 0°C, in order to protect the active part of the transducer from overheating. But, this low water temperature generates the undertreated region, and the volume of untreated tumor depends on the cooling water temperature. Since the cooling circuit cannot be eliminated, the only option to limit this undesired effect is to increase the temperature of the cooling water. It was shown that a water temperature of 10°C is still inefficient (see Fig. IV.14), therefore the temperature of water should be set at higher values. On the other hand, such endocavitary tumors may be treated by impeding the blood supply of tumoral cells. This assumes that complete necrosis of distal borders of the tumor isolates the tumor from its blood supply and may indirectly induce its death [Cranston *et al*, 2006]. In this case, the inner undertreated layer could be considered inoffensive. Henceforth, the water temperature could be decreased to a minimal level, ensuring a total protection of the transducer. This assumption needs however to be validated experimentally.

The objective of the simulation was to define the best treatment strategy for the same tumor, using similar ultrasound parameters. The interest of this study was to choose the type of beam (focused or planar) and the modality for activating the multi-beams. Successively activated plane beams seemed to be the best choice. Nevertheless, the focused beams presented some interest since they can offer a sharper thermal dose gradient, with a very thin separation between treated and untreated regions.

IV.5 Conclusion

Three technological issues were studied in this chapter. First, a RF receive-only coil was permanently integrated within an esophageal therapeutic transducer. The transducer was specially designed to host the coil. This design of the device permitted a 360°-aperture for ultrasound targeting and also for coil sensitivity. The SDT measured with the integrated coil was below 1°C and represented an improvement by a factor 3 compared to a standard external coil. Less than half millimeter spatial resolution became feasible for anatomical images, while accurate thermometry measurements were performed for a spatial resolution of 0.63 x 0.63 x 5 mm^3. The sensitivity field of the integrated coil limited the applicability of the method to tumoral depths of less than 15 mm. Second, a treatment strategy, based on the activation of fast-switched multiple beams, was implemented. Moreover, the temperature feedback loop controlled with high accuracy multiple control points for the same dynamic (temperature error less than 3% and SDT up to 8%). Third, the simulation algorithm permitted the definition of the best treatment strategy for a defined tumor. In addition, the short computing time suggested that in-situ planning of the dosimetry would be realizable.

Chapter V. Design of a new generation of therapeutic ultrasound applicator, general discussion and conclusions of the thesis

V.1 Introduction

This chapter is divided into two sections. The first section presents the early results of acoustic field simulations conducted in order to design a new ultrasound transducer. The simulations were performed in collaboration with an equipe from U642 Inserm (S Esnault and J L Dillenseger). The goal was to ensure the efficacy and the safety of the therapeutic procedure. The main idea was to design a transducer capable to realize a dynamic displacement of the heated region, along its transversal axis. This could be realizable by a vertical focusing of the transducer which implies a 2D phased-array structure. On the other hand, such technology of the transducer demands an air-backing, and therefore an acoustic intensity limited at 10 W/cm². Furthermore, a natural focalization of the transducer should be considered in order to overcome the limitation of intensity. Considering these conditions, a 2D phased-array transducer with an incurved shape was designed. Its acoustic field pattern, for different sets of parameters, was studied with respect to shape, homogeneity, and steep delimitation between treated and untreated regions. Two strategies of treatment were investigated: one-step heating of a volume, or volume covering by multi-displacements of a focal region. The second section of this chapter discusses the results presented in this thesis and the perspectives of the therapeutic method.

V.2 Acoustic simulation for a new ultrasound transducer

V.2.1 Design of the ultrasound transducer

A 256-element tubular transducer (see Fig. V.1) was divided into 32 vertical elements (red lines), and furthermore, each such vertical line was segmented into 8 elements (blue horizontal lines). The inter-element gap was set to 0.1 mm. Each individual element should be able to be controlled in terms of phase and amplitude. The geometry of the transducer was designed in order to permit a natural focalization of the ultrasound beam. Hence, the lateral surface of the transducer was generated by a polynomial curve of a radius r defined as follows:

$$r = R_{\min} + (R_{\max} - R_{\min}) \cdot (z/h)^n, \qquad \text{with} \qquad n = \{2;\ 2.5;\ 3\} \qquad \text{Eq. V.1.}$$

The parameters R_{min}, R_{max} and h (see Fig. V.1.b) characterize the transducer geometry: its height ($H=2h$) and the minimal and the maximal radius. Three types of polynomial curve, corresponding to order $n = \{2;\ 2.5;\ 3\}$, were tested. The z-symmetry of the transducer contributed to a reduction of the computing time by a factor 2. The acoustic field was therefore calculated only for the upper part of the transducer ($z>0$), and then it was inversed for the bottom part of the transducer ($z<0$).

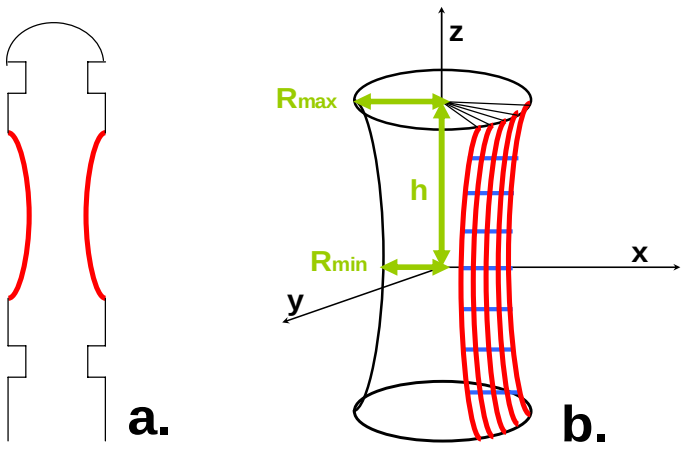

Figure V.1. General view (a) and symmetry axes (b) of the head of the ultrasound transducer, longitudinal plane. The red curves represent the acoustic active surface of the transducer.

Similarly to the phased-array transducers presented in Chapters III and IV, the longitudinal segmentation of the transducer aimed to permit the electronic rotation of the ultrasound beam. Note that an acoustic beam was constituted of 5 vertical lines (or 40 individual elements) activated with an appropriate phase law. In addition, the vertical segmentation was intended to permit the displacement of the focus along the radial direction (here the *x*-axis). This displacement was considered between 3 and 5 mm. This property might be useful for treating non-uniform tumors, particularly those with unequal tumoral depths. The focus displacement (see Fig. V.2.a) was implemented by the mean of a phase law, applied vertically to the 8 constitutive elements of a vertical line. The principles of electronic rotation and dynamic focalization may be used together to treat a slice of a thickness about 5 mm. When the treatment of the entire axial slice would be completed, the endoscopic device should be translated along the head-foot axis, in order to treat another slice, 5 mm further.

However, this 2D segmentation of the transducer implies, for technological reasons, an air-backing reflector instead of a solid backing as for the former phased-array transducers. Therefore, the designed transducer would be limited to 10 W/cm², but should have higher electroacoustic efficiency [Fleury *et al*, 2002]. Moreover, the working frequency for an air-baked transducer may be higher, up to 10 MHz. Since an air-baked transducer is generally fragile, a mechanical structure aimed to ensure its rigidity should be added at the interior.

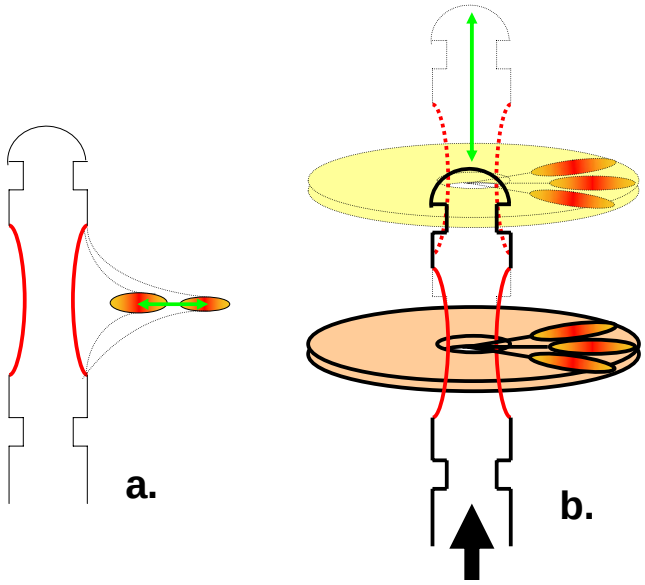

Figure V.2. Principle of the ultrasonic treatment using the new transducer. a) Dynamic focalization (see green horizontal arrow) along the radial axis due to the vertical segmentation. The horizontal displacement was considered between 3 and 5 mm. b) Electronic rotation (with or without dynamic focalization) in the radial plane (one axial slice) and vertical displacement of the transducer (green vertical arrow) in order to treat another slice of the tumor. The longitudinal displacement (~5 mm) of the transducer should be realized with a MR -compatible system, such as a piezoelectric motor.

V.2.2 Multiple configurations investigation

The intensity of the acoustic field for one beam was initially calculated (Rayleigh integral, cylindrical coordinates: rho, θ, z) in the longitudinal plane (here *xz*-plane, see Fig. V.1.b). Two attenuating media were considered: the water inside the cooling balloon and the tissue. The final form of the acoustic intensity field was expressed, using an interpolation operation, in Cartesian coordinates. The observation plane varied from 12 mm to 75 mm in the *x*-axis direction, and from -15.5 mm to + 15.5 mm in the *z*-axis direction. The longitudinal dimension covered the entire height of the transducer. The starting point of the acoustic field calculation along the *x* axis (i.e. the 12 mm-point) corresponded to the maximal value of the R_{max} parameter.

Four parameters of the transducer design were varied (see Table V.1): the generating function of the lateral surface of the transducer, the operating frequency, R_{min}, and R_{max}. The lateral

Parameter	Interval	Step	Unit
Frequency	2-6	0.2	MHz
R_{min}	3-7	0.5	mm
R_{max}	5-12	1	mm

Table V.1. The variation interval and the corresponding incrementation step for three investigated parameters.

surface of the transducer was tested for three types of polynomial curves (order 2, 2.5 and 3). The transducer height was kept constant (30 mm). The transducer was designed for rectal application. Therefore its dimensions, particularly R_{min} and R_{max}, were chosen to be close to those of the available rectal transducer described in Chapter III. The maximal values of diameters were 14 mm (for R_{min}), and 24 mm (for R_{max}). The frequency was investigated between 2 and 6 MHz. Undesired skin burns similar to those observed *in-vivo* with the rectal transducer are not expected with this design of transducer because of its natural geometrical focalization. The scanning of this 4-dimension domain permitted acquisition of a complex data base regarding the acoustic intensity field of the transducer. A number of 3969 configurations were initially simulated, only in the longitudinal plan. A typical example of 25 configurations (same frequency and same polynomial order) can be seen in Fig. V.3.

Figure V.3 (see next page). Example of 25 simulated configurations: polynomial curve of order 2, frequency 4.6 MHz, R_{min} varied from 3 mm to 5.5 mm and R_{max} varied between 5 and 9 mm, longitudinal plane (xz-plane). The observation plane was 75 x 31 mm². Its axes were expressed in sampling points. The curve superposed on the image represents a central plot along the radial direction of the acoustic field (the horizontal x-axis). The transducer is overlaid on the first plot of the figure in order to suggest its position with respect to the acoustic intensity field. The colorbar is expressed in arbitrary units, with acoustic intensity varying from 0 to its maximal value (1).

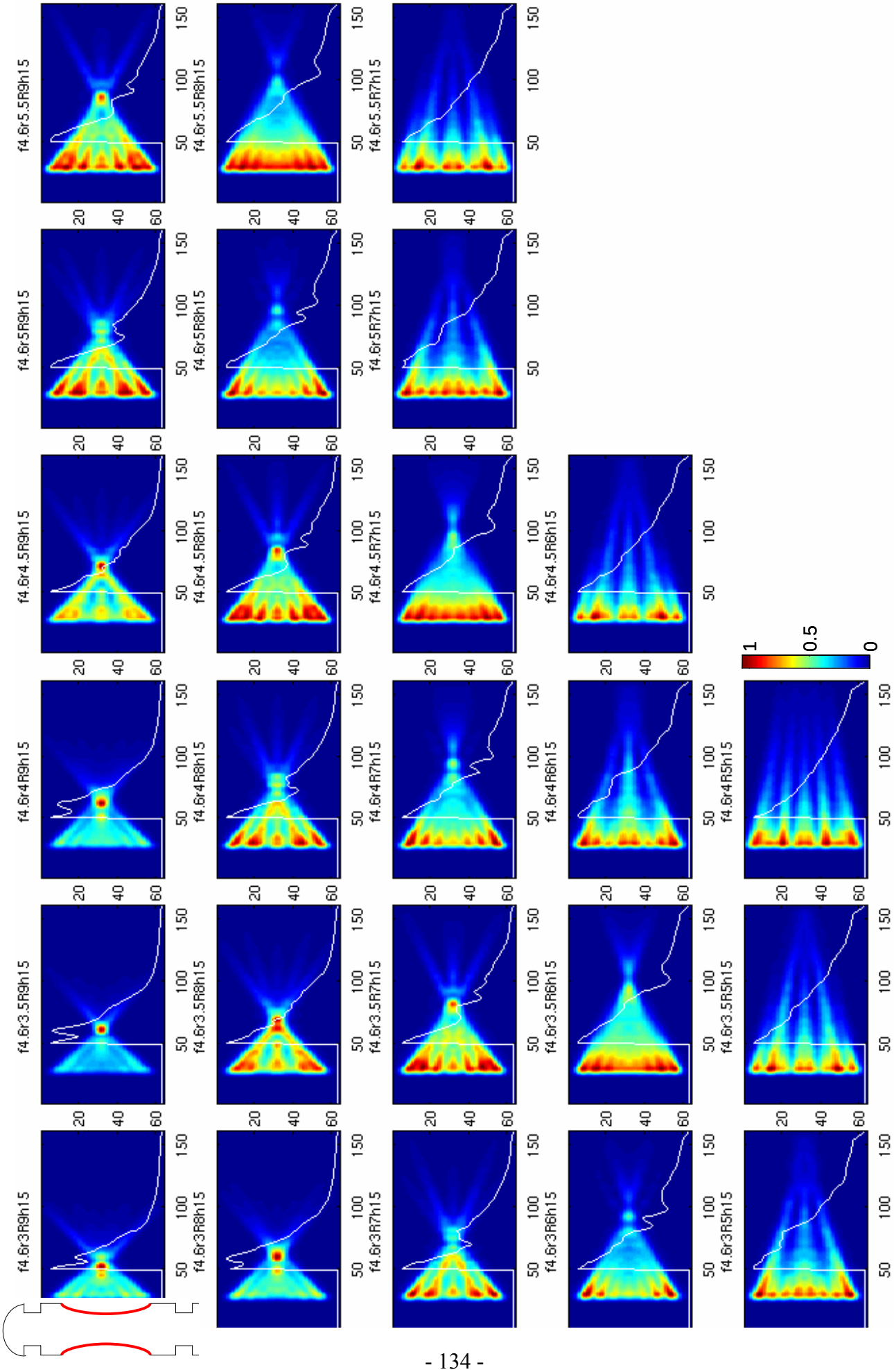
f4.6r5.5R9h15
f4.6r5.5R8h15
f4.6r5.5R7h15
f4.6r5R9h15
f4.6r5R8h15
f4.6r5R7h15
f4.6r4.5R9h15
f4.6r4.5R8h15
f4.6r4.5R7h15
f4.6r4.5R6h15
f4.6r4R9h15
f4.6r4R8h15
f4.6r4R7h15
f4.6r4R6h15
f4.6r4R5h15
f4.6r3.5R9h15
f4.6r3.5R8h15
f4.6r3.5R7h15
f4.6r3.5R6h15
f4.6r3.5R5h15
f4.6r3R9h15
f4.6r3R8h15
f4.6r3R7h15
f4.6r3R6h15
f4.6r3R5h15
1
0.5
0

The acoustic field maps resulted from all combinations (polynomial order, frequency, R_{min} and R_{max}) were visually checked in order to detect the configuration which offered the desired pattern of the acoustic field. Two different approaches of sonication were aimed. One direction investigated the most uniform heating pattern available by a unique set of 4 parameters. The second one was interested on a sharp focal region, which would be further translated horizontally and vertically in order to cover the entire tumor. Both approaches required a good homogeneity for the three observation planes.

Therefore, complete 3D simulations were performed. The 3D simulations were run only for some pre-selected configurations (from the longitudinal plane), which demonstrated already a suitable shape in that plane. In addition to the efficacy of the transducer, another objective was the safety of the treatment. The safety was assessed by observing the radial gradient of the acoustic field, in the distal region. The simulations conducted here were particularly based on focused beams, which are expected to demonstrate a steeper delimitation in the far field. This capability of the transducer, combined with a good MR temperature control, should offer the possibility to eliminate possible fistula at the distal tumoral borders. Moreover, technical limitations needed to be considered when running the 3D simulations. For example, the manufacturer expressed two requests as a limitation of actual technologies for such a design of transducer: a). the frequency should be higher than 4 MHz (acoustic impedance matching); and b). $R_{\min} \geq \frac{R_{\max}}{2}$ (curvature).

V.2.3 Results and discussion

As expected, the variation of the type of the polynomial curve generating the lateral surface of the transducer influenced the pattern of the acoustic field. The same set of parameters (4.8 MHz, R_{min} of 5 mm, R_{max} of 9 mm) lead to a more homogeneous field in the case of a curve of second order, as compared to the other polynomial orders (see Fig. V.4).

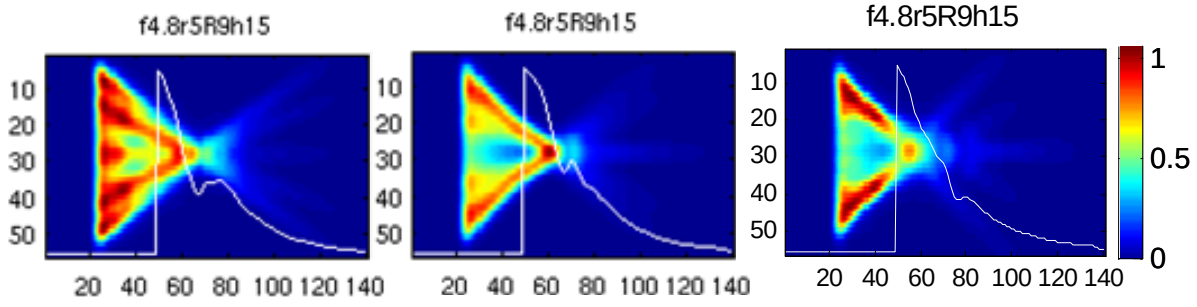

Figure V.4. Acoustic field evolution as a function of the order of the polynomial curve: left (order 2), center (order 2.5) and right (order 3). The frequency (4.8 MHz), R_{min} (5 mm) and R_{max} (9 mm) were kept fixed. The observation longitudinal plane (xz-plane) was 75 x 31 mm² with axes expressed in sampling points. The curve superposed on the image represents a central plot along the radial direction of the acoustic field (the horizontal x-axis). The position of the transducer is the same as in Fig. V.3. The colorbar scale is in arbitrary units, with acoustic intensity varying from 0 to its maximal value (1).

The frequency strongly influenced the pattern of the acoustic field, as seen in Fig. V.5.

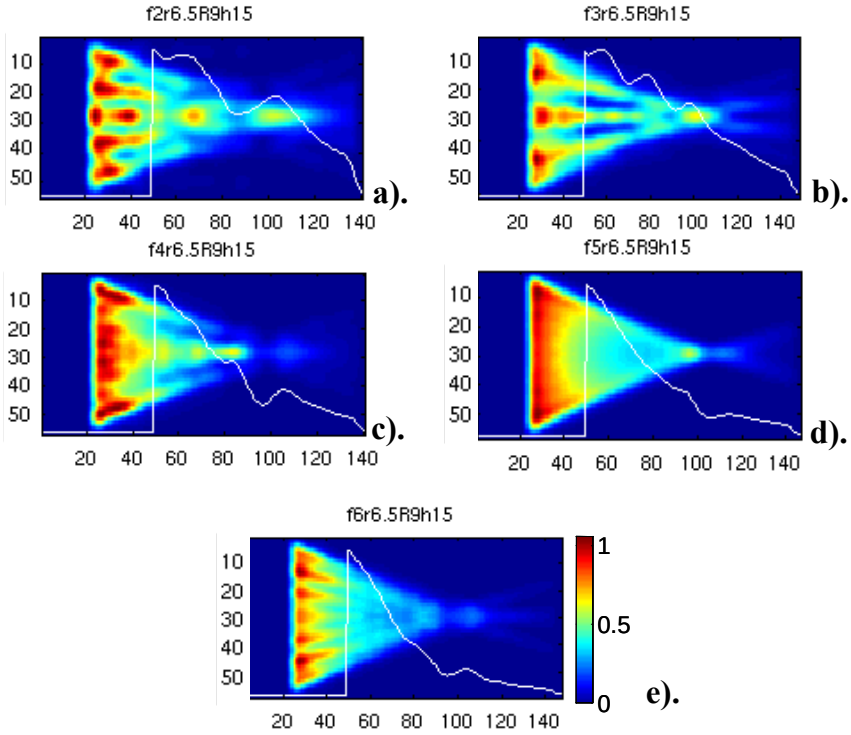

Figure V.5. Acoustic field evolution as a function of frequency, from 2 MHz (a) to 6 MHz (e). Fixed parameters: polynomial curve of order 2, R_{min}: 6.5 mm, and R_{max}: 9 mm. The frequency step was 1 MHz. The observation longitudinal plane (xz-plane) was 75 x 31 mm² with axes expressed in sampling points. The curve superposed on the image represents a central plot along the radial direction of the acoustic field (the horizontal x-axis). The position of the transducer is the same as in Fig. V.3. The colorbar scale is in arbitrary units, with acoustic intensity varying from 0 to its maximal value (1).

These initial observations and the manufacturer considerations were implemented during the 3D simulations. Therefore, the complete simulations were conducted particularly for a lateral surface defined by a function of second order. Moreover, frequencies higher than 4 MHz were considered. Two configurations (see Fig. V.6) corresponded to the first sonication strategy investigated, when a uniform and large acoustic intensity pattern was aimed. In these cases, the effect of the thermal diffusion was also simulated by a smooth filtering by a Gaussian kernel. Note that the *yz*-plane was orthogonal to the resting two planes, in a point x = 60 pixels, which represents about 36 mm away from the isocenter of the transducer. This position is indicated on Fig. V.6 by a black vertical line. The second sonication strategy aimed a sharp focus. In this case, more than two configurations suited the request. Figure V.7 exemplifies two such configurations.

The treatment approach based on the homogeneous heating pattern needs an important heat delivery close to the transducer to compensate the heat-sink phenomenon induced by the cooling balloon. Hence, depositing the main heat quantity close to the transducer may not be a good idea. From this point of view, the second sonication strategy, i.e. the focus point displaced horizontally and vertically, could be preferred. But, in this latter case, the total treatment time will be longer.

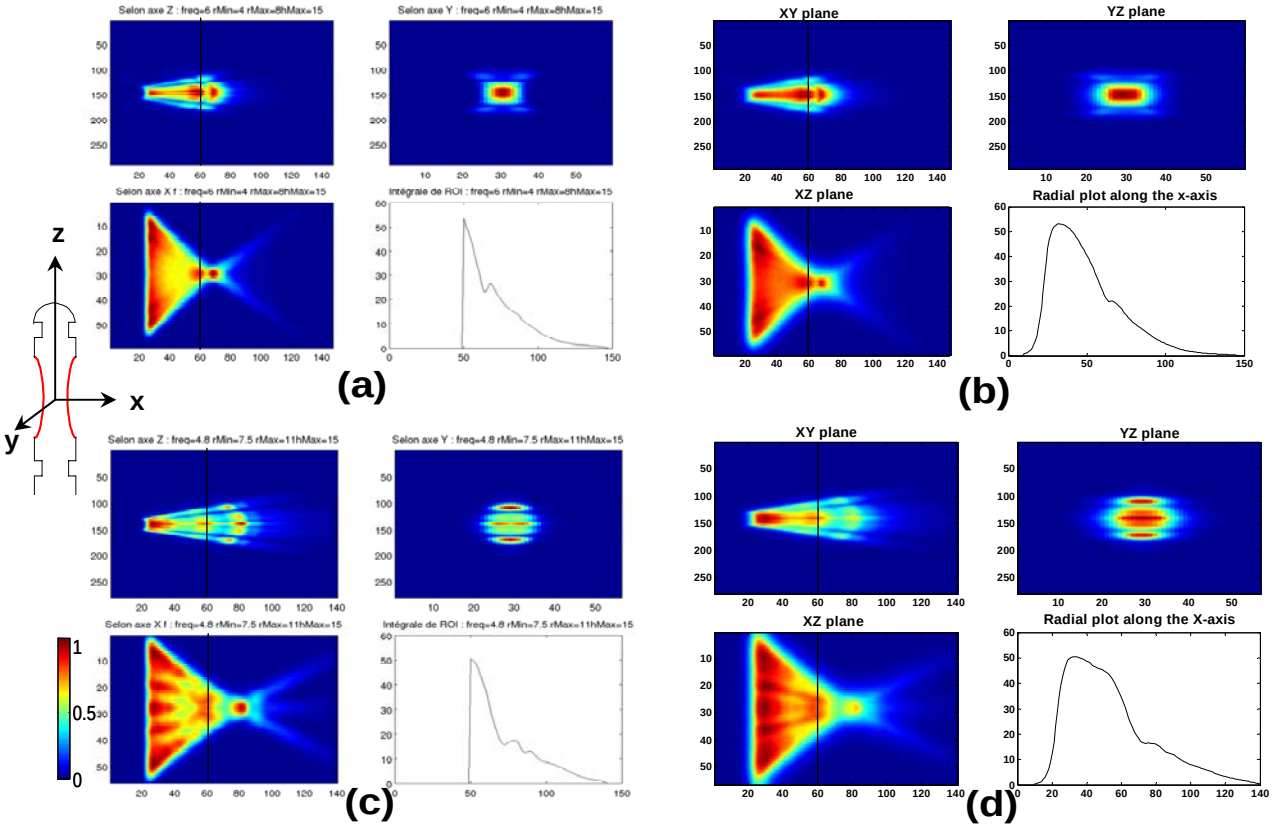

***Figure V.6**. Two configurations (a and c) which offered a homogeneous heating pattern. b) and d) the same configurations, affected by an average diffusion. The vertical black line represents the section for the yz-plane. The curve is a central plot along the radial direction in the xz-plane. Parameters for a, b: polynomial curve of order 2, frequency: 6 MHz, R_{min}: 6 mm, and R_{max}: 8 mm. Parameters for c, d: polynomial curve of order 2, frequency: 4.8 MHz, R_{min}: 7.5 mm, and R_{max}: 11 mm. The simulated volume (x x y x z) was 75 x 25 x 31 mm^3, with axes expressed in sampling points. The transducer's axes are exemplified in the figure. The colorbar scale is in arbitrary units, with acoustic intensity varying from 0 to its maximum.*

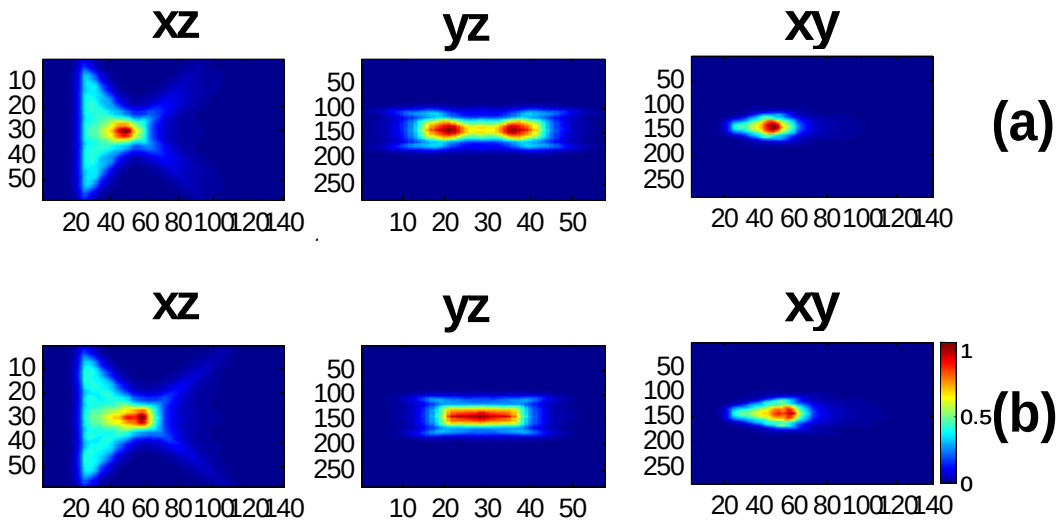

***Figure V.7**. Two configurations (a and b) which produced an appropriate focus of the acoustic field. Parameters: a). polynomial curve of order 2, frequency: 4 MHz, R_{min}: 6 mm, R_{max}: 12 mm. b). polynomial curve of order 2, frequency: 4 MHz, R_{min}: 6.75 mm, R_{max}: 12 mm. The simulated volume (x x y x z) was 75 x 25 x 31 mm^3, with axes expressed in sampling points. The transducer's axes are the same as in the former figure. The colorbar scale is in arbitrary units, with acoustic intensity varying from 0 to its maximum.*

V.3 General discussion and conclusion of this thesis

In this thesis, high intensity contact ultrasound therapy, guided by MR imaging, was investigated in order to propose a viable alternative for the treatment of rectal and esophageal tumors. The general objective was to ensure efficacy and safety of the treatment. The entire tumor must be ablated in a minimum time while avoiding any destruction of the surrounding healthy tissue, beyond the clinically defined safety margins*. In the case of rectal or esophageal cancers, the healthy distal layer must be totally preserved; hence fistula must be avoided. In this context, several issues were tackled within the work presented here: RF coils; temperature automatic control; *in-vivo* feasibility; optimal treatment planning; and new transducer design.

V.3.1 RF receive-only coils

The miniature RF coils, integrated with the transducer, were designed and built in order to improve the safety of the therapy. Compared to an external standard clinical coil, the integrated coil acquired MR images with higher spatial and temperature resolution.

Three coils, adapted to each specific ultrasound transducer were realized. The feedback control of the ultrasound induced temperature elevation was performed in the axial imaging plane. Therefore, the coil geometry was chosen in order to offer a homogeneous sensitivity field in this particular plane. Two types of coil geometry were considered: a loop for a monoelement plane transducer (Chapter II), and opposed-solenoids for the phased-array transducers (Chapters III and IV). Studies investigating the best numbers of turns were conducted for the solenoid coils. Also, the influence of the transducer on the coil performance was explicitly investigated under MR experiments. The coils design was based on measurements of the RF parameters of the coil, particularly on the quality factor, measured in air, water and tissue. The integrated coils were located inside the cooling balloon and this device was positioned in direct contact with the tissue. Hence the experimental loading environment was the worst possible case for a coil, showing minimal values for the Q-factor and the frequency. Generally, a more complete analysis of the RF coils, based on the reciprocity principle [Armenean, 2002] permits the coil optimization. However, this method was difficult to be used with the integrated devices described here, since the transducer characteristics are not exactly known.

The first coil prototype (Chapter II) tested the idea of integrating the coil into the therapeutic transducer, a mono-element esophageal planar applicator. This transducer had no space for hosting the coil wiring. Therefore, the coil was sealed on a plastic support, which covered the

* These safety margins refer to a layer of healty tissue around the tumor cell, and are clinically used in the curative treatment of cancers (by any method). For example, 1 cm-safety margin is generally used in the curative treatment of the rectal cancer.

head of the transducer. An acoustic window of the same size as the active zone of the transducer was open in this support. This initial prototype was an elongated saddle adapted to the dimensions of the active acoustic zone. The second coil prototype (Chapter III) was adapted to the 64 elements phased-array rectal transducer. Its geometry was an opposed-solenoid with a single turn. As for the first coil prototype, the rectal coil was sealed on a plastic support, which was mounted on the head of the transducer. The external connection between the two turns of the coil was superposed over some elements of the transducer, blocking their acoustic activation. Therefore, the acoustic window cut in the support limited the activation of the transducer elements to three quarters of its capacity, i.e. an aperture of 270°. This external connection between the two turns affected also the sensitivity field of the integrated coil, which was not completely circular (see Fig. III.18.b). This rectal coil represented an intermediate phase in the development of the integrated opposed-solenoid coil. The next therapeutic ultrasound transducer (64 elements, phased-array, esophageal application) was designed in order to host the coil. The final coil prototype (Chapter IV) was truly integrated into the transducer using an internal connection between the two groups of turns. The entire 360°-acoustic opening of the esophageal phased-array transducer was available in this case. This final coil prototype showed, in the axial plane, a completely circular sensitivity field (see Fig. IV.17).

As a general rule, all designed coils were sealed in epoxy-resin. The drying process of the resin influenced the RF parameters of the coil, particularly decreasing the resonance frequency and the Q-factor. The static RF parameters of the coil could be considered stabilized after 1 to 2 weeks (no data presented in the thesis). Another general characteristic of the coil was the need to limit its dimensions, especially the outer diameter. A minimal diameter was required for the coil head and for its connecting cable. Sometimes these limitations reduced the coil performance. For example, the connecting cable of the third prototype (Chapter IV) reduced the Q-factor by 50%. Otherwise, the possibility to host the coil wiring directly on the transducer body permitted the reduction of the outer diameter of the coil head.

In order to demonstrate the sensitivity improvement brought by the integrated coils, comparative studies between the miniature coils and an external coil were conducted. For the locations investigated in this thesis, i.e. rectum and esophagus, the most adequate clinical external coil seemed to be the Sense Body coil (4 elements phased-array). Overall, the three prototypes of integrated coil demonstrated higher sensitivity than the external 4-element coil. The coil prototype integrated with the simplest transducer showed the best performance. The rectal integrated coil acquired, under *in-vivo* conditions, high resolution morphological images (voxel 0.4 x 0.4 x 5 mm^3) and accurate thermometry data (voxel 0.75 x 0.75 x 8 mm^3, 2 s/image). In the same time, the measured temperature had a low temperature noise varying from 0.3°C to 1°C over a radius of 20

mm. These values of the SDT were measured from true voxel, without any ROI averaging. These resolutions (spatial, temporal and temperature) represent an important improvement in thermotherapy interventional MR.

Temperature and thermal dose are related by an exponential relationship. Therefore, high value of SDT translates in important overestimation of the measured thermal dose (see Appendix A). This explains why a low SDT is always required and this was also one important reason to develop the integrated coils. Even if the SDT-maps were generally limited to 2°C or higher for some internal/external comparison studies, the sensitivity depths of the integrated coils were always calculated for an SDT value of 1°C, sometimes 0.5°C. Remember that 0.5°C induced a thermal dose overestimation of 6%, compared to 27% overestimation for an SDT of 1°C. A much higher SDT (2°C) generated an unacceptable overestimation of 161%. Therefore, considering its effect on the thermal dose measurements, an acceptable limit of the MR thermometry was set to an SDT of 1°C.

The available sensitivity depths due to the integrated coils should be discussed when considering clinical applications. As it was explained in Chapter I, HICU under MR guidance may be adequate in curative intent only for superficial cancer (stage I and II, without lymph node involvement) while palliation treatment considers only cancers without important stenosis. Both esophageal and rectal cancers manifests as tumor cells proliferation towards the lumen causing therefore its stenosis (see Fig. I.2). Moreover, a tumor not only decreases the lumen diameter, but also affects the extensibility of the duct. Henceforth, very large stenosant tumors are impossible to treat, since there is no physical space to place the contact transducer. On the contrary, the tumor may be treated with this method if its form is spatially extended around the lumen, showing no important thickness* causing stenosis. Such large esophageal tumors with typical thickness of ~1 cm were palliated using the HICU method [Melodelima, 2004]. For the rectal case, the mean average of tumor thickness is less than 2 cm [Maeda *et al*, 2002]. It can be then concluded that the 1°C-sensitivity depth of 20 mm observed *in-vivo* with the integrated rectal coil complies with the clinical tumor sizes, adequate to this ultrasound contact treatment. Of course, increasing the sensitivity depth is always desired and the available performances of the integrated coils are minimally sufficient, particularly for palliation. However, for curative intents, when the temperature control is critical, these depths should be sufficient.

All three coil prototypes showed common characteristics. No RF artifacts from the HICU sonication were detected. Also, no tissue heating by the excitation of the RF pulses was observed, or at least not within the available SDT. The sensitivity field of the integrated coil was better close

* Here tumor thickness means depth of the tumor, through its composing layers. When considering the axial MR imaging slice, the tumor thickness will be the depth measured from the transducer to its distal end.

to the transducer and decreased with the distance. The sensitivity field varied, within acceptable limits (1°C), over a radius of 20-25 mm, for a spatial resolution of infra-millimeter order. A more reduced sensitivity field, i.e. a radius of 15 mm, was observed for the last prototype coil (Chapter IV) due to the bad quality of the connecting thin cable. Overall, higher tumor depths could be treated with an acceptable SDT when lowering the in-plane spatial resolution to 1 mm. Increasing the voxel size will extend the useful radius of the coil sensitivity field. Implicitly, for bigger voxels, the intrinsic SDT will be more accurate. In this thesis, the sensitivity field of the coil was analyzed particularly for thermometry images, and the quantity of interest was the SDT. However, SDT and SNR are reciprocal quantities, see [Conturo *et al*, 1990], [Salomir *et al*, 2000]. Otherwise, the SNR was slightly influenced by the type of MR image. For example, data not shown here demonstrated that the same coil had an SNR of 25 units when acquiring a morphological image, and an SNR of 20 for thermometry images. Hence, in the case of integrated coils, the morphological images showed a higher quality than the thermometry images. A fundamental advantage of this local coil consisted in the capability to acquire images with small FOV, without possible phase wrapping from other regions. This phase wrapping problem usually appears when using external coils and the strategies to eliminate it require extra acquisition-time. Therefore, the small FOV-images were not only of high SNR, but also offered rapid acquisition.

General drawbacks were also observed for the integrated coils. The coils were not adapted to spin-echo acquisitions, showing low quality of the images. The most important problem was the motion artifacts generated by the water flow inside the cooling balloon, which were seen as localized ghost pattern in the phase-encoding direction. These artifacts depended on the flow of the cooling water. However, in function of the sonication direction, the phase-encoding direction could be changed by 90° ensuring an artifact-free target region. Moreover, for anatomical images when no cooling of the transducer is needed, the cooling circuit may be stopped for a reduced time, still maintaining the balloon inflated. If the anatomical images are acquired after sonication, there is necessary to wait some time until any resting water movements inside the cooling balloon are eliminated.

The idea of using autoresonance coils was also tackled (data not shown). This type of coil had a better Q-factor and did not require any cabling. But their use was not overall an issue, because the technology for self-detuning such a self-resonant during the RF pulse coil was not available in the framework of this thesis.

V.3.2 Active temperature control

At temperature above 50°C there is some evidence that denaturation of large molecules contributes to a considerable increase in ultrasound attenuation [Duck, 1990]. For example, Robinson and Lele [1969] studied the changes in attenuation from 30 to 90°C in cat brain, and showed that the attenuation stays essentially constant up to 50°C, and then increases rapidly. Such tissue properties which can change during heating, together with the *in-vivo* variability demand a continuous control of the delivered heat. The temperature controller should be capable to assess the temperature in conditions of variability or unexpected changes. The MR thermometry is a remarkable tool, allowing on-line and automatic control of the heat delivered by ultrasound therapeutic transducers.

An automatic temperature controller, based on a PID algorithm, was implemented here for both mono-element and multi-elements HICU transducers. Chapter III describes the controller implementation for the rectal coil. At the same time, its stability and accuracy was demonstrated over large possible input errors (absorption and diffusion). Its accuracy was better than 10%[*]. Variations of the assumed absorption coefficient strongly influenced the convergence of the feedback-loop, while diffusion errors have only slight influence. Overestimation of absorption caused temperature overshoots, but still showed a stable behavior. More critical was the underestimation of absorption (by a factor 4 or more) which induced, at an unpredictable moment, an unstable behavior. It is therefore preferable to overestimate the absorption rather than to underestimate it.

The temperature control could be performed at various depths, e.g. from 2 to 10 mm, along the ultrasound sonication direction. Moreover, it can be automatically defined (as for example the maximum temperature reached within a defined ROI or the distal border of a tumoral depth), or it can be pointed out on the image. The temperature was controlled on a geometrical grid providing one control point per beam. The fast switched interleaved beams approach presented in Chapter IV, permitted the temperature control for each beam. During the same dynamic acquisition, the temperature was controlled at three points from the target ROI, with high accuracy: temperature error less than 3% and SDT up to 8%. The controller demonstrated also high accuracy during the *in-vivo* experimentation: 4.35% SDT, 0.3% error of the mean temperature. Such values of the SDT induced less than 30% error of the thermal dose. Note that the accuracy of the controller was influenced by the accuracy of the temperature measurements. Hence, indirectly, the sensitivity gain of the integrated coil improves also the accuracy of the temperature controller.

[*] *Ex-vivo* study ; external coils.

V.3.3 Ultrasound transducer efficiency and treatment planning

The RF coils and the automatic temperature control were developed in order to ensure the safety of the therapeutic method. Developments in ultrasound transducer design and optimization of the treatment planning are related to the efficacy of the method.

The first observation regarding the ultrasound transducers was a relative thermal fragility of the phased-array transducers compared to the mono-element transducer. After several utilizations, elements of the phased-array transducer become less efficient. Moreover, in the case of the rectal coil, the diameter of the pipes ensuring the internal cooling circuit was thought insufficient. Generally, even when activating slightly focused beams, the maximum (relative) temperature elevation was around 40°C.

Another main characteristic of the rectal transducer was observed during the *in-vivo* experimentations, when undesired lesion of the skin was produced. This interface problem appeared due to the higher penetration depth available at 3.57 MHz. No such undesired effects were observed with the other two transducers, working at 5.15 MHz, and 9.45 MHz. Moreover, the design of the incurved 256-element transducer (Chapter V) is expected to overcome this problem.

The benefits of the phased-array geometry of the transducer (electronic rotation, choice of planar or focused beam mode, multiple beams activation) were demonstrated *in-vivo* (Chapter III). Focusing the beam at different depths (from 10 to 20 mm) permitted to modulate the location of the lesion. The treatment strategy, based on the fast-switched multiple beams approach, was demonstrated with the new esophageal multi-element transducer (Chapter IV). In these cases, the cross thermal diffusion between the two neighboring beams may be exploited, conducting to a possible fusion of the two individual lesions.

No tumor model was available. Therefore, simulation methods, which permitted to the user to define various shapes of tumor, were considered. The simulation algorithm, based on the multi-beam activation, showed good results (less than 10% error) for a pre-operative therapy planning. The algorithm permitted to define an optimal strategy for the treatment planning of a defined tumor. Moreover, the short computing time suggested that in-situ planning of the dosimetry would be realizable.

V.4 Perspectives

The acoustic simulations presented in Chapter V aimed to design a new transducer, more efficient, and permitting a sharp separation between treated and untreated regions. The natural focalization was considered together with electronic rotation of the beams and the focus displacement along the radial dimension. Moreover, considering the skin lesion which appeared at an operating frequency of 3.57 MHz, higher frequencies should be considered. The results of these simulations could represent an important starting point in order to manufacture a new type of ultrasound transducer.

Another issue that should be analyzed is the determination of the optimal temperature of the water cooling balloon, which induces a minimal heat-sink phenomenon. In addition, higher diameters of the internal cooling pipes are necessary in order to ensure a good cooling of the internal active surface of the transducer. A more intense internal cooling may decrease the thermal fragility of elements of the phased-array transducers.

Regarding the considered applications, rectal or esophageal, the influence of local movements could be critical. It was showed during the *in-vivo* experiments, that a setup holding the transducer was necessary, even when treating the rectum. It is even more critical in the case of the esophagus, since multiple motions appear in this specific region (respiratory, cardiac and peristaltic motion). Motion robust PRFS-based MR thermometry should therefore be implemented when aiming *in-vivo* feasibility studies. When using standard, single reference PRFS method, potential variations in the measured phase, due to local motion and distant susceptibility effects from lungs, would far overweight the small SDT reported here with the integrated coil. Respiratory gating of the acquisition should be sufficient to avoid susceptibility induced errors due to lungs changing their air volume with breathing, although with significant lost in temporal resolution. Multi-reference PRFS thermometry is another option to overcome temperature artifacts. The most important issue, in our opinion, is to avoid intra-scan motion artifacts, i.e. ghosting, that is to be able to perform rapid enough acquisition whilst providing sufficient SNR. The small FOV and the sensitivity improvement provided by the integrated coil are expected to provide significant benefit for ultra-fast acquisition.

References:

Aouba, A., F. Péquignot and A. Le Toullec (2007). "Les causes médicales de décès en France en 2004 et leur évolution 1980-2004." Bulletin épidémiologique hebdomadaire / Institut de veille sanitaire **35-36**: 308-314.

Armenean, C., O. Beuf, *et al*. (2007). "Interventional MRI: risk of burns to the patient and radiologist." J Radiol. **88**(4): 599-600.

Armenean, M. (2002). Spectroscopie et imagerie de faibles volumes par RMN : conception et optimisation de capteurs radiofréquence implantables et endoluminaux. Thesis. Lyon, Université Claude-Bernard Lyon I. **154 p**.

Beets-Tan, R. G., G. L. Beets, *et al*. (2001). "Accuracy of magnetic resonance imaging in prediction of tumour-free resection margin in rectal cancer surgery." Lancet **357**: 497-504.

Belot, A., P. Grosclaude, *et al*. (2008). "Cancer incidence and mortality in France over the period 1980-2005." Rev Epidemiol Sante Publique **56**(3): 159-175.

Beuf, O., F. Pilleul, *et al*. (2004). "In vivo colon wall imaging using endoluminal coils: feasibility study on rabbits." J Magn Reson Imaging **20**(1): 90-96.

Beynon, J. (1989). "An evaluation of the role of rectal endosonography in rectal cancer." Annals of the Royal College of Surgeons of England **71**(2): 131-139.

Bouvier, A. M., C. Binquet, *et al*. (2006). "Management and prognosis of esophageal cancers: has progress been made?" European Journal of Cancer **42**(2): 228-233.

Brennen, C. E. (1995). Cavitation and bubble dynamics. New York, Oxford University Press, 294 p.

Cancer Research UK (2005). "CancerStats report - Oesophageal cancer -UK." Cancer Research UK.

Cancer Research UK (2005). "CancerStats report - Worldwide Cancer " Cancer Research UK.

Cash, B. D., L. R. Johnston and M. H. Johnston (2007). "Cryospray ablation (CSA) in the palliative treatment of squamous cell carcinoma of the esophagus." World J Surg Oncol. **16**: 5-34.

Chapelon, J. Y., J. Margonari, *et al*. (1992). "Effects of high-energy focused ultrasound on kidney tissue in the rat and the dog." Eur Urol. **22**(2): 147-152.

Chapelon, J. Y., M. Ribault, *et al*. (1999). "Treatment of localised prostate cancer with transrectal high intensity focused ultrasound." Eur J Ultrasound. **9**(1): 31-38.

Chen, J., Z. Feng and J. Jin (1998). "Numerical simulation of SAR and B1-field inhomogeneity of shielded RF coils loaded with the human head." EEE Trans Biomed Eng. **45**(5): 650-659.

Chen, L., G. R. ter Haar, *et al*. (1993). "Effect of blood perfusion on the ablation of liver parenchyma with high-intensity focused ultrasound." Phys Med Biol. **38**: 1661-1673.

Chopra, R., M. Burtnyk, M. A. Haider and M. J. Bronskill (2005). "Method for MRI-guided conformal thermal therapy of prostate with planar transurethral ultrasound heating applicators." Phys Med Biol. **50**(21): 4957-75.

Chopra, R., K. Tang, *et al*. (2009). "Analysis of the spatial and temporal accuracy of heating in the prostate gland using transurethral ultrasound therapy and active MR temperature feedback." Phys Med Biol. **54**(9): 2615-2633.

Chung, A. H., K. Hynynen, *et al*. (1996). "Optimization of spoiled gradient-echo phase

imaging for in vivo localization of a focused ultrasound beam." Magn Reson Med. **36**(5): 745-752.
Cline, H. E., K. Hynynen, *et al*. (1994). "MR temperature mapping of focused ultrasound surgery." Magn Reson Med. **31**: 628-636.
Cline, H. E., K. Hynynen, *et al*. (1996). "Simultaneous magnetic resonance phase and magnitude temperature maps in muscle." Magn Reson Med. **35**(3): 309-315.
Collins, C. M., W. Liu, *et al*. (2004). "Temperature and SAR calculations for a human head within volume and surface coils at 64 and 300 MHz." J Magn Reson Imaging. **19**(5): 650-656.
Conturo, T. E. and G. D. Smith (1990). "Signal-to-noise in phase angle reconstruction: dynamic range extension using phase reference offsets." Magn Reson Med. **15**(3): 420-437.
Coussios, C. C., C. H. Farny, G. T. Haar and R. R.A. (2007). "Role of acoustic cavitation in the delivery and monitoring of cancer treatment by high-intensity focused ultrasound (HIFU)." Int J Hyperthermia **23**(2): 105-120.
Cranston, J. M., I. Rivens, G. ter Haar and J. Kennedy (2006). A pilot study investigating the potential of high-intensity focused ultrasound to treat tumours rapidly. Proceedings of the 6th International Symposium on Therapeutic Ultrasound, Oxford, UK, p 382-389.
Damianou, C. A., K. Hynynen and F. Xiaobing (1995). "Evaluation of accuracy of a theoretical model for predicting the necrosed tissue volume during focused ultrasound surgery." IEEE Transactions on Ultrasonics, Ferroelectrics and Frequency Control **42**(2): 182-187.
Damianou, C. (2003). "In vitro and in vivo ablation of porcine renal tissues using high-intensity focused ultrasound." Ultrasound Med Biol. **29**(9): 1321-1330.
Daum, D. R. and K. Hynynen (1998). "Thermal dose optimization via temporal switching in ultrasound surgery." IEEE Trans Ultrason Ferroelectr Freq Control **45**(1): 208-215.
Davidson, F. (1991). Ultrasonic power balances. Output Measurements for Medical Ultrasound. R. C. Preston. London, Springer**:** 75-90.
De Poorter, J., C. De Wagter, *et al*. (1995). "Noninvasive MRI thermometry with the proton resonance frequency (PRF) method: in vivo results in human muscle." Magn Reson Med. **33**: 74-81.
de Zwart, J. A., F. C. Vimeux, *et al*. (1999). "Fast lipid-suppressed MR temperature mapping with echo-shifted gradient-echo imaging and spectral-spatial excitation." Magn Reson Med. **42**: 53-59.
de Zwart, J. (2000). Fast magnetic resonance temperature imaging for control of localized hyperthermia in medicine. Thesis. Bordeaux, Université Victor Segalen Bordeaux 2**:** 187 p.
Dees, J., M. A. Meijssen and E. J. Kuipers (2006). "Argon plasma coagulation for radiation proctitis." Scand J Gastroenterol Suppl. **243**: 175-178.
Dewhirst, M. W., B. L. Viglianti, *et al*. (2003). "Basic principles of thermal dosimetry and thermal thresholds for tissue damage from hyperthermia." Int J Hyperthermia **19**(3): 267-294.
Diederich, C. J., W. H. Nau and P. R. Stauffer (1999). "Ultrasound applicators for interstitial thermal coagulation." IEEE Trans Ultrason Ferroelectr Freq Control **46**(5): 1218-1228.
Dores, G. M., C. Metayer, *et al*. (2002). "Second malignant neoplasms among long-term

survivors of Hodgkin's disease: a population-based evaluation over 25 years." Journal of Clinical Oncology **20**(16): 3484-3494.
Duck, F. A. (1990). Physical Properties of Tissue. A comprehensive reference book. London: Academic press, Harcourt Brace Jovanovich, Publishers.
Eisenstat, T. E. and G. C. Oliver (1992). "Electrocoagulation for adenocarcinoma of the low rectum." World J Surg Oncol. **16**(3): 458-462.
Ell, C., A. May, *et al*. (2000). "Endoscopic mucosal resection of early cancer and high-grade dysplasia in Barrett's esophagus." Gastroenterology **118**(4): 670-677.
Engel, L. S., W.-H. Chow , *et al*. (2003). "Population attributable risks of esophageal and gastric cancers." Journal of the National Cancer Institute **95**(18): 1404-1413.
Ferlay, J., F. Bray, P. Pisani and D. M. Parkin (2004). "GLOBOCAN 2002: Cancer Incidence, Mortality and Prevalence Worldwide." IARC CancerBase No.5, Version 2.0. IARCPress, Lyon.
Fleury, G., R. Berriet, O. Le Baron and B. Huguenin (2002). New piezocomposite transducers for therapeutic ultrasound. Proceedings of the 2nd International Symposium on Therapeutic Ultrasound, Seattle.
Fujii, M., K. Sakamoto, *et al*. (1999). "Study of the cause of the temperature rise at the muscle-bone interface during ultrasound hyperthermia." IEEE Transactions on Biomedical Engineering **46**(5): 494-504.
Gasowski, M., I. Brocheriou and J. C. Vaillant (2003). Les cancers colorectaux (chapitre 16). Univ. Paris VI, Service de radiothérapie - Pr. Baillet (http://www.chups.jussieu.fr/polys/cancero/cancero.pdf, 02.2009)
Germain, D., P. Chevallier, *et al*. (2001). "MR monitoring of laser-induced lesions of the liver in vivo in a low-field open magnet: temperature mapping and lesion size prediction." J Magn Reson Imaging **13**(1): 42-49.
Germain, D., E. Vahala, *et al*. (2002). "MR temperature measurement in liver tissue at 0.23 T with a steady-state free precession sequence." Magn Reson Med. **47**(5): 940-947.
Gianfelice, D., A. Khiat, *et al*. (2003). "MR imaging-guided focused US ablation of breast cancer: histopathologic assessment of effectiveness- initial experience." Radiology **227**(3): 849-855.
Gilderdale, D. J., A. D. Williams, U. Dave and N. M. deSouza (2003). "An inductively-coupled, detachable receiver coil system for use with magnetic resonance compatible endoscopes." J Magn Reson Imaging **18**(1): 131-135.
Glaser, F., P. Schlag and C. Herfarth (1990). "Endorectal ultrasonography for the assessment of invasion of rectal tumours and lymph node involvement." British Journal of Surgery **77**(8): 883-887.
Golay, X., J. A. de Zwart, Y. C. Ho and Y. Y. Sitoh (2004). "Parallel imaging techniques in functional MRI." Top Magn Reson Imaging **15**(4): 255-265.
Gorny, K. R., M. A. Bernstein, *et al*. (2008). "Calorimetric calibration of head coil SAR estimates displayed on a clinical MR scanner." Phys Med Biol. **53**(10): 2565-2576.
Goss, S. A., L. A. Frizzell and L. Dunn (1979). "Ultrasonic absorption and attenuation of high frequency sound in mammalian tissues." Ultrasound Med Biol. **5**: 181-186.
Gossner, L., A. May, *et al*. (1999). "KTP laser destruction of dysplasia and early cancer in columnar-lined Barrett's esophagus." Gastrointest Endosc. **49**(1): 8-12.
Gossner, L. (2006). "The role of endoscopic resection and ablation therapy for early lesions." Best Pract Res Clin Gastroenterol. **20**(5): 867-876.
Graham, A. J., F. M. Shrive, *et al*. (2007). "Defining the optimal treatment of locally advanced esophageal cancer: a systematic review and decision analysis." Ann

Thorac Surg. **83**(4): 1257-1264.
Green, S. H., V. P. Khatri and J. P. McGahan (2008). "Radiofrequency ablation as salvage therapy for unresectable locally recurrent rectal cancer." J Vasc Interv Radiol. **19**(3): 454-458.
Haacke, E. M., R. W. Brown, M. R. Thompson and R. Venkatesan (1999). Magnetic Resonance Imaging: Physical principles and Sequence design, John Wiley & Sons, 893 p.
Hage, M., P. D. Siersema, *et al*. (2006). "Genomic analysis of Barrett's esophagus after ablative therapy: persistence of genetic alterations at tumor suppressor loci." Int J Cancer. **118**(1): 155-160.
Hahn, G. M. (1984). "Hyperthermia for the engineer: a short biological primer." IEEE Transactions on Biomedical engineering **31**: 3-8.
Hazle, J. D., R. J. Stafford and R. E. Price (2002). "Magnetic resonance imaging-guided focused ultrasound thermal therapy in experimental animal models: correlation of ablation volumes with pathology in rabbit muscle and VX2 tumors." J Magn Reson Imaging **15**(2): 185-194.
Heald, R. J., E. M. Husband and R. D. H. Ryall (1982). "The mesorectum in rectal cancer surgery-the clue to pelvic recurrence?" British Journal of Surgery **69**: 613-616.
Hedrick, W. R., D. L. Hykes and D. E. Starchman (1995). Ultrasound Physics and Instrumentation. 3rd edition. Saint Louis, U.S.A., Mosby Inc., 382 p.
Henglein, A. and C. Kormann (1985). "Scavenging of OH radicals produced in the sonolysis of water." Int J Radiat Biol Relat Stud Phys Chem Med. **48**(2): 251-258.
Herzka, D. A., F. H. Epstein and E. R. McVeigh (2000). Improved SNR in breath-hold cardiac cine imaging by slice interleaving. Proceedings of the 8th Annual Meeting of International Society for Magnetic Resonance in Medicine, Denver, USA, p 1529.
Hillenbrand, C. M., D. R. Elgort, *et al*. (2004). "Active device tracking and high-resolution intravascular MRI using a novel catheter-based, opposed-solenoid phased array coil." Magn Reson Med. **51**(4): 668-675.
Hindman, J. C. (1966). "Proton resonance shift of water in gas and liquid states." J Chem Phys. **44**: 4582-4592.
Hricak, H., S. White, *et al*. (1994). "Carcinoma of the prostate gland: MR imaging with pelvic phased-array coils versus integrated endorectal--pelvic phased-array coils." Radiology **193**(3): 703-709.
Huh, C. H., M. S. Bhutani, E. B. Farfán and W. E. Bolch (2003). "Individual variations in mucosa and total wall thickness in the stomach and rectum assessed via endoscopic ultrasound." Physiol Meas. **24**(4): N15-N22.
Hwang, J. J. (2007). "Role of chemotherapy in the treatment of gastroesophageal cancers." Oncology (Williston Park) **21**(5): 579-592.
Hynynen, K. (1991). "The threshold for thermally significant cavitation in dog's thigh muscle in vivo." Ultrasound in medicine & biology **17**(2): 157-169.
Hynynen, K., O. Pomeroy, *et al*. (2001). "MR imaging-guided focused ultrasound surgery of fibroadenomas in the breast: a feasibility study." Radiology **219**: 176-185.
ICNIRP (The International Commission on Non-Ionizing Radiation Protection, 2004). "Medical magnetic resonance (MR) procedures: protection of patients." Health Physics (2): 197-216.
Illing, R. O., J. E. Kennedy, *et al*. (2005). "The safety and feasibility of extracorporeal high-intensity focused ultrasound (HIFU) for the treatment of liver and kidney tumours in a Western population." Br J Cancer. **93**(8): 890-895.

Ishihara, Y., A. Calderon, *et al*. (1995). "A precise and fast temperature mapping using water proton chemical shift." Magn Reson Med. **34**(6): 814-823.
Jolesz, F. A., A. R. Bleier, *et al*. (1988). "MR imaging of laser-tissue interactions." Radiology **168**: 249-253.
Jolesz, F. A., K. Hynynen, *et al*. (2004). "Noninvasive thermal ablation of hepatocellular carcinoma by using magnetic resonance imaging-guided focused ultrasound." Gastroenterology **127**(5 Suppl 1): S 242-247.
Jolesz, F. A., K. Hynynen, N. McDannold and C. Tempany (2005). "MR imaging-controlled focused ultrasound ablation: a noninvasive image-guided surgery." Magn Reson Imaging Clin N Am. **13**(3): 545-560.
Kandarpa, K., P. Jakab, *et al*. (1993). "Prototype miniature endoluminal MR imaging catheter." J Vasc Interv Radiol. **4**: 419-427.
Kapiteijn, E., C. A. Marijnen, *et al*. (2001). "Preoperative radiotherapy combined with total mesorectal excision for resectable rectal cancer." N Engl J Med. **345**(9): 638-646.
Karagoz, I. and M. K. Kartal (2006). "Evaluation of nonscanned mode soft-tissue thermal index in the presence of the residual temperature rise." Ultrasound Med Biol. **32**(5): 741-750.
Kastler, B., D. Vetter, Z. Patay and P. Germain (2006). Comprendre l'IRM: Manuel d'auto-apprentissage, Elsevier Masson (sixième edition).
Keeler, J. (2002). Understanding NMR Spectroscopy, University of Cambridge, Department of Chemistry.
Kennedy, J. E., G. R. ter Haar and D. Cranston (2003). "High intensity focused ultrasound: surgery of the future?" Br J Radiol. **76**(909): 590-599.
Kennedy, J. E., F. Wu, *et al*. (2004). "High-intensity focused ultrasound for the treatment of liver tumours." Ultrasonics **42**: 931-935.
Kneeland, J. B. and J. S. Hyde (1989). "High-resolution MR imaging with local coils." Radiology **171**(1): 1-7.
Kumar, A., D. Welti and R. R. Ernst (1975). "NMR Fourier zeugmatography." J Magn Reson. **18**: 69-83.
Kuroda, K., K. Oshio, *et al*. (1997). "Temperature mapping using the water proton chemical shift: a chemical shift selective phase mapping method." Magn Reson Med. **38**: 845-851.
Kuroda, K., A. H. Chung, K. Hynynen and F. A. Jolesz (1998). "Calibration of water proton chemical shift with temperature for noninvasive temperature imaging during focused ultrasound surgery." J Magn Reson Imaging **8**(1): 175-181.
Kuroda, K. (2005). "Non-invasive MR thermography using the water proton chemical shift." International Journal of Hyperthermia **21**(6): 547-560.
Lafon, C., S. Chosson, *et al*. (2000). "The feasibility of constructing a cylindrical array with a plane rotating beam for interstitial thermal surgery." Ultrasonics **37**(9): 615-621.
Lafon, C., Y. Theillére, *et al*. (2000). "Development of an interstitial ultrasound applicator for endoscopic procedures: animal experimentation." Ultrasound Med Biol. **26**(4): 669-675.
Langevin, P. (1917). "French Patent No. 505, 703 (filed September 17, 1917; issued August 5, 1920)."
Le Bihan, D., J. Delannoy and R. L. Levin (1989). "Temperature mapping with MR imaging of molecular diffusion: application to hyperthermia." Radiology **171**: 853-857.
Lefebvre, J.-P., P. Lasaygue, *et al*. (2004). "L'acoustique ultrasonore et ses applications (1re

partie)." Acoustique & Techniques **36**(Dossier special: ULTRASONS): 4-11.
Lele, P. P. (1977). "Thresholds and mechanisms of ultrasonic damages to "organised" animal tissues." In Hazzard D.G, Litz M.L (eds). Symposium on biological effects and characterisations of ultrasonic sources.DHEW publication FDA 78-8048. United states departement of health, education and welfare, Rockville,MD: 224-239.
Li, J.-H. and F.-F. Liu (1997). "Intracellular pH and heat sensitivity in two human cancer cell lines." Radiotherapy and Oncology **42**(1): 69-76.
Lightdale, C. J., S. K. Heier, *et al*. (1995). "Photodynamic therapy with porfimer sodium versus thermal ablation therapy with Nd:YAG laser for palliation of esophageal cancer: a multicenter randomized trial." Gastrointest Endosc. **42**(6): 507-512.
Lordick, F. (2005). "Neoadjuvant therapy for squamous cell carcinoma of the esophagus." Chirurg. **76**(11): 1025-1032.
Lynn, J. G., R. L. Zwemer, A. J. Chick and A. E. Miller (1942). "A new method for the generation and use of focused ultrasound in experimental biology." J Gen Physiol. **26**: 179-193.
Maeda, K., M. Maruta, *et al*. (2002). "Minimally invasive surgery for carcinoid tumors in the rectum." Biomed Pharmacother. **56**(Suppl 1): 222-226.
Maier, A. and M. Fuchsja¨ger (2003). "Preoperative staging of rectal cancer." European Journal of Radiology **47**: 89-97.
Malcolm, A. L. and G. R. ter Haar (1996). "Ablation of tissue volumes using high intensity focused ultrasound." Ultrasound in Med & Biol. **22**(5): 659-669.
Mariette, C. and J. P. Triboulet (2007). "What's new in esophageal cancer treatment." Presse Med. **36**(3 Pt 2): 496-500.
Martin, A. J., D. B. Plewes and R. M. Henkelman (1992). "MR imaging of blood vessels with an intravascular coil." J Magn Reson Imaging **2**: 421-429.
May, A., L. Gossner, *et al*. (1999). "Local treatment of early cancer in short Barrett's esophagus by means of argon plasma coagulation: initial experience." Endoscopy **31**(6): 497-500.
McDannold, N. J., R. L. King, F. A. Jolesz and K. H. Hynynen (2000). "Usefulness of MR imaging-derived thermometry and dosimetry in determining the threshold for tissue damage induced by thermal surgery in rabbits." Radiology **216**(2): 517-523.
McDannold, N., M. Moss, *et al*. (2003). "MRI-guided focused ultrasound surgery in the brain: tests in a primate model." Magn Reson Med. **49**(6): 1188-1191.
McDannold, N. (2005). "Quantitative MRI-based temperature mapping based on the proton resonant frequency shift: Review of validation studies." Int J Hyperthermia **21**(6): 533-546.
Meijer, S., F. D. Rahusen and L. G. van der Plas (1999). "Palliative cryosurgery for rectal carcinoma." Int J Colorectal Dis. **14**: 177-180.
Melodelima, D., C. Lafon, *et al*. (2002). "Ultrasound cylindrical phased array for transoesophageal thermal therapy: Initial studies." Phys Med Biol. **47**: 4191-4203.
Melodelima, D., C. Lafon, *et al*. (2003). "Transoesophageal ultrasound applicator for sector-based thermal ablation: first in vivo experiments." Ultrasound Med Biol. **29**(2): 285-291.
Melodelima, D. (2004). Applicateur ultrasonore intraluminal à balayage électronique pour le traitement des cancers de l'oesophage guidé par IRM : Optimisation de la profondeur traitée par association de la cavitation. Thesis. Lyon, Université Claude Bernard Lyon 1**:** 142 p.

Melodelima, D., R. Salomir, *et al*. (2005). "Intraluminal high intensity ultrasound treatment in the esophagus under fast MR temperature mapping: in vivo studies." Magn Reson Med. **54**(4): 975-982.

Melodelima, D., F. Prat, *et al*. (2008). "Treatment of esophageal tumors using high intensity intraluminal ultrasound: first clinical results." J Transl Med. **5**: 6-28.

Miller, N. R., K. M. Bograchev and J. C. Bamber (2005). "Ultrasonic temperature imaging for guiding focused ultrasound surgery: Effect of angle between imaging beam and therapy beam." Ultrasound in medicine & biology **31**(3): 401-413.

Minsky, B. D. and J. G. Guillem (2008). "Multidisciplinary management of resectable rectal cancer. New developments and controversies." Oncology (Williston Park) **22**(12): 1430-1437.

Norberto, L., L. Polese, *et al*. (2005). "Laser photoablation of colorectal adenomas: a 12-year experience." Surg Endosc. **19**(8): 1045-1048.

O'Brien, W. D., Jr, and D. S. Ellis (1999). "Evaluation of the unscanned soft-tissue thermal index." IEEE Transactions on Ultrasonics, Ferroelectrics, and Frequency Control **46**(6): 1459-1476.

O'Brien, W. D. J. (2007). "Ultrasound-biophysics mechanisms." Prog Biophys Mol Biol. **93**(1-3): 212-255.

Office for National Statistics (2008). "Cancer Statistics registrations: Registrations of cancer diagnosed in 2005, England." **Series MB1**(36).

Ohliger, M. A. and S. DK. (2006). "An introduction to coil array design for parallel MRI." NMR Biomed. **19**(3): 300-315.

Oosterhof, G. O., E. B. Cornel, *et al*. (1996). "The influence of high-energy shock waves on the development of metastases." Ultrasound in medicine & biology **22**(3): 339-344.

Oulmane, F., V. Detti, *et al*. (2007). Radiofrequency power deposition near metallic wires during MR imaging: feasibility study using T1-weighted thermal imaging. Proceedings of IEEE Eng Med Biol Soc, p 3894-3897.

Parker, D. L., V. Smith, *et al*. (1983). "Temperature distribution measurements in two-dimensional NMR imaging." Med Phys. **10**(3): 321-325.

Parkin, D. M., F. Bray, J. Ferlay and P. Pisani (2005). "Global cancer statistics, 2002." CA Cancer J Clin. **55**(2): 74-108.

Pennes, H. H. (1948). "Analysis of tissue and arterial blood temperature in the resting human forearm." J Appl Physiol. **1**: 93-122.

Pernot, M., J. F. Aubry, *et al*. (2007). "In vivo transcranial brain surgery with an ultrasonic time reversal mirror." J Neurosurg. **106**(6): 1061-1066.

Peters, R. D., R. S. Hinks and R. M. Henkelman (1998). "Ex vivo tissue-type independence in proton-resonance frequency shift MR thermometry." Magn Reson Med. **40**(3): 454-459.

Peters, R. D., R. S. Hinks and R. M. Henkelman (1999). "Heat-source orientation and geometry dependence in proton-resonance frequency shift magnetic resonance thermometry." Magn Reson Med. **41**(5): 909-918.

Piel, J. E., R. O. Giaquinto, *et al*. (2005). A trans-rectal focused ultrasound probe for MR-guided ablation of the prostate. Proceedings of the 13th Annual Meeting of International Society for Magnetic Resonance in Medicine, Miami, USA, p 152.

Pilatou, M. C., E. A. Stewart, *et al*. (2009). "MRI-based thermal dosimetry and diffusion-weighted imaging of MRI-guided focused ultrasound thermal ablation of uterine fibroids." J Magn Reson Imaging **29**(2): 404-411.

Poguet, J., J. Marguet, *et al*. (2002). Phased Array technology : Concepts, probes and

applications. 8th European Congress on Non Destructive Testing, Barcelona, Spain.
Quesson, B., J. A. de Zwart and C. T. Moonen (2000). "Magnetic resonance temperature imaging for guidance of thermotherapy." J Magn Reson Imaging **12**(4): 525-533.
Quesson, B., F. Vimeux, *et al*. (2002). "Automatic control of hyperthermic therapy based on real-time Fourier analysis of MR temperature maps." Magnetic Resonance in Medicine **47**: 1065-1072.
Quick, H. H., J. M. Serfaty, *et al*. (2001). "Endourethral MRI." Magn Reson Med. **45**(1): 138-146.
Rabkin, B. A., V. Zderic, L. A. Crum and S. Vaezy (2006). "Biological and physical mechanisms of HIFU-induced hyperecho in ultrasound images." Ultrasound Med Biol. **32**(11): 1721-1729.
Rao, V. S., A. Al-Mukhtar, *et al*. (2005). "Endoscopic laser ablation of advanced rectal carcinoma--a DGH experience." Colorectal Dis. **7**(1): 58-60.
Rayleigh, L. (1945). Theory of sound. NewYork, Dover Publications, second edition.
Rieke, V., K. K. Vigen, *et al*. (2004). "Referenceless PRF shift thermometry." Magn Reson Med. **51**(1223-1231).
Rieke, V. and K. Butts Pauly (2008). "MR Thermometry." J Magn Reson Imaging **27**: 376-390.
Ries, L. A. G., D. Melbert, *et al*. (2008). "SEER Cancer Statistics Review, 1975-2005." National Cancer Institute. Bethesda, MD, http://seer.cancer.gov/csr/1975_2005/, based on November 2007 SEER data submission, posted to the SEER web site, 2008.
Robinson, T. and P. Lele (1969). "An analysis of lesion development in the brain and in plastics by high-intensity focused ultrasound at lowmegahertz frequencies." J Acoust Soc Am. **51**: 1333-1351.
Ross, A. B., C. J. Diederich, *et al*. (2004). "Highly directional transurethral ultrasound applicators with rotational control for MRI-guided prostatic thermal therapy." Phys Med Biol. **49**(2): 189-204.
Ross, H. M., J. A. Smelstoys, *et al*. (2006). "Photodynamic therapy with motexafin lutetium for rectal cancer: a preclinical model in the dog." J Surg Res. **135**(2): 323-330.
Roychoudhuri, R., H. Evans, D. Robinson and H. Møller (2004). "Radiation-induced malignancies following radiotherapy for breast cancer." British Journal of Cancer **91**: 868-872.
Salomir, R., F. C. Vimeux, *et al*. (2000). "Hyperthermia by MR-guided focused ultrasound: accurate temperature control based on fast MRI and a physical model of local energy deposition and heat conduction." Magn Reson Med. **43**: 342-347.
Salomir, R. (2001). Local hyperthermia by MRI-guided focused ultrasound: Fast MR-thermotherapy and on-line temperature control. Feasibility studies of tumor thermal ablation. Thesis. Bordeaux, Bordeaux 1**:** 194 p.
Salomir, R., J. Palussière, *et al*. (2005). "Local hyperthermia with MR-guided focused ultrasound: spiral trajectory of the focal point optimized for temperature uniformity in the target region." J Mag Reson Imaging **12**(4): 571-583.
Salomir, R., M. Rata, *et al*. (2006). Accurate temperature feedback control for MRI-guided, phased array HICU endcavitary therapy. Proceedings of the 6th International Symposium on Therapeutic Ultrasound, Oxford, UK, p 283-288.
Salomir, R., M. Rata, *et al*. (2009). "Endocavitary thermal therapy by MRI-guided phased-array contact ultrasound: Experimental and numerical studies on the multi-input

single-output PID temperature controller's convergence and stability." Med Phys. **36**(10): 4726-4741.

Santoro, G. A. and G. Di Falco (2006). Endosonographic Anatomy of the Normal Rectum (secttion III). Benign Anorectal Diseases.Diagnosis with Endoanal and Endorectal Ultrasound and New Treatment Options. Milan, Springer**:** 55-60.

Sapareto, S. A. and W. C. Dewey (1984). "Thermal dose determination in cancer therapy." Int J Radiat Oncol Biol Phys. **10**(6): 787-800.

Sauer, R., H. Becker, *et al*. (2004). "Preoperative versus postoperative chemoradiotherapy for rectal cancer." N Engl J Med. **351**(17): 1731-1740.

Saurin, J.-C. (2000). "Traitement endoscopique des cancers superficiels du tube digestif " Gastroentérologie Clinique et Biologique **24**(5): 128-133.

Schaefer, D. J. (1998). "Safety aspects of radiofrequency power deposition in magnetic resonance." Magn Reson Imaging Clin N Am. **6**(4): 775-789.

Schenck, J. F., H. R. Hart, *et al*. (1986). "High resolution magnetic resonance imaging using surface coils." Magn Reson Annu.: 123-160.

Schenck, J. F. (1996). "The role of magnetic susceptibility in magnetic resonance imaging: MRI magnetic compatibility of the first and second kinds." Med Phys. **23**(6): 815-850.

Sebastian, S., S. Johnston, *et al*. (2004). "Pooled analysis of the efficacy and safety of self-expanding metal stenting in malignant colorectal obstruction." Am J Gastroenterol. **99**(10): 2051-2057.

Sharma, V. K., K. K. Wang, *et al*. (2007). "Balloon-based, circumferential, endoscopic radiofrequency ablation of Barrett's esophagus: 1-year follow-up of 100 patients." Gastrointest Endosc. **65**(2): 185-195.

Shirouzu, K., H. Isomoto and T. Kakegawa (1995). "Distal spread of rectal cancer and optimal distal margin of resection for sphincter-preserving surgery." Cancer **76**(3): 388-392.

Sibille, A., F. Prat, *et al*. (1993). "Characterization of extracorporeal ablation of normal and tumor-bearing liver tissue by high intensity focused ultrasound." Ultrasound Med Biol. **19**(9): 803-813.

Siersema, P. D. (2006). "Therapeutic esophageal interventions for dysphagia and bleeding." Curr Opin Gastroenterol. **22**(4): 442-447.

Simon, J. M., J. J. Duron and C. Hoang (2003). Cancer de l'oesophage (chapter 15). Cancérologie. Univ.Paris VI, Service de radiothérapie - Pr. Baillet, (http://www.chups.jussieu.fr/polys/cancero/cancero.pdf, 02.2009)**:** 225-234.

Smith, N. B., N. K. Merrilees, M. Dahleh and K. Hynynen (2001). "Control system for an MRI compatible intracavitary ultrasound array for thermal treatment of prostate disease." Int J Hyperthermia **17**(3): 271-282.

Sokka, S. D., R. King and K. Hynynen (2003). "MRI-guided gas bubble enhanced ultrasound heating in in vivo rabbit thigh." Phys Med Biol. **48**(2): 223-241.

Tempany, C. M., E. A. Stewart, *et al*. (2003). "MR imaging-guided focused ultrasound surgery of uterine leiomyomas: a feasibility study." Radiology **226**(3): 897-905.

ter Haar, G. (1999). "Therapeutic ultrasound." European Journal of Ultrasound **9**(1): 3-9.

Urschel, J., H. Vasan and C. Blewett (2002). "A meta-analysis of randomized controlled trials that compared neoadjuvant chemotherapy and surgery to surgery alone for resectable esophageal cancer." Am J Surg. **183**(3): 274-279.

Van Outryve, M. J., P. A. Pelckmans, H. Fierens and Y. M. Van Maercke (1993). "Transrectal ultrasound study of the pathogenesis of solitary rectal ulcer

syndrome." Gut. **34**: 1422-1426.
Verrall, R. E. and C. M. Seghal (1988). Ultrasound: Its Chemical, Physical and Biological Effects. Sonoluminescence. K. Suslick. New York, VCH Publishers**:** 227 p
Viallon, M., S. Terraz, *et al*. (2010). "Observation and correction of transient cavitation-induced PRFS thermometry artifacts during radiofrequency ablation, using simultaneous Ultrasound/MR imaging." Med Phys. **37**(4): 1491-1506.
Vigen, K. K., B. L. Daniel, J. M. Pauly and K. Butts (2003). "Triggered, navigated, multibaseline method for proton resonance frequency temperature mapping with respiratory motion." Magn Reson Med. **50**: 1003-1010.
Villeneuve, L., L. Alberti, *et al*. (2009). "Assay of hydroxyl radicals generated by focused ultrasound." Ultrasonics Sonochemistry **16**(3): 339-344.
Wehrli, F. W. (1990). "Fast-scan magnetic resonance: principles and applications." Magn Reson Q. **6**(3): 165-236.
Weidensteiner, C., N. Kerioui, *et al*. (2004). "Stability of real-time MR temperature mapping in healthy and diseased human liver." J Mag Reson Imaging **19**: 438-446.
Wells, P. N. T. (1977). Biomedical ultrasonics. London: Academic press.
Wharton, I. P., I. H. Rivens, *et al*. (2007). "Design and development of a prototype endocavitary probe for high-intensity focused ultrasound delivery with integrated magnetic resonance imaging." J Magn Reson Imaging **25**(3): 548-56.
Wild, C. P. and L. J. Hardie (2003). "Reflux, Barrett's oesophagus and adenocarcinoma: burning questions " Nat Rev Cancer **3**(9): 676-684.
Xia, F., J. Mao, J. Ding and H. Yang (2008). "Observation of normal appearance and wall thickness of esophagus on CT images." European Journal of Radiology **Article in Press,doi:10.1016/j.ejrad.2008.09.002**.
Zderic, V., J. Foley, W. Luo and S. Vaezy (2008). "Prevention of post-focal thermal damage by formation of bubbles at the focus during high intensity focused ultrasound therapy." Med Phys. **35**(10): 4292-4299.
Zeqiri, B. (2007). "Metrology for ultrasonic applications." Progress in Biophysics and Molecular Biology **93**(1-3): 138-152
Zieren, J., M. Paul and C. Menenakos (2007). "Transanal endoscopic microsurgery (TEM) vs. radical surgery (RS) in the treatment of rectal cancer: indications, limitations, prospectives. A review." Acta Gastroenterol Belg. **70**(4): 374-380.

Appendix A. Thermal dose calculation

The thermal dose is calculated considering a continuous Gaussian distribution of the measured temperature T around a given value T_0 (expected temperature) with standard deviation denoted as σ. Hence, the experimentally assessed Thermal Dose can be written as follows:

$$TD_{\exp}(T_0) = \int_{-\infty}^{\infty} \rho(T) \cdot 2^{T-43}\, dT = \int_{-\infty}^{\infty} \frac{1}{\sqrt{2\pi}\cdot\sigma} \cdot \exp\left[-\frac{(T-T_0)^2}{2\sigma^2}\right] \cdot 2^{T-43}\, dT$$

$$= \frac{1}{\sqrt{2\pi}\cdot\sigma} \cdot 2^{T_0-43} \int_{-\infty}^{\infty} \exp\left[-\frac{(T-T_0)^2}{2\sigma^2}\right] \cdot 2^{T-T_0}\, dT$$

$$= \frac{1}{\sqrt{2\pi}\cdot\sigma} \cdot 2^{T_0-43} \int_{-\infty}^{\infty} \exp\left(-\frac{x^2}{2\sigma^2}\right) \cdot 2^{x} dx, \quad \text{where } x = T\text{-}T_0.$$

Furthermore, solving the integral we obtain:

$$TD_{\exp}(T_0) = \frac{1}{\sqrt{2\pi}\cdot\sigma} \cdot 2^{T_0-43} \int_{-\infty}^{\infty} \exp\left(-\frac{x^2}{2\sigma^2} + x\cdot\ln 2\right) dx = \frac{1}{\sqrt{2\pi}\cdot\sigma} \cdot 2^{T_0-43} \int_{-\infty}^{\infty} \exp\left[-\frac{1}{2\sigma^2}\left(x^2 - 2\sigma^2\cdot x\cdot\ln 2\right)\right] dx$$

$$= \frac{1}{\sqrt{2\pi}\cdot\sigma} \cdot 2^{T_0-43} \int_{-\infty}^{\infty} \exp\left\{-\frac{1}{2\sigma^2}\left[x^2 - 2\cdot\sigma^2\cdot x\cdot\ln 2 + \left(\sigma^2\cdot\ln 2\right)^2 - \left(\sigma^2\cdot\ln 2\right)^2\right]\right\} dx$$

$$= \frac{1}{\sqrt{2\pi}\cdot\sigma} \cdot 2^{T_0-43} \int_{-\infty}^{\infty} \exp\left\{-\frac{1}{2\sigma^2}\left[\left(x-\sigma^2\cdot\ln 2\right)^2 - \left(\sigma^2\cdot\ln 2\right)^2\right]\right\} dx$$

$$= \frac{1}{\sqrt{2\pi}\cdot\sigma} \cdot 2^{T_0-43} \int_{-\infty}^{\infty} \exp\left\{-\frac{1}{2\sigma^2}\left[\left(x-\sigma^2\cdot\ln 2\right)^2\right]\right\} \cdot \exp\left[\frac{\left(\sigma^2\cdot\ln 2\right)^2}{2\cdot\sigma^2}\right] dx$$

$$= \frac{1}{\sqrt{2\pi}\cdot\sigma} \cdot 2^{T_0-43} \cdot \exp\left[\frac{(\ln 2)^2}{2}\cdot\sigma^2\right] \int_{-\infty}^{\infty} \exp\left\{-\frac{1}{2\sigma^2}\left[\left(x-\sigma^2\cdot\ln 2\right)^2\right]\right\} dx$$

$$= \frac{1}{\sqrt{2\pi}\cdot\sigma} \cdot \frac{\sqrt{\pi}}{\sqrt{\frac{1}{2\sigma^2}}} \cdot 2^{T_0-43} \cdot \exp\left[\frac{(\ln 2)^2}{2}\cdot\sigma^2\right] = 2^{T_0-43} \cdot \exp\left[\frac{(\ln 2)^2}{2}\cdot\sigma^2\right]$$

$$= TD_{theor}(T_0) \cdot \exp\left[\frac{(\ln 2)^2}{2}\cdot\sigma^2\right] \approx TD_{theor}(T_0.) \cdot \exp\left(0.24\cdot\sigma^2\right)$$

Note that the last integral is a type of Gauss integral and was solved using the property of Gauss integral:

$\int_{-\infty}^{\infty} \exp\left(-\alpha\cdot x^2\right) dx = \sqrt{\frac{\pi}{\alpha}}$, when $\alpha > 0$.

Publications

1. Rares Salomir, Mihaela Rata, Cyril Lafon, François Cotton, Anne-Sophie-Delemazure, Jean Palussiere and Jean-Yves Chapelon, **Automatic feedback control of the temperature for MRI-guided therapeutic ultrasound**, *Proceedings of the 29th Annual International Conference of the IEEE EMBS*, Lyon, France, **2007**, 222-225.

2. Mihaela Rata, Rares Salomir, Reiner Umathum, Jurgen Jenne, Cyril Lafon, François Cotton, and Michael Bock, **Endoluminal ultrasound applicator with an integrated RF coil for high-resolution magnetic resonance imaging-guided high-intensity contact ultrasound thermotherapy**, *Phys. Med. Biol.*, **2008**, 53, 6549–6567.

3. Rares Salomir, Mihaela Rata, Daniela Cadis, Lorena Petrusca, Vincent Auboiroux, and François Cotton, **Endocavitary thermal therapy by MRI-guided phased-array contact ultrasound: Experimental and numerical studies on the multi-input single-output PID temperature controller's convergence and stability**. *Med. Phys.,* **2009**, 36(10), 4726-4741.

4. Lorena Petrusca, Rares Salomir, Rene Milleret, Olivier Pichot, Mihaela Rata, Francois Cotton, and Jean-Yves Chapelon, **Experimental investigation of thermal effects in HIFU-based external valvuloplasty with a non-spherical transducer, using high-resolution MR thermometry**, *Phys. Med. Biol.*, **2009**, 54, 5123–5138.

Peer-reviewed abstracts (Oral presentations)

6th International Symposium on Therapeutic Ultrasound (Oxford, UK) 2006

- **M. Rata**, R. Salomir, C. Lafon, J.-Y. Chapelon, F. Cotton, A. Bonmartin, and D. Cathignol: "Optimization of the thermal dosimetry for endocavitary HICU ablation of sectorial digestive tumours"
- R. Salomir, **M. Rata**, D. Cadis, C. Lafon, J.-Y. Chapelon, F. Cotton, A. Bonmartin, and D. Cathignol: "Accurate temperature feedback control for MRI-guided, phased array HICU endocavitary therapy"

6th Interventional MRI Symposium (Leipzig, Germany) 2006

- R. Salomir, **M. Rata**, C. Lafon, F. Cotton, A. Bonmartin, J.-Y. Chapelon, and D. Cathignol: "MRI-based real time control of endocavitary therapy with contact applicator of high intensity ultrasound"

7th International Symposium on Therapeutic Ultrasound (Seoul, Korea) 2007

- **M. Rata**, R. Salomir, R. Umathum, C. Lafon, J.-Y. Chapelon, F. Cotton, J. Jenne, and M. Bock: "Ultrasound applicator with integrated miniature coil for high resolution MRI guided HICU thermotherapy"

29th Annual International Conference of the IEEE Engineering in Medicine and Biology Society (Lyon, France) 2007

- R. Salomir, **M. Rata**, C. Lafon, F. Cotton, A.-S. Delemazure, J. Palussiere, and J.-Y. Chapelon: "Automatic feedback control of the temperature for MRI-guided therapeutic ultrasound"

16th Scientific Meeting of International Society for Magnetic Resonance in Medicine (Toronto, Canada) 2008, Thermal Therapy & Focused Ultrasound session, # 68, May 5th

- **M. Rata**, R. Salomir, R. Umathum, C. Lafon, J.-Y. Chapelon, F. Cotton, J. Jenne, and M. Bock: "Endoluminal ultrasound applicator with an integrated RF coil for high resolution MRI-guided HICU thermotherapy"

17th Scientific Meeting of International Society for Magnetic Resonance in Medicine (Honolulu, Hawaii) 2009, Thermal Therapy & Focused Ultrasound session, # 440, April 22nd

- **M. Rata**, F. Cotton, C. Paquet, V. Bîrlea, M. Bock, and R. Salomir: "Endocavitary phased-array applicator of therapeutic ultrasound with an integrated anti-Helmholtz coil for high resolution MRI -guided thermotherapy: an *in-vivo* study"

Résumé

Cette thèse présente des développements techniques et méthodologiques, visant une alternative viable pour le traitement des cancers digestifs. Par rapport aux méthodes classiques de thérapie (chirurgie et radio-chimiothérapie), l'utilisation d'applicateurs locaux d'ultrasons sous guidage IRM représente une méthode moins invasive. L'objectif principal de cette technique est une délivrance rapide et bien contrôlée de l'énergie ultrasonore à l'endroit souhaité, afin de permettre l'ablation des tumeurs par thermocoagulation. L'énergie ultrasonore est déposée dans le tissu cible par des applicateurs endocavitaires, positionnés en contact direct avec le tissu à traiter. L'environnement IRM offre deux avantages principaux: une bonne résolution spatiale de la région tumorale et, en même temps, un contrôle en temps réel de la dose thermique. La thermométrie basée sur la fréquence de résonance de protons (PRF) affiche en temps réel des cartes de température et de dose thermique obtenues dans les tissus chauffés par les ultrasons.

Une étude bibliographique (premier chapitre) nous offre la possibilité de nous immerger dans les trois domaines abordés dans le cadre de cette thèse: cancers, ultrasons et IRM. D'abord, les statistiques, les caractéristiques et les actuelles thérapies pour les cancers de l'œsophage et du rectum sont décrites. La place de la nouvelle alternative est discutée, en évoquant ses avantages, mais aussi ses limites, par rapport aux méthodes classiques et nouvelles de traitement. Les ultrasons n'ont pas d'effets secondaires, sont moins invasifs et, sous guidage d'IRM de température, permettent un bon contrôle de la chaleur délivrée. Cette méthode de traitement est indiquée dans un but palliatif pour tumeurs partiellement sténosées, mais aussi dans un but curatif pour les cancers peu développés. La deuxième section du chapitre présente les principes physiques généraux des ultrasons thérapeutiques et leurs applications cliniques. Le chapitre se termine par une présentation succincte des principes de l'IRM et, plus particulièrement, de l'IRM de température.

L'objectif de cette thèse est de développer la sécurité et l'efficacité de la nouvelle méthode. Le principe général de la technique consiste à bien cibler le dépôt de chaleur à l'intérieur du tissu tumoral, afin de détruire complètement la tumeur. Par contre, le tissu sain avoisinant doit être protégé. Par conséquent, un contrôle fiable et précis de l'évolution de la température pendant la sonication devient vital pour le succès de la méthode. Pour cela, l'utilisation des mini-antennes locales, intégrées à des transducteurs ultrasonores, a été envisagée avec pour objectif l'amélioration de la résolution (spatiale, temporale et en température) des acquisitions IRM, à 1.5 T. Trois prototypes d'antenne, chacun adapté à un type de transducteur ultrasonore, ont été étudiés. Dans le même but, un algorithme de contrôle de la température avec une boucle de rétrocontrôle a été développé. Cet algorithme, basé sur un régulateur PID (proportionnel intégral dérivé), a été adapté à la spécificité de la méthode: ultrasons de contact, sondes matricielles multiéléments à rotation électronique du faisceau, ballon de refroidissement, tir ultrasonore avec plusieurs faisceaux.

Les antennes intégrées et la boucle de rétrocontrôle de la température ont été développées afin d'améliorer la sécurité de la méthode. Le deuxième axe de recherche vise le développement de l'efficacité du traitement. Dans ce but, plusieurs points ont été abordés. Des études de faisabilité des transducteurs multiéléments ont été conduites *in-vivo,* sur des cochons sains. Des simulations acoustiques solutionnant le problème inverse ont été envisagées, afin de trouver une planification optimale de la séquence de tir ultrasonore. Pour une tumeur d'une forme donnée, les simulations cherchaient à proposer la meilleure stratégie de tir afin de garantir une couverture homogène du volume cible. Par ailleurs, un nouveau concept de transducteur ultrasonore, basé sur une focalisation géométrique naturelle, a été étudié.

Le premier prototype d'antenne (Chapitre II) a été conçu afin d'être intégré à un transducteur monoélément (surface active: 8 x 15 mm², 9.45 MHz, ballon de refroidissement), pour une application oesophagienne. La géométrie de l'antenne était une boucle rectangulaire en cuivre entourant la partie active ultrasonore. Vu son application endoscopique, l'antenne devait respecter des contraintes anatomiques (taille, biocompatibilité). La performance de l'antenne a été comparée *ex-vivo* avec une antenne clinique extracorporelle (4 éléments en réseau phasé), sur des échantillons de muscle de porc frais et des pièces de l'œsophage. Aucun artéfact RF ou de susceptibilité n'a été observé. Les artéfacts de flux causés par l'eau circulante à l'intérieur du ballon de refroidissement ont pu être projetés hors de la région d'intérêt. La sensibilité de l'antenne endocavitaire (mesure de l'écart type de la température ETT) a été améliorée d'un facteur 7 par rapport à l'antenne externe, à une profondeur de 10 mm. Ainsi, des images de haute résolution, anatomiques (T_1-w-TFE ou IR-T_1-w-TSE, voxel: 0.25 x 0.25 x 3 mm^3) et de température (méthode PRFS, EPI, voxel: 0.5 x 0.5 x 5 mm^3, 2.2 s/image, 0.3°C ETT moyen) ont pu être obtenues. Le champ de sensibilité de la mini antenne a montré un ETT inférieur à 1°C jusqu'à 25 mm, au-delà du ballon. De plus, le contrôle automatique de la température a montré une grande précision (ETT de 1.7% et une erreur moyenne de 1.1%).

Le chapitre III présente l'intégration du deuxième prototype d'antenne, cette fois pour un transducteur rectal (barrette cylindrique 1D à 64 éléments), travaillant à une fréquence de 3.57 MHz. La partie active du transducteur était la surface latérale d'un cylindre (diamètre de 14 mm et longueur de 20 mm), divisée longitudinalement en 64 éléments. Afin de s'adapter à cette structure particulière de transducteur, une géométrie différente à été envisagée pour l'antenne: des anti–solénoïdes, c'est à dire deux groupes de spires, à gauche et à droite de la surface active du transducteur. La performance de l'antenne a été étudiée par rapport au nombre de spires, par rapport à la présence du transducteur et aussi, par rapport à l'antenne standard extracorporelle. Cette intégration de l'antenne avec un transducteur rectal multiéléments a été validée *in-vivo* sur des cochons sains. Le nouveau dispositif endocavitaire a permis d'acquérir *in-vivo,* des images

anatomiques de haute résolution (voxel 0.4 x 0.4 x 5 mm^3) et des données de thermométrie avec une grande précision (voxel 0.75 x 0.75 x 8 mm^3, 2 s/image, ETT <1°C pour un rayon de 20 mm). Les expérimentations *in-vivo* ont aussi démontré les avantages de la structure "phased-array" du transducteur: rotation électronique du faisceau, capacité d'activer soit une onde plane soit une onde focalisée, ou encore la possibilité d'activer plusieurs faisceaux en même temps. L'implémentation du contrôleur de température est également expliquée dans ce chapitre. La température peut être contrôlée soit pour un point bien défini dans l'espace, soit pour toute une région d'intérêt. Dans le premier cas, la marge distale de la tumeur peut être utilisée comme un point de contrôle de la température. Dans le deuxième cas, le point de contrôle est la valeur maximale de la température enregistrée à l'intérieur de la région d'intérêt. La stabilité et la précision du contrôleur ont été démontrées pour une large gamme d'erreurs des paramètres d'entrée. L'évolution de la température a été contrôlée en temps réel, pendant la sonification, avec un ET de moins 5%.

La généralisation du contrôleur de température pour plusieurs faisceaux (chapitre IV) a permis de contrôler la température en plusieurs points de contrôle, de manière à avoir un point de contrôle par faisceau. Chapitre IV présente une stratégie de traitement des tumeurs, basée sur l'activation des plusieurs faisceaux, qui sont rapidement interchangés pendant la même dynamique de tir. Une stratégie de traitement optimale pour une tumeur d'une forme et d'une taille précises a été ainsi proposée suite aux simulations. La validation expérimentale de cette stratégie a été réalisée avec un transducteur multiéléments oesophagien. Ce transducteur a été conçu pour avoir la même géométrie que celle du transducteur rectal (barrette cylindrique 1D à 64 éléments), mais avec des dimensions plus réduites, adaptées à son utilisation oesophagienne. Cependant, son corps est beaucoup plus long, car des espaces ont été prévus latéralement autour de la zone active, comme support pour les spires de l'antenne. De plus, des tunnels à l'intérieur du corps du transducteur ont aussi été prévus, afin de pouvoir connecter par l'intérieur les deux groupes des spires. Cette conception a permis l'intégration de l'antenne dans le corps même du transducteur (sans support détachable), et, de plus, une diminution du diamètre total du dispositif. La faisabilité du dispositif endoscopique a été validée *ex-vivo*.

Le dernier chapitre présente des simulations acoustiques conduites afin de définir un nouveau prototype de transducteur avec une meilleure efficacité pour réaliser le balayage de la tumeur. Ces simulations montrent l'intérêt d'un transducteur tubulaire à 256 éléments, découpé à la fois en secteurs dans la dimension circulaire, et en segments dans la dimension longitudinale. La forme du transducteur, définie par une parabole, permettrait une focalisation géométrique naturelle. Le double découpage permettrait une rotation électronique du faisceau, mais aussi un balayage en profondeur (déplacement radial de la tâche focale). Une section comportant les conclusions générales de la thèse est présentée à la fin du chapitre.

TITRE en français. **Applicateur local endocavitaire d'ultrasons thérapeutiques intégré avec antenne réceptrice RF pour la thérapie thermique sous contrôle d'IRM de haute résolution**

RESUME en français. Cette thèse présente des développements techniques et méthodologiques visant une alternative viable pour le traitement des cancers digestifs (rectum, œsophage). Par rapport aux méthodes standards de thérapie, les ultrasons de contact de haute intensité sous guidage IRM sont une approche moins invasive. L'IRM offre 2 avantages: bonne résolution spatiale et contrôle en temps réel de la température. Cette méthode de traitement demande efficacité et sécurité. Trois prototypes d'antenne RF intégrées à des transducteurs ultrasonores ont été réalisés afin d'améliorer la résolution spatiale et temporelle des images IRM et la précision de la mesure de température. Les antennes intégrées ont montré une meilleure sensibilité par rapport à une antenne extracorporelle standard. Des images IRM haute résolution, anatomiques (voxel 0.4x0.4x5 mm^3) et de thermométrie (voxel 0.75x0.75x8 mm^3, 2s/image) ont été acquises *in-vivo*. La température a été mesurée, dans un rayon de 20 mm au-delà du ballon, avec un écart type <1°C. Les artéfacts de flux causés par l'eau circulante à l'intérieur du ballon de refroidissement ont pu être projetés hors de la région d'intérêt. L'évolution de la température a été contrôlée automatiquement, à des profondeurs variables, avec un point de contrôle par faisceau. Le contrôleur a montré une grande précision *in-vivo* (écart type <5%). Le transducteur ultrasonore matriciel permet d'activer successivement plusieurs faisceaux pendant la même dynamique de tir. Des simulations ont été conduites afin de proposer une planification du traitement optimale pour une tumeur désignée. Un nouveau concept de sonde ultrasonore à 256 éléments avec focalisation géométrique naturelle a été proposé.

TITRE en anglais. **Endocavitary applicator of therapeutic ultrasound integrated with RF receiver coil for high resolution MRI-controlled thermal therapy**

RESUME en anglais. This thesis presents technical and methodological developments aiming to offer a viable alternative for the treatment of digestive cancers (rectum and esophagus). Compared to the standard methods of therapy, the high intensity contact ultrasound guided by MRI is a less invasive approach. MRI offers 2 advantages: good spatial resolution, and real-time temperature control. This treatment method requires efficacy and safety. Three prototypes of RF coil integrated with ultrasound transducers were built in order to increase the spatial and temporal resolution of the MR images, and the accuracy of the temperature measurement. The integrated coils showed a better sensitivity compared to a standard extracorporeal coil. Anatomical (voxel 0.4x0.4x5 mm^3) and thermometry (voxel 0.75x0.75x8 mm^3, 2s/image) high resolution MR images were acquired *in-vivo*. The temperature was measured, within a radius of 20 mm from the balloon, with a standard deviation <1°C. The flow artifacts caused by the water circulating inside the cooling balloon could be shifted out of the region of interest. The temperature evolution was controlled automatically, at different depths, with one control point per beam. The controller showed a good accuracy during *in-vivo* experiments (standard deviation less than 5%). The phased-array ultrasound transducer permits the successive activation of multiple beams during the same dynamic of sonication. Simulations were conducted in order to offer an optimal treatment planning for a defined tumor. A new design of ultrasound transducer with 256 elements with revolution symmetry, based on a natural geometrical focalization, was proposed.

DISCIPLINE **Instrumentation Biomédicale**

MOTS-CLES **IRM de température, ultrasons thérapeutiques, cancer digestif, transducteur compatible IRM, antenne réceptrice RF, dispositif endoscopique integré, simulation**
MRI thermometry, therapeutic ultrasound, digestive cancer, MR-compatible transducer, RF receiver coil, integrated endoscopic device, modelization

INTITULE ET ADRESSE DU LABORATOIRE : **INSERM U556, Applications des ultrasons à la thérapie, 151, Cours Albert Thomas, 69 424, Lyon Cedex 03**